Spectroscopic investigation of charge-transfer processes and polarisation pulse shaping in the visible spectral range

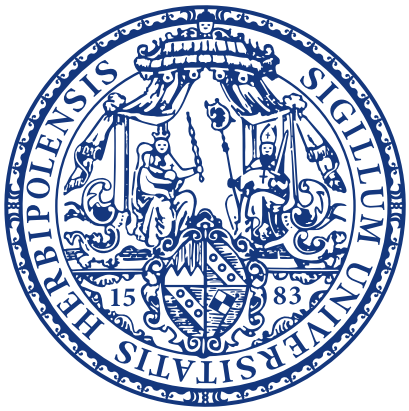

Dissertation zur Erlangung des
naturwissenschaftlichen Doktorgrades
der Julius-Maximilians-Universität
Würzburg

vorgelegt von
Tatjana Quast
aus Detmold

Würzburg 2012

Eingereicht bei der Fakultät für Chemie und Pharmazie
am 26.09.2012

Gutachter der schriftlichen Arbeit

1. Gutachter: Prof. Dr. Tobias Brixner
2. Gutachter: Prof. Dr. Christoph Lambert

Prüfer des öffentlichen Promotionskolloquiums

1. Prüfer: _____
2. Prüfer: _____
3. Prüfer: _____

Datum des öffentlichen Promotionskolloquiums _____

Doktorurkunde ausgehändigt am _____

List of publications

Parts of this work have been published in the following references:

Chapter 4:
D. Reitzenstein, T. Quast, F. Kanal, M. Kullmann, S. Ruetzel, M.S. Hammer, C. Deibel, V. Dyakonov, T. Brixner, and C. Lambert.
Synthesis and Electron Transfer Characteristics of a Neutral, Low-Band-Gap, Mixed-Valence Polyradical.
Chem. Mater **22**, 6641-6655 (2010).

Chapter 5:
J. Köhler, T. Quast, J. Buback, I. Fischer, T. Brixner, P. Nürnberger, B. Geiß, J. Mager and C. Lambert.
Ultrafast charge-transfer dynamics of donor-substituted truxenones.
PhysChemChemPhys **14**, 11081-11089 (2012).

The material of chapter 7 is currently in preparation for publication.

Own publications that are not related to this thesis:
U. Selig, F. Langhojer, F. Dimler, T. Löhrig, C. Schwarz, B. Gieseking, and T. Brixner.
Inherently phase-stable coherent two-dimensional spectroscopy using only conventional optics.
Optics Letters **33**, 2851-2853 (2008).

Contents

Chapter 1

Motivation

> The most exciting phrase to hear in science, the one that heralds new discoveries, is not "Eureka!" but "That's funny...".
>
> — Isaac Asimov, 1920–1992, American Science-Fiction author

The interaction between light and matter is one of the most fundamental processes in nature. On the one hand, it drives reactions like photosynthesis which can be regarded as the basis for life on earth [1]. On the other hand, light–matter interaction allows to study such processes since it is the basis for every spectroscopic technique. A plethora of such techniques exists which have been used to literally shed light on a wide variety of different scientific questions [2, 3]. Many spectroscopists must have muttered something like "That's funny..." since spectroscopy is the field of research that helped elucidate the constitution of matter and has led to a number of unexpected discoveries. These, in turn, have led to the currently accepted theories regarding the constitution of atoms and molecules. Here it becomes apparent how powerful spectroscopy is: With relatively low experimental complexity it allows one to gain information on properties and processes on a molecular level. The advent of pulsed lasers, delivering laser pulses of a duration of less than 100 femtoseconds, increased the importance of spectroscopy even further by facilitating time-resolved measurements that allow one to follow molecular dynamics in real-time [4].

One of the processes on a molecular level that has received special attention is charge transfer, the transfer of electron density from one molecular (sub-)unit to another [5]. It plays a crucial role in many biochemical pro-

cesses like photosynthesis, where the energy of the incident sunlight is converted into chemical energy [6], or in hemoproteins, which are, for example, involved in oxygen delivery in the respiratory system of mammals [7]. To study charge-transfer dynamics systematically, however, one needs to have access to suitable model systems, in which different parameters of the system can be modified selectively. The class of neutral organic mixed-valence compounds has proven to comprise ideal model systems that fulfill this condition [8]. Furthermore, a number of relatively simple theories is available to quantify the charge-transfer dynamics in such systems. Therefore, the concept of mixed valency will be introduced in chapter 3, together with some selected theoretical descriptions of charge transfer. Also the tools of the trade, namely the experimental spectroscopic setup and the data-acqusition and -evaluation routines, will be discussed in this chapter. Together with the basic theoretical fundamentals given in chapter 2, this provides the background that helps to understand the results presented in the following chapters.

In chapter 4 a study of the dynamics of the first polymeric mixed-valence compound will be presented. The monomeric unit comprises a triarylamine donor and a perchloro-triphenylmethyl radical acceptor, a well-known donor–acceptor combination. On average, twelve monomeric units constitute a polymer. To elucidate the influence of the polymeric nature, a reference monomer comprising only one donor and one acceptor, has also been investigated. The results suggest that in the polymer an additional decay pathway exists that corresponds to the fully charge-separated state of the system. A different kind of mixed-valence compound will be discussed in chapter 5. Again, it comprises triarylamines as donor moieties, but now a truxenone moiety is used as the acceptor. Due to its C_{3h}-symmetry, three equivalent donor branches can be attached to one truxenone acceptor. Thus, the donor-substituted truxenones can be regarded as a two-dimensional charge-transfer system and allow one to study the influence of the dimensionality on the charge-transfer dynamics. Since the donor–acceptor distance also has a strong influence on the dynamics, two truxenones with different bridge lengths have been studied. The results suggest that these systems have a counterintuitive charge-transfer behaviour, since it is not dominated by the donor–acceptor distance but rather by steric hindrance which results from a twist of the donor around the donor–acceptor axis. The third charge-transfer system, which is discussed in chapter 6, is substantially different from the former ones. While the former are purely organic compounds, this one is a metal-containing supramolecular polyelectrolyte, thus a polymeric inorganic compound. Incorporating metal into a polymeric structure can give rise to interesting properties and lead to e.g. stimuli-responsive or self-healing materials [9, 10]. However, although they are interesting materials, there is poor knowledge about their dynamics

upon optical excitation. The compound investigated in the course of this thesis comprises iron-ions and terpyridine-based ligands and forms comparably long (several hundreds of monomers) polymer chains by self-assembly. Again, a reference monomer has been studied for comparison. The results of the first time-resolved study of this system show comparatively slow charge-transfer dynamics on the order of several hunderds of picoseconds up to nanoseconds.

The molecular compounds presented in chapters 4, 5 and 6 can already give an idea of the versatility of charge-transfer compounds, the different properties that influence the dynamics and the importance of time-resolved spectroscopy to gain information on such systems and their dynamics. However, it is not only possible to study such systems by the use of femtosecond laser pulses. In fact, one can also control the outcome of a photochemical reaction with suitable laser pulses [11]. This so-called quantum control is based on quantum-mechanical interference effects and therefore sensitive to the spectral phase of the incident light field. Thus, to steer a chemical reaction one needs to modify the phase of the laser pulse which excites the system. Many different pulse-shaping techniques have been developed that allow to tailor the phase, amplitude and/or polarisation state of the laser pulse at will, which greatly advances the field of quantum control [12]. These pulse-shaping techniques are combined with suitable optimisation techniques, in which a feedback signal from the molecular system is used to modifiy the pulse shape iteratively until a pulse shape has been found that is optimally suited to achieve the control goal. In this way, many chemical processes like isomerisation [13], selective bond cleavage [14], bond formation [15] or energy flow in quantum systems [16] have been controlled successfully.

Since shaped laser pulses are a crucial ingredient in any quantum-control experiment, the pulse-shaping techniques have been (and still are) continuously refined. Thus, in chapter 7 a polarisation pulse shaper for ultrabroadband femtosecond laser pulses in the visible spectral range is presented. Shaping the polarisation state of the pulse introduces an additional degree of freedom because of the explicit polarisation dependence of light–matter interaction. Transferring the well-known pulse-shaping techniques from the near-infrared to the visible spectral range opens up the possibility of performing quantum-control experiments on any system that absorbs in this spectral range. However, many interesting quantum systems only exhibit rather broad and unstructured absorption bands in the visible. Thus it is desirable to use pulses with broadband spectra to span the entire absorption range of the quantum system under investigation. The pulse shaper presented in chapter 7 has been designed specifically to fulfill this task.

The thorough characterisation of the shaped pulses is at least as important as the shaping process itself. Firstly, one needs a feedback to evaluate

whether the pulse shaper is working correctly. Secondly, one has to know the pulse shape to be able to analyse the outcome of a quantum-control experiment. The central question that has to be answered is why a certain pulse shape is optimally suited to achieve a control goal. Thus, also the complete pulse-characterisation routine is discussed in chapter 7. The results of spectral interferometry, a well-known characterisation technique, using two different evaluation schemes are compared [17]. In the Fourier-transform evaluation scheme, the spectral phase of the pulse is extracted using a Fourier-filtering method. Although it is very robust, it has certain inherent limitations regarding the temporal ordering and separation of the shaped and reference pulse that cannot be overcome. In the dual-quadrature evaluation scheme, one extracts the phase using the sine- and cosine-contribution to the spectral-interference signal. This technique is adapted to characterise polarisation-shaped pulses and used successfully for this task for the first time. The comparison of both methods shows that they perform equally well in general. However, certain pulse shapes have been found that cannot be characterised by the Fourier-filtering methods due to its limitations. Thus, although the dual-quadrature scheme is experimentally slightly more complex, it may be advantageous in some cases. Finally, in chapter 8 the results of this thesis will be concluded briefly.

Chapter 2

Theoretical background

In this chapter, the theoretical foundations are laid which help to understand the phenomena described in the subsequent chapters of this thesis. Since femtosecond laser pulses are the most important research tool used here, a mathematical description of them is given in section 2.1, including their temporal and spectral properties as well as spatial and propagation effects. In the following section 2.2 the different nonlinear optical processes that are used for pulse generation and characterisation will be discussed. Emphasis will be put on the second- and third-order nonlinear susceptibility and the effects caused by them. After that, an introduction to the concept of molecular energy surfaces is presented in section 2.3, along with the spectroscopic concept of transient absorption spectroscopy that allows to probe the molecular dynamics. In a final step, quantum control schemes and Fourier-transform based pulse shaping will be briefly discussed in sections 2.4 and 2.5, respectively.

2.1 Mathematical description of femtosecond laser pulses

A femtosecond laser pulse can be considered as an electromagnetic wave packet which is generated by the beating between a large number of electromagnetic waves with different oscillation frequencies. For a complete description of the pulse, one uses the space- and time-dependent electric field $\vec{E}(\vec{r},t)$ which is a solution of the inhomogeneous wave equation for isotropic, non-magnetic media:

$$-\nabla \times (\nabla \times \vec{E}(\vec{r},t)) - \frac{1}{c_0^2}\frac{\partial^2}{\partial t^2}\vec{E}(\vec{r},t) = \mu_0 \frac{\partial^2}{\partial t^2}\vec{P}(\vec{r},t) \quad , \tag{2.1}$$

where c_0 is the velocity of light in vacuum and μ_0 is the magnetic permeability of vacuum. The source term $\vec{P}(\vec{r},t)$ describes the interaction of the laser pulse with a dielectric medium. $\vec{P}(\vec{r},t)$ is the induced dielectric polarisation and includes the response of the medium to the electric field as well as the generation of new electric fields.

For many cases it is convenient to separate $\vec{E}(\vec{r},t)$ into a scalar function $u^+(\vec{r})$ and a vectorial quantity $\vec{E}^+(z,t)$ where z is the propagation direction of the laser pulse. $u^+(\vec{r})$ contains information about the spatial beam profile while $\vec{E}^+(z,t)$ describes the propagation along the z-direction and the polarisation state of the laser pulse:

$$\vec{E}(\vec{r},t) \propto \vec{E}^+(z,t) \cdot u^+(\vec{r}) + c.c. \quad , \tag{2.2}$$

where *c.c.* denotes the complex conjugate of the first term. In the following sections, the properties of $\vec{E}^+(z,t)$ and $u^+(\vec{r})$ will be described separately in more detail.

2.1.1 Time and frequency representations of the electric field

To further simplify the description of the electric field, one can restrict the analysis to linearly polarised laser pulses and consider a fixed point in space at a distance z from the origin of the coordinate system, yielding a scalar field $E(t)$. The description of arbitrarily polarised pulses can be found in chapter 2.1.3. Since time and frequency space are connected via Fourier-transform,

one can describe the electric field in both spaces equivalently [18]:

$$E(\omega) = \mathcal{F}\Big\{E(t)\Big\} = \frac{1}{\sqrt{2\pi}} \int_{-\infty}^{\infty} E(t)\, e^{-i\omega t} \mathrm{d}t \quad , \tag{2.3}$$

$$E(t) = \mathcal{F}^{-1}\Big\{E(\omega)\Big\} = \frac{1}{\sqrt{2\pi}} \int_{-\infty}^{\infty} E(\omega)\, e^{i\omega t} \mathrm{d}\omega \quad . \tag{2.4}$$

Because $E(t)$ is a real quantity, it holds that $E(\omega) = E^*(-\omega)$ and it is sufficient to restrict the analysis to positive frequencies ω:

$$E^+(\omega) = \begin{cases} E(\omega) & \text{if} \quad \omega \geq 0 \\ 0 & \text{if} \quad \omega < 0. \end{cases} \tag{2.5}$$

It is convenient to decompose $E^+(\omega)$ into a spectral amplitude $A(\omega) > 0$ and a spectral phase $\phi(\omega)$:

$$E^+(\omega) = A(\omega)\, e^{-i\phi(\omega)} \quad . \tag{2.6}$$

In many cases, the phase $\phi(\omega)$ can be approximated by a Taylor expansion around the center frequency ω_0

$$\phi(\omega) = \sum_{j=0}^{\infty} \frac{b_j}{j!} (\omega - \omega_0)^j \tag{2.7}$$

with the expansion coefficients

$$b_j = \frac{\mathrm{d}^j \phi(\omega)}{\mathrm{d}\omega^j}\Big|_{\omega=\omega_0} \quad . \tag{2.8}$$

In analogy, one can also decompose the temporal field $E(t)$ into a temporal amplitude $A(t)$ and a temporal phase $\phi(t)$:

$$E^+(t) = A(t)\, e^{i\phi(t)} \quad . \tag{2.9}$$

Because of the reciprocity of time and frequency space, a change in the spectral phase $\phi(\omega)$ will result in a change in the temporal shape of the laser pulse. The lowest Taylor coefficient b_0 is called carrier-envelope phase (CEP) and determines the position of the fast oscillations of the electric field relative to the envelope. The influence of the CEP on the pulse shape is most pronounced for single-cycle pulses and can be neglected for the laser pulses used in the course of this work. The linear coefficient b_1 causes a temporal shift

of the laser pulse without changing its envelope, *i.e.* the pulse shape. For $j \geq 2$ the coefficient b_j causes a change in the temporal shape and also in the momentary frequency of the pulse. For a Gaussian-shaped pulse b_2 leads to a linear variation of the momentary frequency $\omega(t)$ with time, resulting in a linear chirp and a temporal broadening of the pulse. Higher-order coefficients may cause a nonlinear chirp and the occurrence of pre- and post-pulses. The effects caused by the nonlinear phase play an important role in the propagation of a laser pulse through transparent media and are also exploited in liquid crystal based pulse shaping (see chapter 2.5).

In the temporal domain, one can further simplify the description of the pulse by separating the nonlinear phase $\varphi(t)$:

$$\phi(t) = \varphi(t) + \omega_0 t \quad . \tag{2.10}$$

Inserting this into equation 2.9 yields

$$E^+(t) = A(t)\, e^{i\varphi(t)} \cdot e^{i\omega_0 t} = \tilde{E}(t)\, e^{i\omega_0 t} \quad . \tag{2.11}$$

If $A(t)$ and $\varphi(t)$ do not change considerably during the oscillation period $T = 2\pi/\omega_0$, equation 2.11 is known as the *slowly varying envelope approximation (SVEA)*. Again, this approximation is valid for the pulses of interest in this work and only breaks down in the case of single-cycle pulses.

Two useful quantities for the characterisation of laser pulses are the spectral bandwidth $\Delta\omega$ and the temporal duration τ_p. They are defined via the full width at half maximum (FWHM) of the spectral or temporal intensity of the pulse, respectively. With the help of equation 2.11, the spectral and temporal intentity can be calculated by integrating the squared field over one optical cycle $T = 2\pi/\omega(t)$:

$$I(t) = \epsilon_0 c_0 n \frac{1}{T} \int_{t-T/2}^{t+T/2} E^+(t')^2 \mathrm{d}t' = 2\epsilon_0 c_0 n A(t)^2 \tag{2.12}$$

and

$$I(\omega) = \epsilon_0 c_0 n \int_{-\infty}^{\infty} \left|E^+(\omega)\right|^2 \mathrm{d}\omega = 2\epsilon_0 c_0 n A(\omega)^2 \quad . \tag{2.13}$$

Here, ϵ_0 describes the dielectric constant of vacuum, c_0 the velocity of light in vacuum and n the index of refraction of the medium in which the intensity is measured. The factor 2 on the right hand side of equations 2.12 and 2.13 results from the fact that only the only the positive-frequency fraction of the

electric field is considered. The bandwidth and temporal duration are given by

$$\Delta\omega = \mathrm{FWHM}\Big\{I(\omega)\Big\} \quad \text{and} \quad \tau_p = \mathrm{FWHM}\Big\{I(t)\Big\}. \tag{2.14}$$

It is important to note that equation 2.14 is only a valid definition if the pulse shape has a well defined half-width and fails to describe multiple pulses or pulse trains reliably.
Again because of the interconnectivity of time and frequency space, the bandwidth and pulse duration cannot be varied independently. The time–bandwidth-product gives a lower limit for the pulse duration for a given bandwidth:

$$2\pi c_B \leq \tau_p \Delta\omega \quad . \tag{2.15}$$

The bandwidth constant c_B depends on the shape of the laser pulse and is usually on the order of 1. For a Gaussian pulse it holds $c_B = 2\ln 2/\pi \approx 0.441$. If a pulse fulfills the constraint $2\pi c_B = \tau\Delta\omega$, it reaches the minimum pulse duration and is called Fourier- or bandwidth-limited.

2.1.2 Spatial propagation of laser pulses

So far, the electric field has only been described at a fixed point in space. To extend the analysis to laser pulses propagating in a dispersive medium, one can use the product ansatz of equation 2.2. The wave equation 2.1 for the propagating wave then reduces to

$$\left(\frac{\partial^2}{\partial z^2} - \frac{1}{c^2}\frac{\partial^2}{\partial t^2}\right) E(z,t) = \mu_0 \frac{\partial^2}{\partial t^2} P(z,t) \quad . \tag{2.16}$$

The response of the medium to the incident electric field is contained in the polarisation $P(z,t)$. A series expansion of the polarisation helps to distinguish the different effects which occur during the interaction of a laser pulse with a dispersive medium:

$$P(z,t) = \sum_{j=0}^{\infty} P^{(j)}(z,t) = P^{(0)}(z,t) + P^{(1)}(z,t) + P_{\mathrm{nonlin}}(z,t) \quad . \tag{2.17}$$

For the course of this work, the static polarisation $P^{(0)}(z,t)$ can be neglected since it only plays a role in media with permanent charges. $P^{(1)}(z,t)$ is the linear polarisation and provides a sufficient description for many well-known effects in light-matter interaction like absorption or refraction where only one light–matter interaction takes place. However, if the intensity becomes large enough like in the case of femtosecond laser pulses, the nonlinear part

of the polarisation $P_{\text{nonlin}}(z,t)$ becomes increasingly important and gives rise to processes like frequency conversion or supercontinuum generation.
For the analysis of propagation effects, it is convenient to transform equation 2.16 into frequency space:

$$\left(\frac{\partial^2}{\partial z^2} + \frac{\omega^2}{c^2}\left[1+\chi(\omega)\right]\right) E(z,\omega) = 0 \quad , \tag{2.18}$$

where $\chi(\omega)$ is the dielectric susceptibility which interrelates the electric field $E(z,\omega)$ to the polarisation $P(z,\omega)$. A more detailed description of this relation can be found in section 2.2.1. A general solution of equation 2.18 is a wave which travels along the z-direction:

$$E(z,\omega) = E^+(0,\omega)\cdot\, e^{-ik(\omega)z} + c.c. \quad , \tag{2.19}$$

with $E^+(0,\omega) = E^+(\omega)$ from equation 2.5. The complex wavenumber $k(\omega)$ is given by

$$k(\omega) = \frac{\omega}{c}\tilde{n}(\omega) \quad \text{with} \quad \tilde{n}(\omega) = n(\omega) - i\kappa(\omega) = \sqrt{1+\chi(\omega)} \quad , \tag{2.20}$$

where $\tilde{n}(\omega)$ denotes the complex-valued index of refraction. Its real part $n(\omega)$ is the index of refraction and gives rise to refraction and dispersion for a pulse that traverses the medium. The imaginary part $\kappa(\omega)$ describes absorption and amplification of the pulse in the medium.

In this work, very short broadband laser pulses have been employed which are very sensitive to phase distortions. Therefore it is instructive to analyse the dispersion caused by a medium in more detail. Because of the frequency-dependent index of refraction, a pulse traversing a medium of length l will gain an additional phase:

$$\phi(\omega,l) = \phi(\omega,0) + k(\omega)l = \phi(\omega,0) + \frac{n(\omega)l\omega}{c_0} \quad , \tag{2.21}$$

where $\phi(\omega,0)$ is the phase of the incident pulse. In analogy to equation 2.7 one can expand this phase into a Taylor series. This yields modified Taylor coefficients b_j:

$$\begin{aligned} b_j &= \left.\frac{\mathrm{d}^j\phi(\omega,l)}{\mathrm{d}\omega^j}\right|_{\omega=\omega_0} \\ &= \left.\frac{\mathrm{d}^j\phi(\omega,0)}{\mathrm{d}\omega^j}\right|_{\omega=\omega_0} + \frac{l}{c}j\left.\frac{\mathrm{d}^{j-1}n(\omega)}{\mathrm{d}\omega^{j-1}}\right|_{\omega=\omega_0} + \frac{l}{c_0}\omega\left.\frac{\mathrm{d}^j n(\omega)}{\mathrm{d}\omega^j}\right|_{\omega=\omega_0} \quad . \end{aligned} \tag{2.22}$$

The first-order coefficient then reads

$$\begin{aligned} b_1(\omega) &= \frac{\mathrm{d}\phi(\omega,0)}{\mathrm{d}\omega}\Big|_{\omega=\omega_0} + \frac{l}{c_0}\left(n(\omega)+\omega\frac{\mathrm{d}n(\omega)}{\mathrm{d}\omega}\right)\Big|_{\omega=\omega_0} \\ &= \frac{\mathrm{d}\phi(\omega,0)}{\mathrm{d}\omega}\Big|_{\omega=\omega_0} + t_g \quad , \end{aligned} \tag{2.23}$$

with the group delay t_g :

$$t_g = \frac{l}{c_0}\left(n(\omega)+\omega\frac{\mathrm{d}n(\omega)}{\mathrm{d}\omega}\right) = \frac{l}{c_0}\left(n(\lambda)-\lambda\frac{\mathrm{d}n(\lambda)}{\mathrm{d}\lambda}\right) \quad . \tag{2.24}$$

The group delay t_g is related to the group velocity v_g via $t_g = l/v_g$.
The second-order coefficient b_2 contains the group delay dispersion GDD:

$$b_2(\omega) = \frac{\mathrm{d}^2\phi(\omega,0)}{\mathrm{d}\omega^2}\Big|_{\omega=\omega_0} + \mathrm{GDD} \quad , \tag{2.25}$$

with

$$\mathrm{GDD} = \frac{l}{c_0}\left(2\frac{\mathrm{d}n(\omega)}{\mathrm{d}\omega}+\omega\frac{\mathrm{d}^2n(\omega)}{\mathrm{d}\omega^2}\right) = \frac{\lambda^3 l}{2\pi c_0^2}\frac{\mathrm{d}^2n(\lambda)}{\mathrm{d}\lambda^2} \quad . \tag{2.26}$$

Because of the different group velocities for different frequencies, the group delay dispersion leads to a temporal broadening of the pulse. In the visible spectral range, transparent media show normal dispersion, which means $\frac{\mathrm{d}n(\lambda)}{\mathrm{d}\lambda} < 0$ and the curvature of $n(\lambda)$ is positive ($\frac{\mathrm{d}^2n(\lambda)}{\mathrm{d}\lambda^2} > 0$). This means that "red" frequencies will traverse the medium faster than "blue" frequencies, leading to a so-called up-chirp of the temporally broadened laser pulse.

If the progression of $n(\lambda)$ is known, for example via the Sellmeier coefficients of the medium, one can calculate the full dispersion imposed on the laser pulse by the medium. For very short laser pulses spanning a broad spectral range in the visible—as used for the experiments presented later in this thesis— the resulting distortions of the pulse shape can be severe. This is firstly because the derivatives of $n(\lambda)$ are rather steep in this spectral region compared to the mid-infrared region around 800 nm and secondly because the pulses used in this work may well span a spectral bandwidth of up to 100 nm (in relation to the onset of the intensity, not to be mistaken for the full width at half maximum). To minimise the influence of material dispersion, one should favour reflective instead of transmissive optics. It is also possible to compensate for the dispersion to some extent with the help of prism or grating compressors or other pulse shaping devices (see chapter 2.5).

2.1.3 Extension to arbitrarily polarised laser pulses

So far, only linearly polarised pulses have been considered. Light is a transverse electromagnetic wave, so any arbitrary polarisation state can be described as a linear combination of two linearly independent components:

$$\vec{E}(t) = \begin{pmatrix} A_1(t) \cdot e^{i\phi_1(t)} \\ A_2(t) \cdot e^{i\phi_2(t)} \end{pmatrix} \quad . \tag{2.27}$$

In analogy to equations 2.6 and 2.9 a vectorial representation of the field is also possible in frequency space:

$$\vec{E}(\omega) = \begin{pmatrix} A_1(\omega) \cdot e^{-i\phi_1(\omega)} \\ A_2(\omega) \cdot e^{-i\phi_2(\omega)} \end{pmatrix} \quad . \tag{2.28}$$

The considerations of chapter 2.1.1 are still valid for this expression of the electric field and have to be applied to each of the single components of the vectorial representation given by equations 2.27 and 2.28. The vectorial representation is also of high importance for Jones calculus, which will be discussed in chapter 7.2.3 in detail.

The polarisation state of a laser pulse can conveniently be described by the elliptical pulse parameters ε and θ [19]. Their definition is demonstrated in figure 2.1 for an elliptically polarised laser pulse. ϑ gives the orientation of the polarisation ellipse relative to the laboratory frame E_1, E_2 while ε defines the ellipticity of the pulse. If one defines the auxiliary quantities χ and δ (see equations 2.29 and 2.30), it is possible to calculate ε and θ from the amplitudes A_1 and A_2 and the corresponding phases ϕ_1 and ϕ_2 in the laboratory system. The angle χ is defined by the ratio of the laboratory frame amplitudes:

$$\chi = \arctan\left(\frac{A_2}{A_1}\right) \quad \in \left[0, \frac{\pi}{2}\right], \tag{2.29}$$

while δ is given by the phase difference between both components:

$$\delta = \phi_2 - \phi_1 \quad \in [-\pi, \pi]\,. \tag{2.30}$$

The orientation of the ellipse is then given by

$$\theta = \begin{cases} \tilde{\vartheta} & \in \left[-\frac{\pi}{4}, \frac{\pi}{4}\right] \quad \text{if} \quad \chi \leq \frac{\pi}{4} \\ \tilde{\vartheta} + \frac{\pi}{2} & \in \left[\frac{\pi}{4}, \frac{\pi}{2}\right] \quad \text{if} \quad \chi > \frac{\pi}{4} \wedge \tilde{\vartheta} < 0 \\ \tilde{\vartheta} - \frac{\pi}{2} & \in \left[-\frac{\pi}{2}, \frac{-\pi}{4}\right] \quad \text{if} \quad \chi > \frac{\pi}{4} \wedge \tilde{\vartheta} \geq 0 \end{cases} \tag{2.31}$$

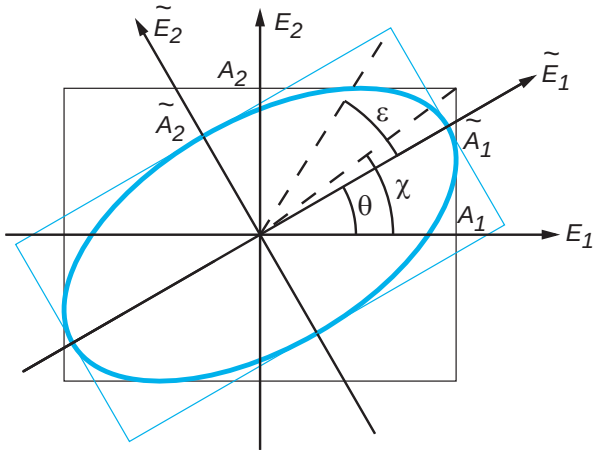

Figure 2.1: Definition of the elliptical pulse parameters ε and ϑ for an elliptically polarised laser pulse. θ describes the orientation of the ellipse relative to the laboratory frame E_1, E_2 while ε is a measure for the ellipticity of the pulse. The auxiliary angle χ is necessary for the calculation of the elliptical pulse parameters from the linear pulse parameters amplitude and phase.

with the angle

$$\tilde{\vartheta} = \frac{1}{2}\arctan\left[\tan 2\chi \cos\delta\right] \quad \in \quad \left[-\frac{\pi}{4}, \frac{\pi}{4}\right]. \tag{2.32}$$

For the ellipticity, one obtains

$$\varepsilon = \frac{1}{2}\arcsin\left[\sin 2\chi \sin\delta\right] \quad \in \quad \left[-\frac{\pi}{4}, \frac{\pi}{4}\right]. \tag{2.33}$$

With these quantities, the polarisation state of the laser pulse is described completely and the time evolution of the polarisation state within the duration of the pulse can easily be visualised, e.g. by a trajectory on the Poincaré surface [20]. This will become important in connection with polarisation-shaped laser pulses discussed in chapter 7.3.

2.1.4 Spatial beam profile

With the foundations laid in chapter 2.1.1 and 2.1.3 the propagating-wave contribution of equation 2.2 can be described satisfactorily. Now it is important to have a closer look at the spatial part $u^+(\vec{r})$. Using the product ansatz made in equation 2.2 the wave equation 2.1 for vacuum ($\vec{P}(\vec{r},t) = 0$)

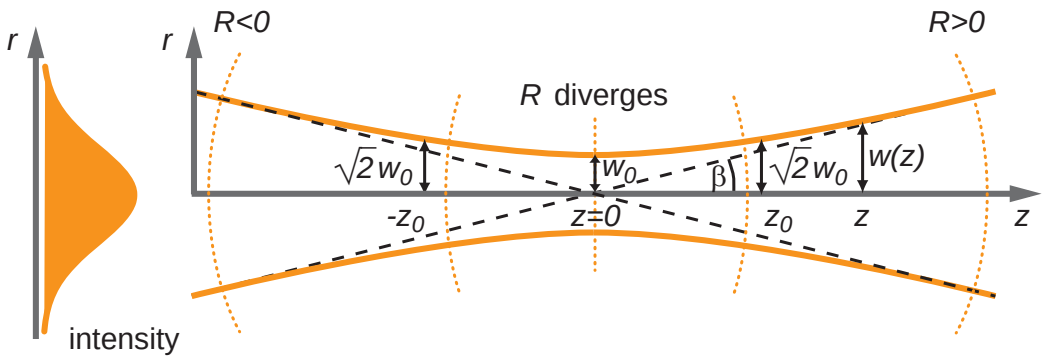

Figure 2.2: Spatial beam profile of a Gaussian beam (equation 2.35). The position dependent intensity can be seen on the left. On the right, the $1/e^2$-value of the maximum intensity is indicated by the solid orange lines. The dotted orange lines correspond to the curved wavefronts of the beam while the dashed lines illustrate the approximation of equation 2.39, valid for the beam diameter far away from the focus of the beam.

can be reduced to the paraxial wave equation

$$\nabla_t^2 u^+(\vec{r}) - 2ik_0 \frac{\partial}{\partial z} u^+(\vec{r}) = 0 \quad . \tag{2.34}$$

The most commonly used solution which corresponds to the TEM_{00} mode of a laser beam is the Gaussian beam profile

$$u^+(\vec{r}) = u_0 \frac{1}{\sqrt{1+\frac{z^2}{z_0^2}}} \cdot e^{-i\psi(z)} \cdot e^{\frac{ik(x^2+y^2)}{2R(Z)}} \cdot e^{\frac{-(x^2+y^2)}{w^2(z)}} \quad . \tag{2.35}$$

The minimum beam waist w_0 is reached at the position $z = 0$. The Rayleigh range z_0 is defined as the range, in which the beam radius increases by a factor of $\sqrt{2}$ relative to the minimum beam radius w_0:

$$w(z) = w_0 \sqrt{1 + \frac{z^2}{z_0^2}} \quad \text{with} \quad z_0 = \frac{\pi}{w_0^2 \lambda} \quad . \tag{2.36}$$

Here, λ is the wavelength of the laser. The Guoy phase $\psi(z) = \arctan\left(\frac{z}{z_0}\right)$ only plays a role within the Rayleigh range and can be neglected for $z \gg z_0$.

The curvation of the wavefronts of the propagating wave is given by the radius of curvature $R(z)$,

$$R(z) = z\left(1 + \frac{z_0^2}{z^2}\right) \tag{2.37}$$

and the half-divergence angle β

$$\beta = \frac{\lambda}{\pi w_0} \quad . \tag{2.38}$$

In a sufficiently large distance from the beam waist, these equations simplify to $R(z) \approx z$ and $\beta \approx \frac{w(z)}{z}$ thus the position dependent beam radius is given by

$$w(z) = \frac{z\lambda}{\pi w_0} \quad . \tag{2.39}$$

In this way, it is possible to approximate the size of the beam focus after passing a lens with given focal length f if the input beam radius w is known:

$$w_0 = \frac{f\lambda}{\pi w} \quad . \tag{2.40}$$

In figure 2.2 a sketch of a Gaussian beam profile is presented. The radial intensity distribution is displayed on the left hand side of the figure. The solid orange line corresponds to the $1/e^2$-value of the maximum intensity at $x, y = 0$. One can clearly see that at $z = 0$, the beam radius w_0 reaches its minimum value. The dotted orange lines indicate the curved wavefronts of the propagating beam. The dashed lines show the simplification of $w(z)$, valid for large distances from the beam waist (see equation 2.39).

2.2 Nonlinear optical processes

Many interesting molecules show broad absorption bands in the visible spectral range. Therefore it is desirable to use laser pulses which span the same spectral range as the molecular absorption in order to investigate and control the photophysical and photochemical behaviour of theses molecules. For the generation of laser pulses tunable in the visible spectral range one can exploit the properties on the nonlinear polarisation (equation 2.17) of a medium. The different processes which are important in this course will be explained in detail in the following sections.

2.2.1 Frequency-space description of the nonlinear polarisation

As was seen from the wave equation 2.1, the polarisation $\vec{P}$ describes the response of a medium to an electric field and acts as the source term for the generation of new electric fields. To study a possible frequency dependence of newly generated electric fields it is instructive to analyse the polarisation in frequency space. For simplicity, the spatial dependence of the polarisation is omitted for this analysis. The most general description of $\vec{P}$ then reads

$$\vec{P}(\omega) = \vec{P}^{(1)}(\omega_m) + \vec{P}^{(2)}(\omega_m, \omega_n) + \vec{P}^{(3)}(\omega_m, \omega_n, \omega_o) + \cdots \quad , \tag{2.41}$$

where $\omega_m, \omega_n, \omega_o$ denote the frequencies of incoming electric fields. To express the polarisation in terms of these fields, one has to make use of the interrelation between $\vec{P}$ and $\vec{E}$ via the dielectric susceptibility χ:

$$\begin{aligned} \vec{P}(\omega) = \epsilon_0 \Big(\chi^{(1)} \vec{E}_1(\omega_m) \quad &+ \quad \chi^{(2)} \vec{E}_1(\omega_m) \vec{E}_2(\omega_n) \\ &+ \quad \chi^{(3)} \vec{E}_1(\omega_m) \vec{E}_2(\omega_n) \vec{E}_3(\omega_o) + \cdots \Big) \quad . \end{aligned} \tag{2.42}$$

The susceptibility $\chi^{(r)}$ is a tensor of rank $r+1$ and describes the response of the medium to an electric field. The symmetry of the medium determines the tensor components of $\chi^{(r)}$ [21].

The nonlinear optical processes that were taken advantage of in the course of this work for pulse generation and characterisation are related to the second and third order nonlinear susceptibility and will be discussed briefly in the following sections.

2.2.2 Second-order susceptibility

If a medium exhibits a nonvanishing $\chi^{(2)}$, this may give rise to optical rectification (OR), sum- and difference-frequency generation (SFG/DFG) and

second harmonic generation (SHG). Consider an incoming electric field of the form $E(t) = A_1\, e^{-i\omega_1 t} + A_2\, e^{-i\omega_2 t} + c.c.$ which traverses a medium with second-order nonlinear susceptibility. Then the generated polarisation comprises the following contributions [21]

$$\begin{aligned} P(0) &= \epsilon_0 \chi^{(2)} \left(|A_1|^2 + |A_2|^2\right) && \text{(OR)} \\ P(2\omega_1) &= \epsilon_0 \chi^{(2)} A_1^2\, e^{-2i\omega_1 t} && \text{(SHG)} \\ P(2\omega_2) &= \epsilon_0 \chi^{(2)} A_2^2\, e^{-2i\omega_2 t} && \text{(SHG)} \\ P(\omega_1 + \omega_2) &= 2\epsilon_0 \chi^{(2)} A_1 A_2\, e^{-i(\omega_1+\omega_2)t} && \text{(SFG)} \\ P(\omega_1 - \omega_2) &= 2\epsilon_0 \chi^{(2)} A_1 A_2^*\, e^{-i(\omega_1-\omega_2)t} && \text{(DFG)} \end{aligned} \tag{2.43}$$

Optical rectification is a special case of difference frequency generation ($\omega_1 = \omega_2$). It creates a static electric field in the medium instead of a travelling electromagnetic wave. Second harmonic generation is a special case of sum-frequency generation ($\omega_1 = \omega_2$). It is exploited in frequency-doubling to access a higher energetic wavelength range and as a feedback signal in pulse characterisation by frequency-resolved optical gating (a comprehensive discussion can be found in chapter 7.2.1). Sum- and difference-frequency generation open up the possibility of converting a laser of a given frequency to a new frequency regime, thus gaining access to more experimental possibilities. DFG is the basis for optical parametric amplification (see chapter 2.2.3) which is a crucial technique in the generation of tunable and broadband laser pulses.

It is important to mention that isotropic materials exhibit $\chi^{(2)} = 0$ because of their inversion symmetry. If the symmetry is broken (at boundaries or in birefringent media like β-barium borate) the above-mentioned effects can be observed. Another constraint for efficient frequency conversion is the so-called phase-matching condition. It is given by the fact that the contributing electric fields have to fulfill momentum conservation:

$$\vec{k}_j = \vec{k}_k + \vec{k}_l \quad , \tag{2.44}$$

where $\vec{k}_{j,k,l}$ are the wave vectors of the contributing fields. This can cause severe complications, especially for ultrabroadband laser pulses. These issues will be discussed in detail in chapters 2.2.3 and 7.2.1.

2.2.3 Third-order susceptibility

Among the processes which originate from a nonvanishing $\chi^{(3)}$ are third harmonic generation, two photon absorption and the optical Kerr effect, which

is related to an intensity-dependent index of refraction [21]:

$$n = n_0 + n_2 I \tag{2.45}$$

with $n_2 \propto \chi^{(3)}$. This effect is the origin of so-called self phase modulation, which causes a spectral broadening of a pulse traversing a medium with third order nonlinear susceptibility. It is important for the generation of "white light" or supercontinua, which have a manifold of applications in pulse generation and spectroscopy. Nevertheless, the underlying mechanism is still a controversial question and has not been completely clarified [22, 23].
Unlike the case of $\chi^{(2)}$, almost all media exhibit a nonvanishing $\chi^{(3)}$. Probing the third order nonlinear susceptibility is possible by means of transient absorption spectroscopy. This widely used technique is the foundation for all spectroscopic research of this work and is discussed thoroughly in chapter 2.3.

Parametric processes

Investigating and controlling the ultrafast dynamics of any system requires a laser pulse which matches the absorption properties of that system. In many cases this necessitates a frequency conversion process to generate a laser pulse in the desired spectral range. A prevalent way to do this is by means of optical parametric amplification (OPA) [24]. An intense narrowband "pump" pulse with central frequency ω_p and a low intensity broadband "signal" or "seed" pulse with central frequency ω_s are overlapped in a medium with nonvanishing $\chi^{(2)}$. If the phase matching condition is fulfilled, the seed pulse is amplified while the pump pulse is depleted. To satisfy the energy and momentum conservation, a third pulse — the so-called "idler" pulse at central frequency ω_i with $\omega_i < \omega_s$ — is generated.

There are two major issues that have to be accounted for in the parametric generation of laser pulses. First of all, the phase matching condition

$$\hbar\vec{k}_p = \hbar\vec{k}_s + \hbar\vec{k}_i \tag{2.46}$$

with $\vec{k}_{p,s,i}$ being the wave vectors of the pump, signal, and idler, respectively, can only be met exactly for one set of frequencies ω_p, ω_s and ω_i. If the signal frequency ω_s increases to $\omega_s + \Delta\omega$, the idler frequency has to decrease from ω_i to $\omega_i - \Delta\omega$ to ensure energy conservation. The phase mismatch Δk [24] can be approximated by

$$\Delta k \cong \Big(\frac{1}{v_{g,i}} - \frac{1}{v_{g,s}}\Big)\Delta\omega \quad . \tag{2.47}$$

$v_{g,i}$ and $v_{g,s}$ are the group velocities of the idler and the signal in the nonlinear medium. This group velocity mismatch determines the full width at half maximum phase-matching bandwidth, which can be approximated in first order as

$$\Delta\nu \cong \frac{2(\ln 2)^{1/2}}{\pi}\left(\frac{\Gamma}{L}\right)^{1/2} \cdot \frac{1}{\left|\frac{1}{v_{g,s}} - \frac{1}{v_{g,i}}\right|} \quad , \tag{2.48}$$

with a crystal length L and a nonlinear coefficient Γ [24]. If one recasts the phase matching condition 2.46 in the form

$$n_p\omega_p = n_s\omega_s + n_i\omega_i \tag{2.49}$$

it is obvious that this condition cannot be met in media with normal dispersion ($n_i < n_s < n_p$). In negative uniaxial birefringent crystals, however, phase matching can be achieved by sending the pump pulse along the extraordinary direction of the crystal, because $n_e < n_o$. The phase matching bandwidth can be adjusted to different signal frequencies by tuning the angle of the optical axis of the crystal with respect to the wave vectors of the interacting beams. If the signal and idler pulses have the same polarisation, perpendicular to that of the pump pulse, this is called type I phase matching. One speaks of type II phase matching, if either the signal or idler pulse is polarised parallel to the pump. Type I and type II phase matching differ substantially in their phase-matching bandwidth. In type I phase matching the bandwidth varies drastically within the tuning range and can become very large to facilitate the generation of ultrashort laser pulses. In contrast to that, the type II phase-matching bandwidth is rather small and does not vary considerably within the tuning range. It can conveniently be used to generate rather narrowband pulses over a large tuning range.

A second important issue originates from the group velocity mismatch between the pump, the signal and the idler pulses. Because of the different group velocities, the three pulses will split spatially after a certain propagation length in the medium, the so-called pulse splitting length $l_{p,(s,i)}$ [24]:

$$l_{p,(s,i)} = \frac{\tau_{\text{pump}}}{\frac{1}{v_{g,(i,s)}} - \frac{1}{v_{g,p}}} \quad , \tag{2.50}$$

where τ_{pump} is the pump pulse duration. The pulse splitting length defines the useful interaction length for the parametric amplification. If the pump and signal pulse are spatially separated from one another, no amplification can take place. Yet it is possible to compensate for the different group velocities of signal and idler by employing a noncollinear beam geometry. In that case, the vectorial nature of the phase matching condition has to be taken into

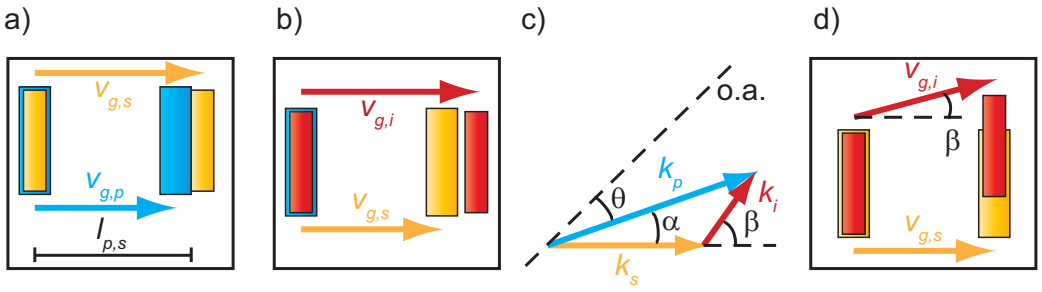

Figure 2.3: The effect of group velocity mismatch in optical parametric amplification (modified from [25]). Because of the different group velocities, the pump, signal and idler pulses are split spatially after propagating a distance $l_{p,s}$ in the medium (figure a)). After this pulse splitting length, no amplification can take place. The group velocity mismatch between the signal and idler pulses gives rise to a spatial splitting of theses pulses, respectively (figure b)). In addition, it reduces the achievable phase matching bandwidth. The problem can be overcome by a noncollinear geometry between the interacting beams (figure c)). The pump and signal beam are oriented under an angle α with respect to each other, while the idler beam forms an angle β relative to the signal. θ is the angle between the pump beam and the optical axis of the crystal. The effect of this geometry on the group velocity mismatch between signal and idler pulses is depicted in figure d): While the longitudinal components of both group velocities are identical, a small lateral shift between the beams can be observed. In this way, the phase-matching bandwidth can be expanded to render the generation of ultrabroadband pulses possible .

account. The principle is depicted in figure 2.3. The wave vectors of the pump and signal pulse form an angle α which is independent of the signal wavelength. The idler pulse is emitted at an angle β with respect to the signal (β depends on the signal wavelength). The projections of the phase mismatch on the directions parallel and perpendicular to the signal direction read

$$\Delta k_{\parallel} = k_p \cos\alpha - k_s - k_i \cos\beta = 0 \quad , \tag{2.51}$$

$$\Delta k_{\perp} = k_p \sin\alpha - k_s \sin\beta = 0 \quad . \tag{2.52}$$

Upon an increase of the signal frequency by $\Delta\omega$, the wave vector mismatches

can be approximated by

$$\Delta k_{\parallel} \cong -v_{g,s}\Delta\omega + v_{g,i}\Delta\omega\cos\beta - k_i\Delta\omega\frac{\partial\beta}{\partial\omega_i}\sin\beta \quad , \tag{2.53}$$

$$\Delta k_{\perp} \cong v_{g,i}\Delta\omega\sin\beta + k_i\Delta\omega\frac{\partial\beta}{\partial\omega_i}\cos\beta \quad . \tag{2.54}$$

This can be rewritten as

$$v_{g,s} = v_{g,i}\cos\beta \quad . \tag{2.55}$$

This means that broadband phase matching can be achieved if the signal group velocity equals the projection of the idler group velocity along the signal direction. In this way, the signal and idler propagate at the same longitudinal velocity throughout the entire crystal, thus augmenting the interaction length for parametric amplification. The lateral walkoff is small compared to the usual beam diameters in the nonlinear medium. With noncollinear optical parametric amplifiers (NOPAs) which employ a noncollinear geometry, it is possible to amplify ultrabroadband laser pulses, which can span the entire visible spectral range [26–28].

2.3 Potential energy surfaces and transient absorption spectroscopy

As was introduced in chapter 2.2.3, the third-order nonlinear susceptibility $\chi^{(3)}$ can act as a source for different nonlinear optical phenomena. So far only its importance for frequency conversion processes and pulse generation was discussed. In addition to that, $\chi^{(3)}$ also acts as a basis for different nonlinear spectroscopy techniques [29] which helped unravelling the dynamics of different systems on an ultrafast time scale like light-harvesting complexes [30], biologically active molecules like photoreceptors [31] or quantum dots [32]. To interpret the spectroscopic data, it is important to understand which processes take place upon optical excitation of a molecule. Within the framework of this thesis, the photophysical processes will be described using the potential energy surfaces of the molecular system under investigation. A brief introduction to that topic will be given in chapter 2.3.1. An experimental method of gaining information about these potential energy surfaces, namely transient absorption spectroscopy, will be introduced in the subsequent chapter.

2.3.1 Electronic transitions in molecules

To describe the energy states of a molecular system comprising j electrons and k nuclei, one has to solve the time-independent Schrödinger equation

$$\begin{aligned} \mathcal{H}\left(\vec{r}_1,\dots\vec{r}_j,\vec{R}_1,\dots\vec{R}_k\right) & \left|\Psi_{\mathrm{mol}}(\vec{r}_1,\dots\vec{r}_j,\vec{R}_1,\dots\vec{R}_k)\right\rangle \\ = E & \left|\Psi_{\mathrm{mol}}(\vec{r}_1,\dots\vec{r}_j,\vec{R}_1,\dots\vec{R}_k)\right\rangle \quad . \end{aligned} \tag{2.56}$$

$\left|\Psi_{\mathrm{mol}}(\vec{r}_1,\dots\vec{r}_j,\vec{R}_1,\dots\vec{R}_k)\right\rangle$ is the wave function of the molecular system, it depends on the electronic coordinates $\vec{r}_1,\dots\vec{r}_j$ as well as the nuclei coordinates $\vec{R}_1,\dots\vec{R}_k$. The energy of the system is given by E. The Hamilton

operator $\mathcal{H}\left(\vec{r}_1,\ldots\vec{r}_j,\vec{R}_1,\ldots\vec{R}_k\right)$ comprises different contributions:

$$\begin{aligned}\mathcal{H}\left(\vec{r}_1,\ldots\vec{r}_j,\vec{R}_1,\ldots\vec{R}_k\right) &= \sum_{i=1}^{j}\mathcal{T}_{\mathrm{e}}(\vec{r}_i)+\sum_{m=1}^{j}\sum_{i>m}^{j}\mathcal{V}_{\mathrm{e}}(\vec{r}_i,\vec{r}_m)\\ &+ \sum_{s=1}^{k}\mathcal{T}_{\mathrm{n}}(\vec{R}_s)+\sum_{t=1}^{k}\sum_{s>t}^{k}\mathcal{V}_{\mathrm{n}}(\vec{R}_s,\vec{R}_t)\\ &+ \sum_{i=1}^{j}\sum_{s=1}^{k}\mathcal{V}_{\mathrm{en}}(\vec{r}_i,\vec{R}_s). \qquad (2.57)\end{aligned}$$

The first two terms of the right hand side of equation 2.57 describe the purely electronic contribution with the kinetic energy $\mathcal{T}_{\mathrm{e}}$ and the Coulomb interaction $\mathcal{V}_{\mathrm{e}}$ between the electrons. The following two terms only apply to the nuclei and describe their kinetic energy $\mathcal{T}_{\mathrm{n}}$ and their Coulomb interaction $\mathcal{V}_{\mathrm{n}}$, respectively. The interaction between the electrons and the nuclei is contained in the last term $\mathcal{V}_{\mathrm{en}}$. In general, it is not possible to find an analytic solution for equation 2.56, for systems more complex than H_2^+. If one goes to more complex molecular systems, the number of degrees of freedom increases rapidly with the number N of atoms in the molecule. For N atoms, at least $3N$-6 internal degrees of freedom have to be considered for a complete description. Nevertheless, in many cases it is sufficient to restrict the analysis to a few "reaction coordinates" which govern the photophysical processes.

Still, one needs to apply approximations to reduce the complexity of equation 2.56. The most common one is the Born–Oppenheimer approximation [33]. It reflects the fact that because of the mass difference between electrons and nuclei the electrons can react instantaneously to a change in the nuclei configuration. In other words, the kinetic coupling element between electrons and nuclei can be neglected. This makes a factorisation of the molecular wave function $\left|\Psi_{\mathrm{mol}}(\vec{r}_1,\ldots\vec{r}_j,\vec{R}_1,\ldots\vec{R}_k)\right\rangle$ into an electronic part $\left|\Psi_{\mathrm{e}}(\vec{r}_1,\ldots\vec{r}_j,\vec{R}_1,\ldots\vec{R}_k)\right\rangle$ and a nuclei contribution $\left|\Psi_{\mathrm{n}}(\vec{R}_1,\ldots\vec{R}_k)\right\rangle$ possible:

$$\begin{aligned}\left|\Psi_{\mathrm{mol}}(\vec{r}_1,\ldots\vec{r}_j,\vec{R}_1,\ldots\vec{R}_k)\right\rangle &=\\ \left|\Psi_{\mathrm{e}}(\vec{r}_1,\ldots\vec{r}_j,\vec{R}_1,\ldots\vec{R}_k)\right\rangle &\cdot \left|\Psi_{\mathrm{n}}(\vec{R}_1,\ldots\vec{R}_k)\right\rangle . \qquad (2.58)\end{aligned}$$

Thus the electronic wave function $\left|\Psi_{\mathrm{e}}(\vec{r}_1,\ldots\vec{r}_j,\vec{R}_1,\ldots\vec{R}_k)\right\rangle$ only shows a parametric dependence on the nuclei coordinates $\vec{R}_1,\ldots\vec{R}_k$. For a complete description, the contributions of the electron spin and molecular rotation to

the wave function would have to be included. However, those contributions can be omitted for the photophysical processes under investigation in this work. Taking these considerations into account, the Schrödinger equation 2.56 can be separated into two differential equations, one for the electronic wave function

$$\begin{aligned}\left(\sum_{i=1}^{j}\mathcal{T}_{\mathrm{e}}(\vec{r}_i) \;+\; \sum_{m=1}^{j}\sum_{i=1,i\neq m}^{j}\mathcal{V}_{\mathrm{e}}(\vec{r}_i,\vec{r}_m)\right.\\ \left.+\;\sum_{i=1}^{j}\sum_{s=1}^{k}\mathcal{V}_{\mathrm{en}}(\vec{r}_i,\vec{R}_s)\right)\left|\Psi_{\mathrm{e}}(\vec{r}_1,\ldots\vec{r}_j,\vec{R}_1,\ldots\vec{R}_k)\right\rangle\\ =\; E_j(\vec{R}_1,\ldots\vec{R}_k)\left|\Psi_{\mathrm{e}}(\vec{r}_1,\ldots\vec{r}_j,\vec{R}_1,\ldots\vec{R}_k)\right\rangle \quad , \end{aligned} \tag{2.59}$$

and another one for the nuclei wave function

$$\begin{aligned}\left(\sum_{s=1}^{k}\mathcal{T}_{\mathrm{n}}(\vec{R}_s) \;+\; \sum_{t=1}^{k}\sum_{s=1,s\neq t}^{j}\mathcal{V}_{\mathrm{n}}(\vec{R}_s,\vec{R}_t)\right.\\ \left.+\;E_j(\vec{R}_1,\ldots\vec{R}_k)\right)\left|\Psi_{\mathrm{n}}(\vec{R}_1,\ldots\vec{R}_k)\right\rangle\\ =\; E\left|\Psi_{\mathrm{n}}(\vec{R}_1,\ldots\vec{R}_k)\right\rangle \quad . \end{aligned} \tag{2.60}$$

To obtain the effective potential which determines the movement of the nuclei, one has to calculate $E_j(\vec{R})$. In order to do so, one has to solve equation 2.59 for each electronic state j and for different sets of nuclei coordinates $\vec{R}$. The result is a multidimensional potential energy surface which determines the photophysical properties of the system.
The first step of the photophysical process, the excitation from an initial molecular state i to a final state f can be treated semi-classically. This means that the electric field $\vec{E}(t)$ couples to the dipole moment of the molecule, which is described by the quantum-mechanical dipole operator

$$\vec{\mu} = -e\sum_{i=1}^{j}\vec{r}_i + \sum_{s=1}^{k}Z_s e\vec{R}_s \quad . \tag{2.61}$$

e is the elementary charge, $Z_s e$ are the charges of the nuclei and $\vec{r}_i$, $\vec{R}_s$ are the coordinates of the electrons and nuclei, respectively. The interaction between the electric field and the dipole moment of the molecule can be described via perturbation theory [33]. Hence, the perturbation

$$\mathcal{H}_E = -\vec{\mu}\cdot\vec{E}(t) \tag{2.62}$$

is added to the Hamiltonian of the unperturbed system. By solving the Schrödinger equation with this perturbed Hamiltonian, it is possible to calculate the dipole matrix elements $\mu_{i,f}$:

$$\mu_{i,f} = \left\langle \Psi_{\mathrm{mol},i}(\vec{r}_1, \ldots \vec{r}_j, \vec{R}_1, \ldots \vec{R}_k) \middle| \vec{\mu} \middle| \Psi_{\mathrm{mol},f}(\vec{r}_1, \ldots \vec{r}_j, \vec{R}_1, \ldots \vec{R}_k) \right\rangle \quad . \tag{2.63}$$

If one only considers electronic transitions, this leads to

$$\mu_{i,f} = -e \sum_{m=1}^{j} \langle \Psi_{\mathrm{e},f} | \, \vec{r}_m \, | \Psi_{\mathrm{e},i} \rangle \cdot \langle \Psi_{\mathrm{n},f} | \Psi_{\mathrm{n},i} \rangle \quad . \tag{2.64}$$

The first term is the electronic transition dipole moment which describes the redistribution of the electrons caused by the transition. The second term is called the Franck–Condon factor. It is a measure of the overlap of the vibrational wave functions of initial and final state. The higher the overlap, the more probable it is that a transition occurs. If the transition is induced with a laser pulse, it is possible to excite a number of vibrational levels coherently. A vibrational wave packet is created, which evolves according to the shape of the potential energy surface of the respective state. This evolution can be monitored by suitable spectroscopic techniques like transient absorption spectroscopy which is introduced in the following section.

2.3.2 Transient absorption spectroscopy

This section will describe the spectroscopic technique called transient absorption spectroscopy which was used in this work to investigate the charge transfer dynamics of different donor–acceptor systems (chapters 3, 4, 5 and 6).

The idea of transient absorption spectroscopy is the following. The molecular system under investigation is excited by a first laser pulse, the pump pulse. The pump-induced absorption changes are then monitored by a second pulse, the probe pulse, which is time-delayed with respect to the pump pulse. By varying the time delay between both pulses one can monitor the dynamics of the system. The absorption of the probe pulse with initial intensity $I_0(\lambda)$ by a homogeneously absorbing medium can be described by the Lambert–Beer law:

$$I(\lambda, \tau) = I_0(\lambda)\, e^{-\kappa(\lambda) d} = I_0(\lambda)\, e^{-\sigma(\lambda) N(\tau) d} \quad , \tag{2.65}$$

where $\kappa(\lambda)$ is the imaginary part of the index of refraction (see equation 2.20), d is the sample thickness and τ the time delay between pump and

probe pulses. It is possible to decompose $\kappa(\lambda)$ into the absorption cross section $\sigma(\lambda)$ and the number of absorbing molecules $N(\tau)$. Because of the temporal evolution of the system, the number of absorbing molecules depends on the time delay τ and so does the intensity after traversing the sample. Since only transient absorption changes are monitored in the experiment, the effect is expected to be very weak. Therefore it is more convenient to focus on the optical density OD rather than intensity:

$$\mathrm{OD}(\lambda,\tau) = -\log_{10}\Big(\frac{I(\lambda,\tau)}{I_0(\lambda)}\Big) = \frac{1}{\ln(10)}\sigma(\lambda)N(\tau)d \quad . \tag{2.66}$$

As a reference, the optical density of the system in its ground state is measured. For this purpose, the probe pulse traverses a non-excited sample volume, yielding the intensity

$$I_{\mathrm{ref}}(\lambda) = I_0(\lambda)\, e^{-\sigma(\lambda)N_0 d} \quad , \tag{2.67}$$

with N_0 being the total number of absorbing molecules in the ground state. The observable in transient absorption spectroscopy is the difference in absorbance ΔAbs between the excited and non-excited sample:

$$\Delta\mathrm{Abs} = -\log_{10}\Big(\frac{I(\lambda,\tau)}{I_{\mathrm{ref}}(\lambda)}\Big) = \frac{1}{\ln(10)}\sigma(\lambda)(N(\tau)-N_0)d \quad . \tag{2.68}$$

In this case, $N(\tau)$ represents the number of excited molecules. By scanning the time delay τ between the pump and probe pulses and employing broadband probe pulses (e.g. white-light supercontinua [34]) one can monitor the temporal evolution of the system under investigation over a broad spectral range.

Positive as well as negative absorbance changes contribute to the total absorbance change. They are sketched schematically in figure 2.4. Contributions with a negative sign can arise from the depletion of the ground state upon optical excitation. If less molecules are present in the ground state, the absorption is reduced compared to the non-excited sample, yielding a negative change in the absorbance ($\Delta\mathrm{Abs} < 0$). Also stimulated emission, caused by a radiative transition from an excited to the ground state, will result in a negative contribution, but for another reason as the ground state bleach: If light is emitted, a larger intensity is detected which comprises the transmitted light of the probe pulse and the light emitted by the sample. Thus the absorption appears to be reduced. A positive contribution arises from an excited state absorption. This corresponds to a transition from the initially excited state which was populated by the pump pulse to a higher lying excited state. During this process a new absorption band appears with

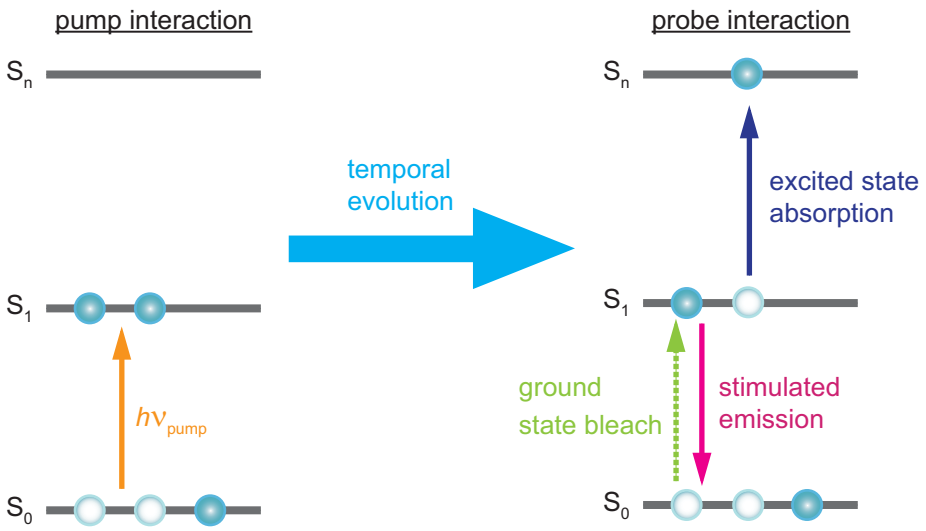

Figure 2.4: The principle of transient absorption spectroscopy: After the pump excitation and a certain evolution time, the probe pulse interacts with the molecular sample. The measured absorbance change is constituted of different contributions. The ground state is depleted upon excitation, giving rise to a negative absorption change, the ground state bleach. Upon absorption of the probe pulse, the system can either return to the ground state in a radiative process called stimulated emission, yielding a negative absorbance change. Alternatively the probe pulse can excite the system to a higher-lying state, giving rise to a positive absorbance change, the excited state absorption. The total absorbance change is the sum of all possible contributions. The temporal evolution between the excitation and the probe pulse is governed by the shape of the participating potential energy surfaces.

$\Delta\mathrm{Abs} > 0$.
The dynamics and the spectral characteristics of the absorbance changes are governed by the shape of the potential energy surfaces of the system of interest. Therefore it is possible to gain insight into the quantum-mechanical properties of the investigated system by means of transient absorption spectroscopy.

2.4 Quantum control with shaped laser pulses

The progress in femtosecond laser technology has not only made it possible to study photoreactions on ultrafast timescales and on a quantum-mechanical level. It also opened up the field of "quantum control" or "coherent control" in which the outcome of a photoreaction can be steered by the appropriate choice of laser pulses interacting with a molecular system. In the case of a strongly-coupled light-matter system, the dynamics of the system can be influenced by the temporal, spectral and phase properties of the radiation which couples to the system. Within the framework of potential energy surfaces to describe molecular states (see chapter 2.3.1), one can understand how quantum interference effects can be utilised to guide the temporal evolution of a molecule [11]. For practical applications, adaptive control schemes with shaped femtosecond laser pulses as an excitation source and a feedback loop to optimise the outcome of a reaction have proven to be the ideal tool for quantum control.

Hence as a first step, a brief introduction into some control schemes will be given in section 2.4.1. The technique of femtosecond pulse shaping in the spectral domain will be reviewed in chapter 2.5.

2.4.1 Quantum control schemes

The aim of quantum control is to steer some kind of light-matter interaction process to yield a desired outcome. This can, for example, be the outcome of a photoreaction. From a quantum-mechanical point of view, this means transferring population from an initial state to a specific final state. Different schemes how to achieve this goal have been suggested and also been proven experimentally. The three most common ones will be introduced here. The Brumer–Shapiro scheme [35, 36] is based on the quantum interference between different pathways which connect the initial state $|\Phi_0\rangle$ and the final state manifold $|\Phi_1^i\rangle$. If the energy separation between those states is $3\hbar\omega_0$, the transition can either be induced by the absorption of one photon of the frequency $3\omega_0$ or by absorbing three photons of frequency ω_0. If two continuous-wave lasers operating at frequencies ω_0 and $3\omega_0$ are utilised, control can be achieved by varying their relative phase. Closely related to the Brumer–Shapiro scheme is a quantum control scheme proposed by Silberberg [37, 38] which also exploits the interference of different quantum-mechanical pathways. However, the different frequency contributions of an ultrashort laser pulse suffice to attain control. Again, a transition from an initial state $|\Phi_0\rangle$ to a final state manifold $|\Phi_1^i\rangle$ is induced. In this case, however, the energy separation between those two state is assumed to be $2\hbar\omega_0$, so the transition

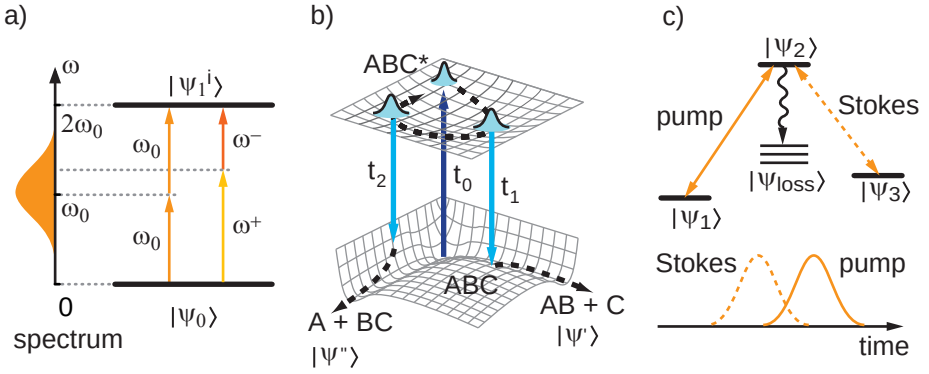

Figure 2.5: Different schemes for quantum control of molecular systems. Figure a) depicts Silberberg's scheme for a two-photon transition which is closely related to the Brumer–Shapiro scheme. Different excitation pathways corresponding to different frequency combinations $\omega^+ + \omega^- = 2\omega_0$ interfere. If one can control the interference between those pathways it is possible to transfer population to a desired target state. The Tannor–Kosloff–Rice scheme is illustrated in figure b). The temporal evolution of a vibrational wave packet is guided by the use of pulse sequences with appropriate timing. Dependent upon the timing, one can "dump" population from the excited state to the desired reaction channel for the ground state, as shown here for a photodissociation which can either yield the fragments AB + C or A + BC from the parent compound ABC. Finally, in figure c) a technique called stimulated Raman scattering involving adiabatic passage is shown. Population transfer from the state $|\Psi_1\rangle$ to the state $|\Psi_3\rangle$ is achieved by coupling those states via an intermediate state $|\Psi_2\rangle$ with the help of two laser pulses. This is possible under the condition that the Stokes pulse precedes the pump pulse, although both pulses have to overlap temporally.

can be excited by absorbing two photons of frequency ω_0 (figure 2.5 a)). If the system is irradiated with a laser pulse with central frequency ω_0 and a certain spectral bandwidth, different excitation pathways are conceivable. The photons involved in the two-photon absorption have to fulfill the condition that the sum of their frequencies is equal to $2\omega_0$. This can be achieved by any combination of two frequencies ω^+ and ω^- with $\omega^+ + \omega^- = 2\omega_0$. Each of these frequency combinations corresponds to an excitation pathway, all of which interfere. If one can control this interference, one can transfer population from $|\Phi_0\rangle$ to the desired final state, thus controlling the outcome of the reaction.

In figure 2.5 b) the Tannor–Kosloff–Rice scheme [39] is depicted for a

photodissociation reaction. Its working principle can be best explained in the time domain comprehensively. After optical excitation, the molecular system ABC can either dissociate into the fragments AB + C or A + BC. As was seen in chapter 2.3.1, a coherent optical excitation at time t_0 creates a vibrational wave packet which evolves along the potential energy surface of the excited state. Irradiating a second laser pulse on the sample at either t_1 or t_2 will "dump" the amplitude of the wavepacket into the desired dissociation channel, *i.e.* predominantly populating the state $|\Psi'\rangle$ or $|\Psi''\rangle$, respectively. The laser pulses are used to guide the temporal evolution of the vibrational wave packet along the potential energy surfaces. Instead of a sequence of laser pulses which transfer the population at distinct times, one can also employ a shaped laser pulse which continuously transfers population back and forth between two states to steer the wave packet dynamics.

In a third approach, population transfer from state $|\Psi_1\rangle$ to state $|\Psi_3\rangle$ is achieved by coupling those states via an intermediate state $|\Psi_2\rangle$ with the help of suitably timed laser pulses [40]. All three states are non-degenerate and no direct coupling is present between states $|\Psi_1\rangle$ and $|\Psi_3\rangle$. A pump pulse couples the states $|\Psi_1\rangle$ and $|\Psi_2\rangle$, while a Stokes pulse couples the states $|\Psi_3\rangle$ and $|\Psi_2\rangle$. If now the Stokes pulse precedes the pump pulse it creates a coherent superposition of the states $|\Psi_1\rangle$ and $|\Psi_3\rangle$. Coupling this superposition state to the populated state $|\Psi_1\rangle$ creates a "trapped state" from which the pump pulse cannot transfer population to $|\Psi_2\rangle$ [11]. Instead, the target state $|\Psi_3\rangle$ is populated directly. During the course of this process, the state $|\Psi_2\rangle$ remains unpopulated at all times. Thus any undesired relaxation pathways to any state $|\Psi_{\text{loss}}\rangle$ have no effect on the population transfer. The important prerequisite for this method is the counterintuitive time ordering of pump and Stokes pulse. The Stokes pulse has to precede the pump pulse, yet both pulses have to overlap temporally. This method is known as stimulated Raman scattering involving adiabatic passage [40] and is illustrated in figure 2.5 c).

Although the different approaches to quantum control presented in the previous section seem to differ strongly from one another, they can still be interpreted within the mutual framework of their descriptions [41]. They can be seen as different views on quantum control which emphasize different aspects of populations transfer. Yet there is one common point in all three approaches: They all require an optimised electric field which allows to achieve the desired control goal. Determining the optimal field theoretically can be a rather demanding task, although the theoretical fundament of quantum control advances continuously [42, 43].

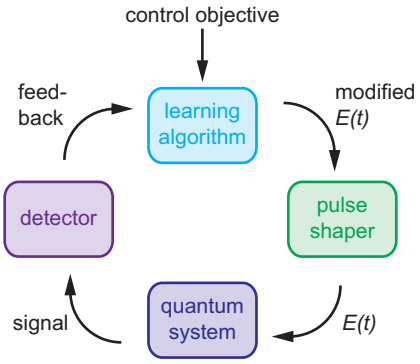

Figure 2.6: Basic concept of adaptive quantum control. A pulse shaper generates a shaped electric field, which is irradiated onto a quantum system. Some kind of signal from the system is detected and used as a feedback for the learning algorithm. According to the control objective, the learning algorithm modifies the pulse shaper setting in order to generate a modified electric field. This field is subsequently irradiated onto the quantum system and the whole process is iterated until the optimal field has been found.

2.4.2 Adaptive quantum control

From a more practical point of view, the concept of adaptive quantum control has established itself as a very successful experimental technique. A number of different electric fields is tested on the molecular system with regard to their performance in achieving the control goal. A feedback signal from the molecular system acts as a criterion to decide whether the electric field attains the goal or not. Then some sort of optimisation algorithm is utilised to modify the electric field such that its performance will improve within the next iteration of the learning loop [44].

The electric field of the employed laser pulses can be controlled in many different ways. However, for this thesis the discussion will be restricted to frequency-domain pulse shaping with a liquid-crystal display as the central ingredient. A detailed discussion can be found in chapter 2.5. Prior to this, attention will be drawn to the optimisation procedure. The basic idea of closed-loop adaptive control is depicted in figure 2.6.

The electric field of the laser pulse is modified by the pulse shaper before it interacts with the quantum system. The system might be a molecular ensemble in the gas phase [14, 45, 46], in the liquid phase [46, 47] or any other suitable quantum system [48, 49]. As a result of the interaction between the electric field and the system, some kind of signal is generated by the latter and recorded by an appropriate detector. Examples of signals are absorp-

tion or emission bands in transient absorption spectroscopy, peaks associated with specific molecular fragments in mass spectrometry or the yield of some frequency-conversion process. This signal is then used to calculate a feedback for the optimisation algorithm. According to the optimisation objective, the learning algorithm evaluates the performance of the tested electric field. This determines the pulse shaper settings and thus the modifications of the electric field for the next iteration. The entire loop is iterated until the optimisation objective is met and the optimal electric field is found.

The choice of the learning algorithm can strongly affect the performance of the optimization. Although a large variety of different algorithms exist (see, e.g. [50–52]), only one will be presented exemplarily, namely a genetic algorithm [53, 54]. Its working principle is based on concepts from biology and molecular genetics: Each individual is unambiguously defined by a set of genes. Depending on these genes, it can adapt to its environment more or less successfully. Those individuals which are best adapted to their environment have a higher chance of survival than the less adapted ("survival of the fittest"). Genetic material can be propagated from one generation of individuals to the next in different ways. An individual can be "cloned", thus simply duplicating its genetic code. In addition, mutation may occur in the cloning process, altering a number of genes randomly. This facilitates the adaptation to modified environmental conditions. Another possibility is that two individuals create offspring, combining their genetic material. Mutation is possible in addition.
Individuals which are best adapted to their environment have a bigger chance of survival and therefore of procreating their genetic material in any of the abovementioned ways. This causes the average fitness, a measure of the degree of adaptation, to rise with each generation until a population with the optimal genetic properties is created.

Related to a quantum control experiment with shaped laser pulses this means the following. Each laser pulse of different shape represents an individual, a generation is built up of a certain number of individuals. Each of these is tested on the quantum system which one wants to control, and yields a signal. From this signal, the fitness of the laser pulse is calculated. To obtain the next generations of individuals, that is for the next iterations of the optimisation loop, the fittest pulses are selected and their genetic material is modified as mentioned above.

The translation of the laser pulse properties (*i.e.* its amplitude and phase distribution) can be encoded into its genes in different ways [55]. The suitable basis set and its performance in the optimisation process depend on the optimisation objective and the definition of the fitness function. Using a genetic algorithm in an adaptive quantum control experiment is a very versatile

method and has been implemented successfully in a variety of experiments. Among them are the control of photodissociation reactions [14], fluorescence efficiency of a laser dye [56], photoisomerisation of Retinal [13] and many more (e.g. [46, 57]).

The entire concept of adaptive quantum control with shaped laser pulses relies on the generation of a large variety of different pulse shapes in an appropriate amount of time. Pulse shaping in the spectral domain has proven the ideal tool to fulfill these conditions. Therefore it will be presented in detail in the following section.

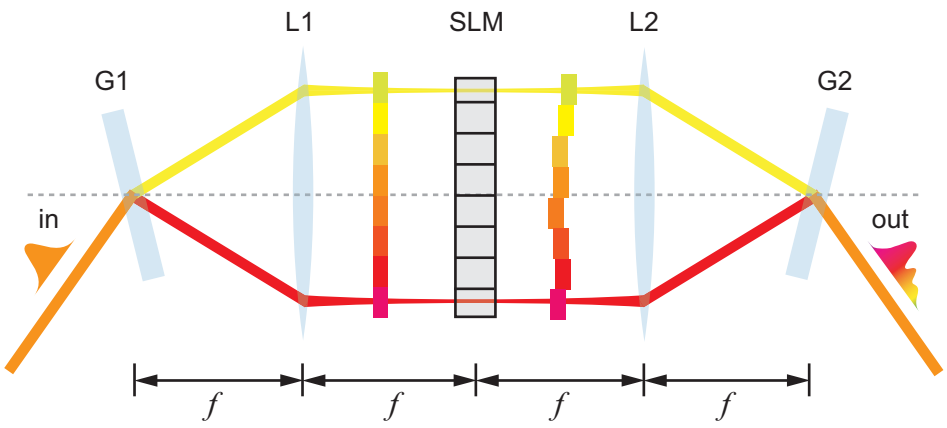

Figure 2.7: Fourier-transform pulse-shaper setup. The unshaped input pulse is spectrally dispersed by grating G1. A subsequent lens with focal length f collimates the beam and focuses each spectral component onto a spatial light modulator (SLM) located in the focal plane of the lens. After having a certain phase profile imprinted by the SLM, the shaped pulse traverses a second lens L2 of focal length f and is spectrally and temporally recombined after the second grating G2.

2.5 Fourier-transform pulse shaping

Pulse shaping, creating a specific target pulse shape from a given input pulse, is a widespread tool in many applications of femtosecond lasers and has been reviewed repeatedly [12, 58, 59]. Although a variety of different experimental implemetations to synthesize the desired pulse shape is possible, this section will place emphasis on Fourier-transform pulse shaping with a liquid crystal modulator [60, 61]. The spectrally dispersed optical frequency spectrum of the pulse is spatially masked to create a target pulse shape. Using a liquid-crystal display to modulate the spectrum is a versatile possibility to generate phase, amplitude or polarisation shaped laser pulses [60–64].

The basic setup of a Fourier-transform pulse shaper is shown in figure 2.7. The unshaped input pulse is spectrally dispersed by a grating G1 which is placed in the focal plane of lens L1 with focal length f. This lens collimates the beam and focuses each spectral component onto a spatial light modulator SLM which is located in the Fourier plane. Dependent on the kind of SLM,

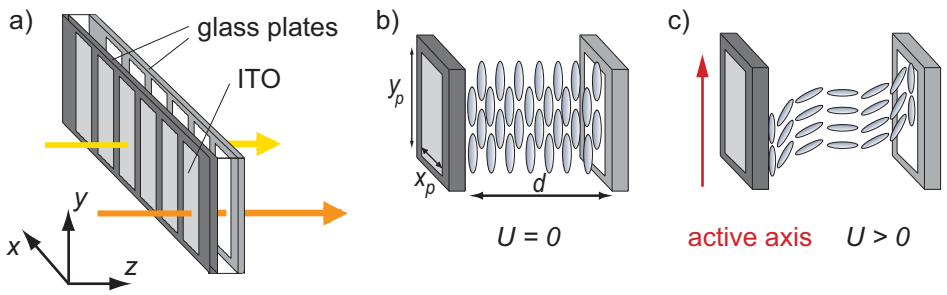

Figure 2.8: Liquid crystal (LC) array as a spatial light modulator. The liquid crystals are sandwiched between two glass plates which are covered with indium tin oxide as electrodes (figure a)). The array consists of a certain number of pixels which can be controlled individually. Neighbouring pixels are separated by small gaps in the ITO layer. In figure b) one single pixel is sketched for the case of zero voltage applied. The LCs are aligned along the y-direction. Applying a non-zero voltage causes the LCs to rotate in the z-y-plane. This changes the index of refraction and therefore the phase for a laser pulse which is polarised along the active axis, in this case the y-direction (figure c)).

one can either shape the phase, phase and amplitude or polarisation of the pulse. Figure 2.7 depicts the situation for phase-only shaping. The different spectral components are temporally delayed with respect to each other, so that a complex temporal pulse shape results. A second lens L2, again with focal length f, is used to image the shaped pulse onto a second grating G2, where it is recombined spectrally and can be applied to the experiment.

The working principle of the liquid crystal (LC) array is depicted in figure 2.8 [60, 65]. The LCs are sandwiched between two glass plates. A structured indium tin oxide (ITO) layer constitutes the electrodes which are necessary to control each pixel. Adjacent pixels are separated by small gaps in the ITO layer (figure 2.8 a)). The case of a single pixel with no voltage applied is shown in figure 2.8 b). The LCs are aligned along the y-direction. The pixel has a lateral extent of x_p times y_p and a thickness d. If a non-zero voltage is applied between the electrodes, the LCs are caused to rotate in the y-z-plane (figure 2.8 c)). This results in a variable index of refraction for a light wave polarised along the active axis of the LC pixel (in this case, the y-direction), depending upon the applied voltage. As can be seen from equation 2.21 this leads to a voltage-dependent phase change of a laser pulse traversing the LC array.

For phase-only shaping, one single LC array is sufficient [60, 61]. For

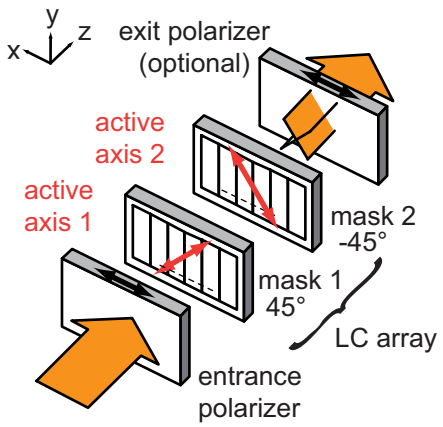

Figure 2.9: Amplitude and phase shaping using a two-mask LC array. The active axes of both LC masks are aligned perpendicular to each other. The entrance polariser ensures that the incoming pulse is x-polarised and has equal projections onto each active axis ($+45°$, $-45°$). The difference of phase shifts introduced by the LC masks determines the resulting phase of the output pulse while the sum controls the amplitude. If the exit polariser is omitted the output pulse exhibits an elliptic polarisation state, dependent on the phase difference between both projections of the electric field on the active axes. This allows for the generation of polarisation-shaped pulses.

maximum shaping efficiency the incoming pulse has to be polarised along the active axis of the LC crystals. Within the limitations of the pulse shaper setup [66, 67] any desired phase profile can be applied to the input pulse.

For the independent control of amplitude and phase an additional degree of freedom is necessary. This is commonly achieved by using a two-mask LC array [68]. The basic setup is depicted schematically in figure 2.9 [65]. The LC assembly consists of two independently controllable LC arrays. The active axes of both masks are aligned perpendicular to each other at an angle of $+45°$ and $-45°$ to the x-direction, respectively. The entrance polariser ensures that the pulse incident on the LC assembly is polarised along the x-direction and therefore has equal projections onto the active axes of both LC masks. For one single pixel and an x-polarised input field, the output

field $\vec{E}_{\text{out}}$ before traversing the exit polariser is given by ([58]):

$$\begin{aligned}\vec{E}_{\text{out}} = \quad & E_{\text{in}} \quad \cdot \exp\left(i\frac{\Delta\phi_1 + \Delta\phi_2}{2}\right) \\ & \cdot \quad \left(\vec{e}_x \cos\left(\frac{\Delta\phi_1 - \Delta\phi_2}{2}\right) + i\vec{e}_y \sin\left(\frac{\Delta\phi_1 - \Delta\phi_2}{2}\right)\right) \quad ,(2.69)\end{aligned}$$

where E_{in} describes the amplitude of the input field and $\Delta\phi_1$ and $\Delta\phi_2$ stand for the phase modulations introduced by LC mask 1 and 2, respectively. After the exit polariser with transmission along the x-direction equation 2.69 simplifies to

$$\vec{E}_{\text{out}} = E_{\text{in}} \exp\left(i\frac{\Delta\phi_1 + \Delta\phi_2}{2}\right) \cdot \vec{e}_x \cos\left(\frac{\Delta\phi_1 - \Delta\phi_2}{2}\right) \quad . \tag{2.70}$$

This corresponds to a phase- and amplitude-shaped pulse which is linearly polarised along the x-direction. The amplitude of the output pulse is determined by the difference of the phase modulations of both LC masks, whereas the sum between both governs the phase of the output pulse. Therefore the two-mask LC assembly allows for the independent control of amplitude and phase.

It is noteworthy that equation 2.69 describes a field with an elliptical polarisation state. Thus it is possible to generate polarisation-shaped pulses with a two-mask LC assembly if the exit polariser is omitted [19, 68]. However, there are some limitations to which polarisation states are accessible by this kind of polarisation pulse shaping since it is equivalent to phase shaping of two orthogonal polarisations components. Therefore the polarisation state is restricted to a great circle on the Poincaré sphere [12]. Different ideas have been proposed to overcome this limitation and to gain full control over the polarisation state. Among these are implementations with multiple LC mask assemblies [63, 64] as well as dual-mask assemblies where different linear polarisations are mapped on different spatial regions of the same LC assembly [69, 70].

Although LC-based pulse shaping is widely used in research applications and the first commercial pulse shapers are available [71], there is one minor drawback all implementations of this technique have in common. The pixelation of the LC masks is the source for different pulse distortions [72]. In addition to the desired output pulse, time-delayed and chirped replica pulses arise from the discrete sampling of a pixelated modulator and from imperfections at the pixel gaps. Dependent on the desired pulse shape, these replica pulses may even overlap and interfere with the desired pulse, causing a heavily distorted waveform.

Fourier pulse shaping also gives rise to an effect called space-time coupling [73–75]. The desired amplitude and phase shaping has the unwanted side-effect of changing the spatial properties of the pulse as well. This originates in the finite extent of the frequency components in the symmetry plane of the pulse shaper setup and in diffraction from the pixel edges in a pixelated modulator. Whether space-time coupling distorts the experimental results depends on the applied modulation, the setup subsequent to the pulse shaper and the kind of (nonlinear) interactions used in the experiment [75]. Therefore results obtained with shaped laser pulses have to be analysed thoroughly to separate the effects of pulse shaping artifacts from the response of the system under investigation.
Despite these limitations, Fourier-transform pulse shaping with a two-mask LC array is a powerful tool which has a variety of applications and has become indispensable for many fields of research.

Chapter 3

Charge-transfer dynamics in various molecular structures

Charge transfer (CT), the transfer of an electron from one molecular subunit to another, is one of the most fundamental processes after the absorption of light. A lot of research has been dedicated to understand this process in detail, as an almost uncountable number of publications and reviews focusing on different aspects of CT shows. To give an idea of the wide variety of different CT systems and processes, a few important examples will be discussed here.

Photosynthesis is nature's ingenious way to convert light into chemical energy. This task is accomplished in the so-called reaction center (RC), a complex of proteins, pigments and other cofactors. In the case of bacterial photosynthesis [6, 76], the RC is a transmembrane pigment–protein complex which performs a light driven charge separation reaction across the photosynthetic membrane. Upon light absorption, the primary electron transfer which is a sequence of individual electron transfer steps between neighbouring chromophores takes place. Coupling electron and proton transfer leads to a proton gradient across the membrane that drives the synthesis of adenosine triphosphate (ATP). The subsequent energy conversion and storage is achieved by ATP-driven reactions. Many ultrafast spectroscopic examinations helped to unravel the route of electron transfer in the RC. The investigation of modified RCs revealed that different transfer routes exist, although one is clearly dominant in wildtype RCs [76]. Thus charge transfer is essential for one of the most crucial reactions making life on earth possible.

Although light is necessary as an energy source for many organisms, it can also have negative effects. Especially high-energy UV radiation has the potential to cause damage in DNA [77]. Yet, light-induced repair mechanisms exist that help to minimise the damage. As an example, DNA photolyase

is an enzyme that splits cyclobutane–pyrimidine dimers that result from a UV light-induced covalent link between two thymine or cytosine bases on the same DNA strand [78]. DNA photolyase is a flavoprotein that contains two chromophores. One acts as an antenna pigment to harvest the light while the other is the catalytic cofactor that carries out the repair. In this enzymatically catalysed reaction, the dimer flips out of the DNA and inserts into the active site of the enzyme. Upon excitation, the catalytic cofactor transfers an electron to the DNA which leads to a splitting of the cyclobutane ring. The photocycle is completed by restoring the active form of the cofactor through an electron back-transfer from the repaired DNA [79]. This illustrates another complex and important mechanism in which charge transfer plays a major role.

Another important charge transfer reaction takes place in cryptochrome. This is a flavin-binding photoreceptor found in plants and animals which mediates responses to blue light like seed-gemination and pigment accumulation in plants or the synchronisation of the circadian rhythm in animals [31]. Upon light absorption, the flavin chromophore is reduced in an electron transfer process. Again, a coupling between electron and proton transfer leads to the biological response.

Of course, charge transfer can not only be found in biologically relevant systems. Using solar cells to convert sunlight into electrical energy as an environmentally friendly energy source is attracting much attention. Great effort is taken to enhance the performance of organic solar cells since they are easier to process and more versatile than silicon based solar cells. Ideas like “solar paint” or easily printable devices are very intriguing.
The most promising implementation of organic photovoltaics is the bulk-heterojunction solar cell [80]. A blend of two molecular compounds, for example a polymer and a fullerene, are sandwiched between two electrodes one of which has to be transparent. The polymer acts as a light absorbing chromophore and as an electron donor, while the fullerene is the electron acceptor. Upon absorption of light, an exciton is created, which diffuses to an interface between donor and acceptor. There an interfacial charge transfer takes place. Subsequently, the separated charges diffuse to the electrodes and enter the external circuit [81]. To achieve a high conversion efficiency, many participating reaction steps have to be optimised, including the charge transfer at the donor–acceptor interface.

There are other charge-transfer systems which are of more academic interest. An example is the photoluminescence of silicon quantum dots with a specially functionalised surface [32]. It was found that surface states have a strong impact on the bulk luminescence of the quantum dots. The ultrafast luminescence properties are determined by an electron transfer from an

initially excited surface state to a bulk state of the quantum dot.

Various theories to quantify the charge-transfer dynamics have been developed. A brief overview will be given in section 3.2.

To experimentally investigate charge transfer, ultrafast spectroscopy techniques have proven the ideal tool, especially transient absorption spectroscopy (see chapter 2.3). The experimental setup used for the measurements in the framework of this thesis will be explained in chapter 3.3, along with the data acquisition and evaluation routine.

Gaining access to model compounds in which charge transfer can be easily monitored and interpreted is crucial. The class of neutral organic mixed-valence (MV) compounds has proven to be an ideal candidate for CT reactions. Two classes of MV compounds will be introduced. The first polymeric MV compound will be discussed in chapter 4. In chapter 5, a two-dimensional MV compound will be examined.
Subsequent to that, a different class of CT compounds is introduced in chapter 6, namely a metallo-supramolecular polymer where an electron is transferred from the metal center to the ligand upon optical excitation.

3.1 Neutral organic mixed-valence compounds

Although a large variety of natural charge transfer systems and the corresponding reactions are known, it is important for the understanding of the underlying principles to have access to suitable model systems for charge transfer reactions. The class of neutral organic mixed-valence compounds provides numerous model compounds to study CT reactions and the influence of different parameters on these in a systematic way. But before going into detail which compounds exactly are concerned here it is important to define the term "neutral organic mixed-valence compound" and give an overview of the crucial properties of this class of compounds.

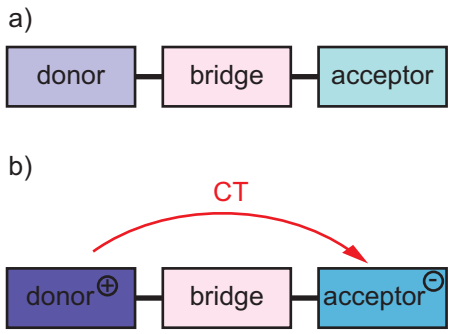

Figure 3.1: Schematic representation of a mixed-valence compound (figure a)). A donor and an acceptor moiety are connected by a bridge. Upon excitation, charge transfer from the donor to the acceptor can take place, yielding an oxidised donor and a reduced acceptor (figure b)).

According to a recently introduced definition [8] organic mixed-valence compounds can be seen as a subclass of donor–acceptor compounds. Two (or more) redox centers in different oxidation states are linked to each other by a bridge or spacer unit (figure 3.1 a)). Charge transfer between both can take place in which one of the redox centers acts as the electron donor, the other one as the acceptor moiety. This charge transfer may be induced thermally or optically, yielding an oxidised donor and a reduced acceptor moiety as depicted in figure 3.1 b). What distinguishes organic mixed-valence from organic donor–acceptor compounds is the fact that the former possess an open-shell configuration in the electronic ground state whereas the latter feature a closed-shell configuration. More precisely, open shell configuration means that unpaired electrons are present, making organic mixed-valence compounds radicals in the ground state. The excited electronic states may exhibit an open-shell configuration for mixed-valence as well as for donor-acceptor compounds. It is important to mention that this definition may only be applied strictly for purely organic compounds [8].

The ground state open-shell configuration of organic mixed-valence compounds leads to several complications and constraints concerning the han-

dling and application of them. Many compounds are charged radical anions or radical cations that can only be generated in situ. They exhibit a lower stability than neutral compounds and are less soluble, especially in relatively non-polar solvents what may render liquid-phase spectroscopic investigation difficult. It is possible to circumvent these problems by combining a radical cation donor and a radical anion as acceptor, yielding a truly *neutral* organic mixed-valence compound. Concerning the synthesis, however, neutral precursors are used instead of the radical ions. The first examples of such compounds comprise a triarylamine (TARA) moiety as electron donor and a perchloro-triphenylmethyl radical (PCTM) as acceptor, linked by different bridges [82, 83]. The donor and acceptor moieties in the neutral species are isoelectronic to that of the charged species. The neutral organic mixed-valence polymer presented in chapter 4 is directly based on this TARA-PCTM motif, a more detailed introduction to this class of compounds will be given in that chapter.

Although countless different examples of organic mixed-valence compounds exist, they can roughly be devided into three classes according to the electronic coupling between the redox centers which determines the localisation of the charge in the system [84]. In a class one compound the donor and acceptor are not coupled electronically at all and can be treated as two completely isolated moieties. As a result, no intramolecular charge transfer can occur. Class two compounds exhibit moderate electronic coupling, the charge is mainly localised at one of both redox centers. The spectroscopic properties of class two compounds can be expected to resemble those of the isolated oxidised and reduced redox centers plus contributions from the bridge and from interaction of all moieties. For class three compounds the electronic coupling is so strong that the charge is delocalised over the entire system. The question of localisation and delocalisation of the charge, in other words the borderline between class two and class three compounds, has been subject of many studies [82, 85–87].

Since the mixed-valence compounds which are subject of this thesis were investigated by time-resolved spectroscopy, it is instructive to have a closer look at the spectroscopic properties of mixed-valence compounds. In the steady-state absorption spectrum, the charge transfer from the donor to the acceptor is associated with the so-called intervalence charge transfer (IVCT) absorption band. It usually appears as the lowest-energy band in the visible or near-infrared spectral region since the charge transfer is the lowest possible transition. In most organic mixed-valence compounds, the IVCT does not overlap with bands from other transitions unlike in inorganic donor-acceptor compounds where the IVCT band may be very weak and overlapped by the metal-to-ligand or ligand-to-metal charge transfer or other bands. Since a

theoretical framework exists which allows to extract important molecular parameters like the electronic coupling between the redox centers from the IVCT band it is of great advantage to have an unambiguously defined IVCT that is not overlapped with other bands. Thus organic mixed-valence compounds are also ideal model systems insofar as a band-shape analysis can be conducted to extract the parameters of interest.

A rich theoretical framework exists which allows for a quantitative analysis of charge-transfer processes, yielding information about the thermodynamic parameters that have an impact on the charge transfer dynamics. It may also facilitate a prediction of charge transfer rates, therefore a theoretical analysis of charge transfer is indispensable for a deeper understanding of the underlying mechanisms. An overview of different theoretical approaches to quantify charge transfer will be given in the next section.

3.2 Theoretical description of charge-transfer processes

In this section, the most important theories to describe charge transfer quantitatively will be introduced briefly. Chapter 3.2.1 will focus on the Marcus theory, a purely classical thermodynamic diabatic approach to predict rate constants of CT reactions. The important thermodynamic parameters that influence the CT will be introduced there. The adiabatic generalisation of Marcus theory, the Marcus–Hush or Mulliken–Hush theory, will be presented in chapter 3.2.2. It allows to extract the electronic coupling between both redox centers from the IVCT band in the absorption spectrum. Finally chapter 3.2.3 will cover the Bixon–Jortner model, a quantum chemical method which renders the determination of important thermodynamic parameters from the absorption spectra possible.

3.2.1 Marcus theory

The theoretical framework initially developed by R. Marcus in the 1950s and refined continuously [88–90] is one of the first approaches to describe charge-transfer reactions in solution quantitatively. It is a purely diabatic treatment, which means that two formally non-interacting states are used to describe the redox centers. This corresponds to a situation where the electronic coupling V between them is smaller than the thermal energy k_BT with the Boltzman constant k_B and temperature T. The free energy surfaces of the system are parabolic profiles with respect to a reaction coordinate which incorporates the structural changes in the CT system and solvent reorganisation effects associated with charge transfer (see figure 3.2). One parabola represents the reactant state (light blue) with its energetic minimum at the equilibrium position $q_{R,0}$ on the reaction coordinate while the other refers to the product state (dark blue) with minimum energy at $q_{P,0}$.

In a degenerate mixed-valence compound both redox centers are identical and the minima of the free energy surfaces of reactant and product state lie at the same energy ΔG. The case of a non-degenerate mixed-valence compound is depicted in figure 3.2 a). The minima of both curves are offset by ΔG^0 with respect to each other. The barrier height for a thermally induced charge transfer is given by ΔG^*. For an optically induced charge transfer a certain amount of energy has to be brought into the system which has to be equal to the reorganisation energy λ in the case that $\Delta G^0 < 0$, which is usually satisfied for charge-transfer reactions. Then a Franck–Condon-like transition from the reactant to the product state can take place.

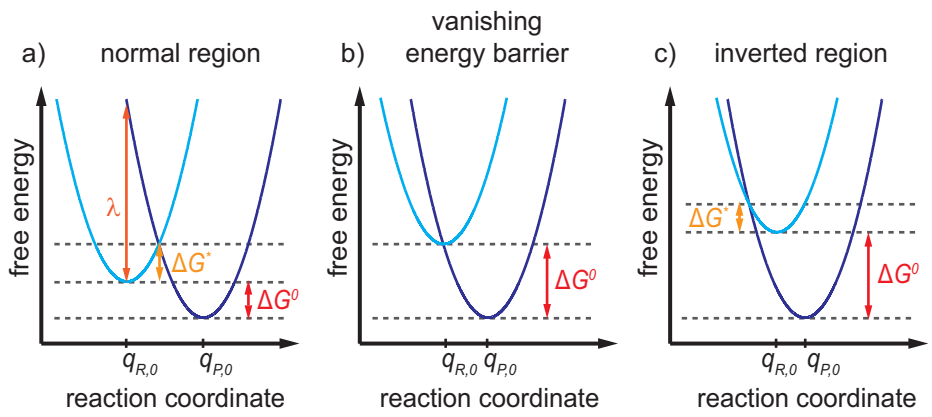

Figure 3.2: Free energy surfaces of the reactant (light blue) and product state (dark blue). In the normal region (figure a)) the reaction rate increases with decreasing ΔG^0. The maximum value for the rate is reached in the case of a vanishing energy barrier as depicted in figure b). Figure c) shows the Marcus inverted region where the reaction rate again decreases with decreasing ΔG^0. The reorganisation energy λ is indicated in red in figure a).

The reorganisation energy λ comprises two contributions. An outer reorganisation energy λ_o and an inner reorganisation energy λ_i. The former is associated with the reorientation of solvent molecules due to a change in the charge distribution of the mixed-valence compound upon charge transfer. The latter reflects a change of geometry caused by the charge transfer like changes of bond lengths and angles. λ_i is an intrinsic parameter of each mixed-valence compound and therefore it is difficult to predict. In contrast, the outer reorganisation energy λ_o can be calculated using a dielectric continuum model for the solvent. The donor and acceptor redox centers are assumed to have a spherical shape with radii r_1 and r_2 and a distance (center to center) of r_{12}. λ_o then depends on the index of refraction n and the permittivity D of the solvent:

$$\lambda_o = \frac{e^2}{4\pi\epsilon_0}\left(\frac{1}{2r_1}+\frac{1}{2r_2}-\frac{1}{r_{12}}\right)\cdot\left(\frac{1}{n^2}-\frac{1}{D}\right). \tag{3.1}$$

The rate constant for the charge transfer is given by an Arrhenius-type equation

$$k = \nu_n \kappa_{\mathrm{el}} \exp\left(\frac{-\Delta G^*}{k_B T}\right). \tag{3.2}$$

ν_n is the nuclear motion frequency through the transition state, κ_{el} is the electron transmission coefficient and ΔG^* can be calculated from the parabolic

shapes to yield

$$\Delta G^* = \frac{(\lambda + \Delta G^0)^2}{4\lambda}. \tag{3.3}$$

From equation 3.3 it can be seen that the charge transfer dynamics strongly depend on the ratio of λ, which always adopts a value larger than zero, and ΔG^0 which is usually negative. Three regions can be distinguished which are depicted in figure 3.2. In the normal region $|\Delta G^0|$ ranges from 0 to λ. With increasing $|\Delta G^0|$ the barrier height ΔG^* decreases and the rate k increases (figure 3.2 a)). The situation depicted in figure 3.2 b) corresponds to a vanishing energy barrier if $|\Delta G^0| = \lambda$. In that case k adopts its maximal possible value. The most surprising prediction of Marcus theory is sketched in figure 3.2 c), the so-called Marcus-inverted region in which $|\Delta G^0|$ can adopt any value larger than λ. Further increase of $|\Delta G^0|$ causes the barrier height ΔG^* to increase again, leading to a smaller reaction rate k for very exergonic reactions (a reaction in which the change in Gibb's free energy is negative). The existence of the Marcus-inverted region was subject to controversial discussion until it could be proven experimentally [91].

The optically induced charge transfer relies on the input of energy into the system to induce a Franck–Condon-type transition. The absorption of a photon leads directly to a charge transfer before the geometry of the mixed-valence system and the solvent orientation can respond to the change in charge distribution. After the CT event, the geometry and solvent orientation relax into the new equilibrium configuration. In contrast to that, also thermally induced charge transfer can occur which is triggered by thermal fluctuations and collisions with solvent molecules. Before the CT event, the charge is localised at one redox center and the solvent molecules are oriented to stabilise the charge while the solvent molecules around the other redox center are oriented more randomly. A gradual transition from the reactant to the product state takes place during charge transfer, the geometries of both redox centers and the orientation of the solvent molecules change as the system passes through the transition state with ΔG^* (at the intersection of both parabolae). The total free energy of the system is kept constant by equilibration with the solvent bath.

It is important to mention that the considerations presented here are only valid for sufficiently high temperature. At low temperature, the thermal energy does not suffice to overcome the barrier any longer and electron tunneling becomes the dominating mechanism which cannot be described by equation 3.2. By treating vibrations of the solvent and of the charge-transfer system quantum-chemically this complication can be eliminated, yielding an expression for the reaction rate which is at low temperatures dominated by electron tunneling and shows an activation-like behaviour for high tempera-

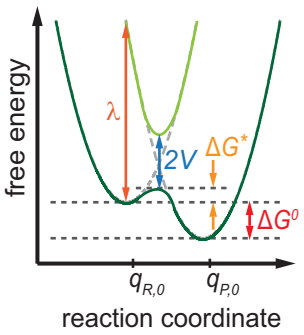

Figure 3.3: Adiabatic free energy surface for a class two mixed-valence compound. The ground state is depicted in dark green, the excited state in light green. The electronic coupling V directly influences the separation of both surfaces.

tures [92].

3.2.2 Marcus–Hush and Mulliken–Hush theory

The Marcus–Hush theory can be regarded as the adiabatic generalisation of classical Marcus theory [93, 94]. The interaction between both redox centers is taken into account in the form of the electronic coupling V, which is a measure for the magnitude of the interaction. The adiabatic free energy surfaces can be constructed by coupling the diabatic ones. The result is shown in figure 3.3 for a class two mixed-valence compound. The adiabatic ground state surface (dark green) exhibits a double-minimum shape, the excited state surface is depicted in light green. Both are separated by a value of $2V$ at the maximum of the barrier in the ground state. The barrier ΔG^* for thermally induced charge transfer is reduced in comparison to Marcus theory because of the electronic coupling and has to be corrected by resonance delocalisation.

Now the optically induced charge transfer starts from the Boltzmann-populated vibrational levels of one minimum of the electronic ground state into the manifold of vibrational states of the excited electronic state according to the Franck–Condon principle. The relaxation from the excited state to the second minimum of the ground state leads to a product configuration in which the charge has been transferred from one redox center to the other. As in classical Marcus theory, these considerations are only valid in the high-temperature limit to ensure a Boltzmann-weighted population of vibrational levels. In other words, the energetic separation of vibrational levels ΔE_{vib} has to be small compared to the thermal energy $k_B T$: $\Delta E_{\text{vib}} \ll k_B T$.

Within the framework of Marcus–Hush theory it is possible to explain the shape of the IVCT band in the absorption spectrum. Since in the high-temperature limit the vibrational manifolds of the ground and excited state are involved, a large variety of transitions contributes to the IVCT band. Because of the Boltzmann-weighted population of levels, the sum of many dif-

ferent inhomogeneously broadened transitions with varying intensities leads to a Gaussian-shaped IVCT band. The maximum of the band corresponds to the transition with highest transition probability with $\nu_{\max} = \Delta G^0 + \lambda$ [8].

If the electronic coupling V is sufficiently small, an almost perfectly Gaussian-shaped IVCT band can be observed. With increasing coupling strength the asymmetry of the IVCT band increases. This can be explained by the separation of the adiabatic free energy surfaces as seen in figure 3.3: The separation in free energy at the crossing point of the diabatic surfaces has a magnitude of $2V$. If V is small this separation is also small and the IVCT band is symmetric. However, for large values of V this separation increases, leading to a cut-off for transitions in the low-energy wing of the band at $2V$ since it reflects the lowest possible electronic transition [85].

For a more quantitative treatment it is useful to have a closer look at the Mulliken–Hush theory [93, 95]. It can be regarded as a generalisation of Marcus–Hush theory. The main differences are that no assumptions are made concerning the shape of the diabatic states or the number of states involved in the charge transfer process. This allows to determine the electronic coupling V between the diabatic states from the IVCT band. V is given by

$$V = \frac{\mu_{ab}\nu_{\max}}{\Delta\mu_{12}} \tag{3.4}$$

with $\nu_{\max} = \Delta G^0 + \lambda$. The transition moment μ_{ab} between the adiabatic states can be calculated by integrating the IVCT band. The main drawback is the dependence on the diabatic dipole moment difference $\Delta\mu_{12}$ which is not directly accessible. Nevertheless, it may be approximated using the adiabatic dipole moment difference $\Delta\mu_{ab}$:

$$\Delta\mu_{12} = \sqrt{\Delta\mu_{ab}^2 + 4\mu_{ab}^2}. \tag{3.5}$$

Still one has to keep in mind that this may introduce major inaccuracies because $\Delta\mu_{ab}$ can often only be estimated from geometrical considerations or be calculated quantum-chemically. Thus the main challenge for the application of the Mulliken–Hush theory is acquiring a reasonable value for $\Delta\mu_{ab}$. However, it is remarkable that molecular parameters that have a strong impact on the charge-transfer behaviour can be extracted from an analysis of the steady-state absorption spectrum.

3.2.3 The Bixon–Jortner model

In addition to the theories discussed so far, the Bixon–Jortner model [96] poses a quantum-chemical approach in which the molecular vibrations are

treated more accurately. It is a truly diabatic theory to describe transitions between different states.

The influence of molecular vibrations is taken into account in the form of a weighted average high-frequency vibrational mode $\tilde{\nu}_i$ of the charge transfer system. This average mode is treated quantum-chemically. The low-frequency vibrational modes of the solvent are treated classically as harmonic potentials.

If the averaged mode is sufficiently high in energy ($\tilde{\nu}_i > 1000\,\mathrm{cm}^{-1}$), this means that only the lowest vibrational level in the electronic ground state is populated because of the large energy separation of vibrational levels. Thus, all possible optical transitions originate from the same vibrational level and lead into the vibrational manifold of the electronically excited state, yielding a Franck–Condon-like progression. In that sense, the Bixon–Jortner theory yields a Golden-rule expression for the transitions. It is important to mention though that the Franck–Condon factor is replaced by a term dependent on the Huang–Rhys factor $S = \lambda_i/\tilde{\nu}_i$. In this way it is possible to fit the experimentally observed IVCT band in order to extract the thermodynamic parameters like λ_o and λ_i independently.

The main limitation of this method is determined by the Huang–Rhys factor. Since it is a diabatic theory, it can only be applied to electronically weakly coupled systems featuring a small Huang–Rhys factor. The IVCT band has to be sufficiently asymmetric for the band fit to be defined. In this way, the Bixon–Jortner model is an ideal complement to the Marcus–Hush theory which is optimally suited for electronically strongly coupled systems.

Many more theories exist that focus on different aspects of charge transfer, a few examples will be discussed briefly. For strongly coupled mixed-valence systems with a rather asymmetric IVCT band it turns out useful to extend the Marcus–Hush theory to include two averaged vibrational modes, a symmetric and an asymmetric one [97–99]. This yields two reaction coordinates and thus two-dimensional potentials for the ground and excited state. The electronic coupling V can then be extracted from the absorption spectrum without the need to estimate the adiabatic dipole moment difference between the ground and excited state, thus overcoming the main difficulty in Marcus–Hush theory.

The generalised Mulliken–Hush model [100] allows for a multistate treatment of charge transfer processes. This is especially important if the redox centers do not only interact with each other but also with the bridging unit. In many cases this leads to additional "bridge bands" that appear in the absorption spectrum at higher energy than the IVCT band.

Also more sophisticated quantum-chemical methods exist which take into account that the electronic coupling in mixed-valence systems is strongly

influenced by the movement of the nuclei in the system [98, 99, 101, 102]. The IVCT bands of mixed-valence compounds can be calculated successfully using these methods [103, 104].

3.3 The transient spectrometer

The basic principle of transient absorption spectroscopy was introduced in chapter 2.3.2. In this chapter, the experimental implementation of a transient spectrometer will be discussed in detail. The transient absorption data presented in the subsequent chapters have been measured at two different experimental setups both of which are depicted schematically in figure 3.4. One setup is driven by a 1 kHz-repetition rate Ti:Sa amplifier and employs a shot-to-shot readout mechanism (figure 3.4 a)) while the other uses a high-repition rate (100 kHz) amplifier and a time-averaged detection scheme (figure 3.4 b)). The similarities and differences of both setups will be explained in detail now.

3.3.1 1 kHz shot-to-shot transient spectrometer

This setup has been described in detail before in references [105] and [106]. The laser source that drives the entire 1 kHz transient absorption spectrometer is a *MaiTai/Solstice* system by Spectra-Physics. The *MaiTai* is a Ti:Sa oscillator which is pumped by a 4.8 W continuous-wave Nd:YVO_4 laser at 532 nm (*Spectra Millenia*). The oscillator output comprises pulses of a central wavelength close to 800 nm, a duration of approximately 100 fs and an energy of 9 nJ at a repetition rate of 80 MHz [107]. The oscillator pulses are then amplified in a chirped-pulse amplification scheme [108, 109]. They are stretched temporally before being injected into the *Solstice* cavity by a Pockels cell at a repetition rate of 1 kHz. A pulsed Nd:YLF laser (*Spectra Empower*) is used to pump the *Solstice* regenerative amplifier. The input pulses are amplified to a pulse energy of about 2.5 mJ. The amplified pulses are ejected from the amplifier cavity and compressed to a duration of approximately 100 fs at a central wavelength of 800 nm [110].

The major fraction of the output power is used to pump a noncollinear optical parametric amplifier (*TOPAS white* by Light Conversion Ltd.) which generates the pump pulse for the transient absorption measurements. The incident 800 nm radiation is split to generate a white-light supercontinuum in a sapphire plate which acts as seed for the amplification. The pump pulse for the amplification is generated by frequency-doubling the 800 nm pulses. In a two-stage amplification process, output pulses in the spectral range between 500 nm and 750 nm can be generated. Their spectral width and pulse energy strongly depend on the *TOPAS* settings. Typically, a spectral FWHM of 30 nm and a pulse energy of up to 50 μJ can be achieved. The pulses can be compressed temporally to some extent by a built-in pulse compressor before leaving the *TOPAS* [111].

Subsequently, the *TOPAS* output pulses are characterised and compressed with the help of a Fourier pulse shaper with a two-layer 640 pixel liquid crystal array by Cambridge Research and Instrumentation. Details about the pulse shaper and the characterisation and compression procedure can be found in chapter 7.1. Depending on the spectral FHWM, the pulses can be compressed to a minimum duration of about 25 fs.

The compressed pulses are then temporally delayed by a motorised linear stage (Newport stage IMS600LM [112] with Newport XPS Controller [113]). A maximum delay of 4 ns with a sub-femtosecond temporal stepsize is possible [112]. After that the pulses traverse a chopper operated at a frequency of 500 Hz (triggered by the *Solstice's* Pockels cell) so that every second pump pulse is blocked.

The minor fraction of the *Solstice* output is used to generate the white-light supercontinuum probe pulse. It is focused into a calcium fluoride plate, yielding a supercontinuum that spans the entire visible and part of the near infrared spectral range. An edge filter was used to block the residual 800 nm fundamental, thus only part of the continuum between 400 nm and 750 nm was used to probe the dynamics. Although calcium fluoride has the advantage of generating very broadband continua, it has a rather low damage threshold as a drawback [114]. This can be overcome at least partially by constantly moving the calcium fluoride plate. Thus its lifetime is expanded because the 800 nm laser pulses interact with different regions of the plate.

The pump and probe pulses are then spatially overlapped in the sample. The sample solution is constantly pumped through a flow cell with a film thickness in the range of 200 μm to 500 μm either by a peristaltic pump or by a micro-annular gear pump. Thus, each laser pulse interacts with a fresh sample volume and artifacts by multiple excitation of the same sample volume can be excluded.

The absorption changes of the probe pulse are detected by coupling the probe pulse into a spectrometer with a charge-coupled device (CCD) camera. The camera chip has 2048 (horizontal) times 512 (vertical) pixels, hardware binning in the horizontal as well as in the vertical direction allows a 1 kHz readout of the camera. In combination with the 500 Hz chopper this allows for a shot-to-shot detection of signal and reference spectra for subsequent shots, that is for an excited and a non-excited sample volume (see equation 2.68) [105]. The shot-to-shot readout mechanism has the big advantage of not being sensitive to low-frequency noise in the output intensity of the amplifier system [115]. Because of the high correlation of subsequent laser pulses, the signal to noise ratio of the recorded signal is very large, resulting in a very good data quality [116, 117] (especially compared to the time-averaged readout mechanism of chapter 3.3.2).

The data acquisition and evaluation (calculation of the change in optical density) is done by a personal computer which is also used to control the measurement sequence in the framework of a homebuilt LabView data acquisition and evaluation environment [25].

3.3.2 High repetition rate transient spectrometer

A more detailed description of this setup can be found in reference [118]. As the laser source for the high repetition rate transient spectrometer an oscillator/amplifier assembly (*Mira/RegA*) by Coherent Inc. is used [119, 120]. It has a similar working principle as the *MaiTai/Solstice*-assembly described above: The *Mira* Ti:Sa-oscillator is pumped by 25% of the intensity output of a frequency-doubled continuous wave Nd:YVO_4 laser (*Verdi V18* [121]). The *Mira* pulses have a duration of approximately 120 fs at a central wavelength of 800 nm, a repetition rate of 76 MHz and a pulse energy of about 4.7 nJ. 30% of the output is used as a seed for the regenerative Ti:Sa amplifier (*RegA*) which is pumped by the residual 75% of the *Verdi* output. Like the *MaiTai/Solstice* system, the *Mira/RegA* system is based on chirped pulse amplification, but in contrast to the MaiTai/Solstice no additional pulse stretcher is employed. Instead, the seed pulse gains a certain amount of chirp with each roundtrip in the amplifier cavity. After ejection from the amplifier cavity, the pulses are compressed in a grating compressor to a duration of about 150 fs at a central wavelength of 800 nm. The output pulses have a pulse energy of 0.7 μJ and a repetition rate of 100 kHz.

Identical to the setup described in chapter 3.3.1, the major fraction (70%) of the amplifier output is used to generate the pump pulse for the transient absorption measurement. This is done in an optical parametric amplifier (Coherent *OPA 9400* [122]). As the seed for the parametric amplification, a supercontinuum generated in a sapphire plate is used. The pump pulse comprises the second harmonic of the 800 nm fundamental. Pump and seed pulses are focused into a β barium borate (BBO) crystal in a collinear fashion. The two-stage amplification process is achieved by traversing the same BBO crystal twice. By adjusting the crystal angle, the central wavelength of the amplified output pulses can be tuned. The characteristics of the output pulses strongly depend on the center wavelength, the pulse energy lies in the range of tens of nJ, the duration varies from approximately 180 fs to 300 fs.

The OPA pulses are characterised with a second harmonic generation frequency-resolved optical gating (SHG-FROG) setup [123, 124]. The input pulse is split into two replica which are temporally delayed with respect to each other and spatially overlapped in a BBO crystal. The generated second-harmonic light is detected in a spectrally-resolved manner in dependence of

the time delay between both replica, thus yielding a two-dimensional spectrogram. From this spectrogram the spectral phase of the input pulse can be retrieved by the help of an inversion algorithm [124, 125].

For pulse compression a prism compressor is employed [126]. The combination of material dispersion induced by traversing the prism and the angular dispersion caused by the prism can be used to generate negative group velocity dispersion (GVD) which can compensate for the positive GVD introduced by any transparent material the OPA pulse has traversed, thus recompressing the pulse to a duration of 60–70 fs. For the data presented later in this thesis, a two-prism sequence was used [118]. However, it is beneficial in terms of tunability to use a folded one-prism compressor [127]. The alignment is greatly simplified if only one prism angle has to be adjusted if the central wavelength of the OPA pulses is changed. Thus, a one-prism compressor has been incorporated into the setup in the meantime [128].

The compressed pulses then traverse a delay line with 4 ns maximum delay and a temporal resolution of $4 \cdot 10^{-18}$ s which comprises the same delay stage (Newport IMS600LM [112] with Newport XPS Controller [113]) as in the shot-to-shot transient spectrometer. Subsequently, the OPA pulses are focused into the sample and act as pump pulses for the spectroscopy.

The probe pulses are generated by the remaining minor fraction of the RegA output. By focusing it into a sapphire plate, a supercontinuum is generated which is used to probe the absorption changes. Although it spans a narrower spectral range than the supercontinnum generated in calcium fluoride, sapphire has the advantage of a higher damage threshold. Therefore it can withstand longer exposure to high-intensity laser radiation and provides a stable supercontinuum without the need for any moving parts, in contrast to the probe pulse generation in the shot-to-shot setup.

The main difference between both setups introduced here is the actual data acquisition. Implementing a shot-to-shot readout mechanism for the high-repetition rate setup constitutes a rather challenging task. Nevertheless, it is possible. The necessary modifications to the existing setup will be discussed in chapter 6.5.2. For the time being, a time-averaged detection scheme is used. Therefore the white light supercontinuum is split into two fractions of equal intensity which traverse different regions of the sample solution. One of both beams is spatially overlapped with the pump pulse and actually detects the pump-induced absorption changes. The other traverses a non-excited volume of the sample solution and acts as a normalisation to reduce the influence of laser power fluctuations [129]. Thus, two additional normalisation spectra are detected: $I^0(\lambda, \tau)$ which corresponds to the probe spectrum that has traversed an excited sample volume (after interaction of the sample with the pump pulse) and the reference normalisation $I^0_{\mathrm{ref}}(\lambda)$

which is related to the case when the pump pulse is blocked and only the reference is detected. Equation 2.68 for the absorption change has to be modified accordingly, thus yielding

$$\Delta\mathrm{Abs} = -\log_{10}\left(\frac{I(\lambda,\tau)/I^0(\lambda,\tau)}{I_{\mathrm{ref}}(\lambda)/I^0_{\mathrm{ref}}(\lambda)}\right). \tag{3.6}$$

Since chopping the pump beam at half of the repetition rate is not necessary in this detection scheme, the pump beam is blocked with a shutter (denoted S1 in figure 3.4 b)) for an acquisition time in the order of 300 ms. A second shutter (denoted S2) can be used to block the probe beam. Thus only the scattered pump radiation is detected and can be used to subtract a scattering correction [118].

Both probe beams are coupled into two fibers of a four-fold fiber tree which leads to a spectrometer with a CCD camera. The CCD chip has 512 times 512 pixels. Both probe spectra are spectrally dispersed onto different vertical regions of the CCD chip and can thus be recorded simultaneously.

The same data acquisition and evaluation environment as in chapter 3.3.1 is used to ensure computer control of the measurement sequence and of the acquisition of the raw data. Postprocessing of the data to calculate the absorption changes is achieved with special LabView programs.

Both transient spectrometers introduced here can be used to monitor the ultrafast absorption changes of any molecular system which can be excited in the visible spectral range (given by the TOPAS/OPA operation range) and which exhibits absorption changes predominantly in the spectral range given by the white-light supercontinua. Examples of such molecular systems and the corresponding results will be presented in the following chapters.

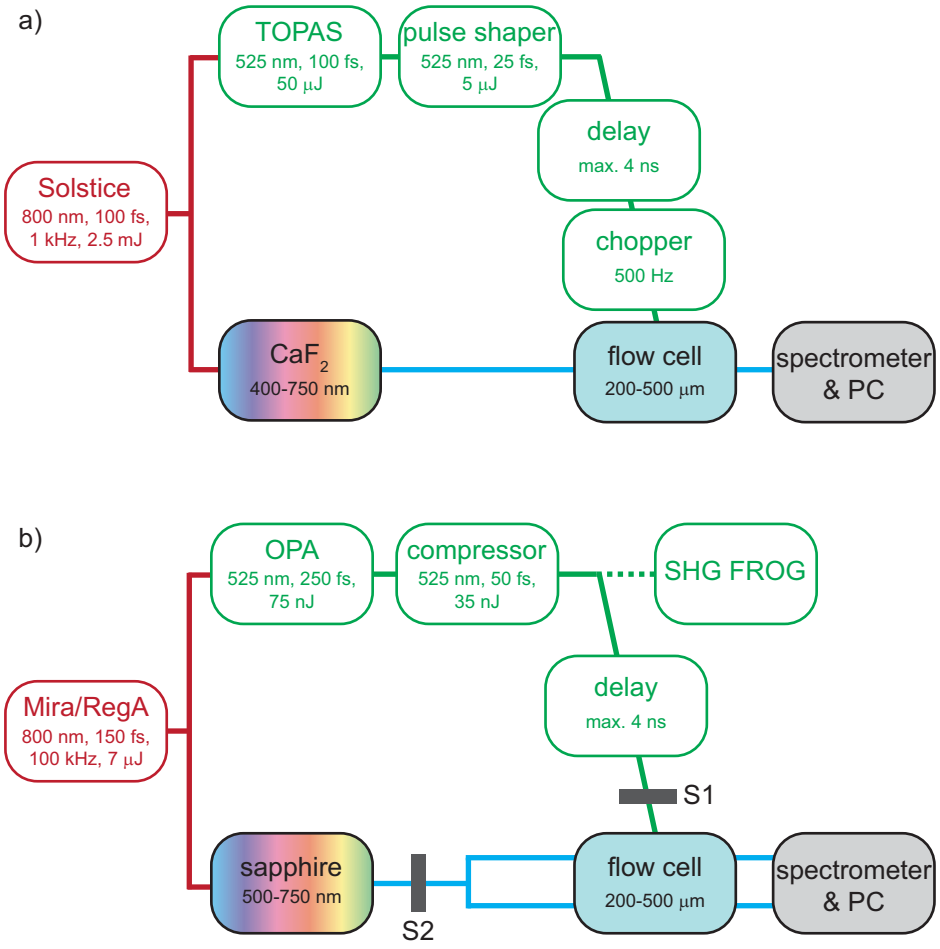

Figure 3.4: Schematic representation of both transient absorption spectroscopy setups used in this work. Figure a) shows a 1 kHz shot-to-shot detection scheme which is driven by a 1 kHz Ti:Sa amplifier. The pump pulse is generated in a noncollinear optical parametric amplifier and characterised and compressed by the aid of the pulse shaper. It is temporally delayed with a motorised linear stage and chopped at 500 Hz so that every second pulse is blocked. A white-light supercontinuum generated in a calcium fluoride plate is used as a probe pulse. Both pulses are spatially overlapped in the sample. In figure b) the high-repetition-rate (100 kHz) setup is depicted in which a time-averaged detection is employed. An optical parametric amplifier is used to generate the pump pulse, which is compressed in a prism-compressor and characterised by second harmonic generation frequency resolved optical gating (SHG FROG). Again the pump pulse is time-delayed with a motorised linear stage. The white-light supercontinuum probe is generated in a sapphire plate and split into two beams, one of which overlaps spatially with the pump in the sampe flow cell while the other acts as a reference.

3.4 Global analysis of transient absorption spectra

The theoretical description given in chapter 3.2 so far focuses either on the analysis of the steady state absorption spectra of mixed-valence compounds or on the relation between the reaction rate for the charge transfer and molecular or thermodynamic parameters. However, a different approach is necessary for the analysis of transient absorption spectra.

As can be seen from equation 2.66, the optical density depends on the number of absorbing molecules $N(\tau)$ and the absorption cross section $\sigma(\lambda)$. This can also be expressed in term of the concentration $c(\tau)$ and the extinction coefficient $\varepsilon(\lambda)$:

$$\mathrm{OD}(\lambda,\tau) = \frac{1}{\ln(10)} N(\tau)\sigma(\lambda)d = \frac{1}{\ln(10)} c(\tau)\varepsilon(\lambda)d. \tag{3.7}$$

If n different chemical species are contained in the sample, the overall optical density is given by the sum of the contributions of all species:

$$\mathrm{OD}(\lambda,\tau) = \frac{1}{\ln(10)} d \sum_{i=1}^{n} c_i(\tau)\varepsilon_i(\lambda). \tag{3.8}$$

$c_i(\tau)$ and $\varepsilon_i(\lambda)$ are the concentration profiles and extinction coefficients of the different species, respectively.

To describe a difference spectrum as measured with transient absorption spectroscopy, the ground state bleach has to be taken into account via

$$\Delta\mathrm{Abs} = \frac{1}{\ln(10)} d \sum_{i=1}^{n} c_i(\tau)(\varepsilon_i(\lambda) - \varepsilon_0(\lambda)). \tag{3.9}$$

Here, $\varepsilon_0(\lambda)$ denotes the absorption spectrum of the ground state. Equation 3.9 describes the transient absorption spectrum in case of particle conservation, thus if no photodescruction by the pump pulse occurs. Examples of different chemical species may be molecules in different excited states or different isomers.

Although equation 3.9 describes the two-dimensional transient data, the major complication regarding the analysis of the data arises from the fact that the spectra and concentration profiles of the different species are often not known a priori. Thus, the aim of data analysis is to disentangle the contributions of the different species and their role in the photophysical or photochemical process of interest. This can be achieved by global or target analysis of the data [130]. The focus will lie on global analysis since no target

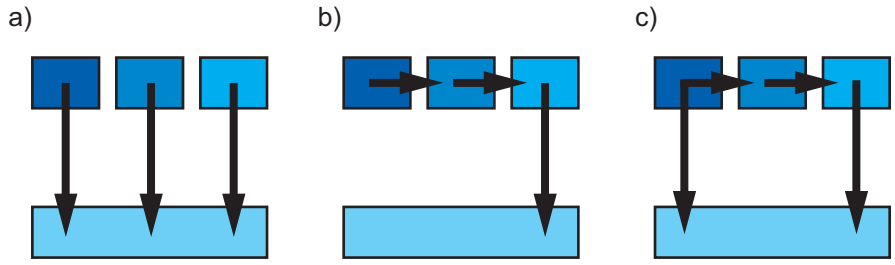

Figure 3.5: Three classes of kinetic models can be distinguished: In figure a) a parallel model is shown. The concentration profiles of all species decay parallel, independent of each other. Figure b) depicts a sequential model in which the system evolves from one state to the next before in finally decays to the ground state. A combination of the former and the latter model is given in figure c), usually called an arbitrary model. This can be used as the target model in target analysis.

analysis was conducted for this thesis. However, it will shortly be mentioned for the sake of completeness.

For transient absorption spectroscopy, global analysis means that the two-dimensional data obtained in the experiment are fitted globally within the framework of a spectral or kinetic model. The discussion here will restrict to kinetic models. Three different classes of models can be distinguished as depicted in figure 3.5 [130]. In a parallel model, the concentrations of different species decay independently to the same ground state (figure 3.5 a)). In contrast to that, the system evolves from one state to the next in a sequential model as can be seen in figure 3.5 b). In figure 3.5 c) an example of an arbitrary model is shown, which can basically be regarded as a combination of the parallel and sequential model and is used in target analysis.

Analytic expressions for the concentration profiles of the different models can be derived if one solves the underlying differential equations. Only first-order kinetics will be considered here, i.e. $\frac{\mathrm{d}c}{\mathrm{d}t} \propto c$. In the case of the parallel

model, the result reads

$$c_i^{\text{para}}(\tau) = e^{-k_i \tau} \tag{3.10}$$

with the rate constant k_i. The inverse of this rate constant gives the lifetime τ_i of the corresponding species, $\tau_i = \frac{1}{k_i}$.

For the sequential model, the concentration profiles are given by

$$c_i^{\text{seq}}(\tau) = \sum_{j=1}^{i} b_{ij}\, e^{-k_j \tau} \tag{3.11}$$

with coefficients

$$b_{ij} = \frac{\prod_{m=1}^{i-1} k_m}{\prod_{n=1, n\neq j}^{i} (k_n - k_j)}. \tag{3.12}$$

The concentration profiles of an arbitrary model depend on the exact choice of the model [130].

With these concentration profiles it is possible to construct a fit function for the different models. For the parallel model, this fit function takes the form

$$\Delta\text{Abs}^{\text{para}}(\lambda, \tau) = \frac{1}{\ln(10)} d \sum_{i=1}^{n} c_i^{\text{para}}(\tau) \text{DADS}_i(\lambda). \tag{3.13}$$

$\text{DADS}_i(\lambda)$ denotes the decay-associated difference spectra for the different exponentially decaying concentration profiles. A similar result is obtained for the sequential model:

$$\Delta\text{Abs}^{\text{seq}}(\lambda, \tau) = \frac{1}{\ln(10)} d \sum_{i=1}^{n} c_i^{\text{seq}}(\tau) \text{EADS}_i(\lambda). \tag{3.14}$$

Here, $\text{EADS}_i(\lambda)$ are the evolution-associated difference spectra. Finally for an arbitrary target model, the fit function yields

$$\Delta\text{Abs}^{\text{target}}(\lambda, \tau) = \frac{1}{\ln(10)} d \sum_{i=1}^{n} c_i^{\text{target}}(\tau) \text{SADS}_i(\lambda). \tag{3.15}$$

In this case, the species-associated difference spectra $\text{SADS}_i(\lambda)$ really correspond to the absorption spectra of the different species contributing to the transient absorption spectrum.

Depending on the model used, the decay-associated, evolution-associated or species-associated difference spectra are free fitting parameters. In other words, the kinetics (rate constants k_i) are identical for all wavelengths while the spectral amplitudes are varied to match the measured data.

For a sound analysis of the measured data, several experimental limitations that show up as artifacts in the data have to be taken into account. First of all, the limited temporal resolution of the experimental setup has to be considered. This can be described by the instrument response function (IRF) which presents a lower limit for the duration of events that can be measured. Its effect on the measured data can be modeled by a convolution of the concentration profiles given in equations 3.10 and 3.11 with the IRF. Of course, the concentration profiles in a target analysis have to be convolved with the IRF as well [130].

In many cases, the IRF can be described by a Gaussian, especially in the case of transient absorption spectroscopy with almost Gaussian-shaped pump and probe pulses. Either the IRF's width and position are known from a separate experiment, or they pose two additional free parameters for the fit of the data.

Another important issue is a possible temporal chirp of a very broadband probe pulse. This can be incorporated into the model by the use of a wavelength-dependent IRF. Fitting the wavelength dependence by a polynomial usually results in a satisfactory description of the chirp, introducing more free parameters to the fit [130].

In the framework of this thesis, global analysis was used to estimate the number of rate constants needed to describe the measured data and to fit the kinetics in order to determine the magnitude of the rate constants.

Chapter 4

Neutral low-band-gap mixed-valence polymer

For device applications in the field of organic electronics, it is advisable to have access to low-band-gap materials. Take as an example a bulk-heterojunction solar cell. Incorporating a low-band-gap material into the device allows to harvest the energy of the near infrared part of the solar spectrum since a low-band-gap material exhibits an absorption band that may span that far into the low-energy part of the spectrum.

The neutral organic mixed-valence compounds introduced in chapter 3.1 based on a triarylamine donor moiety (TARA) and a perchlorotriphenylmethyl radical acceptor moiety (PCTM) can be regarded low-band-gap monomers. Therefore the TARA–PCTM motif may be the basis for successful device applications.

On the other hand, for cost-effective large-scale device fabrication the expertise in the field of polymer science regarding processing techniques is invaluable. Therefore it would be promising to merge the low-band-gap character of TARA-PCTM with polymer chemistry.

The first neutral organic low-band-gap mixed-valence polymer **P** was recently synthesized successfully in the research group of Prof. C. Lambert from the University of Würzburg [131, 132]. The results presented in section 4.3 have been obtained in close cooperation with this group. The polymer's structure is depicted in figure 4.1 a). It comprises alternating TARA donor units (highlighted in green) and PCTM acceptor units (highlighted in blue). On average, 12 donor–acceptor pairs constitute one polymer chain. Being a polymeric low-band-gap material **P** can be regarded as a promising material for device applications. The corresponding reference monomer **M** can be seen in figure 4.1 b).

Since plenty of research has been conducted on TARA–PCTM com-

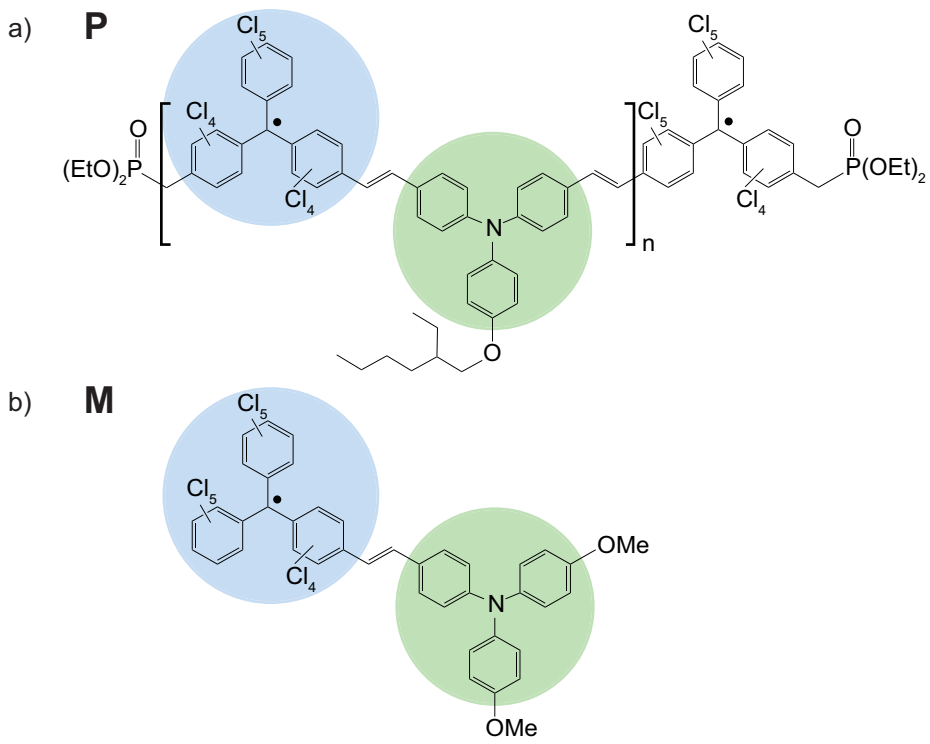

Figure 4.1: Structure of the neutral mixed-valence polymer **P** (figure a)) and the reference monomer **M** (figure b)). The TARA donor moiety is highlighted in green, the PCTM acceptor moiety in blue. Upon optical excitation, a charge transfer from the donor to the acceptor occurs.

pounds, **P** is also of great academic interest. The question arises, how does the polymeric character change the optical and charge transfer characteristics? Are there any processes that can exclusively be observed in the polymer? To shed light onto these questions, the compounds **P** and **M** have been studied with transient absorption spectroscopy in different solvents. The findings and interpretation of these studies will be discussed in chapter 4.3. But prior to that, a short overview of the optical and charge transfer properties of monomeric TARA–PCTM systems will be given in chapter 4.1.

4.1 Previous research on monomeric TARA–PCTM charge-transfer compounds

Since the first neutral-organic mixed-valence compound based on a TARA donor and a PCTM acceptor has been introduced in 2004, a lot of research has focused on this class of compounds, especially on the steady-state and in some cases time-resolved spectroscopic properties. A short overview of the findings so far will be given here.

The solvatochromism of monomer **M** has be examined by analysing the absorption spectrum of **M** in thirteen different solvents [82]. The choice of solvents spanned totally apolar ones such as n-hexane as well as strongly polar ones like acetonitrile. The origins of the different bands in the spectrum can be identified unequivocally; the IVCT band which is the lowest-energy band in the spectrum has received most attention. Upon first glance, the inter-valence charge-transfer (IVCT) band exhibits a weak and non-systematic solvatochromism. Fitting the IVCT band with the Jortner model [133] helps to shed light on this behaviour. As one might expect, the inner part of the reorganisation energy λ_i is almost solvent independent, while the outer part λ_o shows a distinct negative solvatochromism. This means that the value of λ_o increases with increasing solvent polarity. In all solvents with exception of the hexanes, λ_o dominates the total reorganisation energy.

The negative solvatochromism of λ_o is essentially compensated for by the positive solvatochromism of the free energy difference ΔG^0 which decreases with increasing solvent polarity. These two compensating trends are the reason for the weak and non-systematic solvatochromic behaviour of **M**.

Calculating the diabatic dipole moment reveals that the effective charge-transfer distance is shorter than the distance between the central carbon atom of the PCTM moiety and the nitrogen atom of the TARA moiety. This illustrates the complication of defining a clear redox "center" in an organic mixed-valence system. The electronic coupling V is comparatively weak in **M** which indicates a weak interaction between the donor and the acceptor. This can be explained by the steric interaction among the chlorinated ring systems which leads to a twist of the π-systems. This in turn leads to a reduced orbital overlap which is known to have a distinct effect on the charge transfer dynamics [134].

Subsequently, a large variety of differently bridged TARA–PCTM compounds has been synthesized and also the influence of side chain substitution of the donor moiety has been investigated by varying the latter [83]. All TARA–PCTM compounds exhibit a very similar solvatochromic behaviour

to that of **M**, the opposite trends of λ_o and ΔG^0 with increasing solvent polarity. In addition, the electronic coupling adopts values similar to that of **M**. Spectroelectrochemical measurements reveal the absorption bands of the oxidised donor and reduced acceptor, respectively. The former has a characteristic absorption around 690–770 nm, while the latter absorbs in the range of 500 nm to 520 nm. This is a good first indicator where to look for the absorption bands in a transient absorption experiment.

Transient absorption spectra have been recorded for the monomer **M** [135]. The system was excited at 532 nm or 355 nm, respectively. The former corresponds to a localised PCTM transition while the latter can be seen as a delocalised excitation. The data recorded at both excitation wavelengths exhibit no striking differences. This indicates that the charge transfer dynamics are not influenced by the amount of excess energy deposited in the system.

The measured transient absorption spectra are dominated by a very strong absorption band around 800 nm which is ascribed to the TARA radical cation. Only a comparatively weak PCTM anion absorption around 510 nm is visible. Both bands decay monoexponentially with a time constant of 150 ps in hexane. A third contribution can be observed in the low-energy part of the transient absorption spectrum: a negative absorption change which is assigned to an emission from the charge-transfer state to the ground state.

It is noteworthy that no transient absorption signal was observed when the experiment was repeated in tetrahydrofuran (THF), acetonitrile and carbontetrachloride. A rough estimation of the rates for back electron transfer based on a Golden-rule expression [133] may provide an explanation. In THF and acetonitrile, the back electron transfer is probably too fast (< 50 fs) to be measured with the setup used in reference [135]. The situation is different in carbontetrachloride. The absence of the transient absorption signal can probably be explained by a fast electron transfer from the solute to the solvent.

In the same experiment, also a TARA–PCTM compound with a triple bond as bridge has been investigated. It shows a similar transient absorption signature as **M**. The charge transfer proceeds slightly faster, but in the same order of magnitude. This may be caused by the fact that the triple-bond bridge makes the system less flexible than **M**, leading to a higher averaged vibrational mode and thus a higher rate.

Time-resolved experiments have also been performed on a biaryl-type TARA–PCTM compound, which exhibits a shorter bridge than the stilbene-type **M**. Exciting the system directly into the IVCT band leads to a charge

transfer from the donor to the acceptor. The dynamics of the subsequent back-electron transfer have been monitored with transient absorption spectroscopy [136]. Two absorption bands can be observed. The one located at approximately 720 nm is ascribed to the TARA radical cation. The second band is found around 500 nm and is characteristic of the PCTM anion.

Two time constants are necessary to model the observed dynamics. The first one τ_1 describes the formation of the CT state while the second one τ_2 is associated with the back-electron transfer. The latter process depends on the solvent polarity insofar that the rate for back-electron transfer increases with increasing polarity. This can be explained by a better stabilisation of the CT state in more polar solvents with a smaller value of ΔG^0. Since the back-electron transfer proceeds in the Marcus-inverted region, the rate will increase with decreasing ΔG^0.

The solvent dynamics may be the rate-limiting step for charge transfer [137, 138], thus the rise time τ_1 is ascribed to the reorientation of the solvent upon charge transfer [139, 140]. It reaches values between approximately 0.5 and 2 ps, depending on the solvent. This is on the order of solvent relaxation times which are used to model the diffusive movement of solvent molecules [96, 141].

Another interesting finding has been reported for biaryl-type TARA–PCTM compounds. Unlike most organic radicals, the TARA–PCTM compounds show an unusually strong fluorescence with lifetimes in the order of nanoseconds [142]. In the biaryl-type TARA–PCTM compound, the above-mentioned twist of the π-systems is even more pronounced than in **M**. This leads to an electronic decoupling of the redox centers which is the reason for the long fluorescence lifetime.

To tune the donor strength of the TARA, different small electron-donating or -withdrawing substituents were attached to the donor. It was shown that the different substituents only have an influence on the free energy difference ΔG^0 while leaving the other parameters unaltered. Seven differently substituted compounds were examined with transient absorption spectroscopy. The transient absorption spectra exhibit a similar spectral signature as reported in reference [136]. The PCTM anion band can be found around 490 nm while the TARA radical cation band is centered around 710 nm. The decay times of these bands are in good agreement with the fluoresscence lifetimes. This indicates that a remarkable slow back-electron transfer facilitates the long lifetime of the fluorescent state.

It is also noteworthy that the measured rate constants cannot simply be explained by Marcus theory. For some compounds the measured rate constants deviate strongly from the predicted ones. This can probably be

ascribed to the strong influence of the anharmonicity of the potential energy surfaces.

The small electronic coupling in the biaryl-type TARA–PCTM compounds makes them interesting open-shell fluorescence dyes with unusally long fluorescence lifetimes in the order of nanoseconds. The possibility to tune only ΔG^0 and leave the other parameters unaltered helps to disentangle the contributions of the different parameters. Thus the biaryl-type TARA–PCTM dyes are ideal model systems from that point of view, too.

In conclusion, compounds based on the TARA–PCTM motif exhibit interesting optical and charge-transfer characteristics and are worth further investigation. As is known from the previous studies, these compounds are stable, soluble in a large number of different solvents and sufficiently easy to handle. This makes them ideal model systems also from a practical perspective.

4.2 TARA–PCTM polymer

Before turning to the transient absorption experiments, the basic properties of the TARA–PCTM polymer **P** will be discussed. Its structure is depicted in figure 4.1 a). ^{1}H-NMR experiments revealed that **P** consists of on average twelve donor–acceptor pairs and is terminated with diethylphosphonate groups at both ends [131, 132].

It is soluble in THF, chloroform, dichloromethane, toluene and chlorobenzene. **P** exhibits a high stability under ambient conditions. As a solid it can be stored for several months, and even in solution no degradation was observed after two months. The temperature stability is also noteworthy: No signs of decomposition were found up to 250° C.

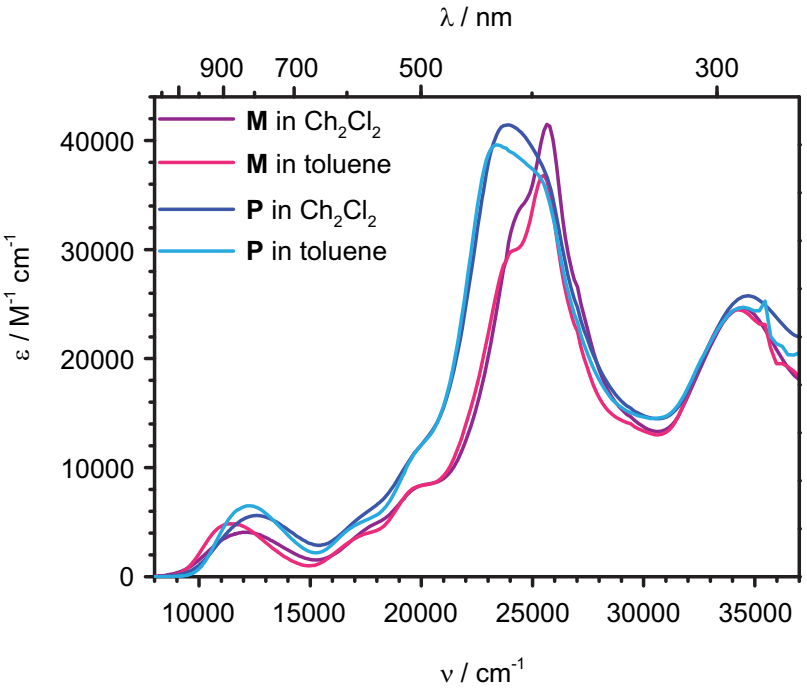

Figure 4.2: Steady-state absorption spectra of **P** and **M** in dichloromethane and toluene. The bands around 290 nm (34500 cm^{-1}) correspond to localised TARA transitions, whereas bands around 390–580 nm (25600–17200 cm^{-1}) belong to the PCTM moiety. The IVCT band is the lowest-energy transition centered at 835 nm (12000 cm^{-1}).

The steady-state absorption spectra of **P** and **M** in dichloromethane (DCM) and toluene are depicted in figure 4.2. The most striking property is

the overall similarity of the spectra of **P** and **M**. The observed bands can be assigned as follows. Bands around 290 nm (34500 cm^{-1}) belong to localised TARA transitions, while the bands around 390-580 nm (25600-17200 cm^{-1}) correspond to the PCTM moiety. The IVCT band is found around 835 nm (12000 cm^{-1}) and constitutes the lowest-energy transition possible.

The most pronounced difference in the spectra is found for the bands around 385 nm (26000 cm^{-1}). These transitions are red-shifted in **P**, caused by the exciton splitting due to the polymeric nature of **P**. The similarity of the IVCT band of both compounds indicates that the intervalence charge transfer in **P** is confined to one monomeric unit.

A thin film of **P** can be obtained by spin-coating a solution of **P** on a substrate. The spectrum of the film of **P** is almost identical to the solution spectrum except for a slight red shift. Annealing of the film does not alter the spectrum. Thus **P** forms amorphous, highly air- and temperature-stable films, which is important for possible device applications.

The HOMO and LUMO energies of **P** were obtained by cyclic voltammetry [143, 144]. Their values are -5.50 eV and -4.47 eV, respectively. This makes **P** perfectly suited for the use in ambipolar OFET devices with gold contacts, since the HOMO and LUMO levels are close to the work function of gold. Thus only a small barrier for charge carrier injection can be expected [145].

From the comparison of the optical band gap and ΔG^0 from Bixon–Jortner analysis (in a manner of speaking the "Bixon–Jortner band gap") a small exciton binding energy can be expected in **P**.

Spectroelectrochemistry [143, 144] allows to record the absorption spectra of the reduced and oxidised species of **P** independently. Upon reduction, the PCTM anion band is found at approximately 585 nm in **P** and 543 nm in **M**, respectively. The oxidation reveals a sharp and intense TARA radical anion band around 709 nm. Interestingly, a new IVCT band shows up around 1124 nm in **P** and around 1053 nm in **M**. This corresponds to a charge transfer fron the PCTM radical to the TARA radical cation. Thus the former donor and acceptor moieties exchange their funcionality in the oxidised species. This behaviour has been observed in TARA–PCTM compounds before [83].

4.3 Transient absorption spectroscopy of TARA–PCTM compounds

To unravel the dynamics of **P**, transient absorption measurements were carried out in two different solvents, namely toluene and dichloromethane. As a reference, the monomer **M** was also examined in the same solvents and under comparable experimental conditions [1].

4.3.1 Transient absorption data for P and M

All data presented in this section were obtained with the 1 kHz shot-to-shot setup described in chapter 3.3.1. The pump pulse was centered around 525 nm, the time resolution was about 50 fs. The absorption changes were monitored over a spectral range of 400 nm to 750 nm. The time steps were adjusted to optimally cover the range of the observed dynamics.

The transient absorption maps for **P** are shown in figure 4.3. The upper panel displays the data with toluene as solvent, while in the lower panel dichloromethane was used. In both cases three characteristic spectral features can be observed. The high energy part below 475 nm is dominated by a negative contribution, stemming from the ground-state bleach. Above 475 nm a strong positive signal can be seen. It comprises the absorption of the PCTM anion centered around 550 nm and the TARA radical cation absorption between 650 nm and 750 nm. The individual spectral contributions can be seen more clearly in figure 4.4 which depicts transient spectra of **P** in toluene (figure 4.4 a)) and dichloromethane (figure 4.4 b)). The data around 525 nm is blanked out in figures 4.3 a) and 4.4 a) because of a strong contribution from scattered pump radiation. The shape of the transient spectra in dichloromethane can well be reproduced by the spectra obtained by spectroelectrochemistry, showing that the assignment of the spectral features is correct [131, 132]. It also indicates that charge transfer from the donor to the acceptor is induced optically.

Although the spectral features observed in both solvents are very similar, the temporal behaviour clearly differs. Note that in dichloromethane most of the signal is decayed after 20 ps, whereas signal can be seen in toluene for more than 150 ps after excitation. The kinetics will be quantified in section 4.3.2.

[1] The results presented in this section have been published in Chem. Mater. **22**, 6641-6655 (2010).

The transient absorption maps and transient spectra for the monomer **M** are shown in figures 4.5 and 4.6, respectively. In both cases, the data obtained in toluene are depicted in the upper panel while the lower panel displays the data measured in dichloromethane. The spectral features of **M** are very similar to those of **P**. The ground-state bleach dominates the spectrum below 450 nm. Two distinct absorption bands can be found around 500 nm and 720 nm. The former corresponds to the PCTM anion while the latter stems from the TARA radical cation. Again, the transient absorption spectra are in good agreement with the data from spectroelectrochemistry [131, 132]. This confirms that charge transfer from the donor to the acceptor is induced upon optical excitation.

As in the case of **P**, the dynamics of **M** are strongly dependent on the solvent, while the spectral shape of the bands is hardly influenced. In dichloromethane the signal completely decays within 5 ps. In toluene, however, it takes more than 60 ps to decay. A detailed analysis of the kinetics of **P** and **M** will be given in the following section.

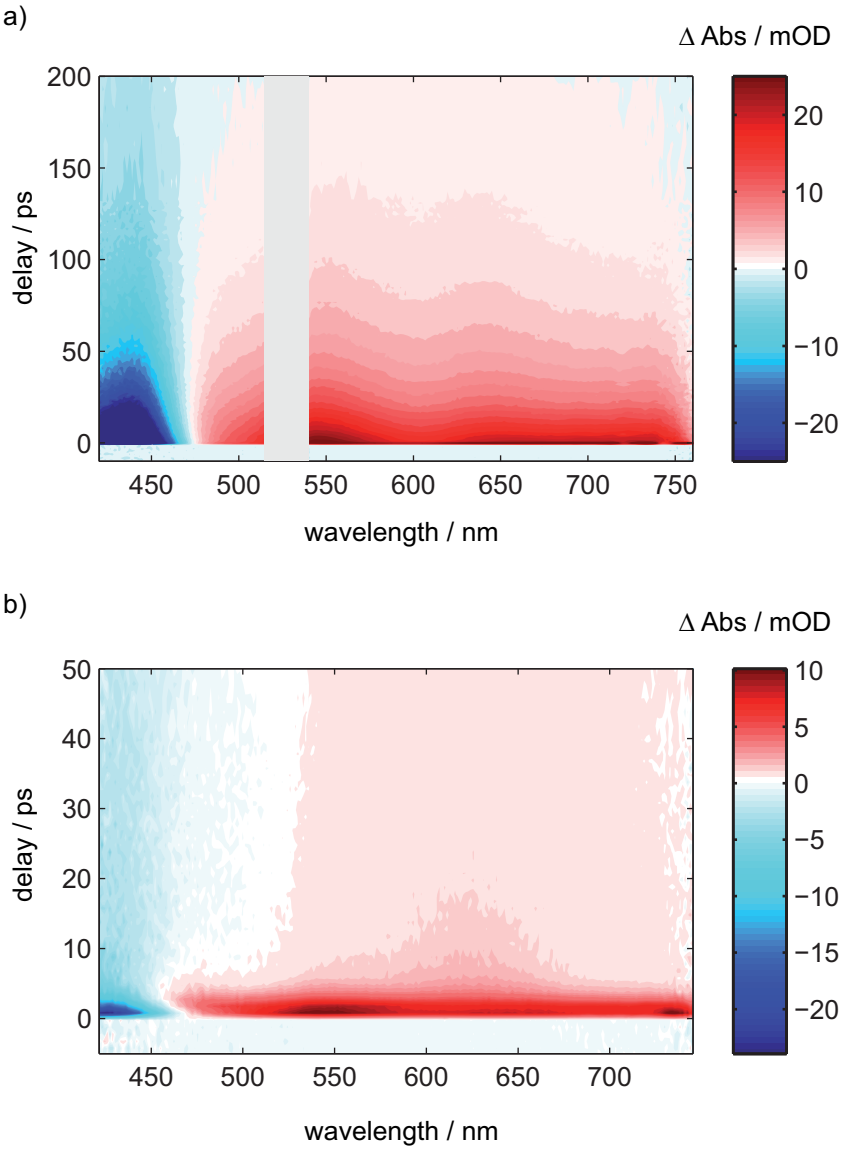

Figure 4.3: Transient absorption maps for **P** in toluene (panel a)) and dichloromethane (panel b)). The high-energy part of the spectrum (below 475 nm) is dominated by the ground-state bleach, while the prominent feature in the low-energy range above 500 nm is a broad absorption band. In a) the data around 525 nm is blanked out because of a strong pump-light scattering contribution.

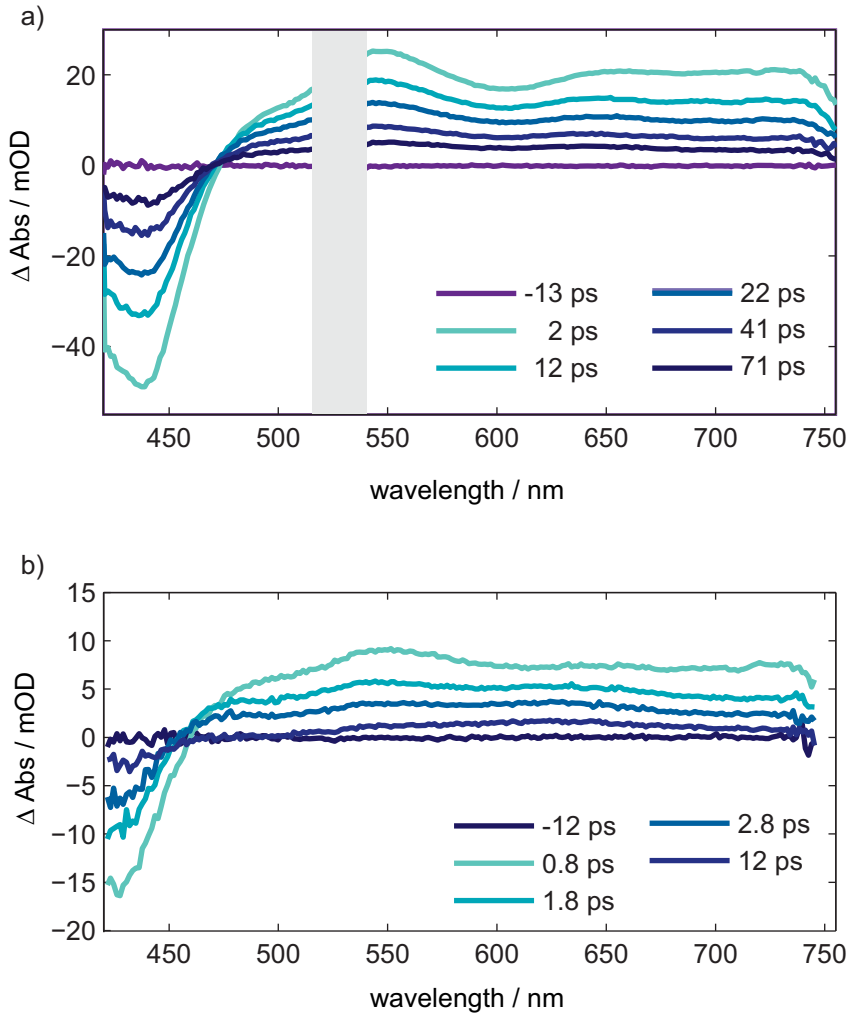

Figure 4.4: Transient spectra for **P** in toluene (a)) and dichloromethane (b)). Below 475 nm the ground-state bleach can be seen while above 475 nm the spectra are dominated by the absorption bands of the PCTM anion and the TARA radical cation. Note that the spectral shape is similar in both solvents, but the timescales vary strongly. Again, the scattered pump light around 525 nm is blanked out in a).

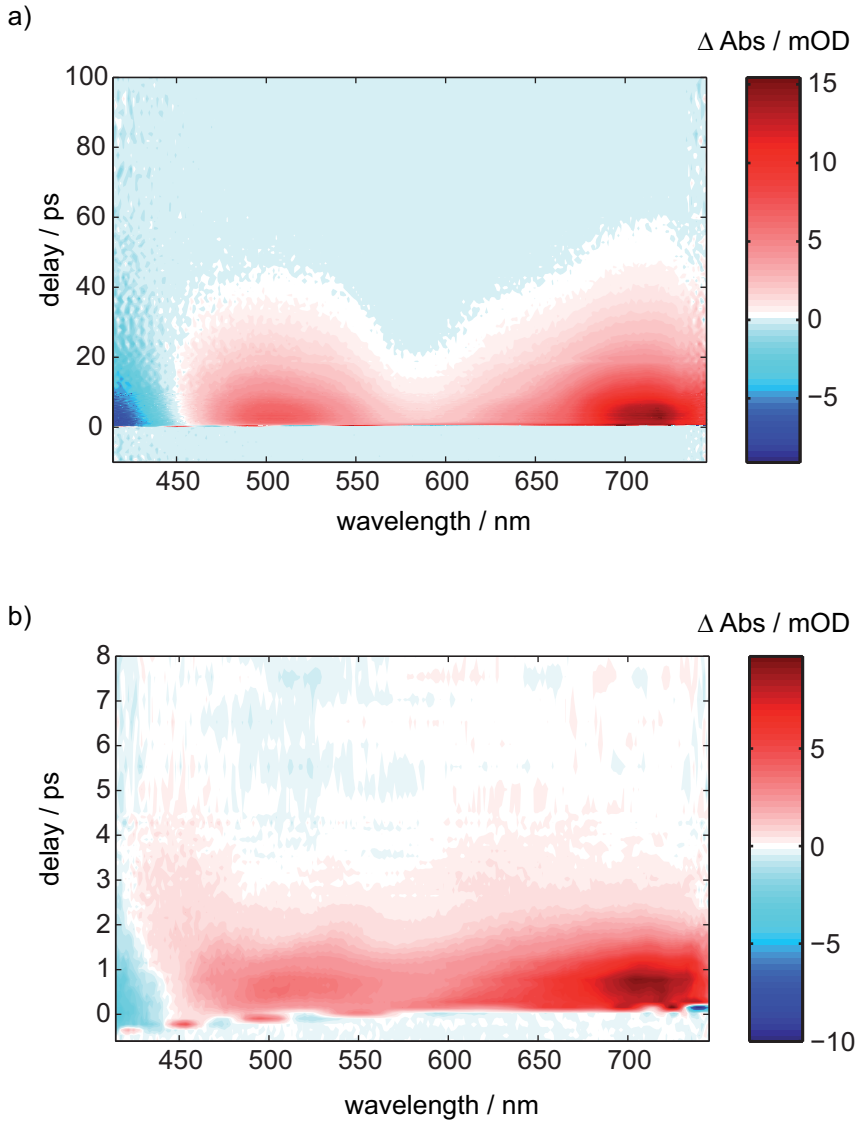

Figure 4.5: Transient absorption maps for **M** in toluene (a)) and dichloromethane (b)). Below 450 nm the ground-state bleach is clearly visible. The absorption band of the PCTM anion is centered around 500 nm, the TARA radical cation absorption band can be found around 700 nm. Again, the spectral signatures are very similar in both solvents while the timescales vary strongly.

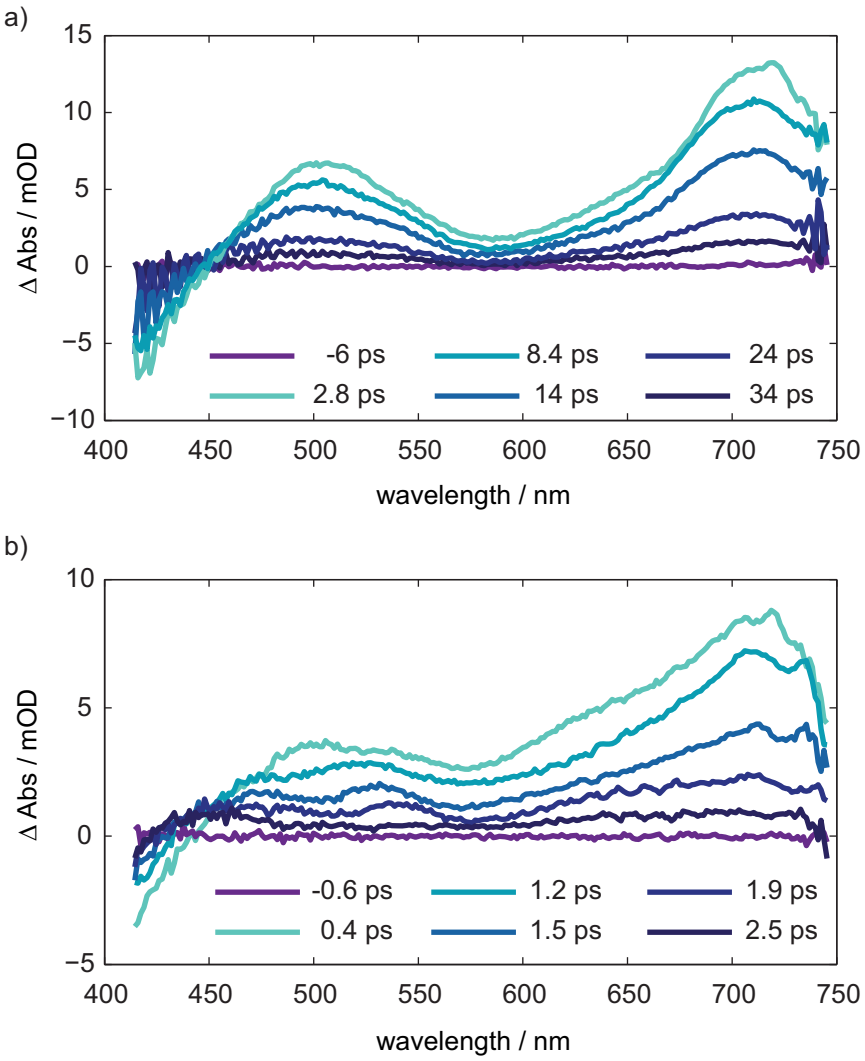

Figure 4.6: Transient spectra for **M** in toluene (a)) and dichloromethane (b)). The ground-state bleach dominates below 450 nm. The PCTM anion absorption is centered around 500 nm, while the TARA radical cation absorbs around 700 nm.

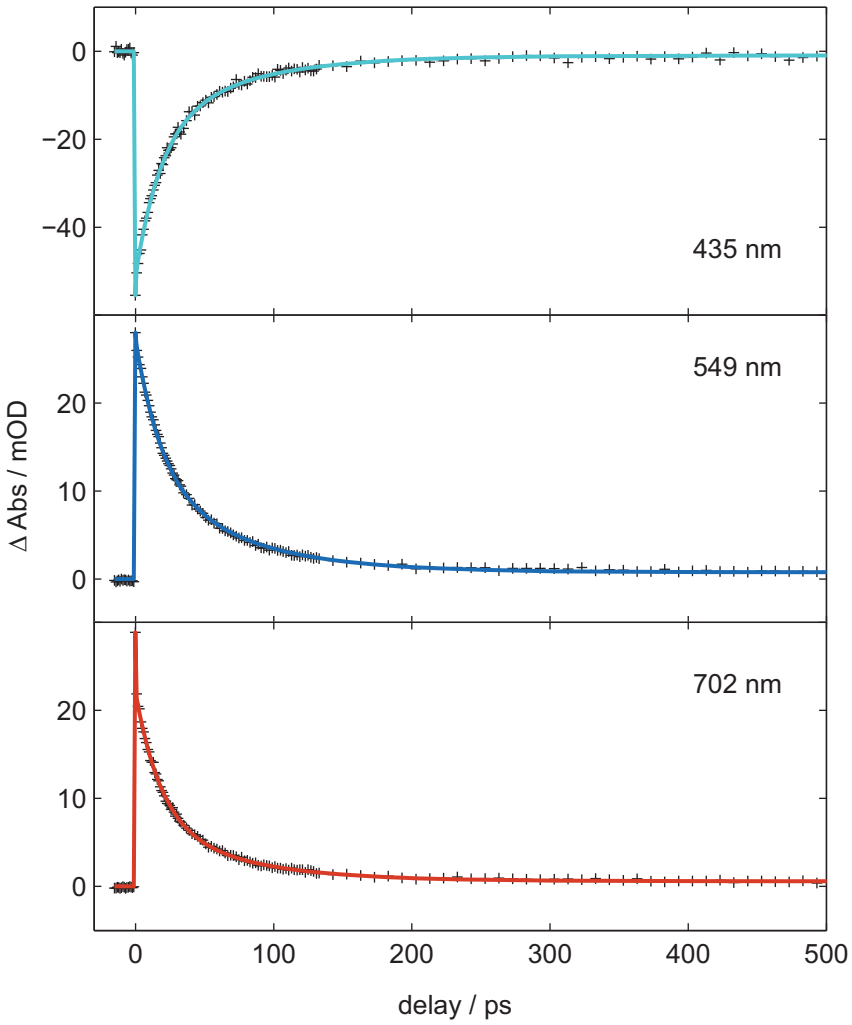

Figure 4.7: Exemplary kinetic traces for **P** in toluene. The data and fit result for the ground-state bleach are shown in the upper panel. The central and bottom panel depict the absorption bands of the PCTM anion and TARA radical cation, respectively. Time constants of 18.1 ps and 66.7 ps were obtained by global analysis of the map shown in figure 4.3 a).

4.3.2 Global analysis of the kinetics

Although the spectral features of **P** and **M** in both solvents are quite similar, the main difference in their behaviour can be found in the kinetics. A global analysis of all transient absorption data was carried out as described in chapter 3.4. As the computational environment to perform this task *Glotaran* was

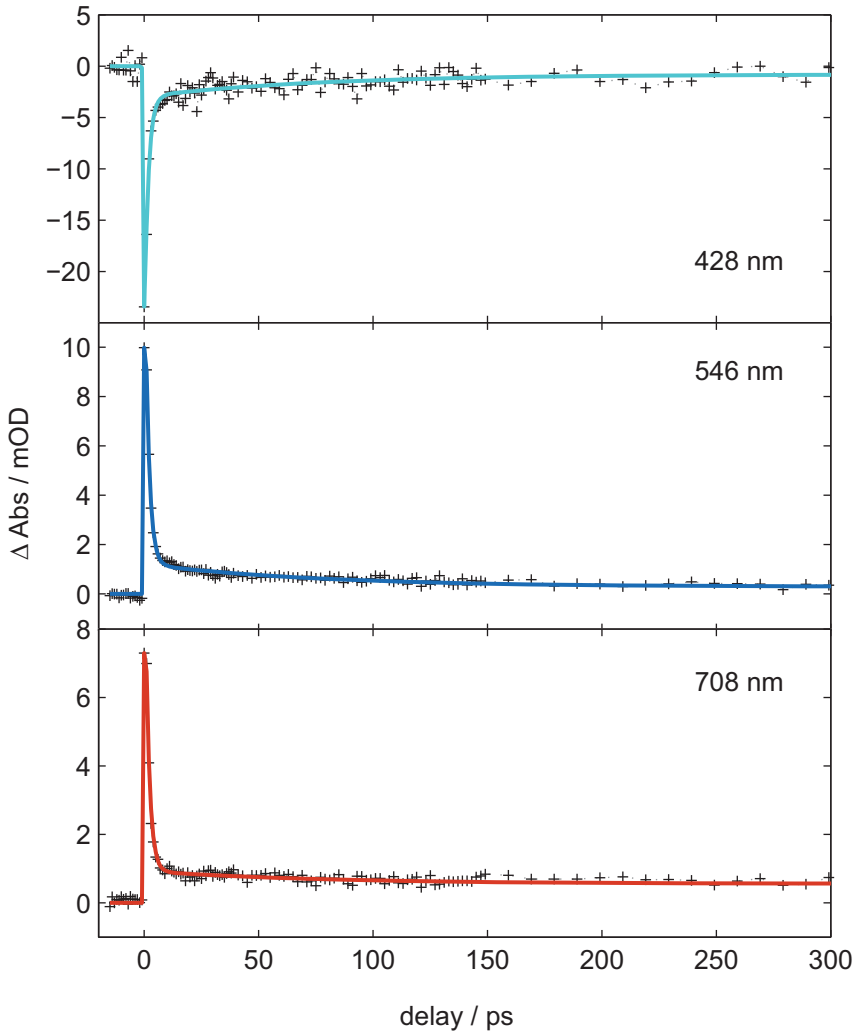

Figure 4.8: Kinetic traces for **P** in dichloromethane. The trace in the upper panel corresponds to the ground-state bleach, the trace in the central panel to the PCTM anion absorption and the trace in the bottom panel to the TARA radical cation absorption. A global fit of the map in figure 4.3 b) yields time constants of 1.8 ps and 76 ps.

used. It is a freeware graphical user interface for *TIMP* [130, 146]. The latter is a statistical computations package, written in the freeware language *R* for statistical computing and graphics.

Glotaran can be used for global as well as for target analysis with different models. It also accounts for the instrument response function, which is

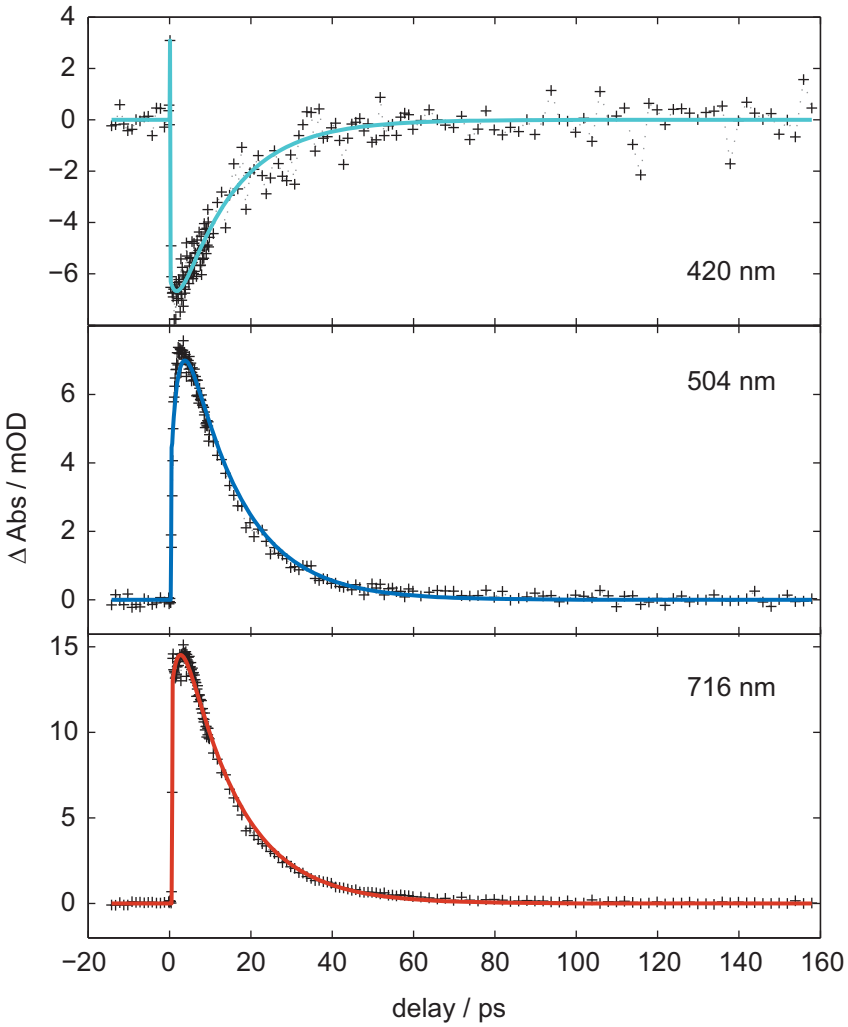

Figure 4.9: Kinetic traces for **M** in toluene. As before, the upper panel depicts the ground-state bleach while the central and bottom panel show the absorption bands of the PCTM anion and the TARA radical cation, respectively. Global analysis of the data yields a rise time of 2 ps and a decay time of 14 ps for the bands.

assumed to have a Gaussian shape. The temporal chirp of the probe pulse is incorporated by fitting a polynomial to the wavelength-dependent temporal zero. The coherent artifact can also be modelled. Thus *Glotaran* provides the functionality to model transient absorption data soundly. Nevertheless, it is still in the process of development and is not completely documented,

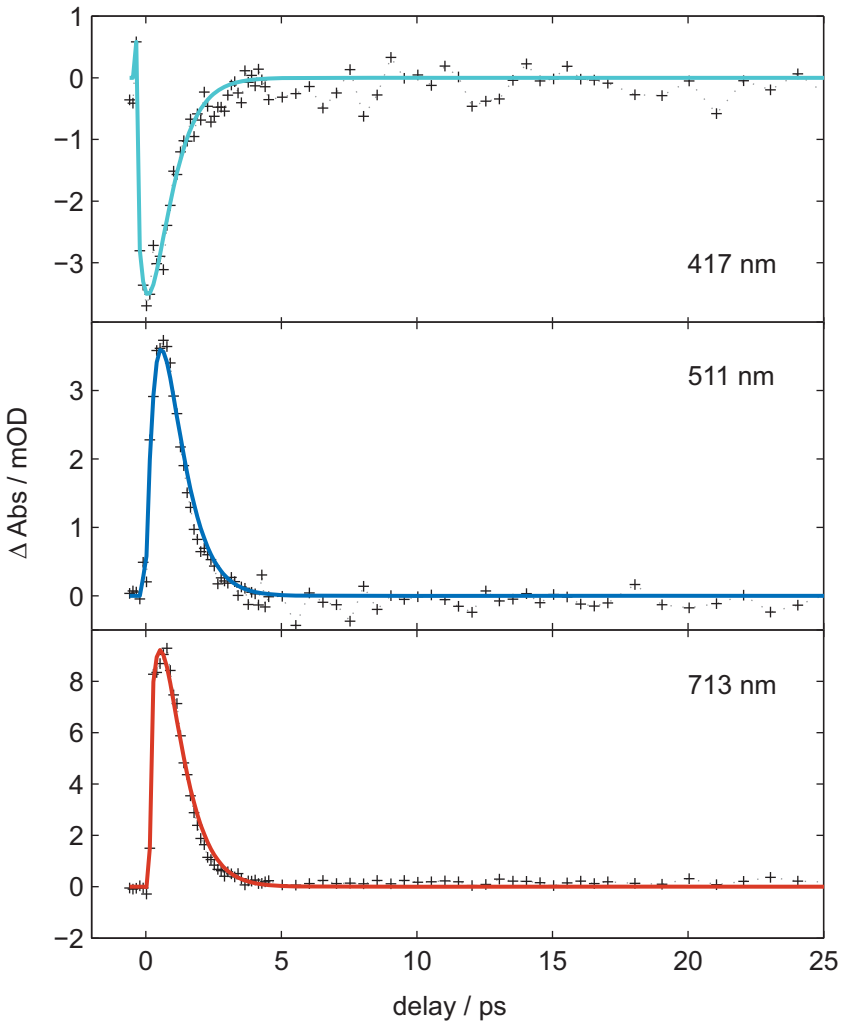

Figure 4.10: Kinetic traces for **M** in dichloromethane. The trace in the upper panel corresponds to the ground-state bleach while the traces in the central and bottom panel represent the PCTM anion and the TARA radical cation absorption, respectively. Time constants of 0.6 ps for the rise and 0.6 ps for the decay of the bands are obtained by global analysis.

yet. A short beginner's introduction to global analysis as it was performed here can be found in [147].

To model the transient absorption data of **P**, a sequential model with a biexponential decay plus a constant offset is used. This yields a satis-

compound	solvent	τ_{rise} / ps	τ_1 / ps	τ_2 / ps
P	toluene	-	18.1 ± 0.02	66.7 ± 0.9
	DCM	-	1.754 ± 0.009	76 ± 1
M	toluene	2.01 ± 0.02	13.51 ± 0.02	-
	DCM	0.57 ± 0.12	0.57 ± 0.12	-

Table 4.1: Time constants obtained by global analysis of the transient absorption data of **P** and **M** in different solvents.

factory description of the data. The short-lived component shows a decay-time of (18.1 ± 0.2) ps in toluene and (1.754 ± 0.009) ps in dichloromethane. The values for the decay-time of the long-lived component in toluene and dichloromethane are (66.7 ± 0.2) ps and (76 ± 1) ps, respectively. Thus, the short-lived component exhibits a strong solvent dependence, while the long-lived component only shows a minor dependence on the solvent.

Some exemplary kinetic traces and the obtained fit data are shown in figures 4.7 and 4.8. In both figures, the top panel depicts a trace that corresponds to the ground-state bleach. The central and bottom panel feature traces from the PCTM anion band and the TARA radical cation band, respectively. In all cases a good agreement between the measured and modeled data can be seen.

For the modeling of the data of **M**, a monoexponential decay suffices. In contrast to **P**, a distinct rise time can be observed for the bands which was taken into account with a monoexponential rise. Again, a sequential model was used. No offset was necessary for a sound description of the transient absorption data of **M**.

The rise time of the bands was (2.01 ± 0.02) ps in toluene and (0.75 ± 0.12) ps in dichloromethane. Values for the decay of the bands were found to be (13.51 ± 0.02) ps in toluene and (0.57 ± 0.12) ps in dichloromethane, respectively. For **M**, the rise as well as the decay time exhibit a strong solvent dependence.

In analogy to **P**, some kinetic traces and fit data for **M** are shown in figures 4.9 (in toluene) and 4.10 (in dichloromethane). Again, the trace in the upper panel corresponds to the ground-state bleach, the trace in the central panel to the PCTM anion band and the trace in the bottom panel to the TARA radical cation band. Also for **M**, the measured and modeled data agree well. An overview of all time constants can be found in table 4.1.

4.3.3 Interpretation of the transient absorption data

Before putting emphasis on the interpretation of the transient absorption data of **P** and **M**, the two most important findings of chapter 4.3.2 shall be summarised briefly. First of all, the back electron transfer proceeds faster with increasing solvent polarity. Second, **P** exhibits an additional deactivation pathway in comparison with **M**.

The former is not surprising since it is known from a similar monomeric TARA–PCTM compound that the back electron transfer takes place in the Marcus-inverted region [136]. The same is the case for **P** and **M**. A polar solvent ensures a better stabilisation of the IVCT state, thus lowering ΔG^0. In addition, an increase in solvent polarity also leads to an increase of the outer reorganisation energy λ_o because of a stronger electrostatic interaction between solvent and solute. Altogether this causes an acceleration of the back electron transfer with increasing solvent polarity. That is why the values for the time constant τ_1 are smaller in the more polar dichloromethane than in toluene.

To explain the origin of the additional deactivation pathway in **P** it is mandatory to understand the simpler system **M** completely. The risetime τ_{rise} of the bands can be assigned to the time it takes to populate the IVCT state from a higher-lying excited state which is initially populated upon optical excitation. The rate-limiting step for this process is the reorientation of solvent molecules upon charge transfer [138, 139]. Thus τ_{rise} reflects the solvent relaxation time and is expected to be solvent dependent. From the time constants obtained by global analysis the solvent dependence of τ_{rise} is obvious.

The decay time τ_1 corresponds to the return of the system from the IVCT state to the ground state, thus the back electron transfer. As discussed before, it exhibits the polarity dependence that is expected for the Marcus-inverted region.

A graphic representation of the kinetic scheme of **M** can be found in figure 4.11 a). The system is optically excited from the ground state GS to some higher-lying excited state (denoted with an asterisk). From there it relaxes to the IVCT state. The rate-limiting step for this process is the solvent reorientation upon charge transfer which determines the magnitude of the rise time τ_{rise}. The system returns from the IVCT state to the ground state with a decay time of τ_1.

In the following the kinetic scheme for **P** will be discussed. On the basis

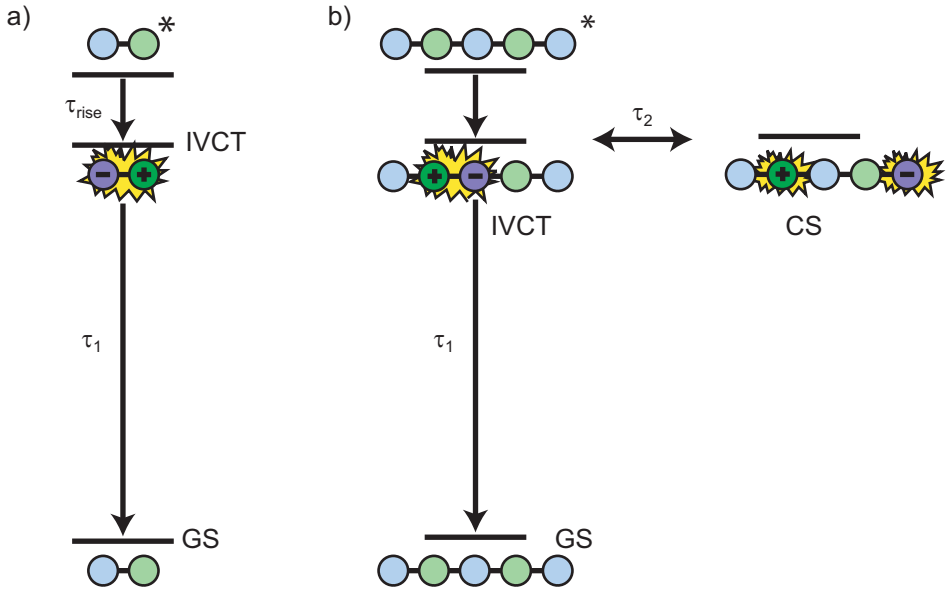

Figure 4.11: Kinetic scheme for the monomer **M** (a)) and the polymer **P** (b)). Both systems are excited from the ground state GS to some higher-lying state (denoted with an asterisk) from which the IVCT state is populated. The monomer can only return to the ground state directly, while in the polymer an equilibrium formation with a fully charge-separated state CS is reached. From the CS state the system can only return to the ground state via the IVCT state.

of the findings for **M** one would also expect a rise time for the formation of the IVCT state since also **P** is optically excited form the ground state to some higher-lying excited state. It is presently unclear why this rise time could not be observed in **P**. Since the step size and temporal resolution was comparable in both measurements.

Once the IVCT state is populated, the system can return directly to the ground state (the same deactivation pathway that is possible in **M** as well). The smaller decay time τ_1 is assigned to this process since it adopts similar values as in **M** and shows a similar solvent dependence. Thus the back electron transfer in **P** also proceeds in the Marcus-inverted region.

The origin of the larger decay time τ_2 has to lie in a structural or electronic transformation within the excited state of **P** (*vide infra*). Different processes are conceivable, nevertheless most of them can be ruled out and τ_2 can be assigned to the formation of a fully charge-separated state. This means that

the electron and the hole are spatially separated from each other and do no longer reside on adjacent donor and acceptor moieties. This fully charge-separated state is expected to have a similar spectral signature to that of the IVCT state but different dynamics.

For the charge recombination, the electron and hole have to be located on adjacent units, thus the system can only return to the ground state via the IVCT state. Therefore, τ_2 can be seen as an averaged time constant for back electron transfer from next-nearest neighbours and those further apart. Upon optical excitation, an equilibrium between the IVCT state and the fully charge-separated state is reached.

The proposed mechanism is also supported by the very low exciton binding energy found in cyclic voltammetry measurements. Since only very little energy is necessary to separate the electron and the hole, charge separation is likely to happen. This model also explains why τ_1 exhibits a strong solvent dependence while τ_2 is almost solvent independent. A transition from the neutral ground state to the charged IVCT state is accompanied with a strong charge redistribution. Thus the solvent molecules have to reorient strongly to adapt to the new charge distribution, making τ_1 strongly solvent dependent. Upon transition from the IVCT to the fully charge-separated state, only comparatively small changes in the charge distribution occur. Therefore the reorientation of the solvent molecules that accompanies this transition is not as severe as in the ground–IVCT state transition. Accordingly, the solvent dependence of τ_2 is not as pronounced as that of τ_1.

The proposed model of the kinetics for **P** is shown in figure 4.11 b). The system is excited from the ground state GS to some excited state (denoted with an asterisk). From there the IVCT state is populated. The system can either return to the ground state directly with the time constant τ_1. Alternatively a transition to the fully charge-separated state CS can take place, leading to an equilibrium between the IVCT state and the CS state. τ_2 then denotes an averaged time constant for the recombination of the charges from next-nearest neighbours and those further apart since the system can only return to the ground state via the IVCT state.

In the following a brief overview of alternative processes that might account for the second deactivation pathway in **P** is given although all of them can be ruled out as the origin of the process corresponding to τ_2.

First of all, states with different spin multiplicity (e.g. singlet and triplet) can contribute to the absorption change. Nevertheless these states are expected to be almost degenerate. Upon excitation the singlet and triplet IVCT states are populated from higher-lying excited singlet and triplet states. Subsequently the IVCT states return to the respective singlet and triplet ground

states. No strong dependence of the decay kinetics on the spin multiplicity is expected. Thus the huge difference between τ_1 and τ_2 cannot be caused by singlet and triplet dynamics.

It is also possible that the exciton that is created by optical excitation migrates along the polymer backbone. This means that the electron and the hole move in a concerted way. This leads to a state that is practically identical to the initially populated IVCT state and exhibits identical decay dynamics as the IVCT state. Thus it can also be excluded as origin of τ_2.

Finally, the structure of **P** might relax into a quinoid form by combination of two adjacent radicals. This process could account for a time constant on the order of τ_2. Nevertheless this relaxation process is unlikely because of the sterically demanding *ortho*-chlorine atoms.

In conclusion, assigning τ_2 to an equilibrium formation between the IVCT state and a fully charge-separated state is a reasonable model. It can describe the observed phenomena satisfactorily.

4.4 Outlook: oligomers and exciton–exciton annihilation

Although the kinetic model introduced in chapter 4.3.3 describes the measured data satisfactorily, still some open questions remain. A few of them will be presented here together with some planned experiments which are suitable to answer these questions.

One major issue is the exact nature of the charge separation when a transition between the IVCT and the fully charge-separated state takes place. By what mechanism can the electron leave the acceptor and go past the neutral donor to the next acceptor moiety? The equivalent question is, how does the hole go past the neutral acceptor? At present it is also unclear how far the charges move once they are separated from each other in the fully charge-separated state.

In the experiments carried out so far, the system has not been excited directly into the IVCT state. Exciting the system at 525 nm leads to a localised PCTM excitation from which the system relaxes into the IVCT state. It would be instructive to excite the system directly at the IVCT band to see if the excitation energy has an impact on the dynamics.

If the power of the pump pulse is sufficiently high, a multiple excitation of one molecule might become possible. From other conjugated polymers in the liquid phase it is known that multiple excitons can be created on one polymer strand and that exciton–exciton annihilation can take place [148–150]. Should it be possible to observe exciton–exciton annihilation, this poses an additional reaction channel. Thus it is interesting to combine spectroscopy and pulse shaping to conduct further research on these polymers. By systematically changing pulse parameters (e.g. the linear chirp), one can study their influence systematically and gain further insight into reaction mechanisms. With adaptively shaped pulses it might also be possible to control the annihilation dynamics, thus extenting the concept of quatum control to a transport phenomenon like exciton diffusion.

Additional insight into the mechanism of the migration of separated charges might be gained by the examination of smaller molecular systems than **P**. For example, oligomers like a donor–acceptor–donor or a acceptor–donor–acceptor system or a dimer comprising two monomeric units similar to **M** are ideal candidates. Their complexity is subsequently increased compared to **M** and the first two mentioned oligomers have already been synthesized. The first time-resolved spectroscopic measurements of these systems are currently in progress. Preliminary results show that the oligomers ex-

hibit a similar spectral signature to that of **P** and **M**. However, conclusions concerning the dynamics of these systems can only be drawn once a thorough kinetic analysis of the transient absorption data has been carried out.

To address the question how far the charges move once they are separated from each other, it would be useful to study polymers with increasing chain length, starting from the dimer (the synthesis of which is underway), going to the trimer, tetramer and so on. In this way, one could find out if a critical chain length exists above which the system shows distinct polymeric behaviour concerning its dynamics. It might also be interesting to see whether the time constant τ_2 depends on the chain length and if so, what exactly this dependence looks like. Maybe one can also extract information on how far the separated charges migrate along the chain depending on its length.

Although it has been shown for **M** and a similar monomeric TARA–PCTM compound that the dynamics are not strongly influenced by the pump wavelength (or the amount of excess energy deposited in the system) [135], it is still expedient to carry out experiments in which the system is excited directly at the IVCT band. Nevertheless, some benefits and also drawbacks have to be taken into account. Exciting the system in the IVCT band with a pump pulse centered at 800 nm makes any frequency conversion processes obsolete. Since the fundamental of the laser system can be used, higher pump intensities are available which is favourable for intensity-dependent studies of exciton dynamics. As a drawback, the temporal resolution of the measurement is reduced. But since these measurements focus on the dynamics corresponding to τ_2, the decrease in temporal resolution is not a major concern.

If it is possible to create more than one exciton on one polymer chain, the interaction of these excitons open up a new reaction channel for the relaxation of excited states. The impact on the dynamics of the system can then manifest itself in different ways, for example in a reduction of the relaxation times [150] or in a change of the exponentiality of the decay [149]. By studying exciton–exciton annihilation it is also possible to gain insight into the exciton diffusion dynamics. This becomes important for possible photovoltaics applications or as a feedback for the synthesis for modified polymers.

After studying the exciton dynamics the next step might be to control these. This would constitute a beautiful example of coherently controlling a transport phenomenon. Incorporating an LCD-based pulse shaper into the transient absorption setup allows to study whether the exciton dynamics can be influenced by the shape of the pump pulse. If so, it might actually be

possible to control these dynamics and steer the system to yield a desired outcome.

To conclude the chapter concerning the research on TARA–PCTM compounds, a short summary will be given here. Transient absorption measurements were carried out on the first organic mixed-valence polymer **P** and a reference monomer **M**. Both belong to the class of neutral organic mixed-valence compounds which are ideal model compounds to study charge transfer. The basic building motif of both **P** and **M** is the use of a triarylamine (TARA) as an electron donor and a perchloro-triphenylmethyl radical (PCTM) as an electron acceptor.

Upon optical excitation, charge transfer from the donor to the acceptor takes place. From the transient spectral signature it was possible to identify the IVCT state unambiguously since it clearly exhibits the absorption bands of the TARA radical cation and the PCTM anion.

Although the spectral signatures of **P** and **M** are very similar, they clearly differ in their dynamics. Global analysis of the transient absorption data revealed that the absorption bands of **M** show a monoexponential rise and a monoexponential decay. The former is attributed to the population of the IVCT state from a higher-lying state, where the relaxation of the solvent molecules according to the new charge distribution in **M** is the rate-limiting step. The decay of the bands corresponds to the return of the system from the IVCT to the ground state, thus to the back electron transfer.

In **P** however, no rise time could be observed due to the chosen experimental parameters. In contrast to **M**, **P** exhibits a biexponential decay of the bands, thus an additional deactivation pathway exists. Upon excitation and population of the IVCT state, the system can either return to the ground state directly or form an equilibrium with a fully charge-separated state. From there it cannot return to the ground state directly but only via the IVCT state. This equilibirum formation is the origin of the second deactivation pathway corresponding to the additional longer time constant found for **P**.

The solvent dependence of all time constants of **P** and **M** indicates that the back electron transfer takes place in the Marcus-inverted region.

A variety of future experiments has been proposed, some of which are already underway. In this way, it should be possible to shed light on charge and exciton migration. In a long-term view also coherent control of exciton migration, a transport phenomenon, might be possible.

This shows that TARA–PCTM oligo- and polymers are interesting systems to study the basic properties of charge transfer and also transport phenomena like exciton migration. They are interesting from a practical point

of view, too, since they are optimally suited to be incorporated in organic solar cells due to their low band-gap.

Since only the first results concerning a polymeric TARA–PCTM compound were presented, many more experiments are waiting to be carried out and many more interesting findings can be expected from this field of research.

Chapter 5

Donor-substituted truxenones

In this chapter, a different kind of mixed-valence system will be introduced. Although it incorporates the same TARA donor as in the TARA-PCTM compounds, the choice of a truxenone moiety makes this system unique [151]. Because of the C_{3h}-symmetry of the truxenone moiety, it is possible to couple three donor branches to one acceptor, making the TARA-substituted truxenone a two-dimensional charge-transfer system. It is of high interest to see which influence this increased dimensionality has on the charge-transfer dynamics.

In the framework of this thesis, two *para*-substituted truxenones with different bridge lengths have been studied which have been synthesized in the research group of Prof. C. Lambert from the University of Würzburg. The results presented in section 5.2 have been obtained in close cooperation with his group and the group of Prof. I. Fischer. Since it is known that the donor-acceptor distance has a profound influence on the charge-transfer dynamics, one would expect a faster charge transfer in the compound with the shorter bridge length.

Both truxenone-compounds have been studied with transient absorption spectroscopy in different solvents, additionally also anisotropy measurements were carried out. The experimental data and their global analysis will be presented in sections 5.2.1, 5.2.2 and 5.2.3, respectively. Subsequently, the interpretation of the data will be given in section 5.2.4, together with a proposed model of the potential energy surfaces of the system. But first of all, a brief overview of the properties of TARA-substituted truxenones will be given in the following section.

5.1 TARA-substituted truxenones

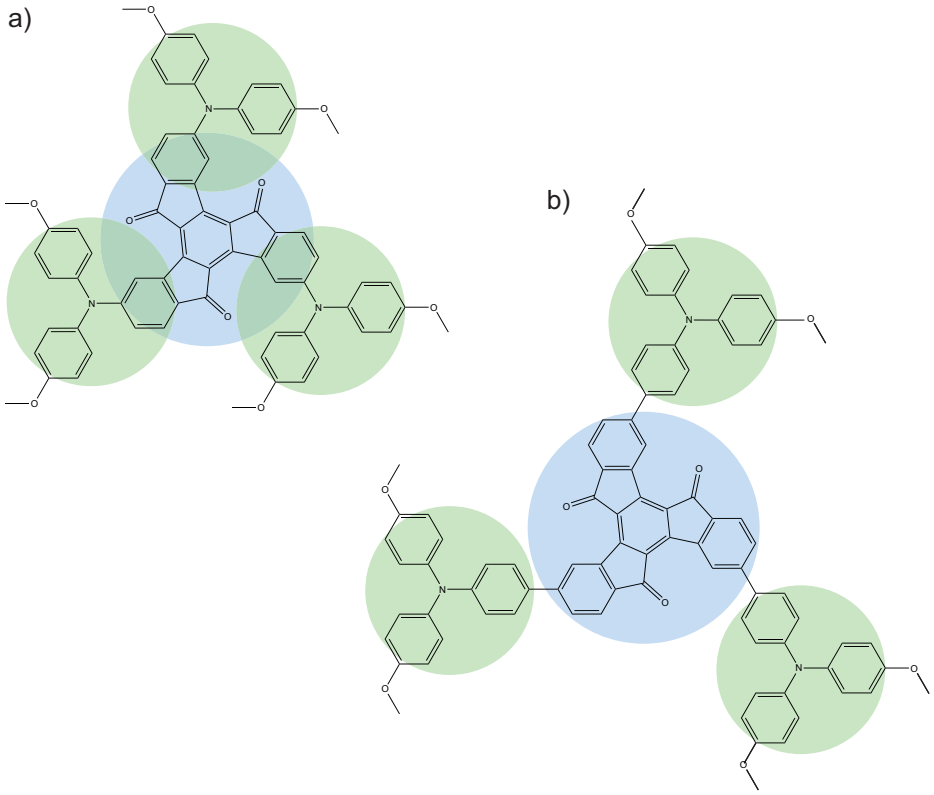

Figure 5.1: Structure of both donor-substituted truxenones. Figure a) depicts **trux1** where the donor is attached to the acceptor directly at the nitrogen atom, so that both "share" a phenyl ring. In **trux2** (b)) the donor and acceptor are linked via a C-C bond. In both cases, the TARA moieties are highlighted in green, while the truxenone moiety is highlighted in blue.

Two different TARA-substituted truxenones have been studied in the course of this thesis. Their structure is shown in figure 5.1. Both comprise a truxenone moiety (highlighted in blue) as an acceptor and three TARA units (highlighted in green) as donor. The compound shown in figure 5.1 a) will be denoted **trux1** in the following. The truxenone and TARA moieties are coupled directly at the nitrogen atom, so that they "share" a phenyl ring. The compound shown in figure 5.1 b), denoted **trux2** in the following, differs from **trux1** only in the spacer length. Here, an additional phenylene spacer is present between the TARA moieties and the truxenone. As a result, one would expect a higher electronic coupling in **trux1** than in **trux2** because

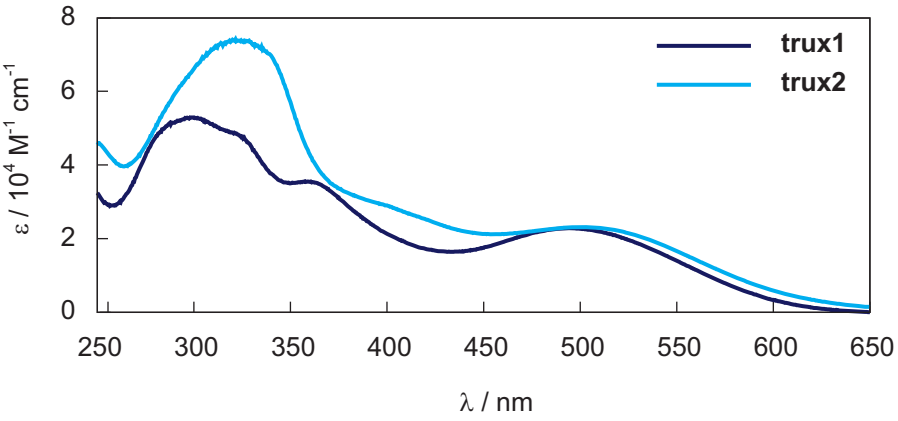

Figure 5.2: Steady-state absorption spectra of **trux1** and **trux2**. The IVCT band can be found around 500 nm. The band around 300–350 nm corresponds to localised TARA transitions.

of the smaller donor–acceptor distance in **trux1**.

As a solid, both compounds are stable under ambient conditions. Both are soluble in a variety of polar solvents like dimethylformamide, dimethylsulfoxide, ethyl acetate, dichloromethane and tetrahydrofurane [152]. The steady-state absorption spectra of **trux1** and **trux2** in dichloromethane are depicted in figure 5.2. The bands between 300 nm and 350 nm can be assigned to localised TARA transitions. Around 500 nm the CT band can be found.

Donor-substituted truxenones exhibit only a negligible fluorescence. For **trux2** a fluorescence quantum yield of less than 1% has been found [152].

Cyclovoltammetric studies revealed that in **trux1** the electronic coupling is stronger than in **trux2** [152, 153]. Surprisingly, no bands were found in **trux1** in spectroelectrochemistry, neither for the oxidised nor for the reduced species [153]. In contrast to that, the reduced species of **trux2** shows a decrease of the IVCT band, while two new bands around 450 nm and 750 nm appear. Upon oxidation, a new band around 750 nm appears which is characteristic of the TARA radical cation [152].

To summarize, the groundwork concerning donor-substituted truxenones is not as abundant as it was in the case of TARA-PCTM compounds. Especially no time-resolved studies have been carried out on this kind of compounds before. Thus, the results presented in sections 5.2.1 and 5.2.2 belong to the first ultrafast time-resolved measurements focusing on the charge

transfer in TARA-substituted truxenones.

5.2 Ultrafast spectroscopy of truxenones

5.2.1 Transient absorption spectroscopy

To shed light onto the charge-transfer dynamics of the truxenones, transient absorption studies have been carried out for **trux1** and **trux2** in two solvents of different polarity (dichloroethane (DCE) and dimethylsulfoxide (DMSO)) [154] [1]. The data was recorded using the shot-to-shot transient spectrometer introduced in chapter 3.3.1. The pump pulses were tuned to a central wavelength of 525 nm, thus both compounds were excited at the red egde of the IVCT band. A FROG measurement (see chapter 7.2.1) revealed a duration of about 70 fs for the pump pulses.

The dynamics were probed in the spectral range between 400 nm and 750 nm. The time delay between pump and probe pulse was scanned up to a maximum delay of 3.5 ns with an exponentially increasing step size.

The transient absorption maps for **trux1** and **trux2** are shown in figures 5.3 and 5.5, respectively. In the upper panel the data measured in DCE are depicted, while in the lower panel DMSO was used as a solvent. In figure 5.3 a) the spectral range around 525 nm is greyed out because of a strong pump scattering contribution.

The spectral signature is roughly similar for both compounds in both solvents. An intensive TARA radical cation absorption dominates the low-energy part of the spectrum above 575 nm. A second absorption band can be found below 475 nm which is attributed to the truxenone radical anion. The negative contribution between 475 nm and 575 nm stems from the ground state bleach, but it is partially overlapped by the absorption bands. This spectral signature, comprising absorption bands for the TARA radical cation and the truxenone radical anion, confirms that a charge transfer from the donor to the acceptor has taken place.

A comparison of the data for both solvents shows a roughly faster dynamic in DMSO than in DCE. However, a thorough global analysis of the data is given in section 5.2.3. Measurements with different pump powers yield no qualitatively different results, thus only one-photon processes contribute to the dynamics.

The most surprising finding in the transient absorption measurements is the shift of the absorption bands to higher energy with increasing time delay. It is more pronounced for **trux1** than for **trux2**. It can be seen clearly in

[1] The results presented in this section have been published in PCCP **14**, 11081-11089 (2012)

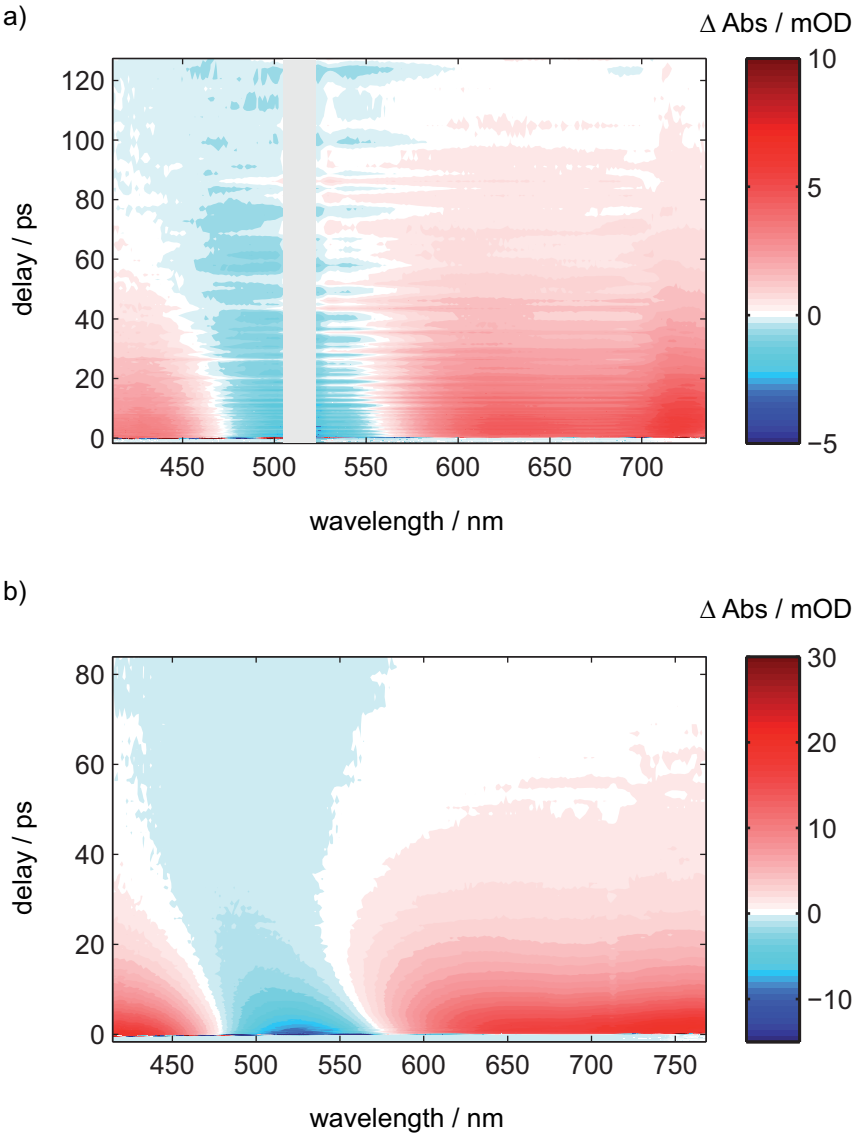

Figure 5.3: Transient absorption maps for **trux1** in DCE (figure a)) and DMSO (figure b)). The absorption band above 575 nm corresponds to the TARA radical cation, while the absorption band below 475 nm is assigned to the truxenone radical anion. Between those bands, the ground state bleach is observed. A striking finding is the shift of the absorption bands, which is most pronounced in DMSO.

figure 5.3, especially for the data measured in DSMO (figure 5.3 a)). The shift is also apparent in figure 5.4, where the transient spectra for **trux1** are

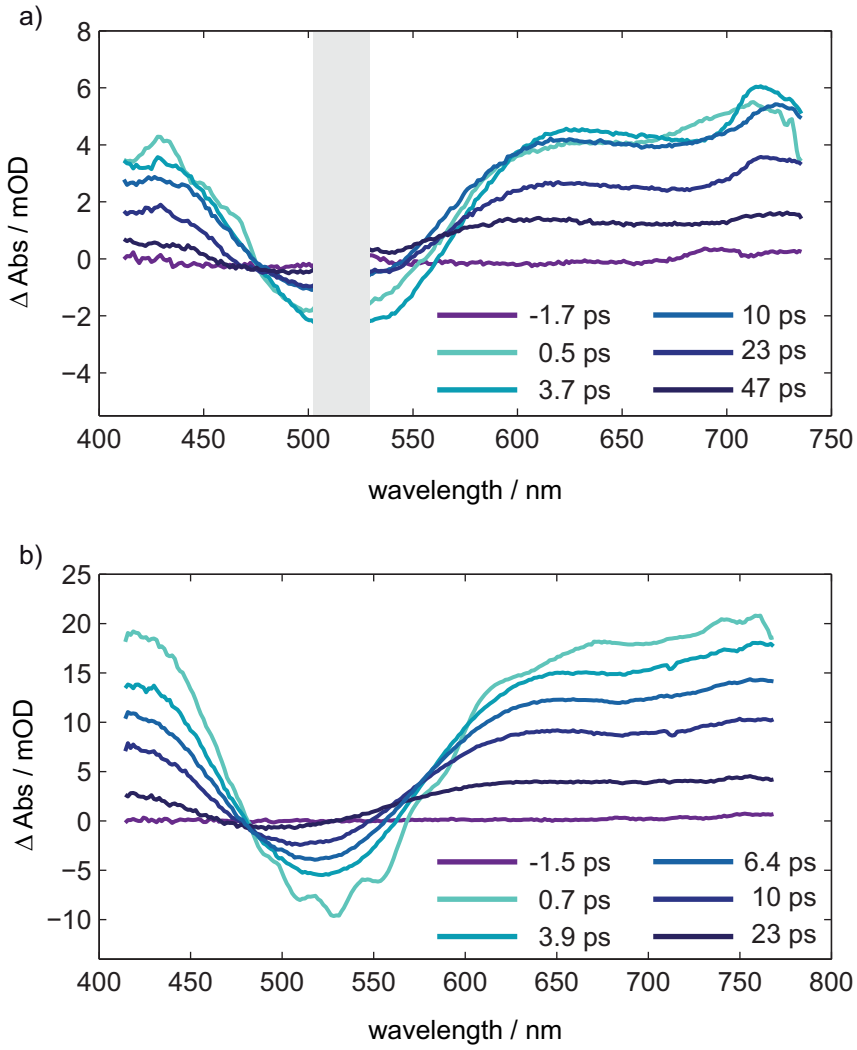

Figure 5.4: Transient spectra for **trux1** in DCE (figure a)) and DMSO (figure b)). The shift of the absorption bands can be seen clearly. The oscillations for short delay times in figure b) stem from a Raman mode of the solvent.

shown. Again, the upper panel displays the data with DCE as solvent, while the lower panel displays the data for DMSO. In contrast, almost no shift can be seen for **trux2**, which becomes most obvious in figure 5.6. The transient spectra for **trux2** are shown for DCE (figure 5.6 a)) and for DMSO (figure 5.6 b)).

To quantify the shift of the absorption bands, the spectral positions of the zero crossing between TARA absorption and the bleach and between

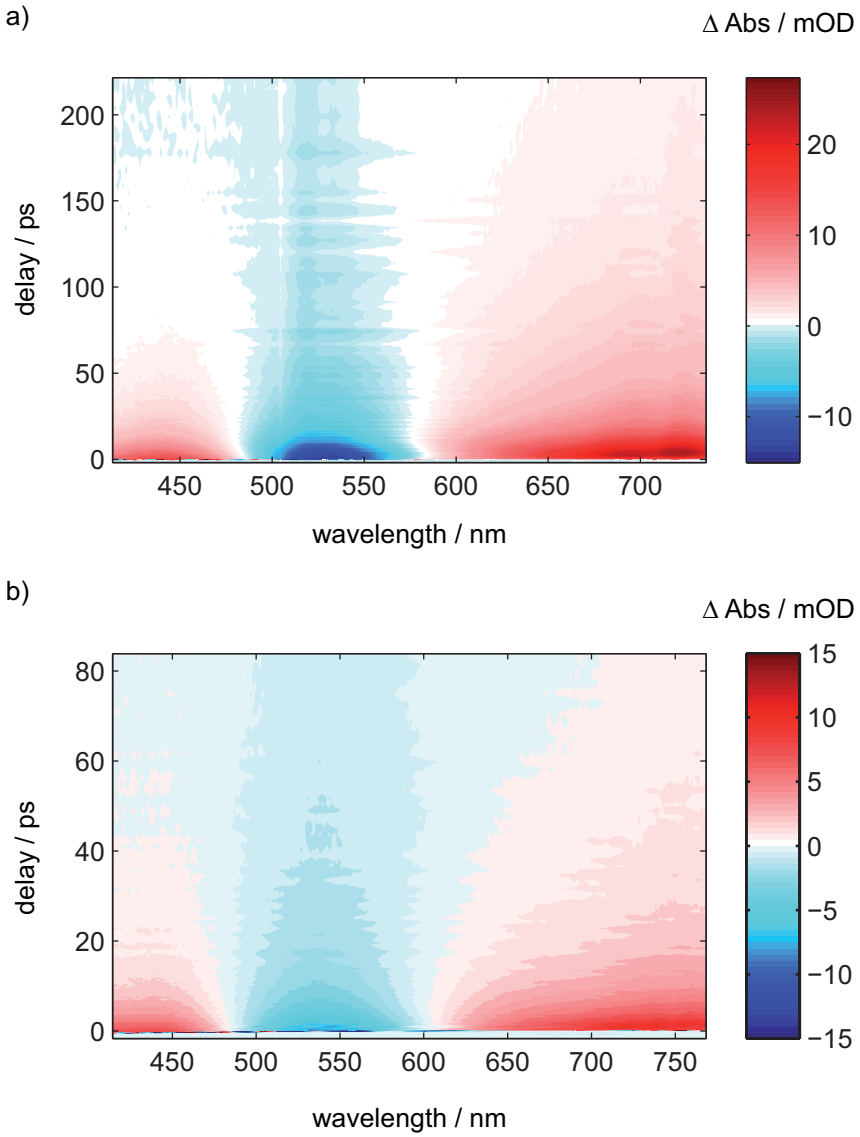

Figure 5.5: Transient absorption maps for **trux2** in DCE (figure a)) and DMSO (figure b)). The spectral signature is similar to that of **trux1**, the same absorption bands can be found. In contrast to **trux1**, almost no shift of the absorption bands is observed.

the bleach and the truxenone absorption band are plotted over a range of 50 ps. The results are depicted in figure 5.7. Figure 5.7 a) shows the spectral positions of both zero crossings for **trux1**. The most pronounced shift is found for the TARA band in DMSO. Over a range of 50 ps it shifts by a

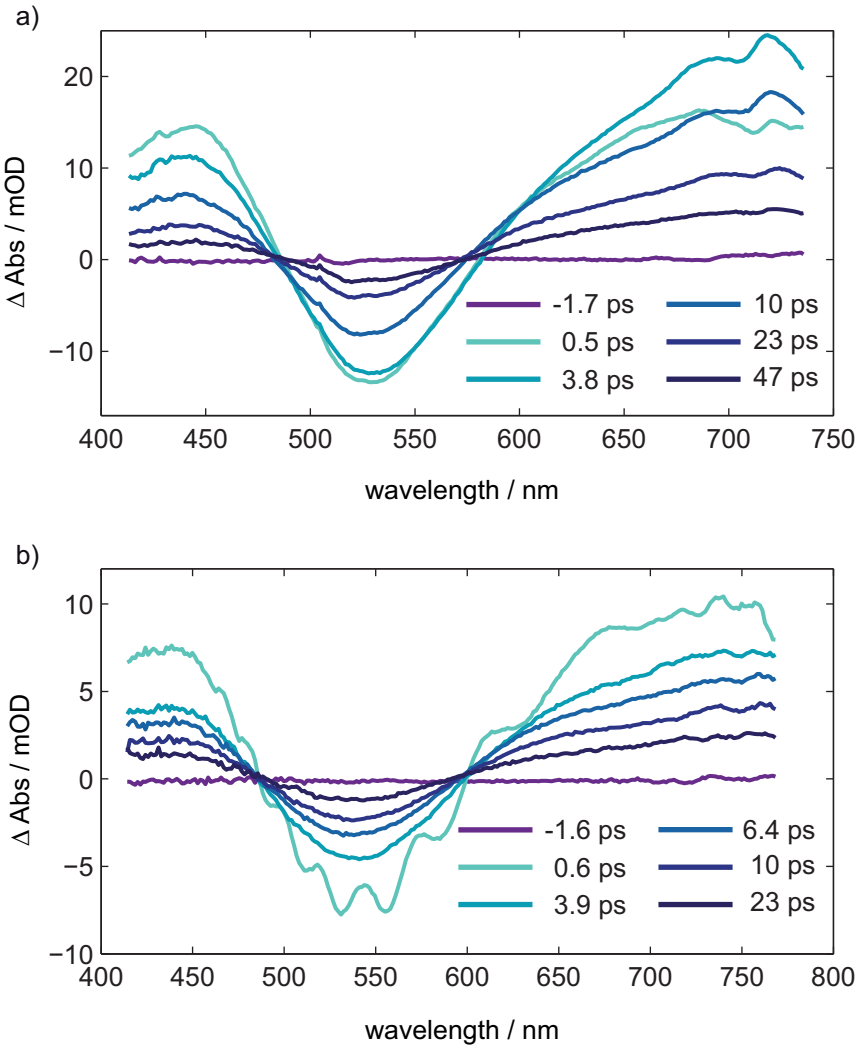

Figure 5.6: Transient spectra for **trux2** in DCE (figure a)) and DMSO (figure b)). No shift of the absorption bands is present. The oscillations for short delay times in figure b) again stem from a Raman mode of DMSO.

value of about 75 nm. The truxenone band shifts by about 30 nm. However, no "saturation" value for the spectral position of the zero crossing seems to be reached. After 50 ps the signal is simply too weak to allow for a further analysis. In DCE, the shifts for the TARA and truxenone bands adopt values of 35 nm and 20 nm, respectively. They are less pronounced than in DMSO, but still clearly visible.

In contrast to **trux1**, the bands in **trux2** exhibit almost no shift. Only

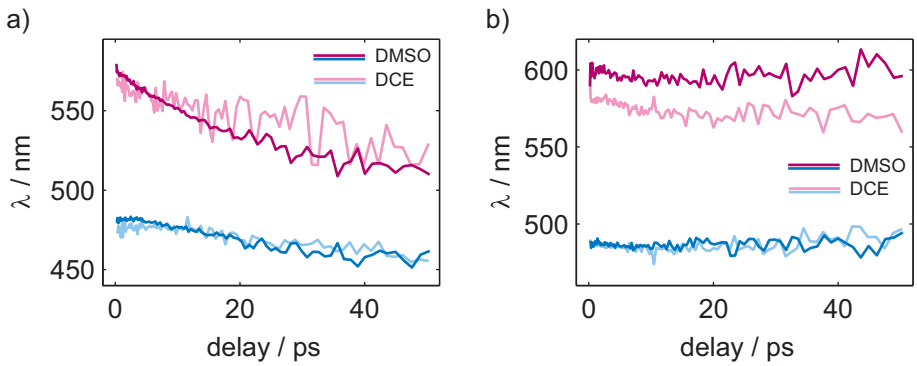

Figure 5.7: Shift of the spectral positions of the zero crossing between the absorption bands and the ground state bleach. As can be seen in figure a), a strong shift is found for **trux1** in either solvent. In contrast to that, almost no shift is observed for **trux2** in figure b).

within the first few picoseconds, a shift of less than 5 nm can be observed. This can be seen in figure 5.7 b), where the spectral positions of the zero crossing for the bands in **trux2** are shown. In both solvents, the spectral positions remain almost constant. This observation will become crucial for the interpretation of the data in section 5.2.4.

For short delay times, another spectral feature is found in DMSO. The spectral oscillations are present in figures 5.4 b) and 5.6 b). Oscillations of this kind have been observed before [155] and can be assigned to a Raman mode of the solvent [156].

5.2.2 Transient anisotropy

So far, all presented transient absorption data have been recorded in magic-angle geometry. In this geometry, the data only depend on the population dynamics [157]. In addition to that, the anisotropy has been measured for both truxenone compounds in DMSO. To do so, transient maps are recorded with the polarisations of the pump and probe beams parallel and perpendicular to each other, respectively. The data recorded in these geometries do not only depend on the population dynamics, but also on the relative orientation of the transition dipole moments of the transitions induced by the pump and probe pulse. The anisotropy r is then defined as

$$r = \frac{\Delta\mathrm{Abs}_{\parallel} - \Delta\mathrm{Abs}_{\perp}}{\Delta\mathrm{Abs}_{\parallel} + 2\Delta\mathrm{Abs}_{\perp}} \tag{5.1}$$

where $\Delta\mathrm{Abs}_{\parallel}$ is the absorption change recorded with parallel polarisations and $\Delta\mathrm{Abs}_{\perp}$ is the absorption change for perpendicular polarisations. In this way, it is possible to gain information about the orientation of the transition dipole moments [157].

In principle, one could calculate an entire anisotropy map from the transient absorption data. However, since the effects are rather small and the signal-to-noise ratio is rather bad, only single anisotropy traces will be shown. To improve the signal-to-noise ratio, the data for the traces are averaged over a certain wavelength range (approximately 15 nm) for each feature in the transient absorption map. For **trux1**, the shift of the bands has been taken into account for the averaging process by shifting the wavelength range, over which the anisotropy is averaged, according to the shift of the absorption bands. Since the TARA radical cation absorption band is rather broad, two traces are shown for this band, denoted with "TARA$^{\bullet+}$ (blue)" for the high-energy part of the band and "TARA$^{\bullet+}$ (red)" for the low-energy part.

The anisotropy traces for **trux1** are shown in figure 5.8 a) and for **trux2** in figure 5.8 b). Neither of the traces exhibit any dynamics. The values of r are rather small and constant over the entire delay range shown here. However, they differ slightly for the different bands in the spectrum. The equilibrium values of the anisotropy for large delay times allow one to make an assumption concerning the symmetry of the molecule. For a planar molecule with symmetry higher than C_2 one would expect a value of $r = 0.1$ [158–160]. For both compounds, the anisotropy of the ground state bleach adopts a value close to 0.1. This observation is not suprising since the ground state exhibits C_{3h}-symmetry. The other bands show slightly different values of r, which means that either the dipole moments no longer lie in the same plane or that a symmetry breaking of the state has taken place.

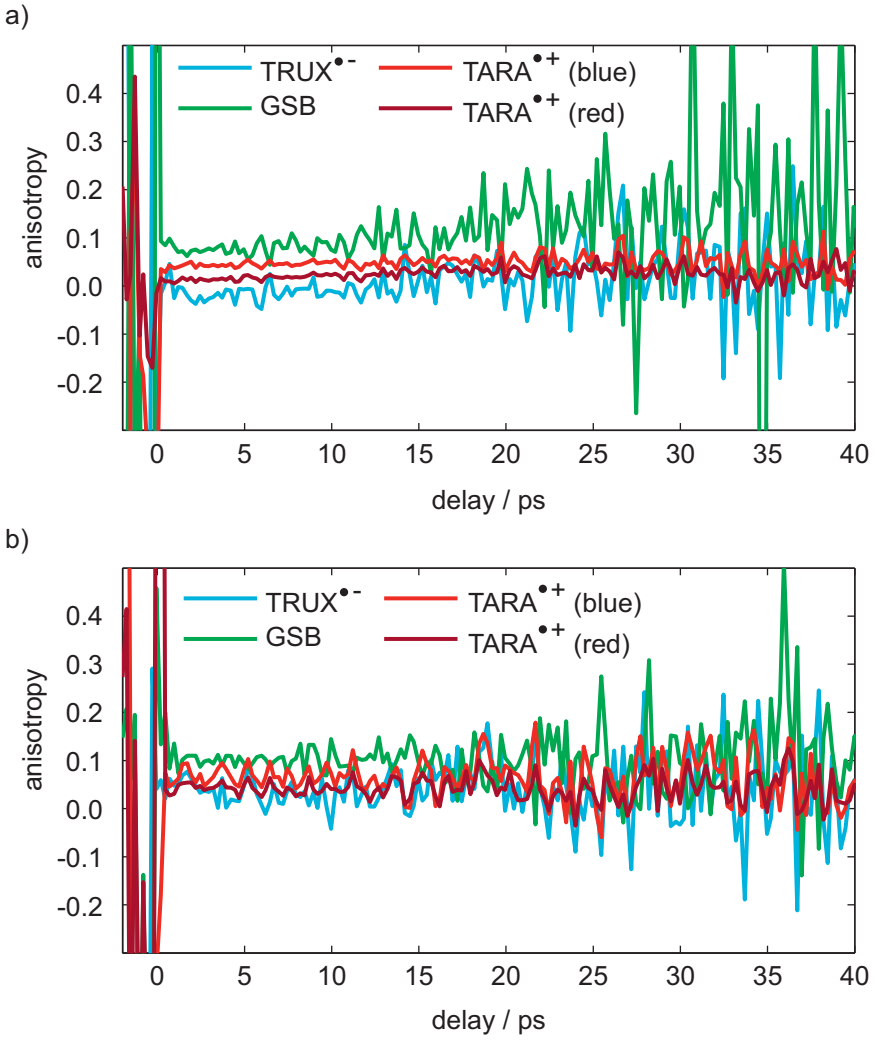

Figure 5.8: Averaged anisotropy traces for **trux1** (figure a)) and **trux2** (figure b)) in DMSO.

For systems with similar symmetry properties, a very fast anisotropy decay could be observed (< 100 fs) [160, 161]. For longer delay times, the anisotropy adopts a value around 0.1. Since the step size for this experiment was chosen to be 200 fs, a process on this fast time scale could not be resolved in the anisotropy decay.

Nevertheless, the different equilibrium values for the anisotropy of the different bands allows to draw the conclusion that the system is symmetry broken for larger delay times and thus that the charges are localised.

5.2.3 Global analysis of the transient absorption data

As for the TARA–PCTM compounds, a global analysis of the transient absorption data has been carried out using *Glotaran* [130]. As a kinetic model, a monoexponential rise and a biexponential decay has been employed. A constant offset was used to model the contribution of scattered pump light. The coherent artifact and the temporal chirp of the probe pulse have also been accounted for. For the data measured in DMSO, the Raman mode of the solvent was filtered out using a Fourier-transform method.

The results are shown in figures 5.9 to 5.12. Exemplary decay traces (experimental data and the result of the global analysis) are shown for both compounds in both solvents. Figures 5.9 and 5.10 display the dynamics of **trux1** in DMSO and DCE, respectively. In figures 5.11 and 5.12 the corresponding data for **trux2** are shown.

The global analysis reveals that for either compound, all bands show the same decay kinetics. In **trux1** time constants of $\tau_1 = 7.5\,\mathrm{ps}$ and $\tau_2 = 18\,\mathrm{ps}$ are found in DMSO. In DCE the time constants adopt values of $\tau_1 = 28\,\mathrm{ps}$ and $\tau_2 = 223\,\mathrm{ps}$, thus the kinetics are considerably slower in DCE.

A similar behaviour is found for **trux2**. Again, the faster dynamics are observed in DMSO with time constants of $\tau_1 = 4.5\,\mathrm{ps}$ and $\tau_2 = 25\,\mathrm{ps}$. In DCE the global analysis yields time constants of $\tau_1 = 9.8\,\mathrm{ps}$ and $\tau_2 = 61\,\mathrm{ps}$ which is again considerably slower than in DMSO.

Within the first few picoseconds, however, the rise dynamics of the bands differ seriously. While the absorption of the truxenone radical anion and the ground state bleach appear instantly, a distinct rise time can be seen for the TARA radical cation absorption. This rise time also strongly depends on the solvent. For **trux1** in DMSO and DCE, values of $\tau_{\mathrm{rise}} = 0.7\,\mathrm{ps}$ and $\tau_{\mathrm{rise}} = 2.1\,\mathrm{ps}$ are found, respectively. The values for **trux2** are slightly smaller. The global analysis yields $\tau_{\mathrm{rise}} = 0.3\,\mathrm{ps}$ in DMSO and $\tau_{\mathrm{rise}} = 1.7\,\mathrm{ps}$ in DCE. For comparison, all time constants are listed in table 5.1.

compound	solvent	τ_{rise} / ps	τ_1 / ps	τ_2 / ps
trux1	DMSO	0.699 ± 0.005	7.49 ± 0.05	15.46 ± 0.09
	DCE	2.05 ± 0.02	28.9 ± 0.2	222 ± 5
trux2	DMSO	0.253 ± 0.003	4.76 ± 0.02	28.8 ± 0.3
	DCE	1.701 ± 0.009	9.876 ± 0.005	61.0 ± 0.4

Table 5.1: Time constants obtained by global analysis of the transient absorption data of **trux1** and **trux2** in different solvents.

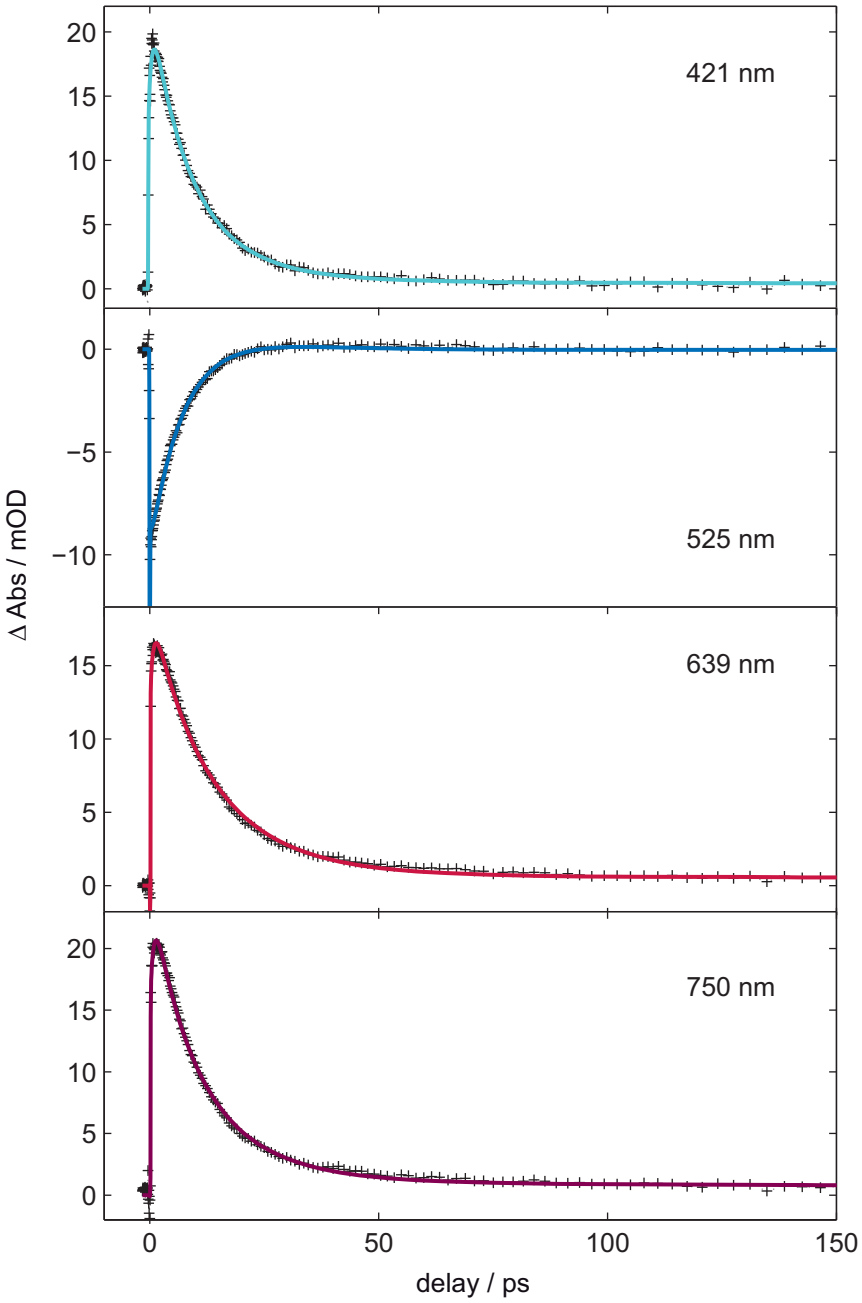

Figure 5.9: Exemplary kinetic traces of **trux1** in DMSO, corresponding to the truxenone radical anion absorption, the ground state bleach and the high-energy and low-energy part of the TARA radical cation absorption (from top to bottom).

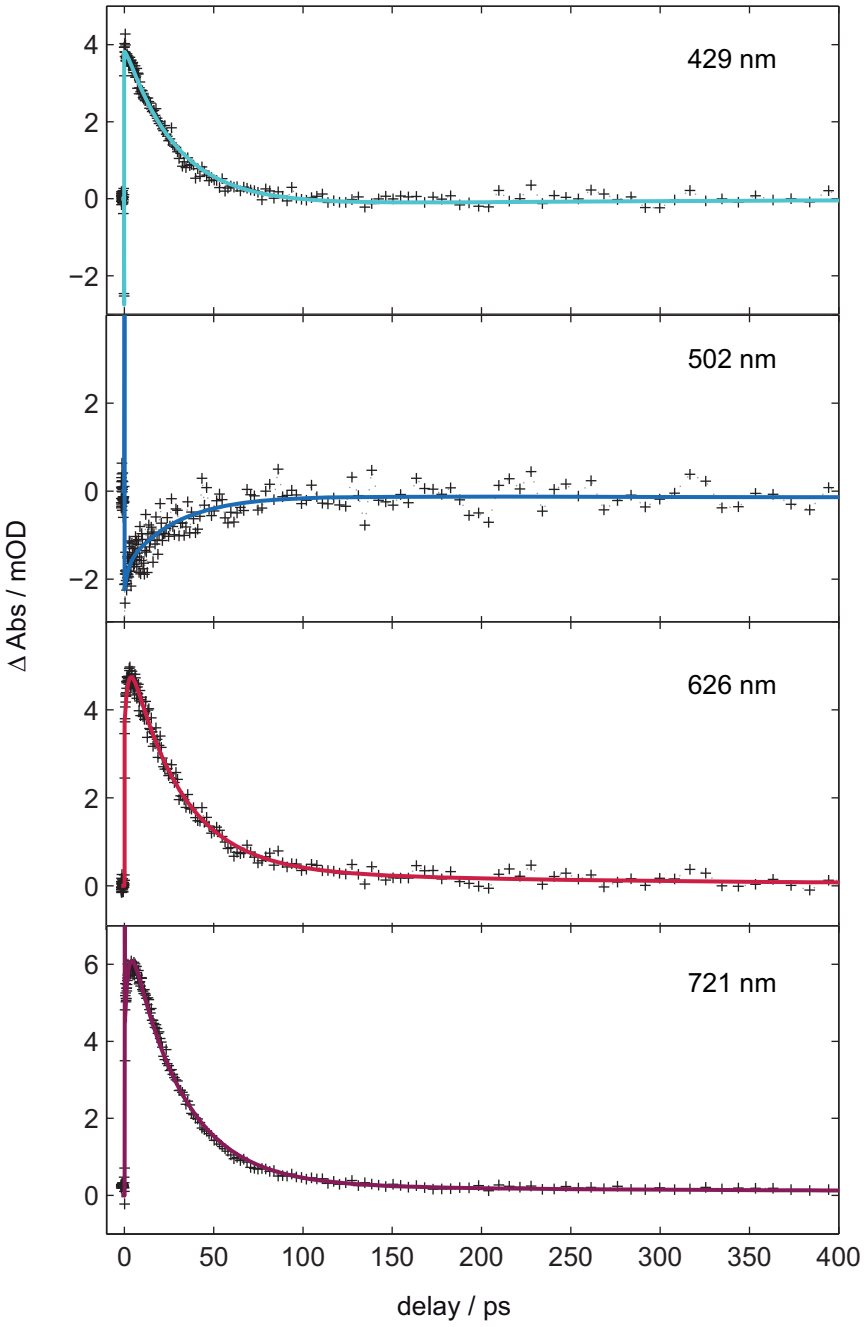

Figure 5.10: Exemplary kinetic traces of **trux1** in DCE, corresponding to the truxenone radical anion absorption, the ground state bleach and the high-energy and low-energy part of the TARA radical cation absorption (from top to bottom).

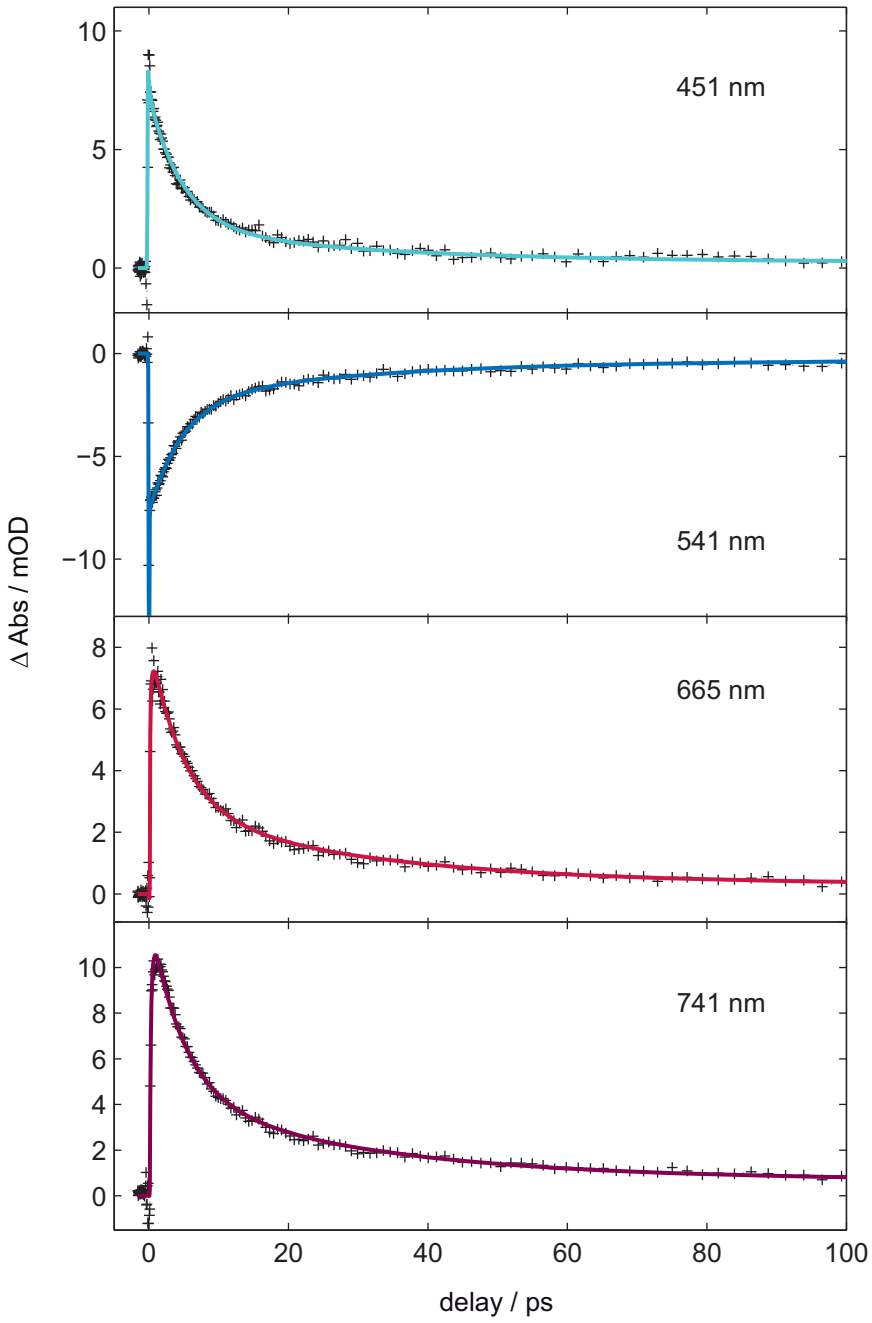

Figure 5.11: Exemplary kinetic traces of **trux2** in DMSO, corresponding to the truxenone radical anion absorption, the ground state bleach and the high-energy and low-energy part of the TARA radical cation absorption (from top to bottom).

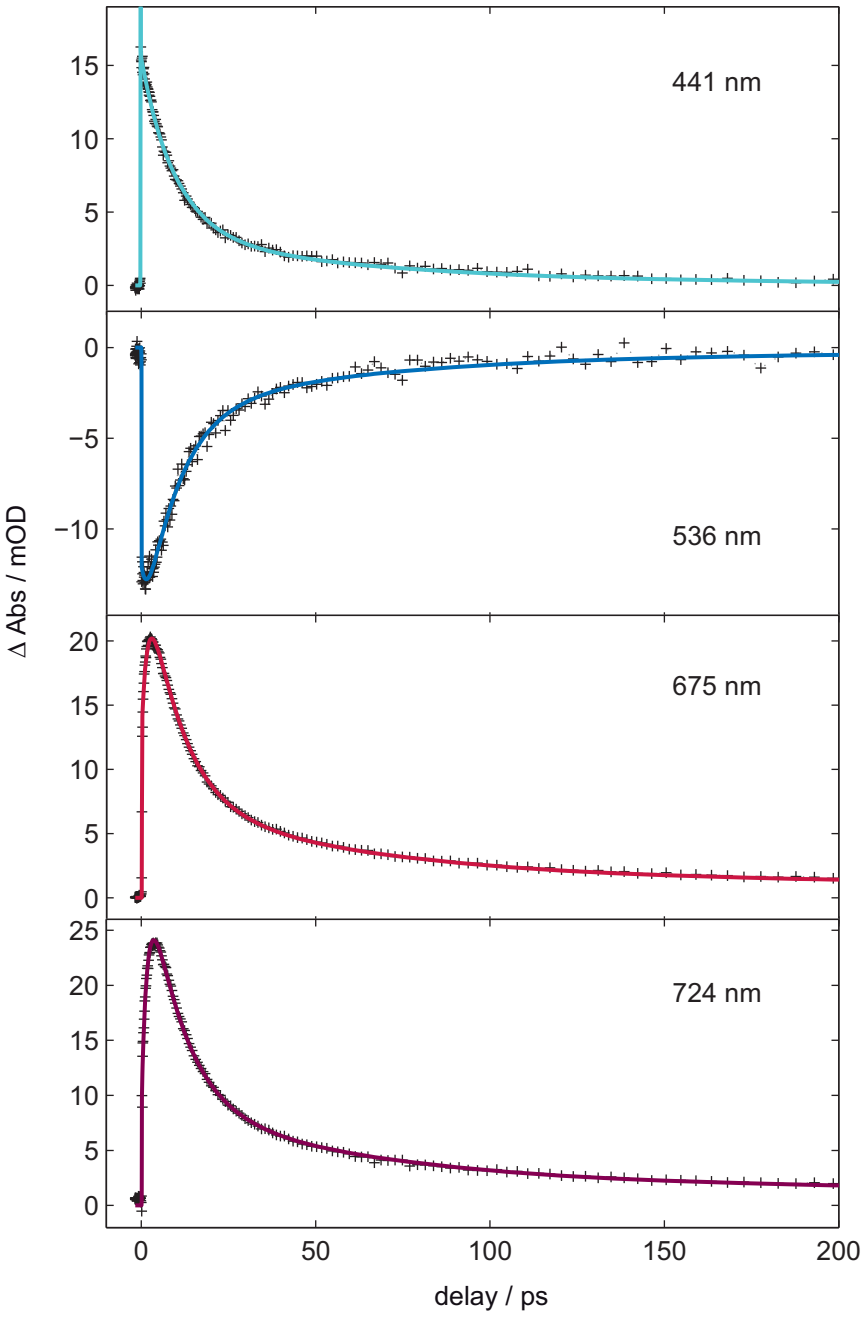

Figure 5.12: Exemplary kinetic traces of **trux2** in DCE, corresponding to the truxenone radical anion absorption, the ground state bleach and the high-energy and low-energy part of the TARA radical cation absorption (from top to bottom).

5.2.4 Interpretation of the truxenone data

Before giving an interpretation of the data, the findings made so far will be reviewed briefly. Upon excitation, the charge-transfer state is populated which can be probed via the absorption bands of the truxenone radical anion and the TARA radical cation. Those absorption bands decay biexponentially, where the time constants strongly depend on the solvent. The decay is considerably faster in DMSO than in DCE for both truxenones. However, no systematic dependence of the time constants on the donor-acceptor distance is found, the values for **trux1** and **trux2** are very similar. A distinct rise time can be observed for the TARA band, whereas the ground state bleach and the truxenone absorption appear instantly. The major difference between both systems is that the absorption bands show a strong blueshift for **trux1** whereas almost no shift is observed for **trux2**. For both systems no dynamics in the anisotropy could be observed. The anisotropy values for larger decay times are close to 0.1 and constant, yet they adopt slightly different values for the different bands.

As mentioned before, the different equilibrium anisotropy values for the different bands indicate that the system is symmetry broken for longer delay times and that the charges are localised. The ground state, however, exhibits a high symmetry since the anisotropy value of the ground state bleach is close to 0.1 which is expected for a planar system of symmetry higher than C_2.

The different rise times for the different spectral features can be explained as follows. The solvent-dependent rise time of the TARA band has been observed before [136] and can be assigned to the solvent reorientation (as in the case of TARA–PCTM compounds, see chapter 4.3.3). No rise time can be seen for the ground state bleach since the ground state is depleted instantly upon excitation. The absence of a rise time for the truxenone radical anion band can be explained by the high acceptor strength of the truxenone. Only minor changes in the charge distribution are expected if an additional electron is transferred to the truxenone, thus no strong solvent reorientation is necessary. It is also possible that the bulky aryl groups of the TARA branches shield the truxenone moiety from the solvent, leading to a reduced influence of the solvent reorientation on the truxenone absorption band. The rise time of the TARA radical cation band indicates that a stronger geometric change takes place as the TARA moiety donates an electron.

The solvent effects can be quantified using the longitudinal solvent relaxation time τ_L [96]. For DCE, a value of $\tau_L = 1.6\,\mathrm{ps}$ has been found [162], which is in good agreement with the data presented here. However, for DMSO a value of $\tau_L = 2.1\,\mathrm{ps}$ would be expected [162], which is clearly

larger than the values found in the transient absorption measurements. Nevertheless, these deviations might be accounted for by the fact that τ_L does not include any solute–solvent interactions.

The decay dynamics and the recovery of the ground state reflect the back electron transfer. This process is faster in DMSO, which is more polar than DCE because of the S–O bond compared to the C-Cl bond in DCE. Thus a better stabilisation of the CT state in DMSO is observed since the free enthalpy is reduced. The longer lifetimes found for the less polar solvent indicate that the back electron transfer takes place in the Marcus-inverted region. Here, the barrier for the back electron transfer increases with decreasing solvent polarity, leading to a longer lifetime of the CT state. This is in good agreement with the results from the global analysis.

However, the origin of the biexponential decay and the shift of the absorption bands still has to be elucidated. As will be seen, both phenomena are closely related. Vibrational cooling [163] can be ruled out as the origin of the shift since it would lead to a redshift of the bands and cannot explain a blueshift as observed here. However, the timescale on which the shift is observed already points at the kind of process involved. The bands shift in a time interval of several tens of picoseconds, which is also the timescale for the rotation of larger molecules [164]. Therefore the shift is assigned to a rotation of one molecular subunit in the TARA-substituted truxenone with respect to the rest of the molecule.

AM1 calculations [165] for a one-dimensional charge-transfer system revealed that geometry of the TARA moiety plays a crucial role [166]. Because of the sterically demanding aryl groups, the TARA moiety is not planar. The aryl groups are twisted out of plane and oriented in a propeller-like fashion around the nitrogen atom. Thus the orientation of the TARA unit with respect to the acceptor becomes important. For the one-dimensional system, two minima were found along a rotational coordinate. One of them corresponds to the case were donor and acceptor are almost parallel while in the second case they are perpendicular with respect to each other [135, 167]. The situation is similar for the TARA-substituted truxenones. It is assumed that two rotational conformers exist, one in which the TARA, from which the charge is transferred, and the truxenone are almost parallel and a second one where both are perpendicular to each other. The latter is the favourable conformation since the steric hindrance of the aryl groups is minimised by the rotation. Both conformers are separated by an energy barrier in the ground as well as in the CT state and can thus not be interconverted. However, there is a trade-off between the minimisation of the steric hindrance and the orbital overlap of the free electron pair of the nitrogen with the π-system

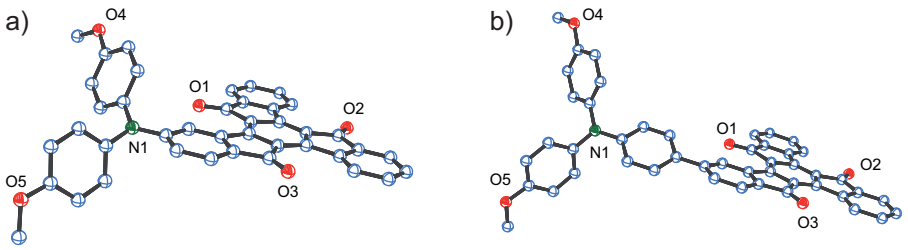

Figure 5.13: Optimised AM1 structures for both TARA-substituted truxenones [168]. For simplicity, only one donor branch is shown and the hydrogen atoms are omitted. To minimise the steric hindrance, the aryl groups are strongly twisted out of the truxenone plane for **trux1** (figure a)). Because of the additional spacer, this twist is less pronounced in **trux2** (figure b)).

of the truxenone. For the perpendicular conformation, the orbital overlap is reduced and thus the electronic coupling is small. In the parallel case, the overlap is larger and thus is the electronic coupling.

The optimised AM1 structures of both truxenones are depicted in figure 5.13. For simplicity, only one donor branch is shown and the hydrogen atoms are omitted. As can be seen in figure 5.13 a) the aryl groups are strongly twisted out of plane for **trux1** since the donor is coupled to the acceptor directly at the nitrogen atom. For **trux2**, however, the twist is less pronounced because of the additional spacer between the donor and the acceptor. This is shown in figure 5.13 b). Thus the steric hindrance has a larger influence in **trux1** than in **trux2**, leading to a reduced orbital overlap and smaller electronic coupling in **trux1** [168]. The electronic coupling is dominated by the steric hindrance and not by the donor–acceptor distance as one might expect from Marcus theory.

The existence of two rotational conformers also explains the observed bi-exponential kinetics. Both conformers are excited and both relax on different decay pathways, but with different time constants due to the different electronic coupling. The smaller time constant τ_1 can be assigned to the almost parallel configuration in which the orbital overlap is maximised, while the larger τ_2 corresponds to the more perpendicular conformation which exhibits a smaller electronic coupling. In this model it is also possible to explain the blueshift of the absorption bands. The spectral position of the bands is determined by the S_1-S_n gap, in this case the gap between the CT state and a higher-lying excited state into which population is transferred upon

absorption of the probe pulse. If the spectral position of the bands changes with time, this means that the abovementioned gap changes with time. This change is caused by a rotation of the TARA unit around the axis that connects the donor with the acceptor. In **trux2** this rotation is easily possible because of the rather small influence of the steric hindrance. Thus both conformations are almost degenerate in energy and no change of the gap and shift of the bands is observed. In other words, the orbital overlap is almost optimal already in the ground state. The situation in **trux1** is different. The steric hindrance has a rather large influence, thus the rotation of the TARA moiety into the almost parallel geometry leads to an increase of the gap since this structure is less favourable. Nevertheless, the rotation is possible because the geometry of the first excited state will be different than that of the ground state (e.g. exhibiting larger bond lengths), maximising the orbital overlap. These considerations are valid under the assumption that the rotation proceeds slower than the back electron transfer.

The schematic potential energy curves which help to visualise the mentioned processes are depicted in figure 5.14. It should be noted, however, that these curves can only describe the processes qualitatively. The exact shape of the potentials is unknown, especially for the higher-lying states. Thus the potentials of figure 5.14 can be regarded an "educated guess".

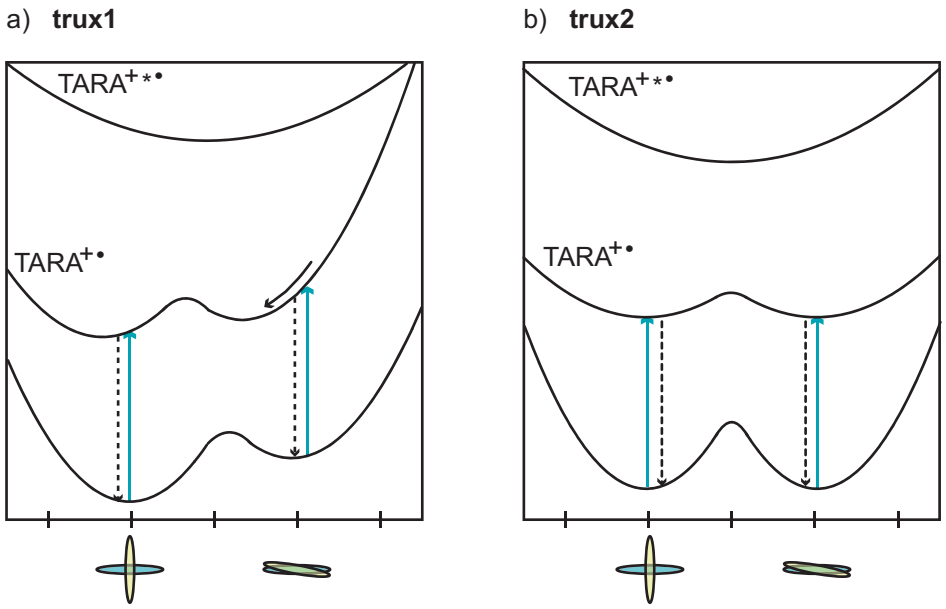

Figure 5.14: Schematic potential energy curves along a rotational coordinate. Two conformers exist that correspond to the perpendicular and parallel orientation of the donor and the acceptor with respect to each other. As can be seen in figure a), the parallel configuration is shifted to higher energy in **trux1** because of the steric hindrance of the aryl groups. In **trux2**, both conformers are degenerate in energy since the steric hindrance is reduced by the additional spacer between the donor and the acceptor (figure b)). The observed biexponential kinetics result from the existence of both conformers which are optically excited and decay with their respective time constants. The blueshift of the absorption bands in **trux1** is caused by an increase of the S_1-S_n gap as it is sketched in figure a).

5.3 Conclusion truxenones

Two different donor-substituted truxenones with different donor–acceptor distance were introduced. Due to the truxenone's C_{3h}-symmetry these systems can be regarded as two-dimensional charge-transfer compounds. The CT dynamics were investigated by transient absorption spectroscopy after excitation into the CT band. The CT was confirmed by the transient spectral signature which comprises absorption bands for the TARA radical cation as well as for the truxenone radical anion.

The dynamics reveal a distinct rise time for the TARA radical cation band which is assigned to the reorientation of the solvent molecules. The truxenone band appears instantly. Its dynamics are not influenced by the solvent reorientation due to the high acceptor strength of the truxenone. Only minor changes result from the additional electron density of the donated electron. Alternatively, also a shielding of the truxenone moiety by the TARA aryl groups can result in a reduced interaction between the acceptor and the solvent.

The back electron transfer proceeds biexponentially. This results from the contributions of two possible rotational conformers. In the configuration where the donor and the acceptor are almost parallel, the orbital overlap of the free electron pair of the nitrogen with the π-system of the truxenone is optimised, leading to a large electronic coupling. This corresponds to the shorter of both decay constants. In the perpendicular configuration, the orbital overlap and thus the electronic coupling are reduced, giving rise to the larger time constant. The perpendicular configuration is especially important for **trux1** because it minimises the sterical hindrance of the TARA aryl groups. Because of the additional spacer in **trux2**, the sterical hindrance only plays a minor role in this system. The sterical hindrance also explains the blueshift of the absorption bands observed for **trux1**. Upon excitation of the sterically hindered system, a geometrical conformation change allows for a rotation into the parallel configuration. This results in a change of the S_1-S_n gap which determines the spectral position of the absorption bands. The solvent dependence of the CT rates indicates that the back electron transfer takes place in the Marcus-inverted region since it is faster for the more polar solvent.

In addition, transient anisotropy measurements have also been carried out. The results indicate that the system is symmetry-broken for larger delay times and thus the charges are localised.

To elucidate the dependence of the CT on the substitution pattern a third truxenone has also been investigated [168]. It is similar to **trux2**, but the TARA branches are substituted in *meta*-position rather than *para*-position.

From the steady state absorption spectrum one can see that the lowest-energy transition is shifted to considerably higher energy. Thus the substitution pattern has an impact on the optical and presumably CT properties. The transient absorption measurements also exhibit a distinctly different behaviour than those of **trux1** and **trux2**. This is caused by the fact that the excited transition is a localised truxenone excitation rather than the charge transfer. TD-DFT calculations [169] support this assumption.

The TARA-substituted truxenones pose an example of CT compounds in which the CT dynamics are strongly dependent on the geometry of the system since it has a drastic influence on the electronic coupling between the donor and the acceptor. From Marcus theory, one might expect a simply dependence of the electronic coupling on the donor–acceptor distance. Here, however, the sterical hindrance plays a crucial role since it determines the twist of the donor with respect to the acceptor and thus the orbital overlap and electronic coupling.

An interesting open question still remains, namely: Is energy being transferred between the donor branches after excitation? Since energy transfer is usually a very fast process, the measurements presented here would have to be repeated with smaller step size and thus higher time resolution. This would be most beneficial especially for the anisotropy measurements.

A different approach would be to study a one-dimensional system as a reference. This has proven insightful for donor-substitutes triarylboranes, a different two-dimensional CT system [170]. However, synthesizing a truxenone with only one donor branch is not very promising. Instead, one could use 9-fluorenone [168, 171, 172] as a model for the acceptor. Coupling 9-fluorenone to a TARA unit is possible [151], thus TARA-substituted 9-fluorenone would be an ideal reference system to study the CT dynamics. This might help elucidate the energy-transfer dynamics in TARA-substituted truxenones after excitation.

Chapter 6

Metallo-supramolecular polyelectrolyte

In this chapter, a substantially different kind of charge-transfer system will be presented. As the title already suggests, a supramolecular metallo-polyelectrolyte (MEPE) can be regarded as a metal-containing, polymeric CT compound. The MEPEs which have been investigated in this chapter have been synthesized in the research group of Prof. D. Kurth from the University of Würzburg. The results presented in section 6.2 have been obtained in close cooperation with this group. Incorporating metal ions into organic structures is often crucial for the functionality of such systems. Many biological examples exist that impressively demonstrate the importance of metal. Porphyrin-based structures like chlorophyll [173] or heme [174] are among the most famous ones. The former contains a magnesium atom and is necessary for the conversion of light into energy, which is the basis of photosynthesis [1]. The latter, heme, is the iron-containing building block of hemoglobin, the red pigment in blood. It is involved in oxygen delivery in the respiratory system of almost all vertebrates [7]. Many enzymes also depend on metal atoms as cofactors to guarantee their functionality, for example DNA polymerase [175]. This enzyme requires magnesium as cofactor to build DNA strands. Although many more examples exist, these few ones already suffice to get an idea of the diverse functionality that is related to metal-containing assemblies.

Metal-containing compounds are also interesting regarding their charge-transfer dynamics. Before the advent of neutral organic mixed-valence CT systems, CT phenomena were investigated in metal-containing complexes. One of the first examples of a metal-containing complex is Prussian blue [176], a pigment used by artists from the 18th century on [177]. Many more

examples followed and a vast amount of literature regarding CT in metal-containing complexes is available [178–182].

As was discussed in chapter 4, polymeric materials are especially important for the fabrication of devices, but also for functional materials. Incorporating metal ions into a polymeric structure provides an additional degree of freedom to influence the functionality of the polymer.

MEPE has the interesting property of self-organising into a specific structure, making device structuring by bottom-up processes possible. Depending on the strength of the metal-ligand bond, dynamic materials can be obtained that can respond to external stimuli. Thus, MEPEs might be important to design "smart" materials.

Examples of MEPEs with interesting energy-transfer and absorption and emission properties are also known [10]. Thus it is promising to conduct spectroscopic experiments on such systems in order to unravel the underlying principles that determine the optical properties.

In summary, MEPEs combine a variety of interesting properties. Ultrafast spectroscopy might help to get insight into the CT dynamics of this metal-containing polymeric compound. In addition it might also be possible to follow the self-assembly dynamics and gain information on this process.

The structure and properties of the investigated MEPE will be discussed in section 6.1. After that, the transient absorption data and their global analysis can be found in sections 6.2 and 6.3, respectively. In section 6.4, the interpretation of the transient absorption data will be given. The chapter concludes with an outlook regarding further research on MEPE and an improved measurement technique for a high-repetition rate shot-to-shot data acquisition.

6.1 Properties of MEPEs

6.1.1 General properties

In general, MEPEs consist of metal ions, which are connected by ligands, and the corresponding counter ions. In many cases, a supramolecular structure is formed by metal-ion induced self-assembly [183–185]. If polymer chemistry is extended by the use of metal ions, one can modify the properties of the polymer by using different metals like main group elements, transition metals and rare earths. The choice of the ligand has a large influence on the structure of the MEPE. In many cases, terpyridin-based ligands are used due to their high thermal and chemical stability. They coordinate in an octahedral geometry with metals like Fe, Ni, Co [186]. Rigid ligands lead to rigid rod-like polymers, while flexible ligands lead to the formation of cyclic structures with three to four repeating units [187]. Single-stranded chiral MEPEs can be achieved by the use of chiral ligands [188, 189]. Also polymers based on porphyrin-derived ligands have been reported [190]. Crosslinking of conventional polymers and terpyridine units leads to networks via metal complexation and results in rubber-like materials [191]. A crosslinked network can also be achieved via Fe-ion induced self-assembly of a tritopic ligand combined with a ditopic ligand [192]. Thus, a wide variety of different supramolecular structures is accessible with different MEPEs.

Introducing metal ions into polymer chemistry offers an additional degree of freedom. First of all, different geometries and coordination numbers can be achieved that are not accessible in carbon-based chemistry. Furthermore, the metal ions introduce new reactive [193], magnetic [194] and optical [195] properties into polymer chemistry.

The properties of the MEPE strongly depend on the strength of the metal–ligand bond. In the intermediate bonding-strength regime, dynamic materials can result. They exhibit a stable macromolecular structure, yet the bonding is reversible, thus they can react to external stimuli [9, 10] and have the ability to self-repair [196]. Intermediate bonding-strength means in this case that the attractive forces responsible for forming bonds are in balance with the repulsive forces that disrupt the system. If the binding forces are too strong, irreversible bonding takes place which leads to less ordered structures. The system loses its ability to compensate for defects. The process that controls the MEPE self-assembly is metal–ligand coordination [184, 185]. The necessary precondition for self-assembly is that several (macro-)molecular modules, which possess a sufficient mobility, interact with each other [197]. As a result, self-assembly often takes place in the liquid phase or at interfaces where the interaction can be guaranteed due to thermal motion of the

modules. In this way, the modules are able to build ordered structures. This is important for bottom-up fabrication of nanostructured devices [198]. In solution, macromolecular equilibrium structures are formed by kinetically labile metals like Fe, Ni, Co while kinetically stable metals like Ru lead to static MEPEs [184, 199].

Controlling the next step in the hierarchy of self-assembled structures can be achieved by adding amphiphilic counter-ions. They lead to a spontaneous formation of a polyelectrolyte-amphiphile complex (PAC). These PACs exhibit a structure-induced spin crossover [200, 201], which is accompanied by a change in magnetic properties from diamagnetic to paramagnetic. Depending on the MEPE and the amphiphile, different PAC structures can be generated, including sandwiched MEPE–amphiphile layers, in which the MEPE rods are uniaxially oriented [202], perfectly straight PAC rods with lengths of up to 200 nm [203] or liquid-crystalline phases comprising alternating MEPE units and interdigitated amhiphiles [204]. Self-sorting of PACs into raft-like structures has also been reported [205].

The steady-state spectroscopic properties of MEPE are governed by the ligand bands and bands that correspond to metal-centered transitions which are mainly found in the UV and an intense metal-to-ligand charge-transfer (MLCT) band. The latter appears in the visible spectral range. Its absorption maximum is influenced by the choice of the metal ion [206, 207]. For Fe-MEPEs, the absorption maximum of the MLCT band can be found around 585 nm [208] while it apperars at 520 nm for Ru-MEPEs [209]. In Co-MEPEs, however, no MLCT absorption can be observed [210]. In all cases, the exact position of the absorption maximum of the MLCT band also depends on the substituents of the ligand. The ligand's spacer length only influences the strength of the absorption [206]. In close relation to that, the electron-donating or -withdrawing nature of the substituents also has a profound influence on the electrochemical properties [207] and probably also on the charge-transfer characteristics.

Due to the manifold of interesting properties of MEPEs, a large variety of possible applications exists. They include stimuli-responsive layers [211], electronic displays and papers or electrochromic windows [192, 210, 212]. MEPEs could also be employed in computer memory on a molecular scale because of their spin-crossover properties [213]. Since the field of research regarding MEPEs is still rather young, many more interesting applications can be expected to emerge.

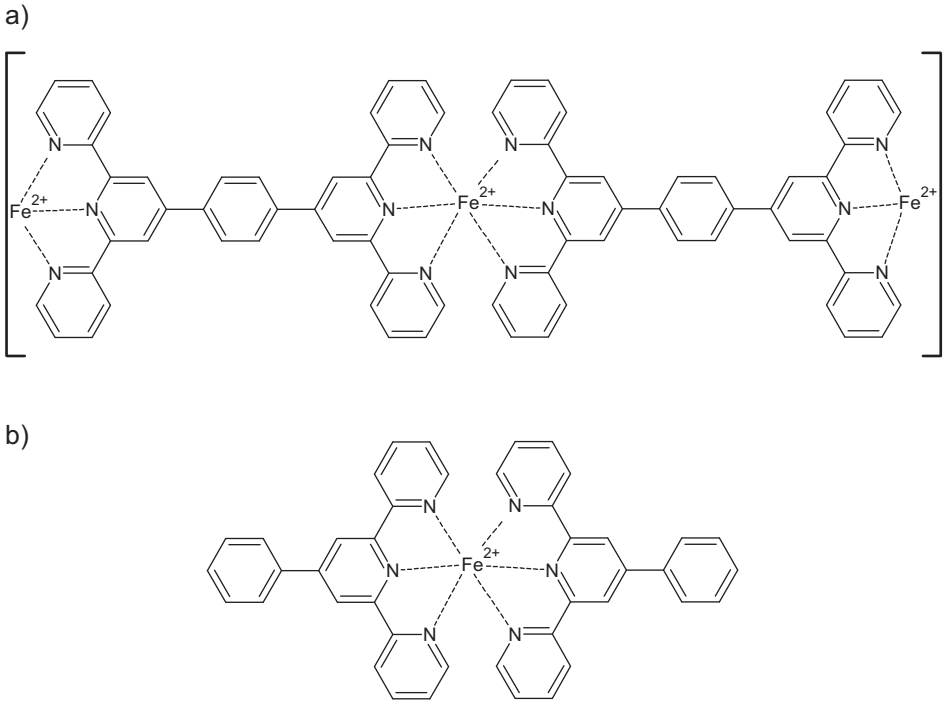

Figure 6.1: Structure of the polymeric **Fe-MEPE-L1** (figure a)) and of its monomeric analogue **Fe-L2** (figure b)). For clarity, the counter ions are not shown.

6.1.2 Properties of Fe-MEPE-L1 and Fe-L2

In the course of this thesis, an Fe(II)-based MEPE with the ditopic terpyridine-based ligand 1,4-bis(2,2',6',2"-terpyrid-4'-yl)benzene has been investigated. This polymeric MEPE will be referred to as **Fe-MEPE-L1** [206, 214]. It comprises Fe^{2+} ions and the ligand **L1** in a stochiometric ratio of 1:1. Its structure is depicted in figure 6.1 a). For the sake of clarity, the counter ions are not shown. As a reference compound, the corresponding monomeric complex **Fe-L2** has been investigated. The slightly modified ligand **L2** (4'-phenyl-2,2':6',2"-terpyridine) [215] has been used because it exhibits only one coordination site for the metal ion, thus the formation of a polymer is reliably suppressed. The structure of the monomeric complex is shown in figure 6.1 b). Terpyridine-based ligands lead to metal complexes with an octahedral geometry and have been used to form monomeric metal complexes [216] as well as polymeric MEPEs with metals like Fe, Ni, Co or Ru [187, 207, 217].

The normalised absorption spectra of **Fe-MEPE-L1** and **Fe-L2** are shown in figure 6.2. The spectrum of the polymeric **Fe-MEPE-L1** (de-

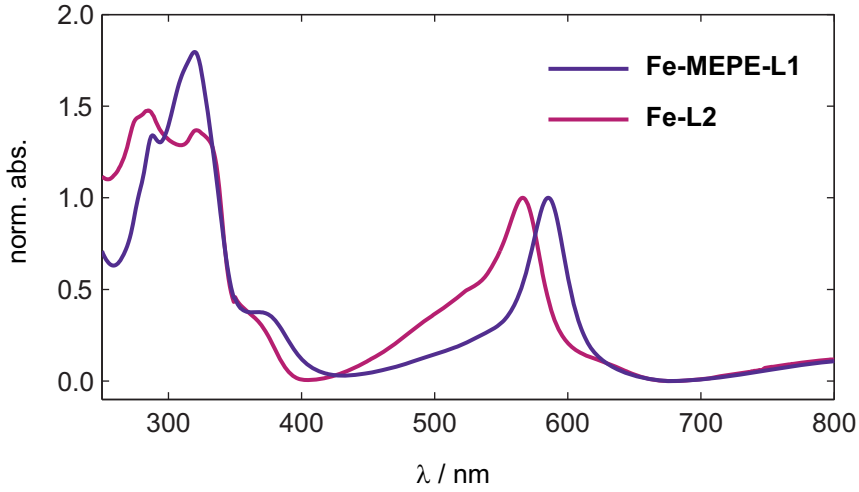

Figure 6.2: The absorption spectra of **Fe-MEPE-L1** (dark violet) and **Fe-L2** (pink) in water. Both are normalised to the MLCT band, which appears at 585 nm and 565 nm in the polymer and the monomer, respectively. The bands in the UV region can be assigned to the ligand and to metal-centered transitions.

picted in dark violet) features several bands in the UV as well as a distinct absorption band in the visible. The former can be assigned to ligand π-π^* transitions [218]. The latter is the MLCT band which corresponds to a charge transfer from the metal to the ligand [214]. For **Fe-MEPE-L1** in aqueous solution, it is centered at 585 nm. The spectrum for **Fe-L2** (depicted in pink) show very similar features. Again, the UV bands can be assigned to ligand transitions. The MLCT band can be found at 565 nm. A blueshift of the MLCT band of the monomeric complex in relation to the MLCT band of the MEPE has been observed before [214].

Due to the octahedral coordination geometry of the terpyridine ligand, **Fe-MEPE-L1** form rigid, rod-like structures. Atomic-force microscopy measurements of **Fe-MEPE-L1**-films spin-coated from solution revealed that single rods have a diameter of approximately 1.5 nm and lengths of up to 550 nm, corresponding to 350 repeating units. From neutron-scattering experiments it can be concluded that rod-like macromolecular assemblies of **Fe-MEPE-L1** also exist in aqueous solution [187].

It is still unclear whether the Fe^{2+} ions in **Fe-MEPE-L1** interact with each other. Although it is assumed that the distance between the metal centers is too large for an interaction [219], some indications for a dipo-

lar coupling between the metal centers exist [218]. In the corresponding polyelectrolyte-amphiphilic complex, however, an antiferromagnetic coupling could be observed for low temperatures [220].

From Mössbauer spectroscopy on a similar MEPE it is known that Fe(II) is the only species present in the polymer, no Fe(III)-centers could be detected [221]. If the Fe(II)-centers are oxidised (e.g. by applying an electric potential), the MLCT absorption can be surpressed [206]. This already indicates that charge transfer is an important process in MEPEs. In order to gain further information on the CT behaviour of MEPE, the dynamics after an optically-induced CT were probed via transient absorption spectroscopy. The results are presented in the subsequent section.

6.2 Transient absorption spectroscopy of MEPEs

To study the CT dynamics of **Fe-MEPE-L1** and **Fe-L2**, both compounds were excited at the MLCT band. The subsequent absorption changes were monitored in the spectral range of the same band. As a solvent, water was used. The data were recorded using the high-repetition rate transient spectrometer described in section 3.3.2. For each time delay, 20 spectra were recorded and averaged to calculate the absorption change. In subsequence, four independently recorded transient absorption maps were averaged and binned in wavelength-direction to reduce the influence of noise. Since the pump and probe beams can be blocked independently, the scattered-light correction as described in [118] was carried out. For **Fe-MEPE-L1**, the pump pulse was tuned to a central wavelength of 585 nm. Due to the blueshift of the MLCT band of **Fe-L2** compared to **Fe-MEPE-L1**, the pump pulse for **Fe-L2** was tuned to a central wavelength of 565 nm. In both cases, a FROG measurement of the pump pulse showed a pulse duration of around 200 fs. Although the probe pulse spanned most part of the visible spectrum, only a comparably narrow spectral range could be monitored due to the limited detection range of the monochromator. Its central wavelength was set to the maximum of the MLCT band, thus a spectral range of only approximately 80 nm around it was monitored.

The transient absorption maps for both compounds are depicted in figure 6.3. In figure 6.3 a) the map for **Fe-MEPE-L1** is shown. A negative contribution, corresponding to the ground state bleach, can be seen spanning the entire detection range. The ground state recovery is not completed within the maximum temporal scanning range of up to 3.5 ns (data only shown up to 700 ps for better visibility of the dynamics). A very similar behaviour is found for **Fe-L2**, which can be seen in figure 6.3 b). The ground state is depleted upon excitation and is not fully recovered.

The ground state bleach and recovery are illustrated again in figure 6.4, which displays the transient spectra for different delay times. Again, the graph in the upper panel corresponds to **Fe-MEPE-L1**, while the data for **Fe-L2** is shown in the lower panel. The bleaching of the ground state is clearly visible as a negative contribution. In both cases, the system does not reach its equilibrium state, since the absorption change at the maximum time delay is still non-zero. For both compounds, the inverse of the steady-state absorption spectrum is also displayed in grey. For **Fe-L2** (figure 6.4 b)) the steady-state spectrum and the spectral shape of the ground state bleach agree reasonably. The slight deviations might be explained by the insufficient

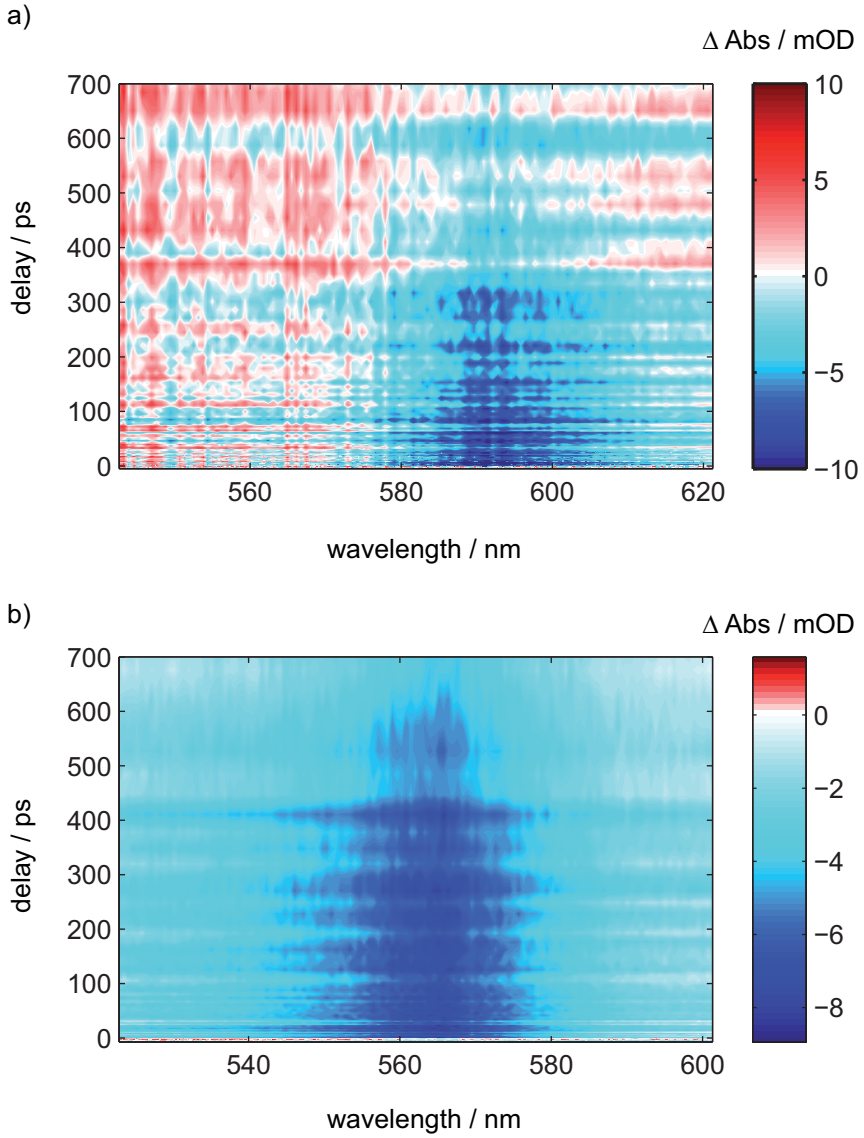

Figure 6.3: Transient absorption maps of **Fe-MEPE-L1** (figure a)) and **Fe-L2** (figure b)). In both cases, the ground state bleach is clearly visible as a negative contribution. The recovery of the ground state is not completed within the maximum temporal scanning range of 3.5 ns (data only shown up to 700 ps for better visibility of the dynamics).

data quality of the transient spectra. For **Fe-MEPE-L1** (figure 6.4 a)), however, the descrepancy between both can be seen clearly. The maximum of the transient spectra is redshifted by approximately 5 nm compared to the

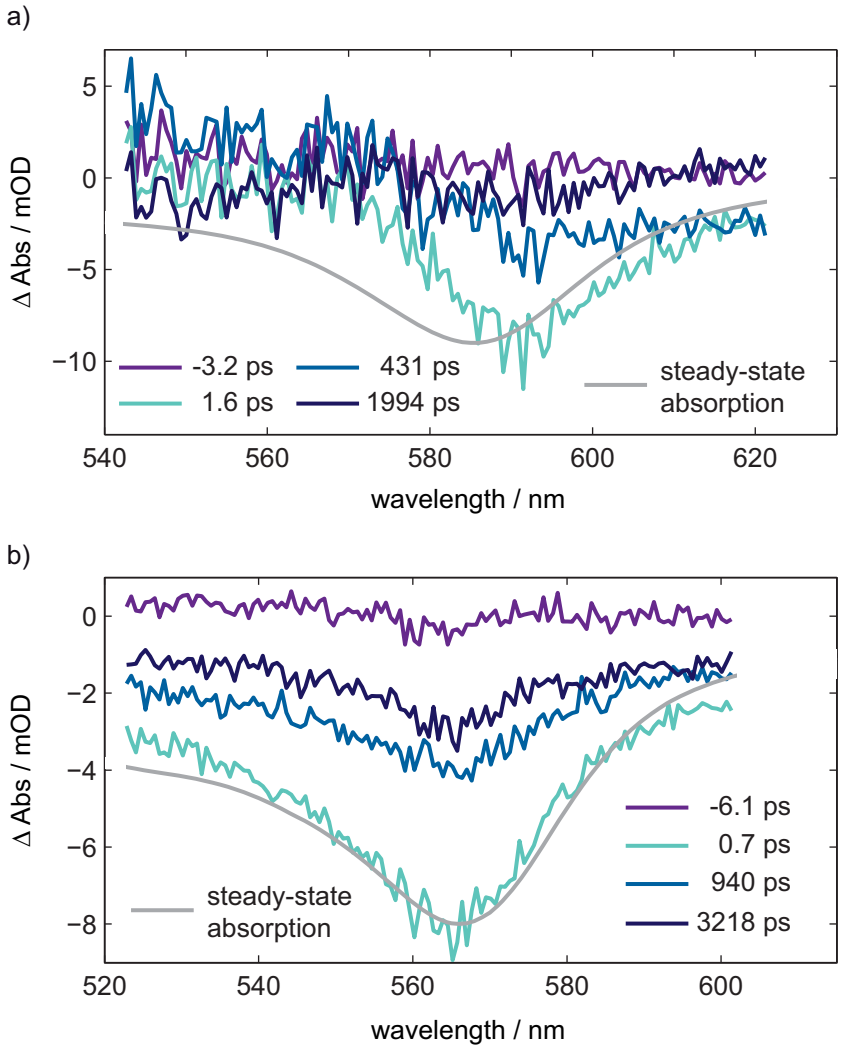

Figure 6.4: Transient absorption spectra of **Fe-MEPE-L1** (figure a)) and **Fe-L2** (figure b)). It can be clearly seen that the ground state is depopulated upon excitation and that its recovery is not completed within the maximum temporal scanning range of 3.5 ns (data only shown up to 700 ps for better visibility of the dynamics).

maximum of the steady-state absorption spectrum. The reason of this shift is presently unclear. Nevertheless, the signal-to-noise ratio of the transient spectra does not allow to draw too detailed conclusions regarding the spectral shape of the band. The global analysis of the kinetics is presented in the following section.

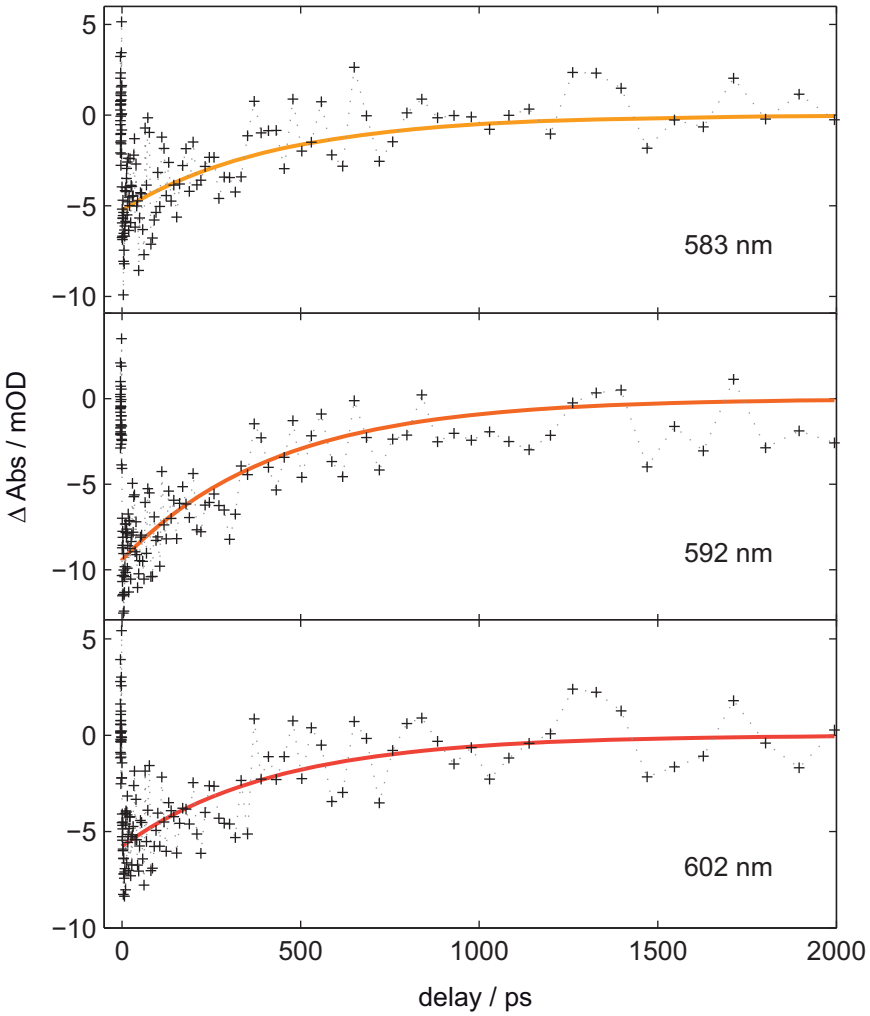

Figure 6.5: Measured time traces and the result of the global analysis for **Fe-MEPE-L1**. All traces correspond to the ground-state bleach.

6.3 Global analysis of the MEPE data

The global analysis of the MEPE data has been carried out with *Glotaran* (see also section 4.3.2). The kinetics were fitted with a monoexponential decay. However, some convergence difficulties arose due to the rather modest quality of the data. They could be overcome by only taking data for delay times greater than zero into account for the fitting procedure. It should also be mentioned that the temporal scanning range was insufficient to record the entire dynamics. This leads to a reduced accuracy regarding the results of

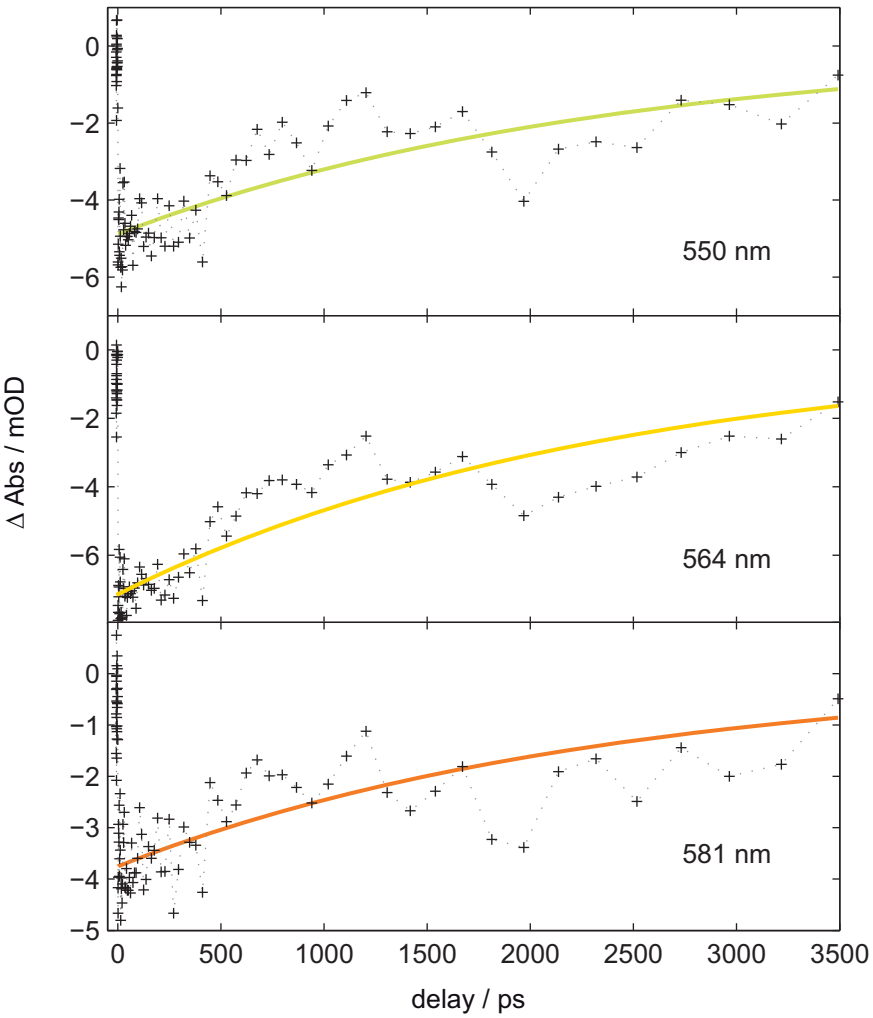

Figure 6.6: Measured time traces and the result of the global analysis for **Fe-L2**. All traces correspond to the ground-state bleach.

the global analysis. Nevertheless, the time constants obtained in this way can give a first impression of the time scales which are relevant for the dynamics after the photoexcitation of MEPE systems.

The measured and fitted time traces for **Fe-MEPE-L1** are depicted in figure 6.5. All traces correspond to the bleach of the ground state. The global analysis yields a time constant of $\tau = (428 \pm 9)\,\mathrm{ps}$. The traces for **Fe-L2** are shown in figure 6.6. As before, all traces correspond to the ground state bleach. A time constant of $\tau = (2369 \pm 24)\,\mathrm{ps}$ has been found for the recovery

of the ground state.

These time constants of several hundreds of picoseconds up to several nanoseconds are rather large compared to the CT dynamics of the organic mixed-valence systems discussed in chapters 4 and 5. The dynamics of the polymeric **Fe-MEPE-L1** are presumably faster than those of its monomeric analouge **Fe-L2**. However, no too detailed conclusion should be drawn due to the insufficient data quality. Some suggestions regarding the interpretation of these dynamics will be given in the next section.

6.4 Interpretation of the MEPE data

From the experiments conducted so far, only a limited amount of information can be gained. Different processes are conceivable as the origin of the observed dynamics. They will be discussed in this section. Before that, the findings will be summarised briefly. Upon excitation into the MLCT state, the ground state is depopulated. The recovery of the ground state was monitored by transient absorption spectroscopy. The global analysis of this data yields time constant for the recovery of about 430 ps for the polymeric **Fe-MEPE-L1** and 2.4 ns for its monomeric analouge **Fe-L2**. For **Fe-L2**, the steady-state absorption spectrum suffices to reproduce the spectral shape of the ground state bleach. Thus no other absorption bands should be present. In **Fe-MEPE-L1**, however, the band shape of the bleach deviates strongly from the shape of the steady-state absorption spectrum. The bleach appears to be redshifted by approximately 5 nm. The data quality of the transient absorption data does not suffice to draw detailed conclusions whether the ground state bleach is overlapped with other absorption bands. Thus the origin of this deviation is presently unclear.

Upon optical excitation in the MLCT band, an electron is transferred from the metal center to the ligand. The time constant of the ground state recovery could simply reflect the dynamics of the electron back-transfer from the ligand to the metal. Compared to the organic mixed-valence compounds, the charge transfer in MEPE appears to be clearly slower. This might be explained by a rather small electronic coupling which would result in small CT rates and thus relatively large time constants. However, since no details on the electronic coupling in MEPE are known, this is only a speculation.

Large time constants for the recovery of the ground state after optical excitation have already been observed in other iron-containing pyridine-based complexes. They have been explained with an optically induced spin-crossover [222–224]. In its ground state, the system adopts a low-spin configuration. Upon optical excitation, the high-spin state can be transiently populated. At room temperature, the decay of the high-spin state proceeds with time constants in the order of several hundreds of picoseconds [223] up to several nanoseconds [222]. It is possible that this process also gives rise to the observed MEPE dynamics, since spin-crossover phenomena are also known for MEPE and their corresponding amphiphilic complexes [225].

As a third possible process, the disassembly of the polymer or its monomeric analogue will be discussed. It is known that after optical excitation, antibonding orbitals become occupied. This leads to an increase in the metal–ligand bond length [223]. It is conceivable that this leads to a loosening or even cleavage of the bond. Since the compounds studied here are built in

a metal-ion induced self-assembly process, the fragments would reassemble after a bond is broken. In this case the time constant for the recovery of the ground state would reflect the dynamics of the self-assembly process. However, the data presented so far does not allow to identify the underlying process unambigously. Further studies are needed to overcome this difficulty, thus several proposals are presented in the following section.

6.5 Outlook: Further research on MEPE

The intention of this chapter is twofold. Firstly, some considerations will be discussed concerning future experiments on MEPE systems. What can be done to unambiguously identify what happens upon optical excitation? A variety of different experiments will be presented which might help in this endeavour. Secondly, a more technical question will be of concern. Since the data quality of the MEPE data is not optimal because of the time-averaged signal detection, a design proposal for a high-repetition rate shot-to-shot readout mechanism will be presented.

6.5.1 Future MEPE experiments

Since the experiments that have been carried out so far on the MEPE systems allow no reliable conclusions regarding the underlying dynamics after optical excitation, it is important to consider different approaches for future experiments. The easiest way to gain additional information is to monitor the dynamics after excitation in a broader spectral range, e.g. spanning the entire visible spectrum. Since only one strong absorption band, the MLCT band, is present in this region, it is also advisable to focus on the UV region, in which a number of different bands corresponding to ligand- and metal-centered transitions can be found. Thus carrying out VIS-pump–UV-probe spectroscopy [226] might be fruitful for MEPE systems.

As could be seen from the organic mixed-valence compounds, solvent-dependent studies are important to elucidate the CT dynamics. Thus it is advisable to study the dynamics of MEPE in different solvents. The drawback is, however, the MEPEs are not very soluble in nonpolar solvents, therefore only a limited range of possible solvents is available.

Instead of studying MEPEs in the liquid phase, one might also use spin-coated films of MEPE as a sample. In these films, the molecules are less mobile compared to the liquid phase. This should have an effect on the assembly-/disassembly dynamics. If the latter is the dominating mechanism after optical excitation, the transient absorption data of spin-coated films should differ from those of MEPEs in solution. To avoid photodamage to the sample, however, one would have to move the sample constantly. This can be achieved with a sample mount that combines a rotational and a translational movement [227]. Thus different laser pulses interact with different regions of the sample, minimising the danger of photodamage. A similar principle is employed in the white-light generation in CaF_2 as was discussed in section 3.3.1.

Of course, conducting pump-power dependent studies or measuring the

transient anisotropy might also help to gain further insight. Both can be easily carried out with the existing setup and should be considered for future experiments.

Once a deeper understanding of the iron-containing MEPEs has been achieved, one might also study the dependence of the CT dynamics on the metal ion or the ligand. A plethora of different interesting systems is available that wait to be studied with time-resolved measurement techniques.

6.5.2 Improvement of data quality

As can be seen from the previous sections, the data quality of the MEPE transient absorption data is insufficient to draw reliable conclusions regarding the dynamics. This originates in the time-averaged detection scheme as described in section 3.3.2. The acquisition time for one spectrum was usually chosen to be 300 ms, corresponding to 30000 laser shots which were averaged. This makes the data prone to the influence of low-frequency laser intensity noise. To improve the data quality, a shot-to-shot readout mechanism is usually employed which reduces the effect of low-frequency noise contributions [117, 228].

Mode-locked lasers exhibit an intrinsic source of low-frequency intensity fluctuations, whose exact origin is still debated [115]. Analysing the output characteristics of the *RegA* amplifier employed in the current experimental setup revealed that strong low-frequency contributions to the noise are present in the system [116]. Their influence cannot be circumvented by averaging over a large number of laser shots, thus they have a strong impact on the transient-absorption data measured with the time-averaged detection scheme.

It is possible, however, to improve the signal-to-noise ratio greatly if one exploits the high correlation of the intensity of subsequent laser pulses. Measuring the statistic autocorrelation of subsequent laser pulses confirms that such pulses are strongly correlated [116, 229]. This correlation can be utilised in transient absorption spectroscopy in the following way. One records the probe spectra of subsequent pulses and chops the pump beam with a frequency that corresponds to half of the repetition rate of the laser. Thus, probe spectra with unblocked and blocked pump beam are recorded alternately. These subsequently recorded spectra are used to calculate the absorption change ΔAbs [117]. For laser sources with a repetition rate of 1 kHz, this has become the standard detection technique as it is described in section 3.3.1.

Adapting this technique to high-repetition rate laser sources, however, is not easily possible. Standard chopper wheels and detectors that are capable

of broadband detection generally do not support repetition rates higher than a few kilohertz, although the use of high-repetition rate chopping has been reported [230]. Nevertheless, a design proposal for a high-repetition rate shot-to-shot transient spectrometer that circumvents these problems has recently been introduced by Kanal and Keiber [116]. Preliminary experimental results recorded with this novel setup indicate that the data quality can be drastically improved in comparison to the time-averaged detection scheme. Thus, the shot-to-shot signal detection is a promising technique for future experiments regarding transient absorption spectroscopy with a high-repetition rate amplifier system as the laser source.

Chapter 7

Broadband visible polarisation pulse shaping

As was seen in the previous chapters, ultrafast spectroscopy is an invaluable tool to observe and understand phenomena on a molecular level. However, its range of applications can be greatly increased by combining spectroscopy with the technique of femtosecond pulse shaping. This combination is beneficial for a variety of reasons. For one, the pulse shaper can be used as a tool for the simple implementation of advanced spectroscopy techniques. One example is the single-beam implementation of a coherent anti-Stokes Raman scattering (CARS) microscopy setup [231, 232]. In this variant of collinear CARS, the pulse shaper serves two purposes. First of all, it compresses the incoming pulses to their minimum time-bandwidth product. Secondly, an additional sinusoidal phase mask is used to create a pulse train of subpulses with equal temporal spacing. This spacing is scanned and a strong CARS signal can only be detected if the temporal separation of the subpulses coincides with the frequency of a molecular vibration of the sample. Thus, it is possible to record the Raman spectrum of the sample with high spatial resolution [233].

Another technique that profits from the use of a pulse shaper is two-dimensional (2D) electronic spectroscopy [234]. 2D spectroscopy allows to gain information on the molecular structure of the sample, on couplings between different electronic dipole moments in one molecule and even on energy transfer. Hence, it is a powerful technique, but it has high requirements regarding the experimental setup. The sample is excited by a sequence of pulses which have to be phase-stable with respect to each other. This can, for example, be achieved in a noncollinear box-geometry without utilising a pulse shaper[235]. However, one can also employ a partially collinear setup, where a pulse shaper creates a phase-stable pair of excitation pulses, which

are incident on the sample collinearly. They are followed by a noncollinear probe pulse which is then spectrally resolved, thus yielding the raw data for the 2D spectra [236]. In this way, a transient-absorption setup and a pulse shaper can be turned into an easy-to-use setup for the collection of electronic 2D spectra.

But not only spectroscopic setups can be greatly simplified by the use of a pulse shaper, also pulse characterisation techniques profit from it [237]. One standard technique, spectral-phase interferometry for direct electric-field reconstruction (SPIDER) [238], has been augmented in this way. In this interferometric technique, two copies of the unknown pulse are generated and time-delayed with respect to each other. Both are upconverted by mixing them with a strongly chirped reference pulse. From the interference between the upconverted pulse copies, the phase of the unknown pulse can be extracted. Usually an interferometric setup is required to create and delay the pulse copies. Alternatively, a pulse shaper can be used for that task [239]. A similar approach can be chosen for another standard characterisation technique, namely frequency-resolved optical gating (FROG) [124]. Again, two pulse copies have to be created which are then both focused onto a nonlinear medium and their relative time delay is scanned. The resulting nonlinear signal contains the desired phase information. This pulse shaper assisted FROG variant will be discussed in more detail later in this chapter.

Besides simplifying the implementation of certain spectroscopic techniques, incorporating a pulse shaper into a spectroscopic setup can also allow to gain deeper insight into the microscopic reaction mechanisms that are investigated. For one, systematic variations of certain pulse parameters help to elucidate their influence on the reaction. An important parameter beyond intensity and central frequency of the pulse is its chirp. It has been found that many reaction pathways like three-photon absorption [240] and fluorescence [241] are chirp-dependent. This dependency allowed to elucidate processes like the population transfer in green fluorescent protein [242] or to gain information on the potential-energy surfaces of interesting molecular systems like zinc-porphyrin [243]. Another mechanism that has attracted great attention is intrapulse dumping, where two sequential interactions of a molecular system with a chirped laser pulse play an important role. The observed effects originate in the dynamics of the system on the potential-energy surface of the excited state. Thus, chirped laser pulses help to shed light onto the dumping mechanism and the potential-energy surface. Similarly, a sequence of adequately timed pulses with different central frequencies can be a useful parametrisation to gain deeper insight into reaction mechanisms. Many related examples are discussed in reference [57].

To go even further, it is not only possible to analyse reactions with spectroscopy and pulse shaping, one can in fact *steer* a chemical reaction to yield a desired output. This kind of closed-loop quantum control (see section 2.4) has successfully been applied to control isomerisation reactions [13, 244–246], selective bond cleavage to yield desired photoproducts [14, 247–249] and recently selective bond formation [15, 250]. It has also been shown that complex molecular systems can be controlled, e.g. by controlling the energy flow in the antenna complex LH2 of purple bacteria [16]. Since decoherence, as well as coherence, is an important issue in quantum systems, decoherence dynamics have also been controlled [251]. Coherent control has also been used to elucidate the reaction mechanism of a complex rearrangement reaction [252]. More technical applications can also profit from closed-loop quantum control, as in the case of the generation of high-harmonic radiation [253]. Certainly, these examples can only give a partial overview regarding the wide range of applications of quantum control with shaped laser pulses. Many more interesting examples from different fields of research can be found in the literature. However, this small excerpt already stresses how important quantum control has become as a research tool.

The examples mentioned so far have one thing in common: In all of them, only the amplitude and/or phase of the laser pulses have been shaped and used as control parameters. Since the electric field is a vectorial quantity and light–matter interaction depends on this vectorial character, shaping the polarisation of the laser pulses adds an additional degree of freedom to quantum control. It has been shown that multiphoton ionisation of sodium dimers depends on the polarisation of the laser pulses since different transitions include various transition dipole moments. Shaping the polarisation has thus a stronger impact on the ionisation dynamics than phase-shaped linearly polarised laser pulses [254]. Similarly, the transient vector properties of light–matter interaction can be manipulated using polarisation-shaped pulses [255]. It is also possible to control optical near-fields in the vicinity of metallic nanostructures by means of polarisation pulse shaping [256, 257]. This allows one to extend the control possibilities to spatial ranges well below the diffraction limit of the excitation laser pulse.

Combining spectroscopic techniques with polarisation-shaped pulses also makes it possible to measure quantities that are not accessible using linearly polarised laser pulses. In CARS spectroscopy, polarisation-shaped pulses have been used to measure specific off-diagonal tensor elements of the dielectric susceptibility [258]. Using polarisation-shaped laser pulses in 2D spectroscopy has been proposed to enhance or suppress different signals in the 2D spectrum [259]. Thus, polarisation pulse shaping opens up a large variety of different applications in spectroscopy and coherent control.

However, most of the quoted experimental results were achieved using the shaped fundamental of a Ti:Sa laser around 800 nm. As a matter of fact, only a limited number of prospective molecular candidates exists which exhibit absorption bands in this spectral range. Many more interesting molecular systems exist which absorb in the visible spectral range, as was seen in the previous chapters. Hence, extending the existing pulse-shaping techniques to broadband visible laser pulses opens up new options, but it also poses new challenges. Most of the presented molecular compounds exhibit broad, unstructured absorption bands in the visible spectral range. Thus if one wants to study or even control the photophysics and photochemistry of such systems, it is mandatory to shape pulses in the visible. Ideally, the spectrum of the pulse covers the entire (or at least most of the) absorption band under investigation. In this way coherences between different electronic states can be excited which is important for spectroscopic techniques like 2D spectroscopy. In addition, the temporal resolution of any spectroscopic experiment can be increased if very short pulses, exhibiting very broadband spectra, are employed as a laser source. Thus, broadband visible polarisation-shaped laser pulses are a promising tool for spectroscopy and coherent control of a wide variety of different quantum systems.

Despite their potential, however, the challenges posed by broadband visible laser pulses should not be underestimated. Already the generation of such pulses is rather demanding. Although commercially available noncollinear optical parametric amplifiers (NOPAs) can generate pulses with fairly broad spectra in the visible, stretching the boundaries towards the generation of few-cycle pulses can only be done using homebuilt NOPAs up to now. Since they are no "turn-key" systems, the proper alignment must be done thoroughly and thus can be time-consuming. Once pulses with sufficiently large bandwidth are created, they have to be compressed to their minimum temporal duration. Again, this can be a demanding task since broadband visible pulses are prone to phase distortions. This originates in the progression of the wavelength-dependent refractive index. Its curvature is larger in the visible than in the near-IR spectral range, thus the additional phase the pulse gains when it traverses a transparent medium strongly effects the pulse shape. For very broadband pulses, even propagation through air can already distort the pulse shape. Thus, broadband visible laser pulses require a careful dispersion management.

The need to carefully characterise the pulses is closely related to the dispersion management. This in itself is a challenging task since many standard characterisation techniques only support a limited spectral bandwidth and can easily yield erroneous results if this bandwidth is exceeded. The characterisation of polarisation-shaped pulses is in general more demanding since

not only the amplitude and phase of the pulse have to be retrieved, but also the complete polarisation state.

In the following sections, these different aspects will be discussed, starting with the pulse-shaper setup in section 7.1. In section 7.2, the pulse-characterisation techniques that have been used in this thesis will be discussed, including frequency-resolved optical gating (FROG) and spectral interferometry (SI). Furthermore, a well-known SI evaluation method will be extended to the characterisation of polarisation-shaped pulses. Jones-calculus will be discussed in section 7.2.3 since it is most useful to describe the modifications to the polarisation state of a laser pulse. Results of pulse shaping and characterisation are presented in section 7.3. The chapter concludes with an outlook regarding possible applications of these polarisation-shaped laser pulses.

7.1 Pulse-shaper setup

The pulse shaper used in the framework of this thesis was designed to optimally meet the requirements for polarisation shaping of ultrabroadband visible laser pulses [260]. The setup of the pulse shaper is depicted schematically in figure 7.1. It is based on the principle of Fourier-transform pulse shaping that was introduced in section 2.5. The incident laser pulse is spectrally dispersed by a volume-phase holographic grating (1000 lines per millimeter, denoted VPHG in figure 7.1). It is then reflected by a folding mirror M1 under an angle such that it no longer travels parallel to the plane of the optical table but slightly upwards. Subsequently, the pulse is incident on the cylindrical mirror cylM (focal length f=25 cm) which collimates the beam and focusses each spectral component onto the liquid-crystal display 2x640SLM (a two-mask LCD with each mask comprising 640 pixels [261]). Between the cylindrical mirror and the SLM, the beam travels parallel to the optical table again. Thus a "z-shaped" kind of folding of the setup is achieved. This can be seen in figure 7.1 a) in a pseudo-3D view or in figure 7.1 b) which presents a side view of the setup. The zero-dispersion compressor of the pulse shaper is arranged in a folded geometry so that a symmetry mirror M2 is placed adjacent to the SLM. This facilitates the alignment of the pulse shaper setup. M2 is slightly tilted so that the outgoing beam passes the setup on a slightly different path, shifted only in height relative to the incident beam. This can be seen in figure 7.1 a) and b) where the path of the incident beam is sketched as a solid line while the path of the outgoing beam is depicted as a dashed line. In the top view of the setup as shown in figure 7.1 c), however, both paths cannot be distinguished since they are only offset in height and not in the lateral direction. During the second pass through the setup (that is, from M2 via cylM and M1 back to VPHG), the spectral components of the pulse are recombined. The shaped pulse can be picked off by the mirror MO and is subsequently sent to the experiment.

Since ultrabroadband laser pulses in the visible spectral range are prone to phase distortions due to material dispersion [260], only reflective optics have been used in the pulse shaper setup. The diffraction grating is the only exception. A transmissive volume-phase holographic (VPH) grating [262–266] was especially manufactured which exhibits a high and flat overall diffraction efficiency for s and p polarisation [260]. Thus it is ideally suited for broadband polarisation shaping.

Although the folded geometry makes the pulse shaper setup more compact and facilitates the alignment, it also introduces a minor drawback. Because of the "z-folding", the beam on the cylindrical mirror is not incident on the latter in a plane perpendicular to the axis of the cylinder, but under a small

angle to the axis. As a consequence, the distance between the grating and the cylindrical mirror has to be adjusted carefully to avoid a nonlinear spatial chirp in the focus of the beam leaving the pulse shaper. This chirp has been observed experimentally [267] and ray-tracing simulations confirmed that it originates in the z-shaped folding [268]. To minimise its influence, the angle of the "z" was chosen to be as small as possible within the experimental limitations. For the pulses presented in section 7.3, however, the influence of the spatial chirp is not critical since their bandwidths do not span the entire operation range for which the pulse shaper was designed. Nevertheless, for pulses with even broader spectra like in reference [267] this effect has to be taken into account.

To ensure reliable pulse shaping operation, the pulse shaper has to be calibrated carefully. First of all, the wavelengths of the spectrum of the input pulse have to be mapped to the SLM pixels. This mapping is referred to as "wavelength calibration". Second, the driving voltages of the SLM pixels have to be correlated with the phase which is introduced by applying this voltage. This "phase calibration" has to be carried out for both SLM masks independently. Details regarding the calibration procedure and the evaluation of the calibration raw data can be found in [25, 260, 267]. Since the pulse shaper is designed for shaping ultrabroadband laser pulses in the visible spectral range, generated in a parametric amplification process, the calibration should also be carried out with very broadband spectra. However, since it is rather difficult to obtain pulses that span the entire spectral range of the pulse shaper (500–750 nm), the calibration procedure can also be carried out by using only the white-light seed for the parametric process as a light source. In this way, the entire spectral range of the pulse shaper is covered and the quality of the calibration is strongly improved.

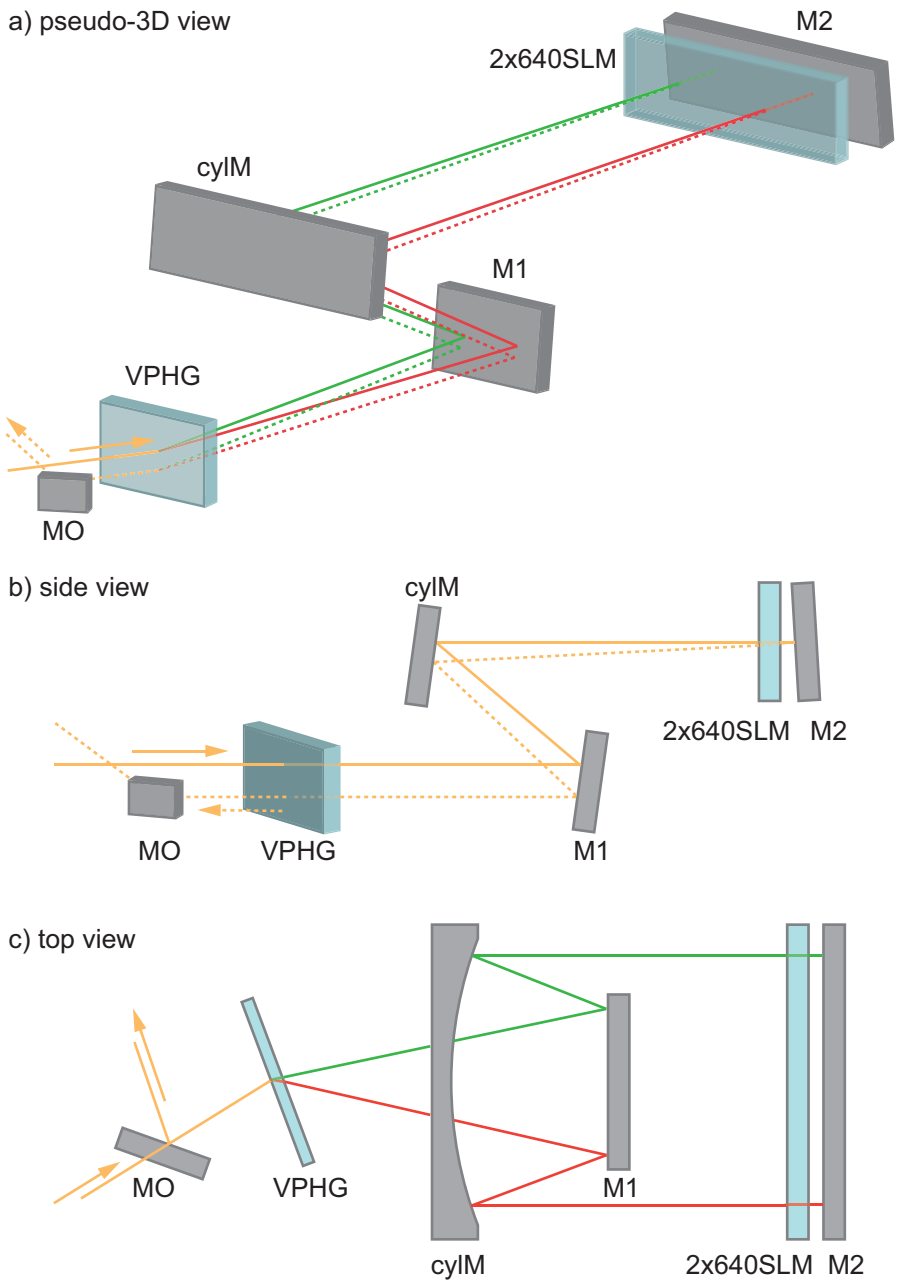

Figure 7.1: Pulse shaper setup in a pseudo-3D view (a)), side view (b)) and top view (c)). The incoming pulse is dispersed by the grating VPHG (1000 lines per mm) and traverses the folding mirror M1. The beam is then collimated and the single frequency components are focussed by the cylindrical mirror cylM (f =25 cm) onto the liquid-crystal array 2x640SLM (2 layers comprising each 640 pixels). The folding mirror M2 sends the shaped pulse back under a slightly different angle so that the shaped pulse can be coupled out by the mirror MO.

7.2 Pulse characterisation

In order to determine the shape of the amplitude-, phase- or polarisation-shaped pulses, thorough pulse characterisation is mandatory. To characterise a laser pulse completely, its amplitude and phase information have to be determined, either in the temporal or frequency domain. Hence, in the case of polarisation-shaped pulses, amplitude and phase have to be known for two linearly independent polarisations (see also section 2.1.3). Since the advent of femtosecond laser sources, pulse characterisation techniques have been developed and continously improved so that a plethora of different characterisation methods exists. The methods relevant for this thesis, namely frequency-resolved optical gating and spectral interferometry, will be introduced in the following sections. However, other approaches also exist, which are described elsewhere [238, 269–272].

7.2.1 Frequency-resolved optical gating

Frequency-resolved optical gating (FROG) is a self-referencing pulse characterisation technique that operates in the time–frequency domain [124, 273]. It is widely used and has successfully been applied to characterise pulses in different spectral ranges and of different complexity [274–279]. The idea of FROG is the following. The unknown laser pulse is gated by a time-delayed copy of itself and a time- and frequency resolved spectrogram, called the "FROG trace", is measured with the help of a nonlinear medium. Determining the complete electric field of the pulse (amplitude and phase) from the FROG trace is an example of a two-dimensional phase-retrieval problem [280]. The information about the pulse shape can be extracted using suitable pulse-retrieval algorithms [281–284].

Experimentally, one creates two time-delayed copies of the unknown laser pulse. Both are overlapped in a nonlinear medium. The resulting nonlinear signal is measured in a frequency-resolved way while the time delay between both pulse copies is scanned. Different nonlinear processes can be employed in a FROG measurement [276, 285–287]. However, the discussion here will be restricted to the generation of the second harmonic [123]. Both pulses are overlapped noncollinearly in a nonlinear crystal such as BBO and the resulting second harmonic radiation is detected. The FROG trace is then given by

$$I_{\mathrm{FROG}}^{\mathrm{SHG}}(\omega,\tau) \propto \left| \int_{-\infty}^{\infty} E(t) \cdot E(t-\tau) \cdot e^{-i\omega t} \mathrm{d}t \right|^2 , \tag{7.1}$$

where $E(t)$ is the complex electric field of the unknown pulse.

In many cases, an interferometer setup is used to create the pulse copies and to introduce the time delay between them. This kind of FROG setup was used to characterise the pump pulses for the high-repetition rate transient spectrometer of section 3.3.2. Details regarding that specific setup can be found in reference [288].

However, if a pulse shaper is available, the pulse shaper itself can act as an interferometer. With a suitable mask function [289], two copies of the pulse can be generated and the time delay between them can be varied. This has the advantage that no external FROG setup is necessary. The pulse can be characterised directly at the point of interaction in the experiment. The major difference in comparison with the external interferometer is that both pulse copies now are incident on the BBO in a collinear geometry as is depicted in figure 7.2. Thus, this technique is also referred to as collinear FROG or cFROG [290, 291]. This leads to a modified FROG trace compared to equation 7.1

$$I_{\mathrm{cFROG}}^{\mathrm{SHG}}(\omega,\tau) \propto \left| \int_{-\infty}^{\infty} \left(E(t) + E(t-\tau)\right)^2 \cdot e^{-i\omega t} \mathrm{d}t \right|^2 \quad . \tag{7.2}$$

The collinear geometry now leads to interference effects. When analysing equation 7.2, one can identify three contributions to the cFROG trace [290]. One is proportional to $E(t)^2$ and represents the unknown pulse interacting with itself. In analogy, also a contribution comprising the interaction of the delayed pulse with itself is present, which is proportional to $E(t-\tau)^2$. Finally, the third contribution contains the interaction of the unknown pulse with its time-delayed copy. It is proportional to $E(t)\cdot E(t-\tau)$, which is also the only contribution present in the SHG FROG trace given by equation 7.1.

A Fourier analysis of equation 7.2 is a useful way to extract the non-collinear FROG trace from the collinear one. A two-dimensional Fourier transform of equation 7.2 yields [290]

$$\begin{aligned} I_{\mathrm{cFROG}}^{\mathrm{SHG}}(\omega,\tau) \;&\propto\; 2I_{\mathrm{SHG}}(\omega) \\ &+\; 2I_{\mathrm{SHG}}(\omega)\cos((2\omega_0+\omega)\tau) \\ &+\; 4\Re\left(E_{\mathrm{SHG}}^{*}(\omega)E_{\mathrm{SHG}}^{\mathrm{FROG}}(\tau,\omega)\left(e^{-i\omega_0\tau} + e^{(\omega_0+\omega)\tau}\right)\right) \\ &+\; 4I_{\mathrm{SHG}}^{\mathrm{FROG}} \end{aligned} \tag{7.3}$$

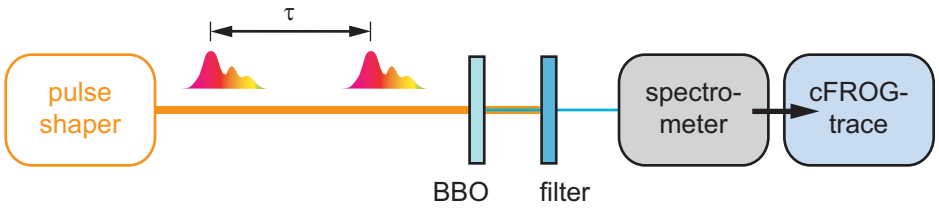

Figure 7.2: Schematic representation of a cFROG measurement. Two copies of the pulse are generated and time-delayed by the pulse shaper. They are incident on a nonlinear crystal such as BBO in a collinear geometry. The resulting second harmonic radiation is detected in a frequency-resolved way whilte the time delay between both pulses is scanned, yielding a cFROG trace. A filter is used to block the fundamental.

with

$$E_{\mathrm{SHG}}(\omega) \propto \int_{-\infty}^{\infty} E(t)^2\, e^{-i\omega t}\mathrm{d}t \tag{7.4}$$

and

$$E_{\mathrm{SHG}}^{\mathrm{FROG}}(\tau,\omega) \propto \int_{-\infty}^{\infty} E(t)E(t-\tau)\, e^{-i\omega t}\mathrm{d}t \quad . \tag{7.5}$$

The intensities are given by the absolute square of the fields,

$$I_{\mathrm{SHG}}(\omega) \propto |E_{\mathrm{SHG}}(\omega)|^2 \quad \text{and} \quad I_{\mathrm{SHG}}^{\mathrm{FROG}}(\omega) \propto \left|E_{\mathrm{SHG}}^{\mathrm{FROG}}(\omega)\right|^2 \quad . \tag{7.6}$$

The first term of equation 7.3 corresponds to the SHG of the unknown pulse and its delayed copy. It can be regarded as a constant intensity background. The second term represents the interference between both SHG pulses and is modulated at $2\omega_0$. The third term contains the interference between the SHG of the individual pulses and the SHG resulting from the field $E(t)E(t-\tau)$. Finally, the fourth term contains the SHG-FROG trace for the noncollinear case. Thus, by Fourier-filtering, back-transformation and subsequent background subtraction one can extract the well-known SHG-FROG trace from the cFROG trace. It can then be reconstructed by the standard algorithms and software for pulse retrieval.

There is another advantage inherent in cFROG. Although an interferometric signal is measured, one can greatly reduce data acquisition time by undersampling. This is possible since only the non-modulated contribution of the signal is used to retrieve the pulse shape [290]. However, two limitations

have to be considered which define the useful temporal step size for which the pulse can be retrieved. One constrain is given by the Nyquist limit. If one undersamples a signal in the delay-frequency domain, frequencies larger than the Nyquist frequency appear shifted to lower frequencies [292]. For a successful Fourier-filtering, these shifted frequencies have to be well separated from the DC component. Thus, the delay-step size has to be small enough to avoid an overlap of these contributions. On the other hand, a sufficiently large delay span has to be covered to ensure a reliable pulse retrieval. The first constrain can be met by choosing a step size of [290]

$$\Delta\tau = \frac{2\pi(n \pm 1/3)}{\omega_0} \tag{7.7}$$

where n is an integer. However, even this delay step may be insufficient to avoid overlap of the different contributions for very large undersampling. A practical upper limit for the step size is given by

$$\Delta\tau < \frac{\tau_{IA}}{10} \tag{7.8}$$

in which τ_{IA} is defined as the full width at 15% of the interferometric autocorrelation trace of the pulse. This means that more than 10 points have to be sampled in the trace envelope. The required delay span τ_{span} is given by

$$\tau_{\text{span}} \geq 2\tau_{IA}. \tag{7.9}$$

Thus, a minimum of 20 samples has to be recorded to retrieve the pulse shape. However, the actual delay step has to be adapted to the complexity of the unknown pulse. For simple pulse shapes, a rather large undersampling is feasible while for more complex pulse shapes the step size has to be decreased to ensure an accurate retrieval of the pulse. Some results of cFROG measurements will be given in section 7.3.

Although SHG FROG is a very versatile pulse characterisation technique and has been applied to characterise ultrashort laser pulses in different wavelength ranges [275, 293–295], one fundamental limitation exists. Its applicability is limited by the phase-matching bandwidth of the nonlinear medium which is used to generate the second harmonic radiation. As already discussed in section 2.2, perfect phase matching in a nonlinear crystal like β-barium borate (BBO) can only be achieved for one certain wavelength. If the pulse spans a broad wavelength range, the conversion efficiency for second-harmonic generation will strongly depend on the wavelength. For pulses

with narrowband spectra, this dependence is negligible. For very broadband spectra, however, it has a strong impact on the shape of the second-harmonic spectrum. This effect is known as spectral filtering [275, 293]. For an SHG FROG measurement this means that the measured FROG trace might be strongly distorted, yielding an erroneous pulse shape in the reconstruction. Nevertheless, it is possible—at least to some extent—to correct for the strongly wavelength-dependent conversion efficiency. The measured FROG trace $I_{\mathrm{meas}}(\Omega,\tau)$ is written as the product of the ideal FROG trace $I^{\mathrm{SHG}}_{\mathrm{FROG}}(\Omega,\tau)$ and a spectral filter function $R(\Omega)$ [275]

$$I_{\mathrm{meas}}(\Omega,\tau) \propto R(\Omega) I^{\mathrm{SHG}}_{\mathrm{FROG}}(\Omega,\tau) \tag{7.10}$$

where Ω is the frequency of the second-harmonic radiation and $I^{\mathrm{SHG}}_{\mathrm{FROG}}$ is the frequency-space description of the SHG FROG trace, equivalent to the time-domain description of equation 7.1

$$I^{\mathrm{SHG}}_{\mathrm{FROG}}(\Omega,\tau) \propto \left| \int_{-\infty}^{\infty} E(\omega) E(\Omega-\omega)\, e^{-i\omega\tau} \mathrm{d}\omega \right|^2 \quad . \tag{7.11}$$

The spectral filter function for type-I phase matching is given by

$$\begin{aligned} R(\Omega) &= Q(\Omega) \frac{\Omega^2}{n_e(\Omega)} \Big(\left(n_e^2(\Omega)-1\right) \left(n_o^2(\Omega/2)-1\right) \Big)^2 \\ &\cdot \quad \mathrm{sinc}^2 \frac{\Delta k(\Omega/2) L}{2} \quad , \end{aligned} \tag{7.12}$$

where $Q(\Omega)$ is the spectral sensitivity of the detector, n_o and n_e are the ordinary and extraordinary index of refraction of the nonlinear crystal and Δk is the wave vector mismatch which reads [294]

$$\begin{aligned} \Delta k(\Omega/2) &= 2k(\Omega/2) - k(\Omega) \\ &= \frac{\Omega}{c_0} \left(n_0(\Omega/2) - n_e(\Omega,\theta) \right) \end{aligned} \tag{7.13}$$

with the phase-matching angle θ. This correction has successfully been applied to correct for the spectral filtering in the measurement of few-cycle laser pulses [275, 293]. However, it can no longer be applied in practice if the conversion efficiency is too close to zero so that no signal can be detected. For the pulses presented later in this chapter, the phase-matching bandwidth of the BBO (thickness 10 µm) did suffice so that no severe distortions of the FROG trace were present. If one increases the spectral width of the pulses even further, e.g. by using the home-built NOPA [25] as a laser source, the

limited phase-matching bandwidth will have a strong impact on the SHG FROG measurement. However, it is possible to characterise pulses that span several hundreds of nanometers [275, 293, 295], but these pulses have the advantage that their central wavelength is located in the near-IR rather than in the visible spectral range. Since the dependence of the refractive index on the wavelength is much more pronounced in the visible than in the near-IR, this will strongly affect the shape of the filter function $R(\Omega)$, leading to an effective narrowing of its width. Thus the characterisation of ultrabroadband laser pulses in the visible spectral range is much more challenging than in the near-IR.

Different approaches exist that might help to overcome this limitation. One could use an even thinner BBO crystal (less than 10 µm) since the phase-matching bandwidth increases with decreasing crystal thickness. However, such crystals are complicated to manufacture and not easily available. They also have the drawback that the signal magnitude decreases with decreasing crystal thickness. This might be a clear disadvantage for strongly chirped pulses that have a low peak intensity and yield only a low SHG signal. As an alternative, other nonlinear crystals exist that exhibit a broader phase-matching bandwidth than BBO [296–298]. Since these crystals have only recently been developed, they are not yet commercially available and have not been put to use in pulse characterisation. Nevertheless, they are promising candidates in the characterisation of ultrabroadband laser pulses, especially in the visible spectral range.

7.2.2 Spectral interferometry

Spectral interferometry (SI) is another widely used characterisation technique for femtosecond laser pulses. The idea behind SI, however, strongly differs from that of the self-referencing FROG technique. The phase of the unknown pulse is retrieved from the interference of the unknown pulse with an known reference pulse [17, 299]. The phase of the unknown pulse is contained in the resulting spectral fringe pattern while the amplitude can easily be obtained by measuring the spectrum of the unknown pulse independently. Two different alternatives regarding the data evaluation and the necessary experimental setup will be discussed later in this section.

At first glance, SI has the drawback that it requires a well-characterised reference pulse which has to overlap spectrally with the unknown pulse. However, this requirement can usually be met. The advantage of SI becomes apparent for the characterisation of polarisation-shaped laser pulses. To fully characterise a polarisation-shaped pulse, one has to retrieve the amplitude and phase for two linearly-independent linear polarisations (see

section 2.1.3). FROG measurements are not well-suited for this task because of the polarisation dependence of the nonlinear process which is employed. In an SHG FROG with type-I phasematching, for example, only the p-component of the laser pulse can be frequency-doubled while no information on the s-component is available. One could, in principle, perform two measurements and rotate the nonlinear crystal so that frequency-doubling of the s-component is possible in the second measurement. This results, however, in a rather intricate measurement procedure. It also introduces other disadvantages like the necessity to measure the relative phase between both components separately. Thus, FROG cannot easily be adapted to measure polarisation-shaped laser pulses.

In contrast to FROG, SI can be easily adapted for polarisation-shaped pulses. Combining SI with polarisation multiplexing results in a measurement technique that allows to measure both polarisation components simultaneously. Typically, one uses the s- and p-component of the shaped laser pulse for this task. The only requirement in this case is that the reference pulse needs to comprise both polarisation components that are to be measured. This can easily be achieved, e.g. by rotating it to be linearly polarised at an angle of 45°, so that it has equal projections on the s- and p-component of the unknown pulse. This variant of SI for polarisation-shaped pulses is also referred to as POLLIWOG [300]. Details regarding the data acquisition and evaluation will be given in the following sections.

Some other advantages of SI will be mentioned before. First, it is possible to characterise very weak pulses. In contrast to FROG, which involves at least a $\chi^{(2)}$-nonlinearity, the sensitivity of SI is much higher since it is a linear technique. Second, it is also suited to measure nearly transform-limited pulses as well as very complex ones. No modifications to the setup are necessary as long as the interference fringes can still be resolved properly. Third, it offers the possibility of real-time characterisation. Since no iterative pulse-retrieval algorithms are needed in the data evaluation, SI can also be used as a single-shot pulse-characterisation technique.

Fourier-transform spectral interferometry

In Fourier-transform spectral interferometry (FTSI), the phase information is extracted form the interference-fringe pattern by a Fourier-transform method [17]. Here, only the POLLIWOG variant of FTSI [300] will be presented since only polarisation-shaped pulses are considered in this section. The setup used for the data acquisition is depicted in figure 7.3 a). The incoming pulse is incident on a beam splitter, where a small fraction is split off to serve as the reference pulse. The major fraction traverses the pulse shaper which modifies

the polarisation state of the pulse (indicated by the ellipse). In the reference arm of the interferometer, a polariser ensures that the reference pulse is polarised linearly along the x-direction. The reference and shaped pulse are then overlapped collinearly at a second beam splitter which leads to spectral interference between them. The polarisation of both pulses is then rotated by a half-wave plate (HWP) by 45°. A Glan–Taylor prism (GT) then splits the combined shaped and reference pulse into their x- and y-components which are dispersed on different regions of the CCD chip of the detector. Both components are offset in height as can be seen in the inset in figure 7.3 a) that depicts a side view of the beam path from the Glan–Taylor prism to the spectrometer.

To describe the interference signal mathematically, the pulse-shaper axes are used as a reference frame. That means that the electric-field vectors are not given in the x–y-coordinate system but rather in one rotated by 45° relative to this since the active axes of the LCD masks are oriented at +45° and -45° relative to the x-direction. These axes will be referred to as directions 1 and 2, respectively. The electric field of the shaped pulse then reads

$$\begin{aligned} \vec{E}_s(\omega) &= \begin{pmatrix} E_{s,1}(\omega) \\ E_{s,2}(\omega) \end{pmatrix} \\ &= \begin{pmatrix} A_{s,1}(\omega) \cdot e^{-i\phi_{s,1}(\omega)} \\ A_{s,2}(\omega) \cdot e^{-i\phi_{s,2}(\omega)} \end{pmatrix} . \end{aligned} \tag{7.14}$$

Accordingly, the reference pulse is defined as

$$\begin{aligned} \vec{E}_r(\omega) &= \begin{pmatrix} E_{r,1}(\omega) \\ E_{r,2}(\omega) \end{pmatrix} \\ &= \begin{pmatrix} A_{r,1}(\omega) \cdot e^{-i\phi_{r,1}(\omega)} \\ A_{r,2}(\omega) \cdot e^{-i\phi_{r,2}(\omega)} \end{pmatrix} . \end{aligned} \tag{7.15}$$

The interference between the shaped and reference pulse can then be calculated via

$$\begin{aligned} I_{\mathrm{SI},i}(\omega) &= \left| E_{s,i}(\omega) + E_{r,i}(\omega)\, e^{-i\omega\tau} \right|^2 \\ &= A_{s,i}(\omega)^2 + A_{r,i}(\omega)^2 \\ &+ 2A_{s,i}(\omega)A_{r,i}(\omega) \cos\left(\phi_{s,i}(\omega) - \phi_{r,i}(\omega) - \omega\tau\right) \end{aligned} \tag{7.16}$$

where $i = 1, 2$. The linear phase $\omega\tau$ corresponds to the temporal delay τ between the shaped and reference pulse, which is introduced by time-delaying

the reference pulse in the interferometer setup shown in figure 7.3. From equation 7.16 it is apparent that the interference spectra are sensitive to the phase difference between both pulses. The phase information is contained in the oscillating term of equation 7.16

$$S_i(\omega) = 2A_{s,i}(\omega)A_{r,i}(\omega)\cos\left(\phi_{s,i}(\omega) - \phi_{r,i}(\omega) - \omega\tau\right) \quad . \tag{7.17}$$

In principle, one could extract the phase by inversion of the cosine-function. However, this is not favourable since it may result in large phase errors in those regions where the cosine adopts a value close to one [17]. One can overcome this problem by making use of the Fourier-transform of $S(\omega)$. To do so, equation 7.17 is rewritten as

$$S_i(\omega) = E^*_{s,i}E_{r,i}\,e^{-i\omega\tau} + E_{s,i}E^*_{r,i}\,e^{i\omega\tau} \quad . \tag{7.18}$$

Carrying out the Fourier-transform then yields

$$\begin{aligned} S_i(t) &= \frac{1}{\sqrt{2\pi}}\int_{-\infty}^{\infty} S_i(\omega)\,e^{i\omega t}\mathrm{d}\omega \\ &= \frac{1}{\sqrt{2\pi}}\int_{-\infty}^{\infty} E^*_{s,i}(\omega)E_{r,i}(\omega)\,e^{i\omega(t-\tau)}\mathrm{d}\omega \\ &+ \left(\frac{1}{\sqrt{2\pi}}\int_{-\infty}^{\infty} E_{s,i}(\omega)E^*_{r,i}(\omega)\,e^{i\omega(-t-\tau)}\mathrm{d}\omega\right)^* \\ &= s_i(t-\tau) + s_i^*(-t-\tau) \end{aligned} \tag{7.19}$$

with

$$s_i(t) = \frac{1}{\sqrt{2\pi}}\int_{-\infty}^{\infty} E^*_{s,i}(\omega)E_{r,i}(\omega)\,e^{i\omega t}\mathrm{d}\omega \quad . \tag{7.20}$$

Since $S_i(\omega)$ is a real quantity, it suffices to retain only the positive-delay contribution of $S_i(t)$. To be able to separate both contributions, the delay τ has to be sufficiently large, that is, the reference and the shaped pulse must not overlap temporally, which poses a severe limitation to the pulse shapes that can be characterised with this method. For the case in which shaped and reference pulse are temporally well separated, one can define

$$S_i^+(t) = s_i(t-\tau) \tag{7.21}$$

which is the contribution that is subsequently transformed back to the spectral domain. As a result, one obtains

$$\begin{aligned} S_i^+(\omega) &= \frac{1}{\sqrt{2\pi}} \int_{-\infty}^{\infty} s_i(t-\tau)\, e^{-i\omega t} \mathrm{d}t \\ &= E_{s,i}^*(\omega) E_{r,i}(\omega)\, e^{-i\omega\tau} \\ &= A_{s,i}(\omega) A_{r,i}(\omega)\, e^{i(\phi_{s,i}(\omega)-\phi_{r,i}(\omega)-\omega\tau)} \quad . \end{aligned} \tag{7.22}$$

The phase information is now contained in the argument of $S_i^+(\omega)$. Taking the argument is less prone to the influence of noise than the inversion of the cosine function. Thus one can obtain the phase via

$$\phi_{s,i}(\omega) - \phi_{r,i}(\omega) - \omega\tau = \arg S_i^+(\omega) \quad . \tag{7.23}$$

Since the phase of the reference pulse is known, one can now easily extract the phase of the shaped pulse by adding the reference phase and the linear phase that corresponds to the known time delay τ. However, some limitations to this Fourier-transform method exist which result from the fringe spacing. This spacing can be approximated by

$$\Delta\omega \approx \frac{2\pi}{\tau + \tau_p} \tag{7.24}$$

where τ is the temporal separation between both pulses and τ_p is the pulse duration. This approximation ensures that the interference fringes can be resolved not only within the spectral FWHM of the pulse but in the entire spectrum, including the flanks with low spectral intensity. On the one hand, τ has to be large enough so that $s(t-\tau)$ can be separated from its counterpart at $-t-\tau$. On the other hand, the interference fringes still have to be resolved properly. Since the fringe spacing becomes smaller if $\tau + \tau_p$ is increased, neither the pulse duration nor the temporal delay between both pulses must become too large. However, it is usually possible to find a compromise that allows one to fulfill both conditions so that the vast majority of pulse shapes can be characterised using FTSI.

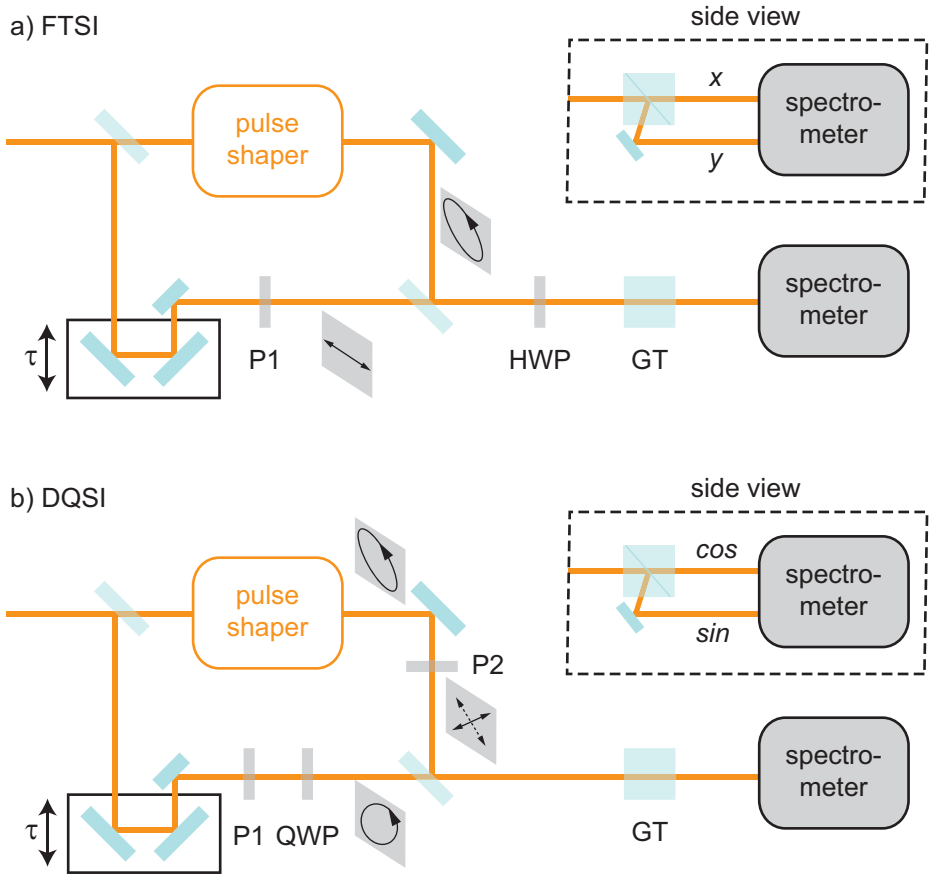

Figure 7.3: Setup for spectral interferometry. In figure a) the data acquisition for FTSI is shown. A linearly-polarised reference pulse interferes with the polarisation-shaped pulse. The polarisation state of the interfering pulses is rotated by 45° via a half-wave plate HWP. A Glan–Taylor prism GT is used for polarisation multiplexing, so that the polarisation components corresponding to both LCD masks are dispersed onto different region of the spectrometer's CCD chip (see inset). Figure b) depicts the setup used for DQSI. In this case, a circularly-polarised reference pulse, achieved with the help of linear polariser P1 and the quarterwaveplate QWP, is overlapped with only one polarisation of the shaped pulse. The projection of the shaped pulse onto one polarisation is selected by a linear polariser P2 in the beam path of the shaped pulse. The Glan–Taylor prism now separates the in-phase- from the quadrature-component of the interference signal. To measure the complete polarisation state of the shaped pulse, the measurement is repeated for the second projection of the polarisation. For both SI methods, wedge plate pairs are used as beamsplitters.

Dual-quadrature spectral interferometry

As was discussed in the previous section, it is advantageous to extract the phase of the unknown pulse from the argument of $S^+(\omega)$ rather than from the cosine-function. Dual-quadrature spectral interferometry (DQSI) is another approach to gain access to the argument without the need of Fourier-transforms. Instead, the experimental setup is slightly modified so that not only the in-phase component (the cosine of the phase difference) is measured, but also the quadrature component, which corresponds to the sine of the phase difference. This is achieved by overlapping the *linearly* polarised unknown pulse with a circularly polarised reference pulse. Polarisation multiplexing then splits the interference signal into its cosine- and sine-components [17]. The generalisation for arbitrarily polarised pulses will be discussed later in this section.

Since polarisation multiplexing is usually employed to separate the x- and y-components of the polarisation, the unknown pulse has to be polarised linearly along 45° or −45° relative to x (that is, along the directions 1 or 2 or rather the pulse-shaper axes defined earlier in this section). It is important to point out that the description of the laser pulses is now carried out in the laboratory x–y-frame in contrast to FTSI, where the pulse-shaper 1–2-frame is used. Thus, the unknown pulse in the laboratory frame is given by

$$\begin{aligned} \vec{E}_s(\omega) &= \begin{pmatrix} E_{s,x}(\omega) \\ E_{s,y}(\omega) \end{pmatrix} \\ &= \begin{pmatrix} A_{s,x}(\omega) \cdot e^{-i\phi_s(\omega)} \\ A_{s,y}(\omega) \cdot e^{-i\phi_s(\omega)} \end{pmatrix} . \end{aligned} \tag{7.25}$$

Ideally, if the pulse is perfectly linearly polarised along 45° or −45° relative to x, both amplitudes should have an equal magnitude, *i.e.* $A_{s,x}(\omega) = A_{s,y}(\omega)$. However, slight deviations are possible due to the polarisation-dependent reflectivity of different optics and the polarisation-dependent efficiency of the spectrometer. These issues will be discussed in more detail in section 7.3. The circularly-polarised reference pulse is defined accordingly

$$\begin{aligned} \vec{E}_r(\omega) &= \begin{pmatrix} E_{r,x}(\omega) \\ E_{r,y}(\omega) \end{pmatrix} \\ &= \begin{pmatrix} A_{r,x}(\omega) \cdot e^{-i\phi_r(\omega)} \\ A_{r,y}(\omega) \cdot e^{-i(\phi_r(\omega)+\pi/2)} \end{pmatrix} . \end{aligned} \tag{7.26}$$

Again, the difference in the amplitudes $A_{r,x}$ and $A_{r,y}$ results from the already mentioned polarisation dependence. The interference term for the

x-component is then given by

$$\begin{aligned} I_{\mathrm{SI},x}(\omega) &= |E_{s,x}(\omega) + E_{r,x}(\omega)|^2 \\ &= A_{s,x}(\omega)^2 + A_{r,x}(\omega)^2 \\ &+ 2A_{s,x}(\omega)A_{r,x}(\omega)\cos\left(\phi_s(\omega) - \phi_r(\omega)\right) \quad , \end{aligned} \tag{7.27}$$

which is the well-known interference term as it is used in FTSI. In this in-phase component, the cosine of the phase difference is contained. For the y-component, however, the additional shift of the reference phase by $\pi/2$ results in the quadrature term, which contains the sine of the phase difference

$$\begin{aligned} I_{\mathrm{SI},y}(\omega) &= |E_{s,y}(\omega) + E_{r,y}(\omega)|^2 \\ &= A_{s,y}(\omega)^2 + A_{r,y}(\omega)^2 \\ &+ 2A_{s,y}(\omega)A_{r,y}(\omega)\sin\left(\phi_s(\omega) - \phi_r(\omega)\right) \quad . \end{aligned} \tag{7.28}$$

So far, in all considerations regarding DQSI, the linear phase $\omega\tau$ which corresponds to the time delay between both pulses, is included in the phase of the reference pulse. This is legitimate since in DQSI the restrictions regarding the time delay between both pulses are not as strict as for FTSI, as will be shown later. To extract the phase, one only needs the oscillating contributions of equations 7.27 and 7.28. Thus one has to subtract the single spectra and divide by the corresponding amplitudes, yielding only the cosine- and sine-contributions. The phase can then be calculated via

$$\phi_s(\omega) - \phi_r(\omega) = \arg\left(e^{i(\phi_s(\omega)-\phi_r(\omega))}\right) \quad , \tag{7.29}$$

with

$$e^{i(\phi_s(\omega)-\phi_r(\omega))} = \cos\left(\phi_s(\omega) - \phi_r(\omega)\right) + i\sin\left(\phi_s(\omega) - \phi_r(\omega)\right) \quad . \tag{7.30}$$

After doing so, only the reference phase has to be subtracted to end up with the desired phase $\phi_s(\omega)$ of the unknown pulse.

So far, only linearly polarised unknown pulses have been considered for the DQSI pulse characterisation. The question therefore is: How can one extend DQSI for the characterisation of polarisation-shaped pulses? In this thesis, a relatively simple approach has been chosen. The polarisation components corresponding to the 45°- and −45°-orientation relative to x are measured consecutively. In figure 7.3 b) the setup used for the pulse characterisation via DQSI is depicted. It is basically the same setup as for FTSI with some slight modifications. Again, a small fraction of the beam is split off before the pulse shaper to serve as the reference pulse. To ensure that it is circularly polarised, a linear polariser P1 and a broadband quarter-wave

plate QWP are placed in the reference arm. After traversing those optical elements, the reference pulse exhibits a circular polarisation as indicated by the circle. As before, the pulse shaper creates an arbitrary polarisation state as indicated by the ellipse. Before both pulses are recombined at the second beamsplitter, a second linear polariser P2 is placed in the beam path of the shaped pulse. It is aligned such that only the 45°- or the −45°-component is transmitted. Since the Glan–Taylor prism GT splits the incoming light field into its x- and y-components, the half-wave plate in front of the spectrometer can be omitted. Either projection of the shaped pulse has approximately an equal amount of amplitude in both of these components so that no further rotation of the polarisation state is required. Here, the Glan–Taylor prism is used to decompose the SI signal into its in-phase and quadrature contributions as given by equations 7.27 and 7.28.

Since the Glan–Taylor prism cannot be used for polarisation multiplexing as in the case of FTSI, both polarisation components (45° and −45°) have to be measured consecutively. The polariser P2 has to be realigned between both measurements so that either component is transmitted. This necessitates an additional measurement to determine the relative phase between both polarisation components. The first two measurements yield the 45°- and −45°-components of the unknown pulse, thus it can be written (in the pulse shaper 1–2-frame)

$$\begin{aligned} \vec{E}_s(\omega) &= \begin{pmatrix} E_{s,1}(\omega) \\ E_{s,2}(\omega) \end{pmatrix} \\ &= \begin{pmatrix} A_{s,1}(\omega) \cdot e^{-i(\phi_{s,1}(\omega)+\delta)} \\ A_{s,2}(\omega) \cdot e^{-i\phi_{s,2}(\omega)} \end{pmatrix} \quad , \end{aligned} \tag{7.31}$$

where the relative phase δ has to be determined in the third measurement. In order to do so, the spectrum of the shaped pulse is measured with polariser P2 aligned at a different angle than in the two measurements before, e.g. so that only the x-component is transmitted. The measured spectrum is then given by the interference between the projections of $E_{s,1}(\omega)$ and $E_{s,2}(\omega)$ onto the x-direction:

$$\begin{aligned} I_{SI}^{\mathrm{rel}}(\omega) &= \left| \tilde{A}_{s,1}(\omega)\, e^{-i(\phi_{s,1}(\omega)+\delta)} + \tilde{A}_{s,2}(\omega)\, e^{-i\phi_{s,2}(\omega)} \right|^2 \\ &= \tilde{A}_{s,1}(\omega)^2 + \tilde{A}_{s,2}(\omega)^2 \\ &+ 2\tilde{A}_{s,1}(\omega)\tilde{A}_{s,2}(\omega) \cos\left(\phi_{s,1}(\omega) + \delta - \phi_{s,2}(\omega)\right) \quad . \end{aligned} \tag{7.32}$$

The amplitudes $\tilde{A}_{s,1}(\omega)$ and $\tilde{A}_{s,2}(\omega)$ are simply the projections of $A_{s,1}(\omega)$ and $A_{s,2}(\omega)$ onto x, respectively,

$$\tilde{A}_{s,1}(\omega) = A_{s,1}(\omega) \cos\left(\pi/4\right) \tag{7.33}$$

and

$$\tilde{A}_{s,2}(\omega) = A_{s,2}(\omega)\cos(-\pi/4) \quad . \tag{7.34}$$

To improve the reliablility of this phase determination, the SI spectrum which contains information about the relative phase can be measured for different orientations of the polariser, thus yielding a kind of "tomographic" phase retrieval. For the example pulse shapes presented later in this chapter, the determination of the relative phase was restricted to two projections, the x-direction as given in equation 7.32 as well as the y-direction. Both resulting cosine terms are then fitted simultaneously to yield the relative phase. Since the single phases $\phi_{s,i}(\omega)$ and the amplitudes $A_{s,i}(\omega)$ are known, the cosine terms are fitted with δ as the only fitting parameter, thus yielding the relative phase. Results of this procedure will be presented in section 7.3.

7.2.3 Jones-matrix calculus

The reflection and transmission properties of optical elements strongly depend on the polarisation of the incident electric field. Hence, every optical element after the output of the pulse shaper changes the polarisation state of the laser pulse. In addition, already the optical elements before and within the pulse-shaper setup have a great impact on the polarisation state, giving rise to unwanted side effects and distortions of the polarisation state in addition to the desired polarisation state modification introduced by the SLM itself. These unwanted effects can be modelled theoretically within the framework of Jones-matrix calculus and can even be determined experimentally. The following section is dedicated to the introduction of the necessary theoretical framework of Jones calculus.

As was seen in the sections before, it is often very useful to describe the electric field of an arbitrarily polarised laser pulse with the help of a two-component vector. Thus, the transfer function of any linear optical element can be written as a two-by-two matrix, called the Jones-matrix $J(\omega)$ [301]. The single components $J_{ij}(\omega)$ are complex and frequency-dependent. The resulting electric field $\vec{E}_{\mathrm{out}}(\omega)$ is related to the incident electric field $\vec{E}_{\mathrm{in}}(\omega)$ via $J(\omega)$:

$$\vec{E}_{\mathrm{out}}(\omega) = J(\omega)\vec{E}_{\mathrm{in}}(\omega) \quad , \tag{7.35}$$

or written component-wise

$$\begin{pmatrix} E_{\mathrm{out},1}(\omega) \\ E_{\mathrm{out},2}(\omega) \end{pmatrix} = \begin{pmatrix} J_{11}(\omega) & J_{12}(\omega) \\ J_{21}(\omega) & J_{22}(\omega) \end{pmatrix} \begin{pmatrix} E_{\mathrm{in},1}(\omega) \\ E_{\mathrm{in},2}(\omega) \end{pmatrix} \quad . \tag{7.36}$$

This is a simple way to take the modifications of the polarisation state of the pulse by optical elements into account. The reflection and transmission efficiencies are contained in the diagonal components of $J(\omega)$, while the off-diagonal entries contain the mixing between both polarisation components which leads to further modification of the polarisation state. However, it can be difficult to predict the influence on the polarisation state using equation 7.36, since the frequency-dependent refractive indices as well as the precise orientations of all optical elements involved have to be known. Therefore it has proven useful to measure the Jones-matrix of a pulse-shaper setup rather than calculating it [19]. In principle, one compares a series of target pulse shapes comprising different polarisation states, defined by the applied phases at both SLM layers, to the actual measured polarisation states of the pulses.

To determine the Jones matrix, equation 7.35 is rewritten as

$$\vec{E}_{\mathrm{out}}(\omega) = J^2(\omega) J^{PS}(\omega) J^1(\omega) \vec{E}_{\mathrm{in}}(\omega) \quad , \tag{7.37}$$

where the influence of all optical elements between the first beam splitter and the SLM are contained in $J^1(\omega)$:

$$J^1(\omega) = \begin{pmatrix} J^1_{11}(\omega) & J^1_{12}(\omega) \\ J^1_{21}(\omega) & J^1_{22}(\omega) \end{pmatrix} \tag{7.38}$$

and the phase modulation $\phi_1(\omega)$ and $\phi_2(\omega)$ introduced by both SLM layers are contained in $J^{PS}(\omega)$:

$$J^{PS}(\omega) = \begin{pmatrix} e^{-i\phi_1(\omega)} & 0 \\ 0 & e^{-i\phi_2(\omega)} \end{pmatrix} \quad . \tag{7.39}$$

Finally, $J^2(\omega)$ contains the influence of all optical elements between the SLM and the experiment. In the case of SI, the interference between the shaped and reference pulse takes place at the second beamsplitter, so that all optical elements up to the second beamsplitter are included:

$$J^2(\omega) = \begin{pmatrix} J^2_{11}(\omega) & J^2_{12}(\omega) \\ J^2_{21}(\omega) & J^2_{22}(\omega) \end{pmatrix} \quad . \tag{7.40}$$

Carrying out the matrix multiplication in equation 7.37 explicitly and rearranging the equation yields

$$\begin{pmatrix} E_{\mathrm{out},1}(\omega) \\ E_{\mathrm{out},2}(\omega) \end{pmatrix} = \begin{pmatrix} a_{11} & a_{12} \\ a_{21} & a_{22} \end{pmatrix} \begin{pmatrix} e^{-i\phi_1(\omega)} \\ e^{-i\phi_2(\omega)} \end{pmatrix} \tag{7.41}$$

with the coefficients a_{ij}

$$\begin{aligned} a_{11} &= J_{11}^2 \left(J_{11}^1 E_{\mathrm{in},1} + J_{12}^1 E_{\mathrm{in},2} \right) \\ a_{12} &= J_{12}^2 \left(J_{21}^1 E_{\mathrm{in},1} + J_{22}^1 E_{\mathrm{in},2} \right) \\ a_{21} &= J_{21}^2 \left(J_{11}^1 E_{\mathrm{in},1} + J_{12}^1 E_{\mathrm{in},2} \right) \\ a_{22} &= J_{22}^2 \left(J_{21}^1 E_{\mathrm{in},1} + J_{22}^1 E_{\mathrm{in},2} \right) \quad . \end{aligned} \tag{7.42}$$

Here, the frequency dependence has been omitted for clarity. The action of the only active element in the pulse-shaper setup, the SLM, is now contained in the vector on the right-hand side of equation 7.41. All passive optical elements are contained in the matrix given by the coefficients a_{ij}. This matrix is identical for all possible pulse shapes. Strictly speaking, it is not the Jones-matrix since it is still containing the amplitudes of the incident laser pulse. They have to be factored out to finally yield the Jones-matrix. However, this matrix suffices to determine the influence of the setup on the polarisation state of the laser pulse, and it will be referred to as the experimentally determined Jones-matrix of the setup. Since the coefficients a_{ij} are complex, a set of four linear equations is necessary to describe one pulse shape. Measuring a sufficient number of different pulse shapes, the matrix coefficients results from the solution of an overdetermined system of linear equations. A detailed description of this procedure can be found in reference [302].

Using this procedure, the Jones-matrix of the pulse-shaper setup has been determined, the results can be found in section 7.3.4. With this matrix it is now possible to predict the influence of the optical elements in the setup on any given pulse shape for pulses which exhibit the same incoming spectral shape as those used for the Jones-matrix determination.

7.3 Generation and characterisation of polarisation-shaped laser pulses

In this section, example pulse shapes will be presented that were generated using the pulse-shaper setup of section 7.1. They span a spectral range of roughly 600 nm to 680 nm. The pulses were characterised with FT- as well as DQSI and compared to the pulse shapes predicted by the measured Jones matrix. An accuracy criterion for the pulse retrieval will be defined that allows one to quantify the quality of the pulse measurement.

7.3.1 Pulse compression

The broadband visible laser pulses, which are used as input pulses for the pulse shaper, are generated in a commercially available noncollinear optical parametric amplifier (*TOPAS white* [111]). The fundamental 800 nm-radiation from a Ti:Sa amplifier system (*Spectra Solstice* [110]) is used to generate a supercontinuum, which acts a seed for the amplification, as well as—after frequency doubling—to pump the amplification process (see also sections 2.2.3 and 3.3.1). Depending on the *TOPAS* settings, the generated pulses can span different ranges of the visible and near-IR spectral range. They were chosen to span a broad range around 630 nm, since this is approximately the wavelength which is incident on the central pixel of the pulse shaper's SLM.

In the *TOPAS* setup, the pulses can be compressed to a certain degree by the use of two glass wedges. However, the minimum time-bandwidth product can usually not be achieved by this compression only. Thus, the pulses which are later polarisation-shaped have to be compressed to their minimum duration with the help of the pulse shaper. This is done by measuring the cFROG-trace of the uncompressed pulse as described in section 7.2.1. The spectral phase which is retrieved form this measurement is inverted and applied by the pulse shaper as an additional offset. This procedure can be iterated several times until the pulse is sufficiently well compressed.

In figure 7.4 the result of the cFROG measurement of the uncompressed pulse is shown. While figure 7.4 a) shows the FROG-trace which is extracted from the oscillating cFROG trace (not shown), the reconstructed FROG trace can be seen in figure 7.4 b), whereas the reconstructed spectrum and spectral phase are presented in figure 7.4 c). The spectral bandwidth coincides very well with the measured spectrum and the spectral phase is clearly non-zero. This is also reflected in a rather complex temporal pulse shape as can be seen in figure 7.4 d). The pulse shape exhibits pre- and post-pulses and the

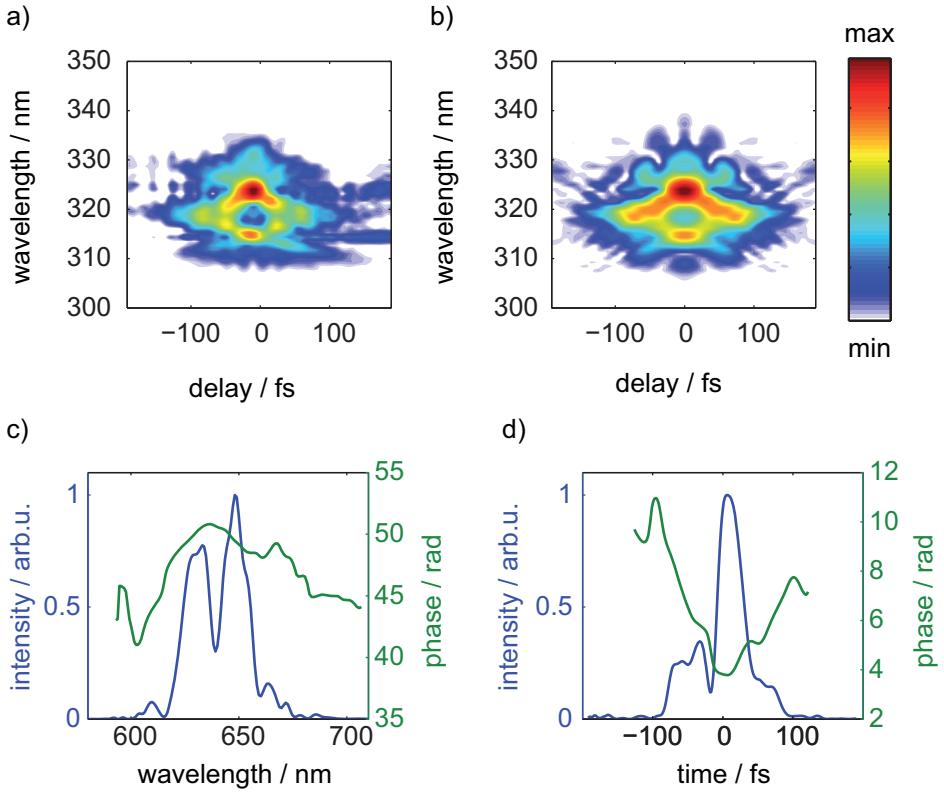

Figure 7.4: cFROG measurement of the uncompressed pulse. The FROG trace (panel a)) is retrieved from the oscillating cFROG trace (not shown). Panel b) depicts the reconstructed FROG trace. The reconstructed spectrum and spectral phase are given in panel c) while panel d) shows the reconstructed temporal pulse shape and temporal phase. One can clearly see that the phase is not flat and the pulse shape is rather complex, including pre- and post-pulses in the time domain.

temporal phase varies over a large range.

However, after the pulse-compression procedure described above the pulse shape presented in figure 7.5 results. Again, the measured and reconstructed FROG traces (figure 7.5 a) and b)) as well as the reconstructed spectrum and spectral phase (figure 7.5 c)) and temporal pulse shape and temporal phase (figure 7.5 d)) are shown. Obviously, the pulse shape is much cleaner than before the compression procedure. Pre- and post-pulses only have negligible intensity and the temporal phase is almost perfectly flat. The temporal FWHM was found to be 25 fs. Although the compression is sufficient for all following experiments, it should be noted that the retrieved pulse duration is

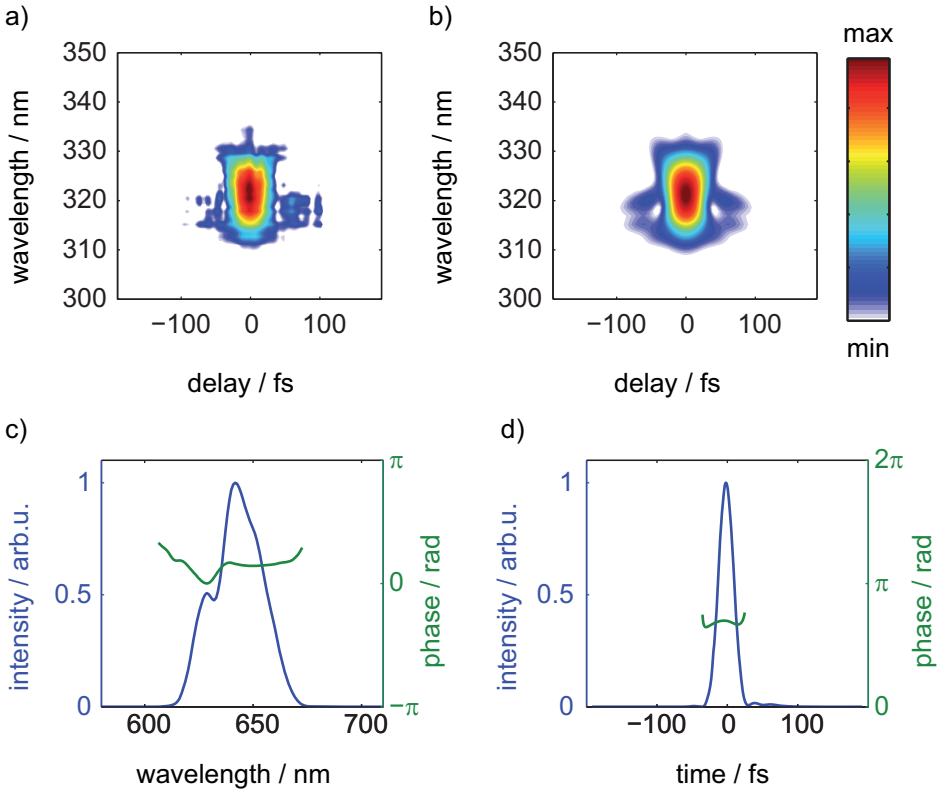

Figure 7.5: cFROG measurement of the compressed pulse. Already the measured and reconstructed FROG traces (panels a) and b), respectively) indicate a much cleaner pulse shape. The reconstructed spectrum and spectral phase are depicted in panel c), indicating that the phase is much flatter than in the case of the uncompressed pulse (see figure 7.4 c)). The temporal pulse shape (panel d)) only features one pulse, the intensity of pre- and post-pulses is negligibly small. The temporal phase is flat and the pulse exhibits an FWHM of 25 fs.

still approximately a factor of 1.5 larger than the minimum possible duration, which can be predicted by Fourier-transforming the *TOPAS* spectrum with a perfectly flat spectral phase.

The offset phase for compression of the pulse is used as an offset-phase for all example pulse shapes presented in the following sections, unless noted otherwise.

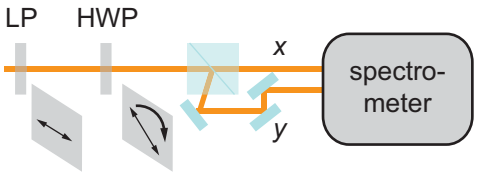

Figure 7.6: Measurement of the polarisation-dependent efficiency of the used spectrometer. A linear polariser LP ensures that the incident pulse is linearly polarised along the x-direction. The polarisation is rotated by rotating the half-wave plate HWP. For each orientation of the wave plate, the spectra of transmitted and reflected polarisation components are measured by the CCD detector of the spectrometer.

7.3.2 Correction factor for polarisation-dependent detection efficiency

All SI measurements presented here, no matter which evaluation routine is employed, have one thing in common. The detection scheme can be broken down to using a Glan–Taylor prism to separate the s- and p-polarisation components of the incident pulse. Both components are then coupled into a spectrometer and dispersed onto different regions of the detector's CCD chip. The spectrometer, especially the gratings, have different efficiencies for both polarisation components. Additionally, the reflected component is reflected by three more mirrors than the transmitted component. This cannnot be avoided since it is neccessary to couple the reflected component into the spectrometer, as depicted schematically in figure 7.6. The different number of mirrors in both beam paths leads to an intensity reduction of the reflected component compared to the transmitted one. In addition, the measured intensity is very sensitive already to slight changes in the coupling into the spectrometer. This originates in the non-homogeneous spatial beam profile of the laser pulse. Thus, special care has to be taken with the delicate process of coupling both beams after the Glan–Taylor prism into the spectrometer. To characterise the pulses correctly, the coupling dependence and the different spectrometer efficiencies have to be taken into account. In other words, one has to determine a correction factor which is used to rescale the intensity of the reflected polarisation component.

In principle, it is sufficient to use a linear polariser and a half-wave plate before the pulse is incident on the Glan–Taylor prism as depicted in figure

7.6. These elements are used to ensure that the pulse is polarised linearly along the x- or y-direction, then the spectrum is measured. In these two cases, the polarisation of the pulse is oriented parallel to one and perpendicular to the other axis of the Glan–Taylor prism. Hence, ideally only in one of both beam paths measurable intensity should be detected. By defining two regions of interest (ROIs), one can gain two spectra per measurement. However, due to the orientation of the optical elements, only one ROI should exhibit measurable intensity in both cases mentioned above. The quotient of both measured spectra (for the polarisation oriented parallel to either Galn–Taylor axis) then yields the correction factor that accounts for the different efficiencies [303].

However, this procedure is prone to intensity fluctuations. So instead of measuring the spectra at only two orientations of the wave plate, the wave plate is rotated in small steps until the full 360° rotation has been accomplished, and for each step the spectra of both ROIs are measured. This yields two two-dimensional intensity data sets (dependent on the wavelength of the pulse and on the rotation angle of the wave plate) which are out of phase for the reflected and transmitted polarisation component. Both data sets are depicted in figure 7.7 a) and b), respectively. This behaviour reflects the fact that if the polarisation is oriented along the x-component, maximum intensity is measured in one beam path whereas no intensity can be detected in the other path, and vice versa. Each single-wavelength contribution shows a sinusoidal behaviour, depending on the orientation of the wave plate. An exemplary curve is shown in figure 7.7 c). Every single oscillating curve is then fitted with a sinusoidal function of the form

$$f(\beta) = a_1 \sin(a_2\beta + a_3) + a_4 \quad , \tag{7.43}$$

where β is the orientation angle of the wave plate. The wavelength-dependent fit amplitudes a_1 contain the desired information, namely the shape of the spectra, while the other coefficients a_2, a_3, and a_4 are almost identical for all wavelengths. It should in principle be possible to set these coefficients to constant values and keep only a_1 is a free parameter. The parameter a_2 is only a scale factor for the β-axis, while a_3 is a constant phase offset and a_4 an intensity offset, which are identical for all wavelengths. Figure 7.7 d) depicts the wavelength-dependent fit amplitudes a_1 for the reflected and transmitted data sets. As expected, the progression of the fit amplitudes follows the shape of the measured spectra, but due to the fitting procedure, the influence of intensity fluctuations is minimised. Dividing the fit amplitudes of the transmitted spectra by those of the reflected ones then yields the correction factor, which is shown in figure 7.7 e).

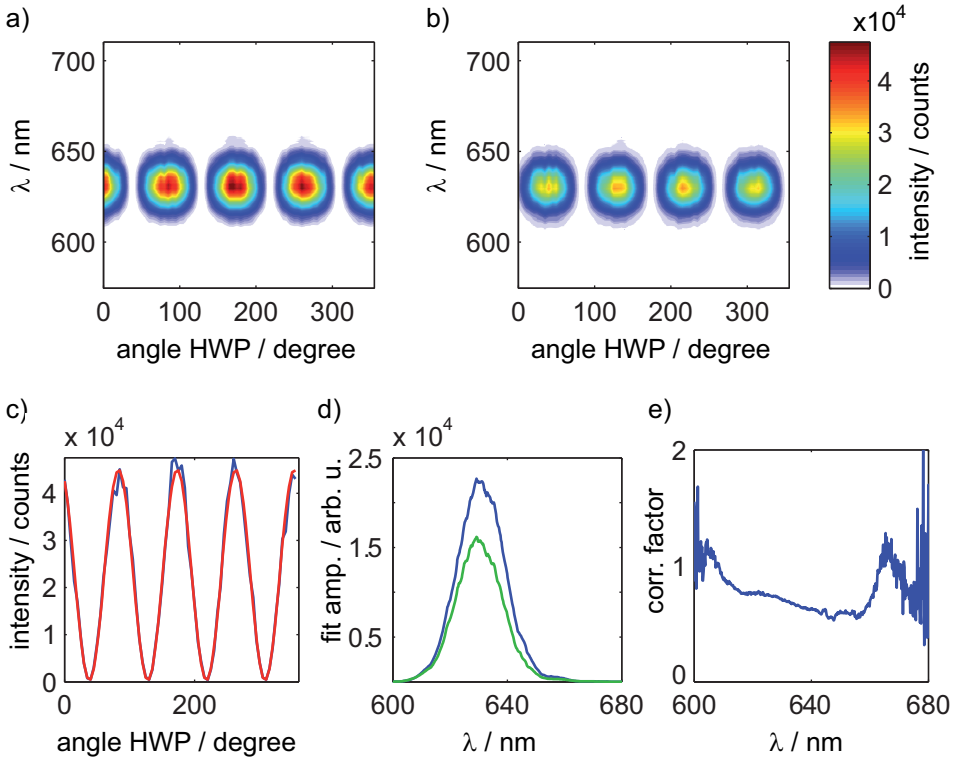

Figure 7.7: Determination of the polarisation-dependent correction factor for the spectrometer efficiency. The measured data sets for the reflected and transmitted fraction (ROI) of the intensity in dependence of the half-wave-plate orientation are depicted in figure a) and b), respectively. Each single-wavelength contribution is fitted by a sinusoidal function, shown exemplary in figure c) (blue: data, red: fit). The wavelength-dependent fit amplitudes for reflected (blue) and transmitted (green) fraction are shown in figure d) and reproduce the shape of the spectrum of the input pulse. Dividing those fit amplitudes then leads to the correction factor (figure e)), which is used to rescale the spectra of the reflected fraction.

As mentioned before, not only the polarisation-dependent efficiency of the optical components determines the correction factor, but also the coupling into the spectrometer. If the correction factor was only determined by the efficiencies, it should adopt values below 1 for all wavelength due to the intensity reduction caused by the three more mirrors in the reflected beam path. However, values above 1 result from the sensitivity to the coupling into the spectrometer. All reflected measured spectra have been rescaled using this correction factor.

Since the transmitted and reflected intensities are sensitive to changes in the alignment of the beam path from the pulse shaper to the Glan–Taylor prism as well as the separated beam paths behind the Glan–Taylor prism, the correction factor has to be determined again if any changes to the alignment have been made. Thus, no changes to the beam path alignment may be made between the measurement of the data sets for the correction factor and the measurement of the SI data.

7.3.3 Determination of the reference phase

Since SI is not a self-referencing pulse-characterisation technique, the reference pulse has to be characterised independently. In both SI variants presented here, a small fraction of the incident pulse is split off just before the pulse-shaper setup and travels along a delay line before it is recombined with the shaped pulse (see figure 7.3). This weak reference pulse has insufficient intensity to be characterised by nonlinear methods like FROG. Instead, it is expedient to use SI as a method of characterising the reference pulse. In a manner of speaking, the reference and shaped pulses change their roles. The shaped pulse has been characterised and compressed using cFROG, thus its phase is known and can be assumed to be flat. Since the reference pulse cannot be characterised otherwise, its phase is unknown and has to be determined. The compressed shaped pulse can therefore act as a known "reference" pulse to characterise the unknown reference pulse.

As described in section 7.2.2, the spectra of the shaped pulse, the reference pulse and of the SI between both have to be measured and the phase can be extracted using the FTSI or DQSI method. The results for FTSI and DQSI are shown in figures 7.8 and 7.9, respectively. The spectra in figure 7.8 correspond to 45°- and −45°-components of the polarisation of the shaped pulse (a)), reference pulse (b)) and SI between both (c)). The phases that have been extracted for both polarisations are shown in figure 7.8 d). The large linear-phase contribution corresponds to the temporal separation of compressed and reference pulse (approximately 400 fs).

In figure 7.9, the results for DQSI are shown. Figure 7.9 a), b) and c) again depict the spectra of the shaped pulse, the reference pulse and the SI between them for one polarisation component. However, in this case the two spectra correspond to the in-phase- and quadrature contribution. Thus, six spectra are required to extract the phase of one polarisation component. This cosine- and sine-signal that can be calculated from equations 7.27 and 7.28 are depicted in figure 7.9 d). One can see that they are phase-shifted by approximately $\pi/2$ with respect to each other. The resulting phase is shown in figure 7.9 e). The phase for the second polarisation component is almost identical and is therefore not shown here. As discussed in section 7.2.2, SI only measures the phase difference between the reference phase and the phase of the shaped pulse. As an additional phase term, the linear phase $\omega\tau$, which corresponds to the temporal separation between both pulses, is present. Here, this linear contribution is absorbed in the phase of the reference pulse as depicted in figures 7.8 and 7.9. For all example pulse shapes in the following section, this reference phase including the linear contribution is subtracted to display only the phase of the shaped pulse, i.e. the phase introduced by

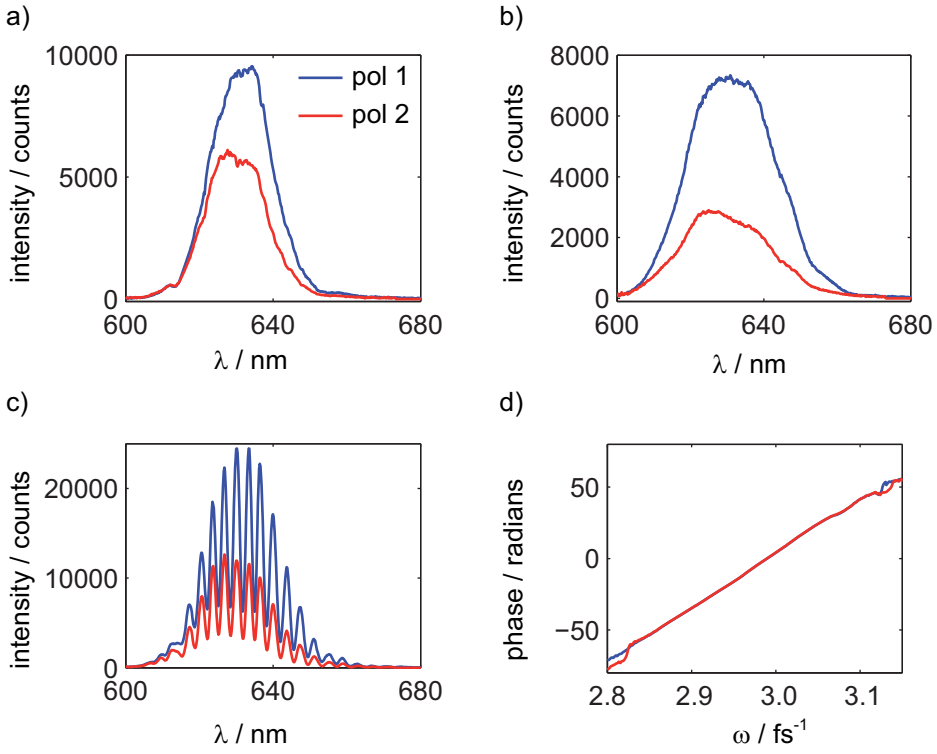

Figure 7.8: Determination of the reference phase via FTSI. The spectra of the shaped pulse for both polarisation components are given in figure a), while b) depicts the spectra of the reference pulse. The difference in their spectral shape is due to the different and non-homogeneous spatial beam profiles of shaped and reference pulse. The spectral interference between both is shown in figure c). Evaluating the interference as described in section 7.2.2 for FTSI leads to the spectral phase which is given in figure d).

the pulse shaper.

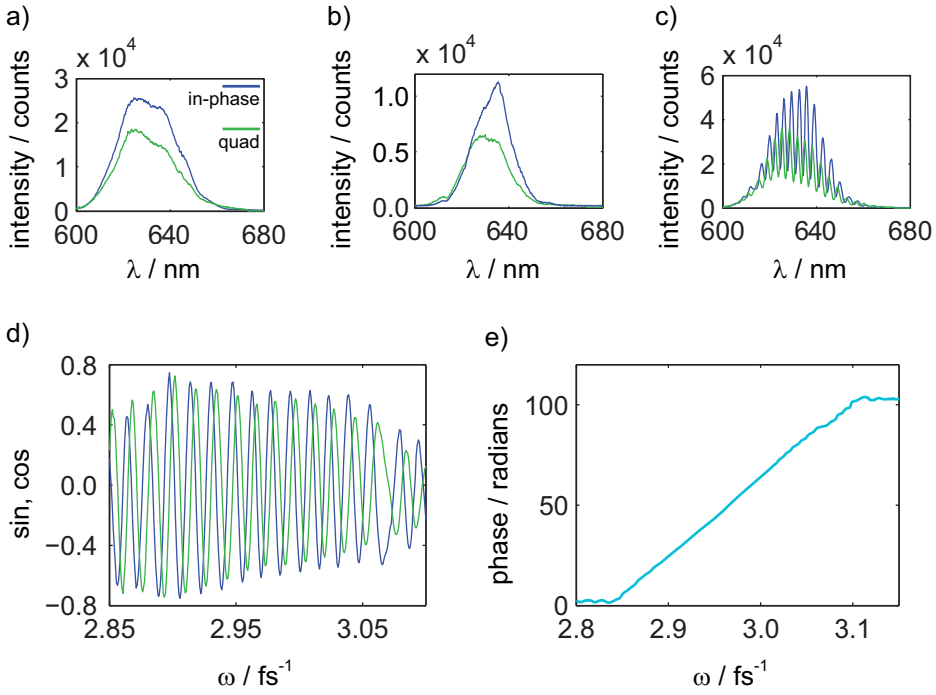

Figure 7.9: Raw data for DQSI (only one polarisation component). The spectra of the shaped and reference pulse are shown in figures a) and b), respectively, while c) depicts the spectral interference between both. The spectral shape of the shaped and reference pulse fro DQSI differ slightly from those of FTSI, which is a result of the sensitivity to the coupling into the spectrometer. Calculating the sine- and cosine term according to equations 7.27 and 7.28 results in the oscillations shown in figure d). One can clearly see that they are out of phase by $\pi/2$ as expected. The resulting phase which is extracted as described in section 7.2.2 is shown in figure e).

7.3.4 Jones-matrix measurement

The Jones matrix of the pulse-shaper setup has been experimentally determined using FTSI and evaluated as described in section 7.2.3. Eight different pulse shapes have been used to construct the overdetermined system of linear equations. These pulse shapes are the only examples in this thesis in which the uncompressed pulse has been used and thus the compression phase was not applied at the LCD of the pulse shaper. The applied phase for one polarisation component (one LCD layer) has been set to zero and was identical for all pulses. The phase for the other component, however, has been varied between zero and 6π in eight equidistant steps. Thus, by varying only the constant phase difference between both polarisation components, different polarisation states have been obtained. The maximum phase difference of

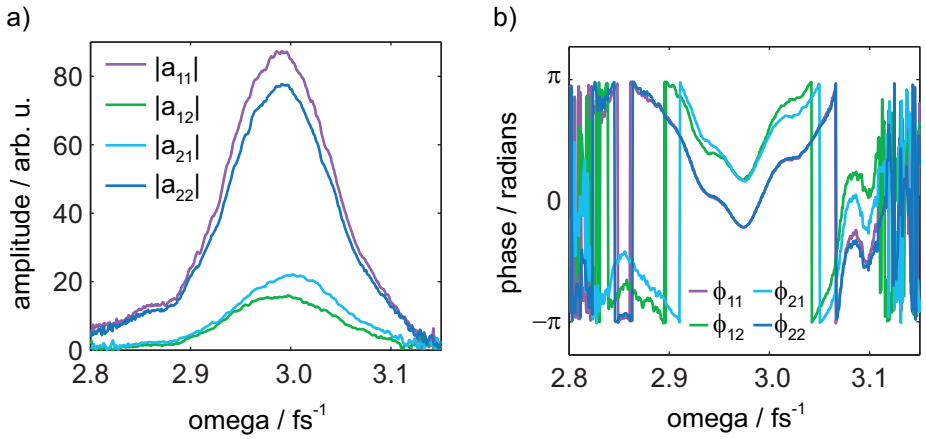

Figure 7.10: Experimentally determined Jones matrix. Panel a) depicts the Jones amplitudes $|a_{ij}|$. The diagonal entries $|a_{11}|$ and $|a_{22}|$ contain the polarisation-dependent reflection and transmission efficiencies while the off-diagonal entries $|a_{12}|$ and $|a_{21}|$ cause a mixing of both polarisation components. The phases $\phi_{ij}(\omega)$ depicted in panel b) are non-zero, indicating that the incoming pulse is temporally stretched in the pulse-shaper setup.

6π results from the phase calibration, which allows for a maximum usable phase range of 6π. Thus the available phase range is sampled optimally and a broad variety of polarisation states is used to measure the Jones matrix, which is important to ensure a reliable Jones-matrix determination.

The experimentally determined Jones-matrix elements are shown in figure 7.10. Panel a) depicts the Jones amplitudes $|a_{ij}(\omega)|$, where the diagonal entries $|a_{11}|$ and $|a_{22}|$ are the dominant contributions in the matrix. The

off-diagonal entries $|a_{12}|$ and $|a_{21}|$ have a much lower amplitude than the diagonal entries. However, they cannot be neglected since their influence still results in a rather strong mixing of both linear polarisation components. The non-zero Jones phases $\phi_{ij}(\omega)$ in panel b) indicate that the incoming pulse is temporally stretched within the pulse-shaper setup. Thus it cannot be regarded as an ideal zero-dispersion compressor, but the introduced phase has to be compensated for in order to compress the pulse.

With this Jones matrix, any pulse shape can be predicted using the applied phase including the compression phase as an input. Results of these calculations will be shown in section 7.3.7.

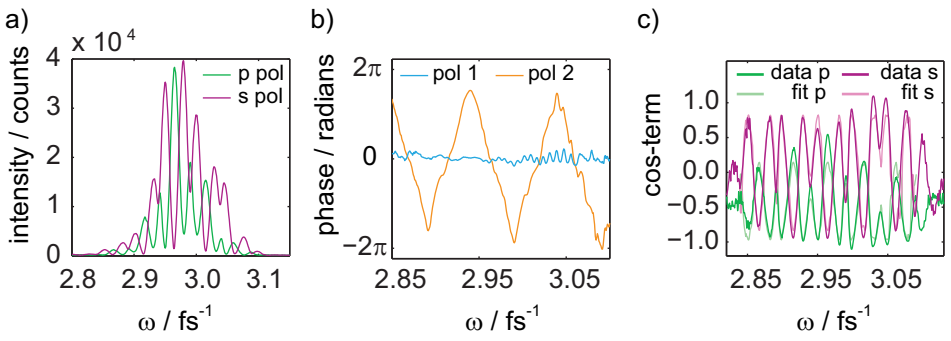

Figure 7.11: Determination of the relative phase between both polarisation components. The spectra needed for the tomographic phase retrieval are shown in figure a). Figure b) depicts the phases that are obtained for the single polarisation components as described in section 7.2.2. Together they can be used to calculate the oscillating contribution to the spectra and fit it to obtain the relative phase δ. The oscillating terms and corresponding fit curves are given in figure c). The agreement between both is very good, considering that both curves are fitted simultaneously and only one free parameter, the relative phase δ, is used. In this case, the fit reveals a value of $\delta = 1.158$.

7.3.5 Relative phase DQSI

As mentioned earlier, the relative phase between both polarisation components has to be determined with additional measurements. An example of this procedure is given in figure 7.11. The spectra corresponding to the s- and p-polarisation projection of the shaped pulse are depicted in figure 7.11 a). The phases for the single polarisation component along the SLM axes (45 degree and −45 degree, respectively) that have been extracted using the DQSI data-evaluation routine described in section 7.2.2 are depicted in figure 7.11 b). Together with the projections of the measured intensity onto the s- and p-directions, they are used for the tomographic phase retrieval. The oscillating contribution to the spectra of figure 7.11 a) are calculated using equations 7.44 and 7.45 and are plotted in figure 7.11 c).

$$S^s(\omega) = 2\tilde{A}^s_{s,1}(\omega)\tilde{A}^s_{s,2}(\omega)\cos\left(\phi_{s,1}(\omega) + \delta - \phi_{s,1}(\omega)\right) \quad , \tag{7.44}$$

$$S^p(\omega) = 2\tilde{A}^p_{s,1}(\omega)\tilde{A}^p_{s,2}(\omega)\cos\left(\phi_{s,1}(\omega) + \delta - \phi_{s,1}(\omega)\right) \quad , \tag{7.45}$$

where $\phi_{s,i}(\omega)$ are the phases for the single polarisation components, retrieved as discussed in section 7.2.2 and exemplary shown in figure 7.11 b). The amplitudes $\tilde{A}^s_{s,i}(\omega)$ and $\tilde{A}^p_{s,i}(\omega)$ are the projections of the measured amplitudes

as defined in equations 7.33 and 7.34. The unknown relative phase δ is determined from $S^s(\omega)$ and $S^p(\omega)$. This is achieved by fitting both simultaneously with a cosine function of the form

$$S^s(\omega) = a_1 \cos\left(\phi_{s,1}(\omega) + \delta - \phi_{s,1}(\omega)\right) + a_2 \tag{7.46}$$

and

$$S^p(\omega) = a_3 \cos\left(\phi_{s,1}(\omega) + \delta - \phi_{s,1}(\omega)\right) + a_4 \quad , \tag{7.47}$$

where δ is the only free parameter that has a physical meaning since it yields the relative phase. The other parameters a_i are only necessary as scaling and offset parameters and have no influence on the relative phase. The fit result is also shown in figure 7.11 c). The agreement between the oscillating term and the fit is remarkable, considering the fact that both oscillating curves are fitted simultaneously. For this example pulse shape, δ adopts a value of 1.158 radians. This phase offset is then added to the phase of polarisation component 1, according to the definition of the electric field of the shaped pulse given in equation 7.31. All DQSI phases that are presented in the following section have been evaluated accordingly, the agreement between measured data and fit is similar to the one of the example shown in figure 7.11.

7.3.6 Error calculation

In order to compare both SI evaluation methods, it is important to have a reliable criterion for the quality of the phase retrieval. Therefore an error definition will be introduced in this section based on an accuracy criterion presented for SPIDER pulse measurements [304]. It utilises the root-mean-square field error, which is given by

$$\begin{aligned} \varepsilon &= \|E_1 - E_2\| \\ &= \Big(\int_{-\infty}^{\infty} |E_1(t) - E_2(t)|^2 \mathrm{d}t\Big)^{1/2} \\ &= \Big(\frac{1}{2\pi}\int_{-\infty}^{\infty} |E_1(\omega) - E_2(\omega)|^2 \mathrm{d}\omega\Big)^{1/2} \end{aligned} \tag{7.48}$$

where E_1 and E_2 are the complex electric fields of the laser pulses which are compared, either in the temporal or in the spectral domain. Since the spectral phases are retrieved by SI, the discussion will focus on the spectral representation of the fields. Then, equation 7.48 can be rewritten by using the definition of the spectral field given in section 2.1.1:

$$\begin{aligned} \varepsilon &= \Big(\frac{1}{2\pi}\int_{-\infty}^{\infty} |E_1(\omega) - E_2(\omega)|^2 \mathrm{d}\omega\Big)^{1/2} \\ &= \Big(\frac{1}{2\pi}\int_{-\infty}^{\infty} |A_1(\omega)\, e^{-i\phi_1(\omega)} - A_2(\omega)\, e^{-i\phi_2(\omega)}|^2 \mathrm{d}\omega\Big)^{1/2} \end{aligned} \tag{7.49}$$

with the spectral amplitudes $A_i(\omega)$ and the spectral phases $\phi_i(\omega)$.

However, the error definition given in equations 7.48 and 7.49 does only apply to linearly polarised pulses and therefore has to be extended to include arbitrary polarisation states of the electric fields. The most obvious way to do so is to calculate an error for two linearly independent polarisation projections and use their quadratic sum as a measure of the overall pulse reconstruction quality. In the following, this procedure will be applied since both SI methods already reveal such two polarisation projections. However, although this definition renders a quantitative comparison possible the qeustion arises, what shall the measured pulse be compared to? Although one could in principle compare the measured phase to the applied phase at the LCD of the pulse shaper and the spectrum of the shaped pulse to that of the unshaped pulse, but this would neglect important effects. As was seen in

section 7.3.4, the Jones matrix of the setup exhibts considerable off-diagonal elements and nonlinear phases, which lead to modifications of the desired pulse shape. These modifications have to be taken into account when determining the accuracy of the pulse measurement. Thus it is useful to compare the measured spectra and phases to those that have been predicted by the experimentally determined Jones matrix. The error definition then reads

$$\begin{aligned}
\varepsilon_1 &= \Big(\frac{1}{2\pi}\int_{-\infty}^{\infty} |A_{m,1}(\omega)\, e^{-i\phi_{m,1}(\omega)} - A_{c,1}(\omega)\, e^{-i\phi_{c,1}(\omega)}|^2 \mathrm{d}\omega\Big)^{1/2} \quad , \\
\varepsilon_2 &= \Big(\frac{1}{2\pi}\int_{-\infty}^{\infty} |A_{m,2}(\omega)\, e^{-i\phi_{m,2}(\omega)} - A_{c,2}(\omega)\, e^{-i\phi_{c,2}(\omega)}|^2 \mathrm{d}\omega\Big)^{1/2} \quad , \\
F &= \varepsilon_1^2 + \varepsilon_2^2 \quad . \qquad (7.50)
\end{aligned}$$

Here, $A_{m,1}$ and $\phi_{m,i}$, $i = 1, 2$ are the measured spectral amplitude and phase of polarisation component 1 and 2, respectively, while the amplitudes and phases that have been calculated by utilising the Jones matrix are given by $A_{c,1}$ and $\phi_{c,i}$, $i = 1, 2$ for both polarisation components.

Still, this definition does not take all effects into account that have an impact on the pulse-retrieval accuracy. Since the setup for the interferometric measurement is not interferometrically stabilised, path-length fluctuations in both interferometer arms can lead to an additional linear phase. Especially the delay stage in the reference path can cause severe path-length fluctuations since the mechanical position is fixed by a spring. Thus, each pulse may exhibit an additional linear phase term $b_1(\omega - \omega_0)$ which is not related to the pulse-shaping process but results from path-length fluctuations. Thus, the value of b_1 may be different for each pulse. Furthermore, the constant phase offset b_0 does not influence the pulse shape and can be regarded as an additional free parameter. This leads to the following modification of the error definitions for both polarisation components:

$$\begin{aligned}
\varepsilon_1 &= \Big(\frac{1}{2\pi}\int_{-\infty}^{\infty} |A_{m,1}(\omega)\, e^{-i(\phi_{m,1}(\omega)+b_1(\omega-\omega_0)+b_0)} \\
&- A_{c,1}(\omega)\, e^{-i\phi_{c,1}(\omega)}|^2 \mathrm{d}\omega\Big)^{1/2} \quad , \\
\varepsilon_2 &= \Big(\frac{1}{2\pi}\int_{-\infty}^{\infty} |A_{m,2}(\omega)\, e^{-i(\phi_{m,2}(\omega)+b_1(\omega-\omega_0)+b_0)} \\
&- A_{c,2}(\omega)\, e^{-i\phi_{c,2}(\omega)}|^2 \mathrm{d}\omega\Big)^{1/2} \quad . \qquad (7.51)
\end{aligned}$$

It is important to mention that b_0 and b_1 have to be identical for both polarisation components of one pulse so that no further modifications of the polarisation state of the pulse are introduced by these additional parameters. In order to determine the overall error F, the parameters b_0 and b_1 are varied such that the value of F is minimised. If normalised fields are used to calculate ε_1 and ε_2, i.e. $\|E_i\| = 1$, the value of F ranges from 0 to 8 since each ε_i can adopt values between 0 and 2, where 0 results for perfect agreement between two fields and the maximum value indicates that both fields are inversions of each other. However, the choice of boundaries for which the pulse retrieval can be considered sucessfull is arbitrary and depends on the question under consideration.

7.3.7 Comparison of FTSI and DQSI

In this section, a selection of example pulse shapes will be presented that have been measured both with FTSI and DQSI. In this way, the performance of both techniques can be compared directly. All measured phases and spectra are compared to those predicted using the experimentally determined Jones matrix, thus the effects of unwanted modifications of the polarisation state are already taken into account. Relatively simple phase patterns have been chosen to generate the example pulse shapes of this section. Nevertheless, already these simple phase pattern can lead to relatively complex temporal profiles of the pulse, as will be shown in the following.

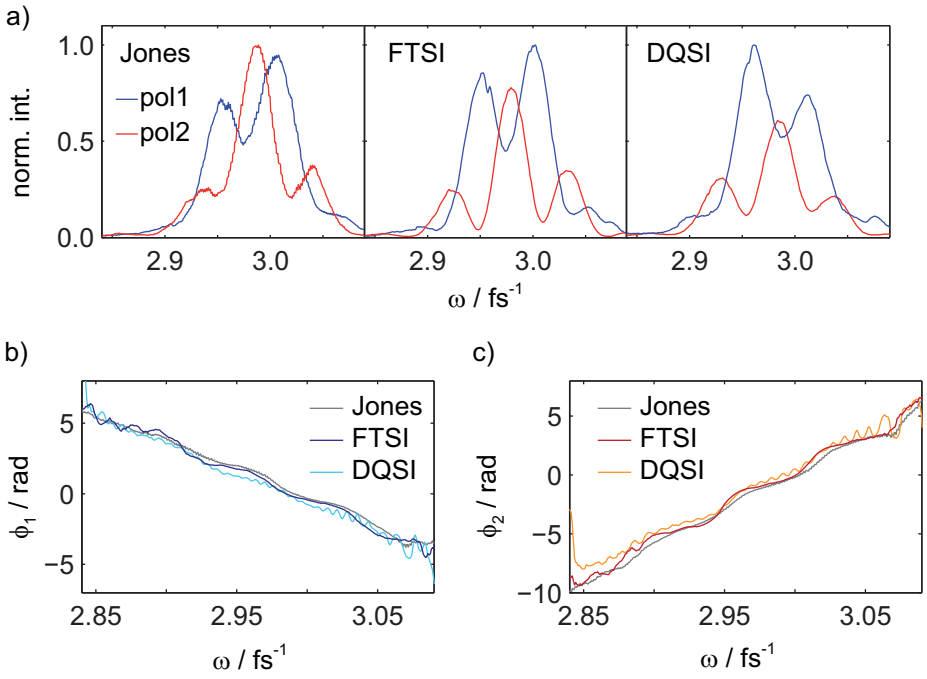

Figure 7.12: Example pulse shape with linear phases with equal magnitude (50 fs), but opposite sign at both SLM layers. The measured spectra (figure a)) as well as the measured phases (figure b) and c)) agree quite well with the spectra and phases predicted by Jones calculus.

A very simple example pulse shape is presented in figures 7.12 and 7.13, for which only linear phases have been applied to both SLM layers. The absolute value of the linear phase was identical for both layers (50 fs), but with opposite sign for both layers. The spectra for both polarisation components are depicted in figure 7.12 a) for Jones calculus, FTSI and DQSI (left

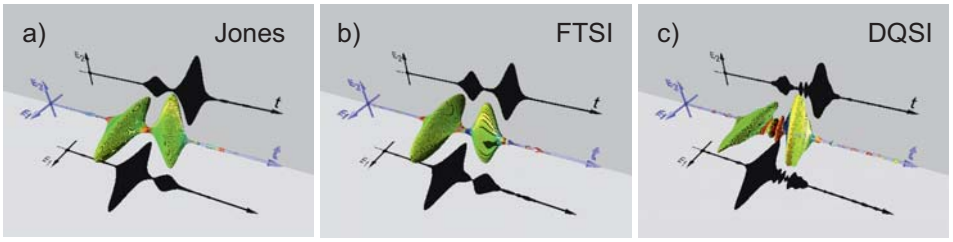

Figure 7.13: Pseudo-3D representation of the example pulse of figure 7.12. The opposite linear phases lead to a double pulse in which both subpulses are polarised mostly linearly and perpendicular to each other. The temporal separation of both subpulses ($\approx$ 100 fs) agrees well with the applied linear phases (+/-50 fs). The result of Jones calculus (a)) agrees pretty well with FTSI (b)) as well as DQSI (c)).

to right). The mixing of both polarisation components which results from the non-diagonal Jones matrix leads to modulations in the spectra of both polarisation components. In all three cases, the spectra exhibit the same features. The phases for polarisations 1 and 2 are shown in figures 7.12 b) and c), respectively. The overall agreement between the measured phase and the phase from Jones calculus is pretty good, although for FTSI the agreement is slightly better than for DQSI. The most pronounced difference is that the DQSI phase exhibits small oscillations which are not present for FTSI. They result from the fact that the reference pulse for DQSI is not polarised perfectly circularly over its entire spectral range because of the wavelength dependence of the retardance of the achromatic quarter-wave plate. This influence is known and has been observed before [17].

A second effect that can lead to spectral oscillations in the phase is the spatial chirp of the laser pulse. The spatial beam profiles of the shaped and reference pulse are not perfectly homogeneous and slightly different due to the different beam paths of both. Thus, it is difficult to overlap both beams perfectly at the second wedge-plate pair after the pulse shaper. The measured interference spectra do not only contain the desired spectral interference between both pulses, but also non-interfering contributions from both pulses. This in turn leads to an incomplete modulation depth for the spectral interference patterns and thus also for the resulting cosine- and sine-terms which are calculated from the interference patterns according to equations 7.27 and 7.28. As a result, the cosine- and sine-term do not oscillate perfectly between -1 and +1 as can be seen in figure 7.9 d). Using these imperfectly modulated terms to retrieve the phase can also lead to spectral oscillations of the phase.

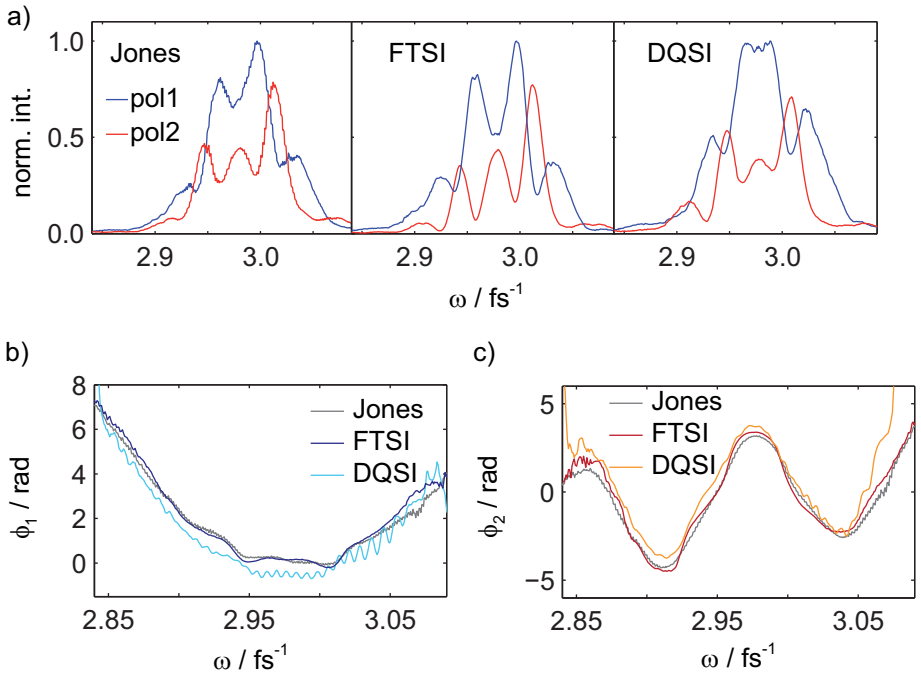

Figure 7.14: Example pulse shape with quadratic and sinusoidal phase patterns. The measured spectra (a)) as well as the phases (b) and c)) agree reasonably well with the predicted ones from Jones calculus.

However, the overall agreement of the results from both SI methods with Jones calculus is still pretty good. This is also supported by the temporal pulse shape which can be calculated from the spectral phases and amplitudes shown in figure 7.13. The applied linear phases lead to a temporal double pulse in which both subpulses are polarised mainly linearly and perpendicular to each other, as can be seen from the result of Jones calculus in figure 7.13 a). The temporal separation of both subpulses corresponds to the relative linear phase between both layers (100 fs). The shadows represent the projection of the pulse shape onto each polarisation component. Again, the pulse shape from FTSI (figure 7.13 b)) and DQSI (figure 7.13 c)) agree very well with the predicted pulse shape. The pulse shape resulting from DQSI is not as smooth as the one from FTSI, which is due to the small oscillations in the spectral phase mentioned earlier.

A second, more complex example pulse shape is given in figure 7.14 and 7.15. This time, a quadratic phase with a curvature of $b_2 = 750\,\mathrm{fs}^2$ was applied to one SLM layer while a sinusoidal phase was applied to the second layer. The amplitude of the sine was equal to π and its frequency was set

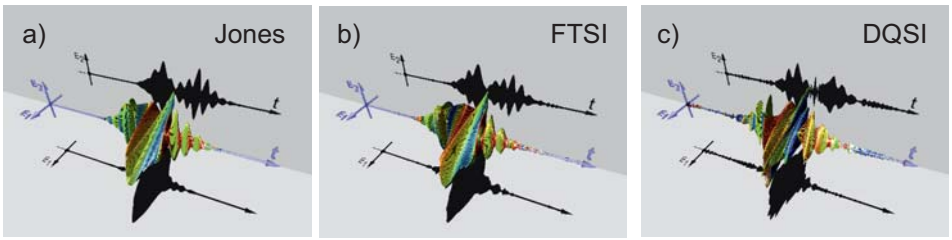

Figure 7.15: Pseudo-3D representation of the pulse shape resulting from the spectra and phases of figure 7.14. The simple phase patterns result in a complex temporal pulse shape and polarisation state. The results of either SI method (b) and c)) agree well with the pulse shape predicted by Jones calculus (a)).

to $50\,\mathrm{fs}^{-1}$. These two simple phase patterns lead to a rather complex pulse shape. The quadratic phase causes a temporal lengthening and linear chirp of the first polarisation component while the sinusoidal phase generates a pulse train for the second component. However, although the shapes of the single polarisation components are not too complex, the superposition of both components then results in a complex pulse shape as can be seen in figure 7.15. Again, the mixing of both polarisation components leads to modulations in the spectra as can be seen in figure 7.14 a). As in the first example, the spectra resulting from Jones calculus, FTSI and DQSI show basically the same features. The same applies to the phases for both polarisations, which are given in figure 7.14 b) and c). The overall shape is well reproduced with both SI methods, although the agreement between the phase from Jones calculus and FTSI is again better than for DQSI.

The resulting temporal pulse shape is shown in figure 7.15. Both projections onto the single polarisation components, indicated by the shadows, show that the applied phases change the shape of each component as expected. As a result, the overall polarisation state of the laser pulse is very complex. The ellipticity, the orientation of the ellipse and the momentary frequency change on a femtosecond timescale. Again, Jones calculus (figure 7.15 a)) and both SI techniques (figure 7.15 b) and c)) reveal comparable results.

These first two examples already show that DQSI is also suitable as a characterisation techniques for broadband polarisation-shaped laser pulses. Its overall performanc is roughly comparable to that of FTSI for simple as well as rather complex polarisation-shaped pulses. Nevertheless, due to experimental limitations, especially the lack of a truly achromatic broadband

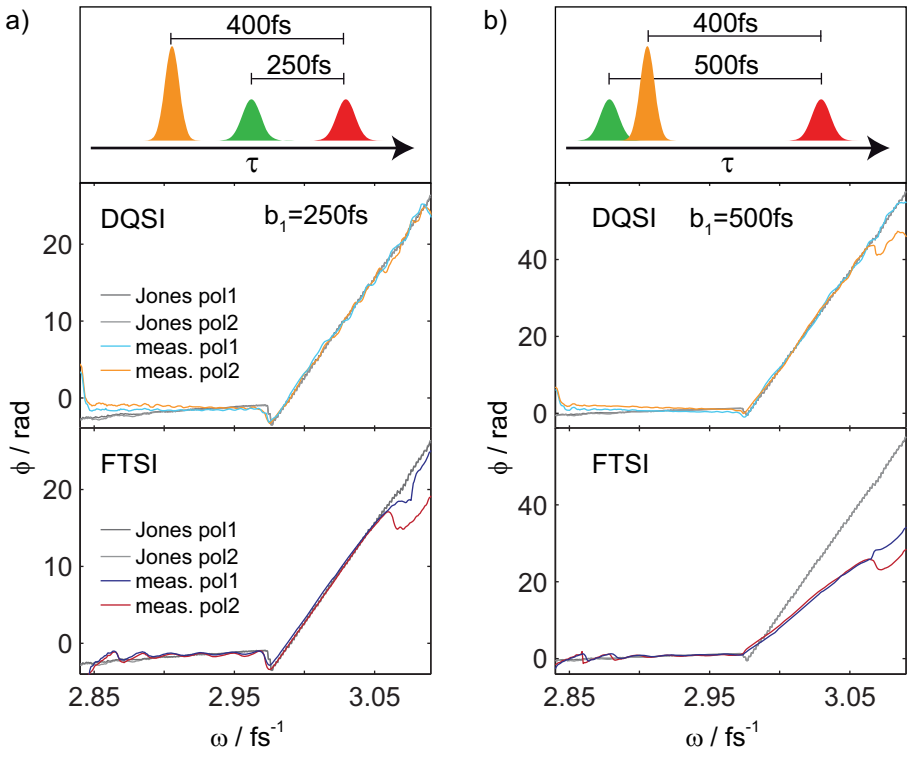

Figure 7.16: Proof of principle that the delay and temporal ordering of pulses do not affect the performance of DQSI. If a coloured double pulse is created and both subpulses (red and green at the top of panel a)) arrive before the reference pulse (orange), both SI methods yield the correct phase, as can be seen from comparison with the phase predicted ny Jones calculus (middle and bottom of panel a)). If the phase slope is increased so that one subpulse arrives before, the other after the reference pulse (top of panel b)), DQSI still yields the correct result (middle of panel b)). In contrast, FTSI fails: The slope is off by a factor of approximately two and the phase jump at the apex is not reproduced (bottom of panel b)).

quarter-wave plate, the performance of DQSI is typically slightly lower than that of FTSI.

However, this in itself does not justify the more intricate measurement and data evaluation procedure of DQSI. But there is one big advantage DQSI has over FTSI. As was seen in section 7.2.2, the temporal delay between the shaped and the reference pulse has to be sufficiently large to avoid an overlap of both pulses and to insure the applicability of the Fourier-filtering method. If the delay is insufficient, the positive and negative delay contribution of

equation 7.16 cannot be separated and the FTSI evaluation fails. Closely related is the temporal ordering of the pulses. If the shaped pulse comprises several subpulses, all of them have to arrive well before or after the reference pulse and have to be well separated from the reference pulse.

These limitations are not present in DQSI. The only condition that has to be fulfilled is that both SI patterns have to be shifted by $\pi/2$ with respect to each other to yield the cosine and sine term (see equations 7.27 and 7.28). This is even possible in the temporal overlap of shaped and reference pulse or if the reference pulse arrives in between several subpulses of the shaped pulse.

This is demonstrated in figure 7.16, where a coloured double pulse [305] has been created by applying a "phase kink". Zero phase is applied at the low-energy part of the spectrum while a linear phase with a certain slope was applied at the high-energy part. Additionally, a phase jump of π was introduced at the apex. In this example, the same phase pattern was applied to both SLM layers. For a slope of 250 fs, this phase pattern leads to a pulse sequence as sketched in the top panel of figure 7.16 a). Both subpulses (red and green) of the shaped pulse arrive before the reference pulse (orange) and are well separated from it. In this case, both SI methods yield the correct phase, as can be seen from the middle and bottom panel of figure 7.16 a) from DQSI and FTSI, respectively. Comparison with the phases that are predicted by Jones calculus reveals that the slope shows the correct value and the phase jump at the apex is well reproduced. However, if the slope is increased to 500 fs, the ordering of the pulses is different. The "red" subpulse does not change its position and still arrives before the reference pulse. In contrast, the "green" subpulse is temporally delayed so that it arrives after the reference pulse and still partly overlaps with it, as is shown in the top panel of figure 7.16 b). While DQSI still yields the correct result for the phase as predicted by Jones calculus (middle panel of figure 7.16 b)), FTSI fails. The phase of the low-energy part (the non-overlapping "red" subpulse) is correct, but the result for the high-energy part of the phase is wrong. The slope is off by a factor of approximately two and the phase jump at the apex is not reproduced (bottom panel of figure 7.16 b)). The disagreement between the phases calculated using the Jones matrix and the phases retrieved by FTSI is obvious.

Thus, this kind of coloured double pulse with phase jump can be regarded as an examplary pulse shape for a proof of principle regarding the fewer restrictions of DQSI compared to FTSI. For the latter, the temporal ordering and delay of the shaped and reference pulse with respect to each other do play a crucial role so that the evaluation of certain pulse shapes fails, while this restricition is not present in DQSI. The phase can well be reproduced,

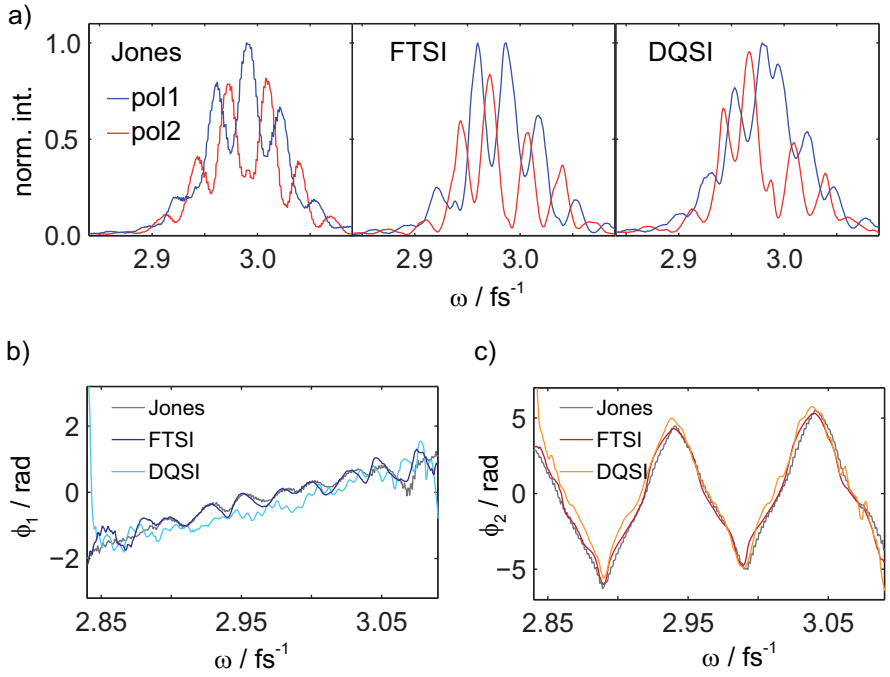

Figure 7.17: Example pulse shape with zero phase for one component and a triangular phase pattern for the second component. For a slope of the triangle of 200 fs, both methods yield comparable results. The spectra (a)) show similar features, although the deviations from the result of Jones calculus are larger than before. The phases, however, are similar for both methods (b) and c)).

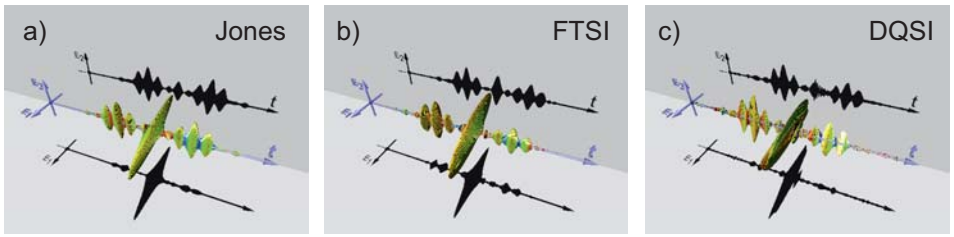

Figure 7.18: Pulse shape obtained from the spectra and phases of figure 7.17. The results of Jones calculus (a)), FTSI (b)) and DQSI (c)) agree very well.

no matter what time ordering or delay between the pulses is present, as long as the interference fringes can still be properly resolved.

To show that the same also applies to more complex pulse shapes, one

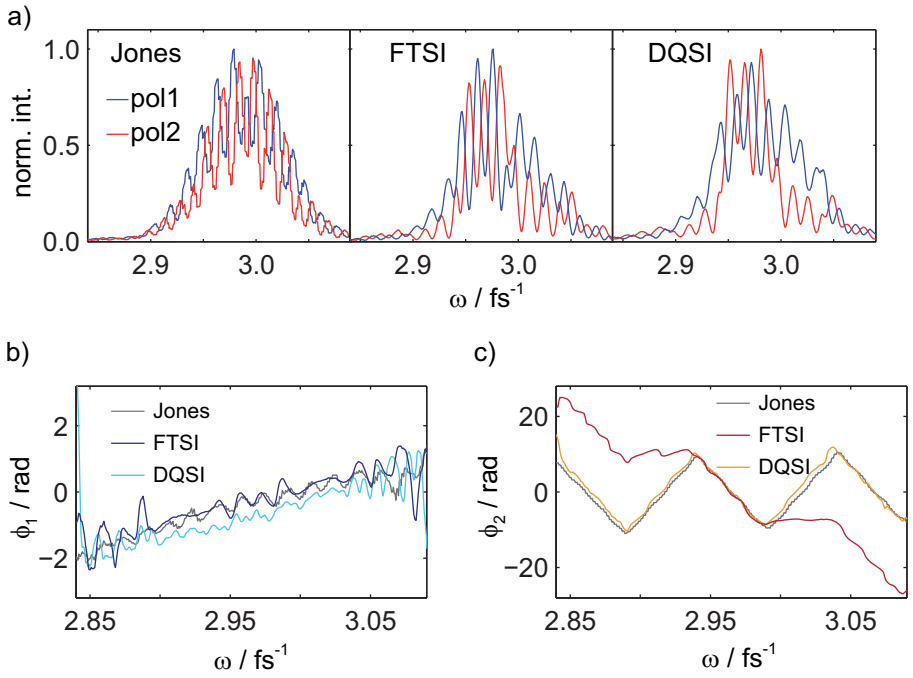

Figure 7.19: Example pulse shape similar to figure 7.17, but with a slope of 400 fs. This leads to a partial temporal overlap between the shaped and reference pulse. The spectra (a)) of both SI methods and the phase of the compressed component (b)) agree rather well with Jones calculus, but the phase of the triangular sawtooth (c)) can only be retrieved correctly by DQSI.

more example pulse shape will be given. This time, one component remains compressed to its minimum duration since no additional phase is applied. The other component is modified by a triangular phase pattern. This leads to two sets of subpulses for this polarisation component, which are temporally delayed to $+\tau$ and $-\tau$, respectively, where τ is equal to the slope of the triangle. For the example presented in figure 7.17, the slope was set to 200 fs, so that the subpulses are still fairly well temporally separated from the reference pulse. As before, FTSI and DQSI yield comparable results. The spectra (figure 7.17 a)) show the same features, although in this case the discrepancy is larger than before. However, the quality of the retrieved phases, which are given in figures 7.17 b) and c), is again comparable for both methods. Also the temporal pulse shapes, shown in figure 7.18, agree very well. One polarisation component is compressed, the second component exhibits two sets of subpulses at positive and negative delay as predicted by Jones calculus.

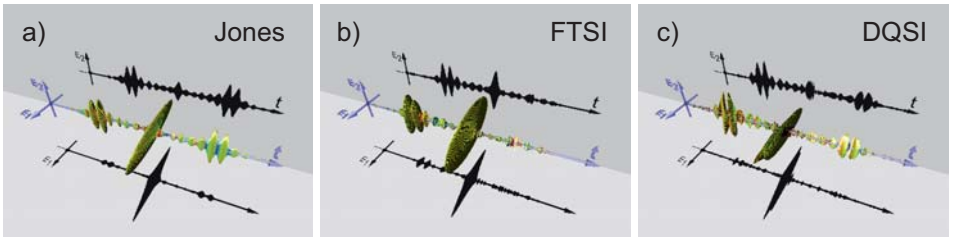

Figure 7.20: Temporal pulse shape corresponding to the results of figure 7.19. While the results of Jones calculus and DQSI agree very well, FTSI yields a completely different pulse shape.

If the slope of the triangle is increased to 400 fs, however, one set of subpulses of this polarisation component is delayed so that it temporally overlaps with the reference pulse. In this case, the pulse characterisation with FTSI fails. Although the spectra of both SI techniques exhibit similar features (see figure 7.19 a)), the obtained phases differ strongly. The phase of the compressed component is retrieved correctly by both methods (figure 7.19 b)), but only DQSI obtains the correct result for the triangular phase pattern. While the slope of both egdes is in agreement with the prediction from Jones calculus for DQSI, only the falling edge is retrieved correctly for FTSI. For the rising edge, FTSI fails because this set of subpulses overlaps temporally with the reference pulse.

The effect on the temporal pulse shape can be seen in figure 7.20. While the pulse shape from DQSI agrees well with the prediction from Jones calculus, the pulse shape from FTSI strongly deviates from the latter. The compressed component and the first set of subpulses of the second component are correct, but the second set of subpulses is completely missing. In other words, the result of FTSI suggests a substantially different pulse shape than the one which is actually generated. Thus DQSI is again more successful for the phase retrieval of a more complex pulse shape than FTSI, even if the shaped pulse partially overlaps temporally with the reference pulse.

To quantitatively asses the quality of the pulse characterisation, the error definition of section 7.3.6 is used. The results for the component-wise errors ε_1 and ε_2 as well as the combined error F are given in table 7.1. For all examples, in which the shaped and the reference pulse do not overlap temporally, the criterion F supports the trend observed in the corresponding figures of this section. Since the agreement between the predicted phases

pulse shape	**method**	ε_1	ε_2	F
linear phase	FTSI	0.291	0.386	0.23
	DQSI	0.560	0.565	0.63
sinus, quadratic phase	FTSI	0.200	0.360	0.17
	DQSI	0.609	0.702	0.86
coloured double pulse 250 fs	FTSI	0.516	0.447	0.47
	DQSI	0.540	0.529	0.57
coloured double pulse 500 fs	FTSI	1.009	1.094	2.21
	DQSI	0.771	0.699	1.08
triangle 200 fs	FTSI	0.200	0.440	0.23
	DQSI	0.470	0.661	0.66
triangle 400 fs	FTSI	0.293	0.817	0.75
	DQSI	0.497	1.001	1.25

Table 7.1: Component-wise and combined errors for all example pulse shapes discussed in this section.

and spectra from Jones calculus is better for FTSI than for DQSI, the values of F are slightly smaller for FTSI. In the case of the coloured double pulse with a slope of 500 fs, only DQSI yields the correct result while FTSI fails. Accordingly, the error F is larger by a factor of two for FTSI than for DQSI.

Nevertheless, one exception was found for which F is not a reliable accuracy criterion. In the case of the triangular phase pattern with a slope of 400 fs, again only DQSI yields the correct phase and FTSI fails, as was seen in figure 7.19 c). Unfortunately, this conclusion cannot be drawn only from the values of F, since in this case FTSI reveals a smaller value of F than DQSI, the reason of this behaviour is presently unclear. One possible explanation is that the deviations in the phase can be found mostly at frequencies where only a low spectral intensity is present. Since in the error calculation the phase is weighted with the spectral amplitude, this might lead to a lower error than one might expect from the shaped of the phase alone. Thus, F should not be used as the only criterion to asses the quality of the pulse characterisation. A direct, naked-eye comparison between the expected and measured phases and spectra is also advisable.

However, in all cases except the one just mentioned a successful pulse retrieval corresponds to a value of F in the range of or smaller than $F = 1$. Together with the naked-eye comparison of the phases, $F \leq 1$ indicates that the pulse characterisation was successful.

7.4 Conclusions on polarisation pulse shaping

In this chapter, the generation and characterisation of broadband visible polarisation-shaped femtosecond laser pulses has been discussed. Exemplary pulse shapes that have been generated in a specifically designed LCD-based pulse-shaper setup have been presented. The additional unwanted modifications to the polarisation state, caused by the optical elements in the setup, have been predicted using Jones matrix calculus with an experimentally determined Jones matrix.

For the pulse characterisation, frequency-resolved optical gating in a collinear geometry (cFROG) and spectral interferometry (SI) have been used. The cFROG measurements have served as a feedback to compress the unshaped pulse to its minimum temporal duration with the help of the pulse shaper. This compressed pulse has then been modified by applying different phase patterns at the SLM layers and the resulting pulse shape determined by SI. Two SI techniques have been compared that differ in the data acquisition scheme as well as in the data evaluation process. The well-known Fourier-transform (FT) SI is a standard technique for the characterisation of polarisation-shaped pulses and is based on a Fourier-filtering method to retrieve the phase from the interference pattern. For the first time, the method of dual quadrature (DQ) SI has been employed as a characterisation technique for broadband polarisation-shaped femtosecond laser pulses. Here, both quadratures of the SI signal are measured in order to determine the pulse shape.

Comparing the measured phases of both methods to the predicted phases from Jones calculus shows that both SI techniques perform comparably well. For most pulse shapes, the agreement between FTSI and Jones phases is slightly better than between DQSI and Jones. This might have several reasons. One is that small oscillations are present on the phases retrieved using DQSI. They stem from the imperfectness of the circular polarisation over the broad spectral range of the reference pulse. This leads to the behaviour that both SI spectra are no longer perfectly sine- and cosine-shaped over their complete spectral range and causes the mentioned oscillations. The spatial chirp of shaped and reference pulse can also lead to oscillations of the spectral phase. Due to their different and inhomogeneous beam profiles, the measured interference spectra also comprise non-interfering contributions from both pulses. Thus, the cosine- and sine-terms that are calculated from those spectra are not perfectly modulated and do not oscillate exactly between -1 and +1. Calculating the phase from those imperfetcly modulated terms can also lead to oscillations. Another reason for the better agreement between FTSI and Jones phases than for DQSI might be that the measured

phases are compared to the phases predicted by the Jones matrix which has also been measured using FTSI. Thus it is not surprising that the agreement between two quantities, that have been measured using the same technique, is higher than if different methods have been used. Thus, any non-obvious experimental error present in FTSI might favour the agreement between FTSI and Jones phases. Nevertheless, the overall performance of both SI methods is comparable for most example pulse shapes.

Although the measurement and data evaluation procedure is more intricate for DQSI and the agreement with the phases predicted from Jones matrix is not as good as for FTSI, there is one big advantage of DQSI over FTSI. The temporal ordering and temporal overlap of the shaped and reference pulses poses no restriction to DQSI. In contrast, the Fourier-filtering in FTSI can only be applied successfully if the entire shaped pulse arrives before or after the reference pulse and is temporally well separated from it. Usually a compromise for the delay between reference and shaped pulse can be found so that both are temporally well separated and the SI fringes can still be resolved properly. Still, there are some situations in which it is useful to have a characterisation method that is not affected by these restrictions. For example in the case of strongly chirped pulses or complex pulse shapes resulting from quantum-control experiments, it might be difficult to meet all requirements of FTSI. Especially if the reference pulse is not well compressed, this might render FTSI useless. This can be the case for pulses with very broadband spectra, e.g. when using the homebuilt NOPA as a laser source, since pulse compression outside the pulse shaper becomes increasingly difficult with increasing spectral width. However, for DQSI the temporal delay between the shaped and reference pulse does not have any negative effect on the phase retrieval, as long as the interference fringes can still be properly resolved. Thus, DQSI can be regarded as a useful pulse-characterisation technique also for polarisation-shaped pulses.

For a qualitative assessment of the pulse characterisation quality, an accuracy criterion has been defined in analogy to [304], based on the root-mean-square field error. Together with a naked-eye comparison of the measured and expected phase, this can serve as a reliable criterion for the quality of the pulse retrieval. Thus, in summary it is possible to generate and characterise polarisation-shaped broadband visible pulses which can be applied in a variety of experiments.

One particularly interesting field, namely chiral control, might greatly benefit from this development. Chiral control [306] can be regarded as an advancement of the quantum-control schemes discussed in section 2.4. Dif-

ferent approaches to achieve the goal of controlling the chirality using laser pulses are discussed. For example, one idea is to transform a racemic mixture of two enantiomers of a chiral substance into an equilirium state in which one enantiomer is dominant by the means of suitably shaped femtosecond laser pulses. This process is referred to as purification [307, 308]. Different theoretical approaches regarding the feasibility of chiral control exist [309–311], but so far the experimental confirmation is still lacking.

To implement the abovementioned purification process in a liquid-phase chiral-control experiment, this means in principle: One has to induce chirality in an achiral solution. Since quantum control is based on photochemical reactions, this means one can introduce the chiral information into the reaction by the use of a "chiral" electromagnetic field. This in turn can be achieved by using polarisation-shaped excitation pulses for the quantum-control experiment. Why polarisation-shaped pulses can be considered as chiral becomes clear when looking at one particularly simple polarisation state, namely circular polarisation. Depending on its handedness, the electric field of the pulse describes a right- or left-handed spiral. Both cannot be brought to coincide by rotation and/or translation alone and can thus be regarded as two "enantiomers" of one laser pulse. The same holds true for more complex polarisation-shaped pulses, thus they are a promising ingredient for a successful chiral-control experiment.

However, chiral control is experimentally very challenging and many requirements have to be met [25]. In the example of purification, a suitable molecular system has to be available which can undergo a photophysical reaction that can lead from an achiral educt to a chiral product and is spectroscopically well characterised. A robust feedback signal is necessary to determine the chirality of the sample solution, and one needs the ability to generate pulse enantiomers with very high precision. Nevertheless, different approaches exist to fullfil these conditions [25, 106, 312, 313]. Thus the availability of well characterised polarisation-shaped laser pulses may help to advance the field of chiral control.

Chapter 8

Summary

Two different questions have been addressed in this thesis. The first part dealt with the spectroscopic investigation of ultrafast light-induced charge-transfer processes in different molecular compounds. In the second part, the question of the generation and characterisation of broadband visible polarisation-shaped laser pulses was treated.

Charge transfer (CT) is one of the most basic light-induced processes in nature and plays an important role in a variety of systems. Ultrafast light-induced CT processes can be ideally studied by utilising transient-absorption spectroscopy. From the time-resolved absorption changes after excitation on the femtosecond timescale, it is possible to draw conclusions regarding the ultrafast molecular dynamics of the system under investigation. Ideal model systems to study CT dynamics stem from the class of neutral organic mixed-valence compounds. Two different examples of such systems have been discussed in chapters 4 and 5. In both cases, the structure of the molecular system has a large influence on the CT dynamics.

In chapter 4, the CT dynamics of the first polymeric neutral organic-mixed valence compound have been studied. The polymer consists of on average 12 monomeric building blocks, each comprising a triarylamine donor and a perchlorinated triphenylmethyl radical acceptor. As a reference system, the monomer was studied as well. In addition to the well-known back electron transfer from the CT state to the ground state, the transient-absorption measurements revealed an additional relaxation pathway that only exists in the polymer. It is ascribed to the equilibrium formation between the CT state and a fully charge-separated state in which the electron and the hole are no longer located on adjacent acceptor and donor units. A kinetic scheme has been proposed that explains the observed dynamics and the solvent-dependence of the reaction rates.

A two-dimensional neutral organic mixed-valence compound has been

discussed in chapter 5. Because of the C_{3h}-symmetry of the truxenone acceptor, three triarylamine donor branches can be attached to one acceptor unit, thus the resulting donor-substituted truxenones can be regarded as two-dimensional CT systems. To study the influence of the donor–acceptor distance, two truxenone systems with different bridge lengths have been examined. Although the donor–acceptor distance is expected to influence the CT dynamics, it is not the dominant factor in these truxenones. Instead, the dynamics are rather dominated by steric hindrance. Two different rotational conformers contribute to the transient absorption signals. Both conformers differ by the orientation of the donor branches with respect to the acceptor moiety and thus the electronic coupling between donor and acceptor. Qualitative potential energy surfaces along a rotational coordinate have been proposed that explain all features that can be observed in the transient-absorption data. Thus, the CT dynamics of the polyradical of chapter 4 and the truxenones of chapter 5 are both dominated by the structure and geometry of the molecular system.

As a third example, in chapter 6 the CT dynamics in a supramolecular metallo-polyelectrolyte (MEPE) have been studied. MEPEs are polymers consisting of Fe-ions, terpyridine-based ligands and the corresponding counter ions. Depending on the strength of the metal–ligand bond, dynamic materials which are stimuli-responsive can result. Upon optical excitation, a metal-to-ligand CT takes place. To unravel the CT dynamics, a MEPE polymer comprising several hundreds of monomers and the corresponding monomeric analogue have been studied. The monomeric Fe-complex shows CT dynamics comparable to those of similar Fe-terpyridine complexes. In contrast, the polymer exhibits a surprisingly small rate for the electron back-transfer. Different processes are conceivable that might explain this behaviour, i.e. an optically induced spin-crossover or a partial disassembly of the polymer. However, these are the results of the very first femtosecond time-resolved studies of MEPE and further research is needed to clarify the dominant underlying processes after optical excitation in MEPE polymers.

As a second topic, the generation and characterisation of broadband visible polarisation-shaped laser pulses has been discussed in chapter 7. The pulses are shaped in an LCD-based pulse shaper which was designed for optimal shaping of broadband visible pulses, using unshaped pulses from a noncollinear optical parametric amplifier (NOPA) as input. The characterisation and compression of the unshaped pulses was carried out using cFROG, a pulse-shaper-assisted collinear variant of frequency-resolved optical gating. To characterise the polarisation state of the shaped pulse, spectral inter-

ferometry (SI) has been used. The phase information is contained in the spectral interference between the unknown shaped and the known reference pulse. Two different SI techniques have been compared. The well-known Fourier-transform (FT) SI is a standard technique for the characterisation of polarisation-shaped laser pulses. The analysis is based on a Fourier-filtering method to retrieve the unknown phase. The less common dual-quadrature (DQ) SI has only been used for amplitude- and/or phase-shaped pulses so far and has now been extended for the characterisation of polarisation-shaped pulses. In DQSI both quadratures of the interferogram are measured simultaneously, by using a circularly polarised reference pulse, and are then used for phase retrieval. The results of both methods have been compared to the prediction from Jones calculus, using an experimentally determined Jones matrix. For the quantification of the pulse retrieval quality, an accuracy criterion has been introduced which is based on the root mean-square field error.

It was found that both SI techniques perform comparably well, although the agreement between measured and Jones-phase is slightly better for FTSI than for DQSI. Nevertheless, in DQSI—unlike in FTSI—the phase retrieval works even in the temporal overlap of shaped and reference pulse, and independent of the temporal ordering of the pulses, which has been verified experimentally. It was shown that DQSI is also a suitable characterisation technique for polarisation-shaped laser pulses, and it is furthermore more versatile regarding the temporal ordering and separation of the pulses than FTSI. Thus, broadband visible polarisation-shaped laser pulses can be generated and characterised sucessfully.

These pulses can be useful in a variety of applications ranging from spectroscopy to quantum control. They can be especially useful for the advancement of the field of chiral control, in which the polarisation state of the utilised laser pulses plays a crucial role.

Zusammenfassung

Im Rahmen dieser Dissertation wurden zwei verschiedene Fragestellungen diskutiert. Der erste Teil der Arbeit behandelte die spektroskopische Untersuchung von ultraschnellen lichtinduzierten Ladungstransferprozessen in unterschiedlichen molekularen Verbindungen. Im zweiten Teil wurde die Erzeugung und Charakterisierung von breitbandigen polarisationsgeformten Laserpulsen im sichtbaren Spektralbereich diskutiert.

Ladungstransfer (charge transfer, CT) ist einer der grundlegenden lichtinduzierten Prozesse in der Natur und spielt in einer Vielzahl von Systemen eine wichtige Rolle. Ultraschnelle lichtinduizerte CT-Prozesse lassen sich besonders gut unter Zuhilfenahme von transienter Absorptionsspektroskopie untersuchen. Anhand der zeitaufgelösten Absorptionsänderungen nach Anregung auf der Femtosekundenzeitskala lassen sich Rückschlüsse ziehen auf die ultraschnelle molekulare Dynamik des zu untersuchenden Systems. Ideale Modellsysteme liefert die Klasse der neutralen organischen gemischtvalenten Verbindungen. Zwei unterschiedliche Beispiele aus dieser Verbindungsklasse wurden in den Kapiteln 4 und 5 vorgestellt. In beiden Fällen hatte die Struktur der Verbindung einen großen Einfluss auf die CT-Dynamik.

In Kapitel 4 wurde die CT-Dynamik der ersten polymeren neutralen organischen gemischtvalenten Verbindung untersucht. Das Polymer setzt sich aus durchschnittlich 12 Monomereinheiten zusammen, die wiederum aus einem Triarylamin-Donor und einem perchlorierten Triphenylmethyradikal-Akzeptor bestehen. Das Monomer diente als Referenzsystem, daher wurde seine CT-Dynamik ebenfalls untersucht. Durch transiente Absorptionsmessungen stellte sich heraus, dass zusätzlich zum Elektronen-Rücktransfer vom CT- in den Grundzustand ein weiterer Relaxationspfad existiert, der jedoch nur im Polymer beobachtet werden kann. Dieser wird einem Gleichgewicht zugeschrieben, das sich zwischen dem CT-Zustand und einem völlig ladungsgetrennten Zustand einstellt, in dem sich das Elektron und das Loch nicht länger an benachbarten Akzeptor- und Donoreinheiten befinden. Es wurde ein Reaktionsschema vorgestellt, im Rahmen dessen sich sowohl die beobachtete Dynamik als auch die Lösemittelabhängigkeit der Reaktionsraten erklä-

ren lassen.

Eine zweidimensionale neutrale organische gemischtvalente Verbindung wurde in Kapitel 5 vorgestellt. Aufgrund der C_{3h}-Symmetrie des Truxenon-Akzeptors ist es möglich, drei gleichwertige Triarylamin-Donoren mit dem Akzeptor zu verknüpfen, weswegen die so entstandenen Donor-substituierten Truxenone als zweidimensionale CT-Systeme betrachtet werden können. Um den Einfluss des Donor-Akzeptor-Abstands auf die CT-Dynamik zu untersuchen, wurden zwei Truxenon-Systeme mit unterschiedlich langen Brücken zwischen Donor und Akzeptor verwendet. Obwohl erwartet wird, dass der Donor-Akzeptor-Abstand die CT-Dynamik durchaus beeinflusst, ist dies nicht der dominante Effekt in den hier vorliegenden Truxenonen. Die Dynamik wird vielmehr durch sterische Hinderung im System dominiert. Zwei unterschiedliche Rotationskonformere tragen zum transienten Absorptionssignal bei. Beide unterscheiden sich durch die relative Orientierung von Donor und Akzeptor zueinander, wodurch sie eine unterschiedlich starke elektronische Kopplung zwischen Donor und Akzeptor aufweisen. Qualitative Potentialhyperflächen entlang einer Rotationskoordinate wurden vorgestellt, mit deren Hilfe sich alle Charakteristika erklären lassen, die in den transienten Absorptionsdaten beobachtet wurden. Folglich lässt sich sagen, dass sowohl im Polyradikal aus Kapitel 4 als auch in den Truxenonen aus Kapitel 5 die CT-Dynamik durch die Struktur und die Geometrie des molekularen Systems dominiert wird.

Als drittes Beispiel wurde in Kapitel 6 die CT-Dynamik eines supramolekularen Metallo-Polyelektrolyts (MEPE) untersucht. MEPEs sind Polymere, die aus Fe-Ionen, Terpyridin-basierten Liganden und den entsprechenden Gegenionen aufgebaut sind. Abhängig von der Stärke der Metall–Liganden-Bindung können dynamische Materialien enstehen, die auf externe Stimuli reagieren. Nach optischer Anregung findet ein Metall-Liganden-CT statt. Um dessen Dynamik genauer zu verstehen, wurden ein MEPE-Polymer, bestehend aus einigen Hundert Monomereinheiten, und der entsprechende monomere Komplex untersucht. Dabei weist der monomere Fe-Komplex eine CT-Dynamik auf, die vergleichbar ist mit der CT-Dynamik ähnlicher Fe-Terpyridin-Komplexe. Im Gegensatz dazu zeigt das MEPE-Polymer eine überraschend kleine Rate für den Elektronen-Rücktransfer. Dafür können unterschiedliche Prozesse verantwortliche sein, z.B. ein optisch induzierter Spin-Übergang oder ein partielles Auseinanderbrechen des Polymers. Da es sich hier um die Ergebnisse aus den ersten femtosekunden-zeitaufgelösten Untersuchungen an MEPE handelt, sind weitere Untersuchungen notwendig, um abschließend zu klären, welche Prozesse in MEPE-Polymeren die Dynamik nach optischer Anregung dominieren.

Die zweite Fragestellung dieser Arbeit, die Erzeugung und Charakterisierung breitbandiger polarisationsgeformter Laserpulse im sichtbaren Spektralbereich, wurde in Kapitel 7 diskutiert. Pulsformung wird mittels eines LCD-basierten Pulsformers erreicht, der speziell für die Formung breitbandiger Pulse im Sichtbaren entwickelt wurde. Zur Erzeugung der ungeformten Eingangspulse wurde ein nichtkollinearer optisch-parametrischer Verstärker (NOPA) verwendet. Diese Pulse wurden mit Hilfe von cFROG charakterisiert und zeitlich komprimiert, wobei es sich bei cFROG um eine kollineare Pulsformer-gestütze Variante des frequenzaufgelösten optischen Gatterns handelt. Um den Polarisationszustand der geformten Pulse zu ermittel wurde spektrale Interferometrie (SI) genutzt. Hierbei ist die Phaseninformation in der spektralen Interferenz zwischen dem unbekannten geformten Puls und einem bekannten Referenzpuls enthalten. Zwei unterscheidliche SI-Methoden wurden miteinander verglichen. Die weit verbreitete Fourier-Transformation(FT)-SI hat sich zu einer Standard-Charakterisierungsmethode für polarisationsgeformte Laserpulse entwickelt. Die Auswertung stützt sich dabei auf eine Fourier-Filterung, um die unbekannte Phase zu bestimmen. Die weniger verbreitete Zwei-Quadratur (dual quadrature, DQ)-SI wurde bisher nur zur Charakterisierung von amplituden- und/oder phasengeformten Laserpulsen verwendet. Sie wurde im Rahmen dieser Arbeit erweitert, so dass die Charakterisierung von polarisationsgeformten Laserpulsen mittels DQSI jetzt auch möglich ist. Bei der DQSI werden beide Quadraturen des Interferenzsignals gleichzeitig gemessen, indem man einen zirkular polarisierten Referenzpuls verwendet. Beide Quadraturen werden zur Bestimmung der Phase herangezogen. Die Ergebnisse beider SI-Methoden wurden mit der Vorhersage einer Jones-Matrix-Berechnung verglichen, wobei eine experimentell bestimmte Jones-Matrix verwendet wurde. Um die Qualität der Pulscharakterisierung zu quantifizieren, wurde ein Kriterium für die Genauigkeit eingeführt, dass auf der Wurzel des mittleren quadratischen Fehlers der elektrischen Felder basiert.

Es stellt sich heraus, dass beide SI-Methoden eine durchaus vergleichbare Leistung bringen, wobei die Übereinstimmung zwischen gemessener und mit Jones-Matrix berechneter Phase für FTSI etwas besser ist als für DQSI. Nichtsdestoweniger ist bei DQSI, anders als bei FTSI, die Bestimmung der Phase auch dann noch möglich, wenn geformter und Referenzpuls zeitlich überlappen, unabhängig von der Reihenfolge der einzelnen (Sub-)Pulse. Dies wurde experimentell bestätigt. Damit wurde gezeigt, dass DQSI auch zur Charakterisierung breitbandiger polarisationsgeformter Pulse geeignet ist. DQSI ist des Weiteren vielseitiger in Bezug auf die zeitliche Reihenfolge und den zeitlichen Abstand zwischen den einzelnen Pulsen als FTSI. Damit

ist es möglich, breitbandige polarisationsgeformte Laserpulse im sichtbaren Spektralbereich sowohl zu erzeugen als auch zu charakterisieren.

Es existieren zahlreiche Anwedungsmöglichkeiten für diese Pulse, vor allem im Bereich der Spektroskopie und Quantenkontrolle. Besonders das Forschungsgebiet der chiralen Kontrolle, bei dem der Polarisationszustand der verwendeten Laserpulse eine wichtige Rolle spielt, kann von der Verfügbarkeit breitbandiger polarisationsgeformter Laserpulse profitieren.

Bibliography

[1] R. E. Blankenship.
Molecular mechanisms of photosynthesis.
Blackwell Science, Oxford [u.a.] (2002).

[2] D. L. Andrews.
Applied Laser Spectroscopy: Techniques, Instrumentation and Applications.
First edition. Wiley & Sons (1992).

[3] W. W. Parson.
Modern Optical Spectroscopy: With Exercises and Examples from Biophysics and Biochemistry.
Second edition. Springer-Verlag (2009).

[4] F. C. DeSchryver, S. DeFeyter, G. Schweitzer, and S. D. Feyter.
Femtochemistry. With the Nobel Lecture of A. Zewail.
Wiley-VCH (2001).

[5] V. May and O. Kühn.
Charge and Energy Transfer Dynamics in Molecular Systems.
Second edition. Wiley-VCH Verlag GmbH (2004).

[6] W. Zinth and J. Wachtveitl.
The First Picoseconds in Bacterial Photosynthesis—Ultrafast Electron Transfer for the Efficient Conversion of Light Energy.
ChemPhysChem **6**, 871–880 (2005).

[7] D. Voet, J. G. Voet, and C. W. Pratt.
Fundamentals of biochemistry: life at the molecular level.
Wiley (2006).

[8] A. Heckmann and C. Lambert.
Organic Mixed-Valence Compounds: A Playground for Electrons and Holes.

Angewandte Chemie International Edition **51**, 326–392 (2012).

[9] J. B. Beck and S. J. Rowan.
Multistimuli, Multiresponsive Metallo-Supramolecular Polymers.
J. Am. Chem. Soc. **125**, 13922–13923 (2003).

[10] S. J. Rowan and J. B. Beck.
Metal–ligand induced supramolecular polymerization: A route to responsive materials.
Faraday Discuss. **128**, 43–53 (2004).

[11] S. A. Rice and M. Zhao.
Optical Control of Molecular Dynamics.
Wiley-Interscience, New York (2000).

[12] A. M. Weiner.
Ultrafast optical pulse shaping: A tutorial review.
Optics Communications **284**, 3669–3692 (2011).

[13] V. I. Prokhorenko, A. M. Nagy, S. A. Waschuk, L. S. Brown, R. R. Birge, and R. J. D. Miller.
Coherent Control of Retinal Isomerization in Bacteriorhodopsin.
Science **313**, 1257–1261 (2006).

[14] A. Assion, T. Baumert, M. Bergt, T. Brixner, B. Kiefer, V. Seyfried, M. Strehle, and G. Gerber.
Control of Chemical Reactions by Feedback-Optimized Phase-Shaped Femtosecond Laser Pulses.
Science **282**, 919–922 (1998).

[15] P. Nuernberger, D. Wolpert, H. Weiss, and G. Gerber.
Femtosecond quantum control of molecular bond formation.
Proceedings of the National Academy of Sciences **107**, 10366 –10370 (2010).

[16] J. L. Herek, W. Wohlleben, R. J. Cogdell, D. Zeidler, and M. Motzkus.
Quantum control of energy flow in light harvesting.
Nature **417**, 533–535 (2002).

[17] L. Lepetit, G. Chériaux, and M. Joffre.
Linear techniques of phase measurement by femtosecond spectral interferometry for applications in spectroscopy.
Journal of the Optical Society of America B **12**, 2467–2474 (1995).

[18] M. Wollenhaupt, A. Assion, and T. Baumert.
Femtosecond Laser Pulses: Linear Properties, Manipulation, Generation and Measurement.
In *Springer Handbook of Lasers and Optics*, pp. 937–983 (2007).

[19] T. Brixner, G. Krampert, P. Niklaus, and G. Gerber.
Generation and characterization of polarization-shaped femtosecond laser pulses.
Applied Physics B: Lasers and Optics **74**, 133–144 (2002).

[20] T. Brixner.
Poincaré representation of polarization-shaped femtosecond laser pulses.
Applied Physics B: Lasers and Optics **76**, 531–540 (2003).

[21] R. W. Boyd.
Nonlinear Optics.
Third edition. Academic Press (2008).

[22] G. Yang and Y. R. Shen.
Spectral broadening of ultrashort pulses in a nonlinear medium.
Optics Letters **9**, 510–512 (1984).

[23] M. Ziolek, R. Naskrecki, and J. Karolczak.
Some temporal and spectral properties of femtosecond supercontinuum important in pump-probe spectroscopy.
Optics Communications **241**, 221–229 (2004).

[24] G. Cerullo and S. De Silvestri.
Ultrafast optical parametric amplifiers.
Review of Scientific Instruments **74**, 1 (2003).

[25] F. Langhojer.
New techniques in liquid-phase ultrafast spectroscopy.
Dissertation, Universität Würzburg (2009).

[26] E. Riedle, M. Beutter, S. Lochbrunner, J. Piel, S. Schenkl, S. Sporlein, and W. Zinth.
Generation of 10 to 50 fs pulses tunable through all of the visible and the NIR.
Applied Physics B: Lasers and Optics **71**, 457–465 (2000).

[27] T. Kobayashi and A. Baltuska.

Sub-5 fs pulse generation from a noncollinear optical parametric amplifier.
Measurement Science & Technology **13**, 1671–1682 (2002).

[28] G. Cerullo, M. Nisoli, S. Stagira, and S. De Silvestri.
Sub-8-fs pulses from an ultrabroadband optical parametric amplifier in the visible.
Optics Letters **23**, 1283–1285 (1998).

[29] S. Mukamel.
Principles of Nonlinear Optical Spectroscopy.
Oxford University Press, New York (1999).

[30] R. Berera, R. van Grondelle, and J. T. M. Kennis.
Ultrafast transient absorption spectroscopy: principles and application to photosynthetic systems.
Photosynthesis Research **101**, 105–118 (2009).

[31] V. Sundström.
Femtobiology.
Annual Review of Physical Chemistry **59**, 53–77 (2008).

[32] C. Cimpean, V. Groenewegen, V. Kuntermann, A. Sommer, and C. Kryschi.
Ultrafast exciton relaxation dynamics in silicon quantum dots.
Laser & Photonics Reviews **3**, 138–145 (2009).

[33] F. Schwabl.
Quantenmechanik.
6th edition. Springer, Berlin (2007).

[34] S. A. Kovalenko, A. L. Dobryakov, J. Ruthmann, and N. P. Ernsting.
Femtosecond spectroscopy of condensed phases with chirped supercontinuum probing.
Physical Review A **59**, 2369–2384 (1999).

[35] M. Shapiro and P. Brumer.
Laser control of product quantum state populations in unimolecular reactions.
The Journal of Chemical Physics **84**, 4103 (1986).

[36] P. Brumer and M. Shapiro.
Control of unimolecular reactions using coherent light.
Chemical Physics Letters **126**, 541–546 (1986).

[37] D. Meshulach and Y. Silberberg.
Coherent quantum control of two-photon transitions by a femtosecond laser pulse.
Nature **396**, 239–242 (1998).

[38] D. Meshulach and Y. Silberberg.
Coherent quantum control of multiphoton transitions by shaped ultrashort optical pulses.
Physical Review A **60**, 1287 (1999).

[39] D. J. Tannor and S. A. Rice.
Control of selectivity of chemical reaction via control of wave packet evolution.
The Journal of Chemical Physics **83**, 5013–5018 (1985).

[40] U. Gaubatz, P. Rudecki, S. Schiemann, and K. Bergmann.
Population transfer between molecular vibrational levels by stimulated Raman scattering with partially overlapping laser fields. A new concept and experimental results.
The Journal of Chemical Physics **92**, 5363 (1990).

[41] D. J. Tannor.
Introduction to Quantum Mechanics: A Time-Dependent Perspective.
Palgrave Macmillan (2007).

[42] S. Shi and H. Rabitz.
Optimal control of bond selectivity in unimolecular reactions.
Computer Physics Communications **63**, 71–83 (1991).

[43] R. Chakrabarti and H. Rabitz.
Quantum control landscapes.
International Reviews in Physical Chemistry **26**, 671 (2007).

[44] R. S. Judson and H. Rabitz.
Teaching lasers to control molecules.
Physical Review Letters **68**, 1500–1503 (1992).

[45] T. Baumert, M. Grosser, R. Thalweiser, and G. Gerber.
Femtosecond time-resolved molecular multiphoton ionization: The Na2 system.
Physical Review Letters **67**, 3753–3756 (1991).

[46] T. Brixner and G. Gerber.
Quantum Control of Gas-Phase and Liquid-Phase Femtochemistry.

ChemPhysChem **4**, 418–438 (2003).

[47] T. Brixner, N. H. Damrauer, P. Niklaus, and G. Gerber.
Photoselective adaptive femtosecond quantum control in the liquid phase.
Nature **414**, 57–60 (2001).

[48] T. Dekorsky, W. Kütt, T. Pfeifer, and H. Kurz.
Coherent Control of LO-Phonon Dynamics in Opaque Semiconductors by Femtosecond Laser Pulses.
Europhysics Letters (EPL) **23**, 223–228 (1993).

[49] N. H. Bonadeo, J. Erland, D. Gammon, D. Park, D. S. Katzer, and D. G. Steel.
Coherent Optical Control of the Quantum State of a Single Quantum Dot.
Science **282**, 1473 –1476 (1998).

[50] S. Kirkpatrick, C. D. Gelatt, and M. P. Vecchi.
Optimization by Simulated Annealing.
Science **220**, 671 –680 (1983).

[51] G. Bhanot.
The Metropolis algorithm.
Reports on Progress in Physics **51**, 429–457 (1988).

[52] C. Gollub and R. de Vivie-Riedle.
Modified ant-colony-optimization algorithm as an alternative to genetic algorithms.
Physical Review A **79**, 021401 (2009).

[53] D. E. Goldberg.
Genetic Algorithms in Search, Optimization, and Machine Learning.
First edition. Addison-Wesley Professional (1989).

[54] H. Schwefel.
Evolution and Optimum Seeking.
Har/Dis edition. Wiley-Interscience (1995).

[55] S. Ruetzel, C. Stolzenberger, F. Dimler, D. J. Tannor, and T. Brixner.
Adaptive coherent control using the von Neumann basis.
Physical Chemistry Chemical Physics (2011).

[56] C. J. Bardeen, V. V. Yakovlev, K. R. Wilson, S. D. Carpenter, P. M. Weber, and W. S. Warren.
Feedback quantum control of molecular electronic population transfer.
Chemical Physics Letters **280**, 151–158 (1997).

[57] P. Nuernberger, G. Vogt, T. Brixner, and G. Gerber.
Femtosecond quantum control of molecular dynamics in the condensed phase.
Physical Chemistry Chemical Physics **9**, 2470–2497 (2007).

[58] A. M. Weiner.
Femtosecond pulse shaping using spatial light modulators.
Review of Scientific Instruments **71**, 1929 (2000).

[59] A. Monmayrant, S. Weber, and B. Chatel.
A newcomer's guide to ultrashort pulse shaping and characterization.
Journal of Physics B: Atomic, Molecular and Optical Physics **43**, 103001 (2010).

[60] A. M. Weiner, D. E. Leaird, J. S. Patel, and J. R. Wullert.
Programmable femtosecond pulse shaping by use of a multielement liquid-crystal phase modulator.
Optics Letters **15**, 326–328 (1990).

[61] A. M. Weiner, D. E. Leaird, J. S. Patel, and J. R. Wullert.
Programmable shaping of femtosecond optical pulses by use of 128-element liquid-crystal phase modulator.
IEEE Journal of Quantum Electronics **28**, 908–920 (1992).

[62] T. Brixner and G. Gerber.
Femtosecond polarization pulse shaping.
Optics Letters **26**, 557–559 (2001).

[63] L. Polachek, D. Oron, and Y. Silberberg.
Full control of the spectral polarization of ultrashort pulses.
Optics Letters **31**, 631–633 (2006).

[64] F. Weise and A. Lindinger.
Full control over the electric field using four liquid crystal arrays.
Optics Letters **34**, 1258–1260 (2009).

[65] *SLM Spatial light modulator.*
rev. 1.5 edition. CRI Cambrigde Research and Instrumentation (2006).

[66] M. M. Wefers and K. A. Nelson.
Analysis of programmable ultrashort waveform generation using liquid-crystal spatial light modulators.
Journal of the Optical Society of America B **12**, 1343–1362 (1995).

[67] T. Brixner.
Kohärente Kontrolle von Photodissoziationsreaktionen mit optimal geformten ultrakurzen Laserpulsen.
Diplomarbeit, Universität Würzburg (1998).

[68] M. M. Wefers and K. A. Nelson.
Generation of high-fidelity programmable ultrafast optical waveforms.
Optics Letters **20**, 1047–1049 (1995).

[69] M. Ninck, A. Galler, T. Feurer, and T. Brixner.
Programmable common-path vector field synthesizer for femtosecond pulses.
Optics Letters **32**, 3379–3381 (2007).

[70] O. Masihzadeh, P. Schlup, and R. A. Bartels.
Complete polarization state control of ultrafast laser pulses with a single linear spatial light modulator.
Optics Express **15**, 18025–18032 (2007).

[71] *Silhouette Ultrafast Pulse Shaping and Measurement.*
Coherent Inc. (2011).

[72] J. Vaughan, T. Feurer, K. Stone, and K. Nelson.
Analysis of replica pulses in femtosecond pulse shaping with pixelated devices.
Optics Express **14**, 1314–1328 (2006).

[73] M. B. Danailov and I. P. Christov.
Time-space Shaping of Light Pulses by Fourier Optical Processing.
Journal of Modern Optics **36**, 725–731 (1989).

[74] M. Wefers and K. Nelson.
Space-time profiles of shaped ultrafast optical waveforms.
IEEE Journal of Quantum Electronics **32**, 161–172 (1996).

[75] F. Frei, A. Galler, and T. Feurer.
Space-time coupling in femtosecond pulse shaping and its effects on coherent control.
The Journal of Chemical Physics **130**, 034302–14 (2009).

[76] M. E. van Brederode and R. van Grondelle.
New and unexpected routes for ultrafast electron transfer in photosynthetic reaction centers.
FEBS Letters **455**, 1–7 (1999).

[77] L. Marrot and J. Meunier.
Skin DNA photodamage and its biological consequences.
Journal of the American Academy of Dermatology **58**, S139–S148 (2008).

[78] A. Sancar.
Structure and Function of DNA Photolyase and Cryptochrome Blue-Light Photoreceptors.
Chem. Rev. **103**, 2203–2238 (2011).

[79] Y. Kao, C. Saxena, L. Wang, A. Sancar, and D. Zhong.
Femtochemistry in enzyme catalysis: DNA photolyase.
Cell Biochemistry and Biophysics **48**, 32–44 (2007).

[80] P. W. M. Blom, V. D. Mihailetchi, L. J. A. Koster, and D. E. Markov.
Device Physics of Polymer: Fullerene Bulk Heterojunction Solar Cells.
Advanced Materials **19**, 1551–1566 (2007).

[81] R. D. Pensack, K. M. Banyas, L. W. Barbour, M. Hegadorn, and J. B. Asbury.
Ultrafast vibrational spectroscopy of charge-carrier dynamics in organic photovoltaic materials.
Physical Chemistry Chemical Physics **11**, 2575 (2009).

[82] A. Heckmann, C. Lambert, M. Goebel, and R. Wortmann.
Synthesis and Photophysics of a Neutral Organic Mixed-Valence Compound.
Angewandte Chemie International Edition **43**, 5851–5856 (2004).

[83] A. Heckmann and C. Lambert.
Neutral Organic Mixed-Valence Compounds: Synthesis and All-Optical Evaluation of Electron-Transfer Parameters.
Journal of the American Chemical Society **129**, 5515–5527 (2007).

[84] M. B. Robin, P. Day, H. Emeléus, and A. Sharpe.
Mixed Valence Chemistry-A Survey and Classification.
volume Volume 10, pp. 247–422. Academic Press (1968).

[85] C. Lambert and G. Nöll.
The Class II/III Transition in Triarylamine Redox Systems.
J. Am. Chem. Soc. **121**, 8434–8442 (1999).

[86] K. D. Demadis, C. M. Hartshorn, and T. J. Meyer.
The Localized-to-Delocalized Transition in Mixed-Valence Chemistry.
Chem. Rev. **101**, 2655–2686 (2001).

[87] S. F. Nelsen, K. P. Schultz, and J. P. Telo.
Interpretation of Mixed-Valence Compound Optical Spectra Near the Class II/III Border: Dinitrobiphenyl and Dinitrophenanthrene Radical Anions.
J. Phys. Chem. A **112**, 12622–12628 (2008).

[88] R. A. Marcus.
On the Theory of Oxidation-Reduction Reactions Involving Electron Transfer. I.
The Journal of Chemical Physics **24**, 966 (1956).

[89] R. A. Marcus and N. Sutin.
Electron transfers in chemistry and biology.
Biochimica et Biophysica Acta (BBA) - Reviews on Bioenergetics **811**, 265–322 (1985).

[90] B. S. Brunschwig and N. Sutin.
Energy surfaces, reorganization energies, and coupling elements in electron transfer.
Coordination Chemistry Reviews **187**, 233–254 (1999).

[91] J. R. Miller, L. T. Calcaterra, and G. L. Closs.
Intramolecular long-distance electron transfer in radical anions. The effects of free energy and solvent on the reaction rates.
Journal of the American Chemical Society **106**, 3047–3049 (1984).

[92] J. Jortner.
Temperature dependent activation energy for electron transfer between biological molecules.
The Journal of Chemical Physics **64**, 4860 (1976).

[93] N. S. Hush.
Homogeneous and heterogeneous optical and thermal electron transfer.
Electrochimica Acta **13**, 1005–1023 (1968).

[94] N. S. Hush.
Distance Dependence of Electron Transfer Rates.
Coordination Chemistry Reviews **64**, 135–157 (1985).

[95] R. S. Mulliken.
Molecular Compounds and their Spectra. II.
J. Am. Chem. Soc. **74**, 811–824 (1952).

[96] J. Jortner and M. Bixon.
Intramolecular vibrational excitations accompanying solvent-controlled electron transfer reactions.
The Journal of Chemical Physics **88**, 167 (1988).

[97] L. J. Root and M. J. Ondrechen.
Adiabatic potentials for a bridged three-site electron-transfer system.
Chemical Physics Letters **93**, 421–424 (1982).

[98] S. B. Piepho.
Vibronic coupling model for the calculation of mixed-valence line shapes: the interdependence of vibronic and MO effects.
J. Am. Chem. Soc. **110**, 6319–6326 (1988).

[99] D. S. Talaga and J. I. Zink.
Symmetry and Local Mode Coupling in Absorption and Raman Spectroscopy of Intervalence Electronic Transitions.
J. Phys. Chem. A **105**, 10511–10519 (2001).

[100] R. J. Cave and M. D. Newton.
Generalization of the Mulliken-Hush treatment for the calculation of electron transfer matrix elements.
Chemical Physics Letters **249**, 15–19 (1996).

[101] S. B. Piepho, E. R. Krausz, and P. N. Schatz.
Vibronic coupling model for calculation of mixed valence absorption profiles.
J. Am. Chem. Soc. **100**, 2996–3005 (1978).

[102] J. Seibt, A. Schaumlöffel, C. Lambert, and V. Engel.
Quantum Study of the Absorption Spectroscopy of Bis(triarylamine) Radical Cations.
J. Phys. Chem. A **112**, 10178–10184 (2008).

[103] V. Coropceanu, M. Malagoli, J. M. André, and J. L. Brédas.

Charge-Transfer Transitions in Triarylamine Mixed-Valence Systems: A Joint Density Functional Theory and Vibronic Coupling Study.
J. Am. Chem. Soc. **124**, 10519–10530 (2002).

[104] V. Coropceanu, C. Lambert, G. Nöll, and J. Brédas.
Charge-transfer transitions in triarylamine mixed-valence systems: the effect of temperature.
Chemical Physics Letters **373**, 153–160 (2003).

[105] M. Kullmann.
Transiente Absorptionsspektroskopie an einem molekularen Schalter auf Spiropyranbasis.
Diplomarbeit, Universität Würzburg (2009).

[106] Johannes Buback.
Femtochemistry of Pericyclic Reactions and Advances towards Chiral Control.
Dissertation, Universität Würzburg (2011).

[107] Spectra Physics.
Mai Tai-Series - User's Manual (2009).

[108] D. Strickland and G. Mourou.
Compression of amplified chirped optical pulses.
Optics Communications **56**, 219–221 (1985).

[109] P. Maine, D. Strickland, P. Bado, M. Pessot, and G. Mourou.
Generation of ultrahigh peak power pulses by chirped pulse amplification.
IEEE Journal of Quantum Electronics **24**, 398–403 (1988).

[110] Spectra Physics.
Solstice - One-box ultrafast amplifier system - User's manual (2008).

[111] Light Conversion.
Topas Series Traveling-wave Optical Parametric Amplifiers, User's Manual (2009).

[112] Newport.
(M-)IMS-LM High-Performance Long-Travel Linear Motor Stages, User's Manual (2009).

[113] Newport.
XPS Controller Universal High-Performance Motion Controller/Driver, User's Manual (2006).

[114] A. Brodeur and S. L. Chin.
Band-Gap Dependence of the Ultrafast White-Light Continuum.
Physical Review Letters **80**, 4406 (1998).

[115] D. Linde.
Characterization of the noise in continuously operating mode-locked lasers.
Applied Physics B Photophysics and Laser Chemistry **39**, 201–217 (1986).

[116] S. Keiber.
Investigation of the electron transfer properties of a neutral mixed-valence polymer and introduction of a shot-to-shot readout mechanism for high repitition rates.
Masterarbeit, Würzburg (2011).

[117] C. Schriever, S. Lochbrunner, E. Riedle, and D. J. Nesbitt.
Ultrasensitive ultraviolet-visible 20 fs absorption spectroscopy of low vapor pressure molecules in the gas phase.
Review of Scientific Instruments **79**, 013107 (2008).

[118] S. Karg.
Transiente Absorptionsspektroskopie im sichtbaren Spektralbereich.
Diplomarbeit, Würzburg (2009).

[119] Coherent Inc.
Operator's Manual, Mira Model 900-B Laser (1993).

[120] Coherent Inc.
Operator's Manual, RegA Model 9000 Laser (1997).

[121] Coherent Inc.
Operator's Manual, Verdi V-18 Diode-Pumped Lasers (2005).

[122] Coherent Inc.
Operator's Manual, The Coherent Model 9400 Optical Parametric Amplifier (OPA) (1994).

[123] K. W. DeLong, R. Trebino, J. Hunter, and W. E. White.
Frequency-resolved optical gating with the use of second-harmonic generation.
Journal of the Optical Society of America B **11**, 2206–2215 (1994).

[124] R. Trebino.
Frequency-Resolved Optical Gating: The Measurement of Ultrashort Laser Pulses.
Har/Cdr edition. Springer Netherlands (2002).

[125] D. J. Kane.
Real-time measurement of ultrashort laser pulses using principal component generalized projections.
IEEE Journal of Selected Topics in Quantum Electronics **4**, 278–284 (1998).

[126] R. L. Fork, O. E. Martinez, and J. P. Gordon.
Negative dispersion using pairs of prisms (1984).

[127] S. Akturk, X. Gu, M. Kimmel, and R. Trebino.
Extremely simple single-prism ultrashort- pulse compressor.
Optics Express **14**, 10101–10108 (2006).

[128] F. Kanal.
Untersuchung lichtinduzierter Ladungstransfer-Prozesse mittels transienter Absorptionsspektroskopie im sichtbaren Spektralbereich.
Diplomarbeit, Würzburg (2010).

[129] A. Maciejewski, R. Naskrecki, M. Lorenc, M. Ziolek, J. Karolczak, J. Kubicki, M. Matysiak, and M. Szymanski.
Transient absorption experimental set-up with femtosecond time resolution. Femto- and picosecond study of DCM molecule in cyclohexane and methanol solution.
Journal of Molecular Structure **555**, 1–13 (2000).

[130] I. H. M. van Stokkum, D. S. Larsen, and R. van Grondelle.
Global and target analysis of time-resolved spectra.
Biochimica et Biophysica Acta (BBA) - Bioenergetics **1657**, 82–104 (2004).

[131] D. Reitzenstein, T. Quast, F. Kanal, M. Kullmann, S. Ruetzel, M. S. Hammer, C. Deibel, V. Dyakonov, T. Brixner, and C. Lambert.
Synthesis and Electron Transfer Characteristics of a Neutral, Low-Band-Gap, Mixed-Valence Polyradical.
Chem. Mater. **22**, 6641–6655 (2010).

[132] D. Reitzenstein.
Donor-Acceptor Conjugated Polymers for Applications in Organic Electronic Devices.

Dissertation, Würzburg (2010).

[133] I. R. Gould, D. Noukakis, L. Gomez-Jahn, R. H. Young, J. L. Goodman, and S. Farid.
Radiative and nonradiative electron transfer in contact radical-ion pairs.
Chemical Physics **176**, 439–456 (1993).

[134] M. D. Newton.
Quantum chemical probes of electron-transfer kinetics: the nature of donor-acceptor interactions.
Chem. Rev. **91**, 767–792 (1991).

[135] S. Dümmler, W. Roth, I. Fischer, A. Heckmann, and C. Lambert.
Excited-state dynamics in a neutral organic mixed-valence compound.
Chemical Physics Letters **408**, 264–268 (2005).

[136] R. Maksimenka, M. Margraf, J. Köhler, A. Heckmann, C. Lambert, and I. Fischer.
Femtosecond dynamics of electron transfer in a neutral organic mixed-valence compound.
Chemical Physics **347**, 436–445 (2008).

[137] P. F. Barbara and W. Jarzeba.
Dynamic solvent effects on polar and nonpolar isomerizations.
Acc. Chem. Res. **21**, 195–199 (1988).

[138] M. J. Weaver and G. E. McManis.
Dynamical solvent effects on electron-transfer processes: recent progress and perspectives.
Acc. Chem. Res. **23**, 294–300 (1990).

[139] H. Heitele.
Dynamische Lösungsmitteleffekte bei Elektronentransferreaktionen.
Angewandte Chemie **105**, 378–398 (1993).

[140] R. M. Stratt and M. Maroncelli.
Nonreactive Dynamics in Solution: The Emerging Molecular View of Solvation Dynamics and Vibrational Relaxation.
J. Phys. Chem. **100**, 12981–12996 (1996).

[141] M. L. Horng, J. A. Gardecki, A. Papazyan, and M. Maroncelli.
Subpicosecond Measurements of Polar Solvation Dynamics: Coumarin 153 Revisited.

J. Phys. Chem. **99**, 17311–17337 (1995).

[142] A. Heckmann, S. Dümmler, J. Pauli, M. Margraf, J. Köhler, D. Stich, C. Lambert, I. Fischer, and U. Resch-Genger.
Highly Fluorescent Open-Shell NIR Dyes: The Time-Dependence of Back Electron Transfer in Triarylamine-Perchlorotriphenylmethyl Radicals.
The Journal of Physical Chemistry C **113**, 20958–20966 (2009).

[143] P. T. Kissinger and W. R. Heineman.
Laboratory Techniques in Electroanalytical Chemistry.
Revised, expand. edition. Marcel Dekker Inc (1996).

[144] A. J. Bard and L. R. Faulkner.
Electrochemical Methods: Fundamentals and Applications.
Second edition. John Wiley & Sons (2001).

[145] J. Zaumseil and H. Sirringhaus.
Electron and Ambipolar Transport in Organic Field-Effect Transistors.
Chem. Rev. **107**, 1296–1323 (2007).

[146] K. M. Mullen and I. van Stokkum.
TIMP: An R package for Modeling Multi-way Spectroscopic Measurements.
Journal of Statistical Software **18** (2007).

[147] A. Hipke.
Ultrafast dynamics of the novel, intrinsically chiral model bisporphyrin beta,beta-prime linked Bis[Tetraphenylporphyrinato-Zinc(II)].
Masterarbeit, Würzburg (2011).

[148] Q. Xu, D. Moses, and A. J. Heeger.
Direct observation of a time-delayed intermediate state generated via exciton-exciton annihilation in polyfluorene.
Physical Review B **68**, 174303 (2003).

[149] V. Gulbinas, I. Mineviciute, D. Hertel, R. Wellander, A. Yartsev, and V. Sundström.
Exciton diffusion and relaxation in methyl-substituted polyparaphenylene polymer films.
The Journal of Chemical Physics **127**, 144907 (2007).

[150] A. Lewis, A. Ruseckas, O. P. Gaudin, G. Webster, P. Burn, and I. Samuel.

Singlet exciton diffusion in MEH-PPV films studied by exciton-exciton annihilation.
Organic Electronics **7**, 452–456 (2006).

[151] C. Lambert, G. Nöll, E. Schmälzlin, K. Meerholz, and C. Bräuchle.
Synthesis, (Non)Linear Optical and Redox Properties of a Donor-Substituted Truxenone Derivative.
Chemistry - A European Journal **4**, 2129–2135 (1998).

[152] J. Mager.
Synthese neuer Truxenonderivate.
F-Praktikumsbericht, Würzburg (2007).

[153] G. Nöll.
Elektronentransferprozesse in Triarylaminsystemen.
Dissertation, Regensburg (2001).

[154] J. Köhler, T. Quast, J. Buback, I. Fischer, T. Brixner, P. Nuernberger, B. Geiß, J. Mager, and C. Lambert.
Ultrafast charge-transfer dynamics of donor-substituted truxenones.
Physical Chemistry Chemical Physics **14**, 11081–11089 (2012).

[155] U. Megerle, I. Pugliesi, C. Schriever, C. Sailer, and E. Riedle.
Sub-50 fs broadband absorption spectroscopy with tunable excitation: putting the analysis of ultrafast molecular dynamics on solid ground.
Applied Physics B: Lasers and Optics **96**, 215–231 (2009).

[156] W. N. Martens, R. L. Frost, J. Kristof, and J. Theo Kloprogge.
Raman spectroscopy of dimethyl sulphoxide and deuterated dimethyl sulphoxide at 298 and 77 K.
Journal of Raman Spectroscopy **33**, 84–91 (2002).

[157] P. Anfinrud, C. Johnson, R. Sension, and R. Hochstrasser.
Ultrafast spectroscopic methods.
In *Applied Laser Spectroscopy*. VCH Publishers, Inc. (1992).

[158] R. Hall, B. Valeur, and G. Weber.
Polarization of the fluorescence of triphenylene. A planar molecule with three-fold symmetry.
Chemical Physics Letters **116**, 202–205 (1985).

[159] R. S. Knox and D. Gülen.
Theory of Polarized Fluorescence from Molecular Pairs: Förster Transfer at Large Electronic Coupling.

Photochemistry and Photobiology **57**, 40–43 (1993).

[160] O. P. Varnavski, J. C. Ostrowski, L. Sukhomlinova, R. J. Twieg, G. C. Bazan, and T. Goodson.
Coherent Effects in Energy Transport in Model Dendritic Structures Investigated by Ultrafast Fluorescence Anisotropy Spectroscopy.
J. Am. Chem. Soc. **124**, 1736–1743 (2002).

[161] M. I. Ranasinghe, O. P. Varnavski, J. Pawlas, S. I. Hauck, J. Louie, J. F. Hartwig, and T. Goodson.
Femtosecond Excitation Energy Transport in Triarylamine Dendrimers.
J. Am. Chem. Soc. **124**, 6520–6521 (2002).

[162] W. Fawcett and C. A. Foss Jr.
Solvent effects on simple electron transfer reactions: A comparison of results for homogeneous and heterogeneous systems.
Journal of Electroanalytical Chemistry and Interfacial Electrochemistry **270**, 103–118 (1989).

[163] T. Elsaesser and W. Kaiser.
Vibrational and Vibronic Relaxation of Large Polyatomic Molecules in Liquids.
Annual Review of Physical Chemistry **42**, 83–107 (1991).

[164] G. R. Fleming.
Chemical Applications of Ultrafast Spectroscopy, volume 13 of *International Series of Monographs on Chemistry.*
Oxford University Press, USA (1986).

[165] M. J. S. Dewar, E. G. Zoebisch, E. F. Healy, and J. J. P. Stewart.
Development and use of quantum mechanical molecular models. 76. AM1: a new general purpose quantum mechanical molecular model.
J. Am. Chem. Soc. **107**, 3902–3909 (1985).

[166] S. O. Dümmler.
Pikosekunden-zeitaufgelöste Spektroskopie gemischtvalenter Verbindungen.
Dissertation, Universität Würzburg (2007).

[167] A. V. Szeghalmi, M. Erdmann, V. Engel, M. Schmitt, S. Amthor, V. Kriegisch, G. Nöll, R. Stahl, C. Lambert, D. Leusser, D. Stalke, M. Zabel, and J. Popp.

How Delocalized Is N,N,N',N'-Tetraphenylphenylenediamine Radical Cation? An Experimental and Theoretical Study on the Electronic and Molecular Structure.
J. Am. Chem. Soc. **126**, 7834–7845 (2004).

[168] J. Köhler.
Dynamik der angeregten Zustände Bor-haltiger pi-Systeme und Donor-substituierter Truxenone.
Dissertation, Würzburg (2011).

[169] E. Runge and E. K. U. Gross.
Density-Functional Theory for Time-Dependent Systems.
Physical Review Letters **52**, 997–1000 (1984).

[170] U. Megerle, F. Selmaier, C. Lambert, E. Riedle, and S. Lochbrunner.
Symmetry-dependent solvation of donor-substituted triarylboranes.
Phys. Chem. Chem. Phys. **10**, 6245–6251 (2008).

[171] K. Yoshihara.
Spectroscopic Properties of the Lower-Lying Excited States of Fluorenone.
The Journal of Chemical Physics **45**, 1991 (1966).

[172] L. J. Andrews, A. Deroulede, and H. Linschitz.
Photophysical processes in fluorenone.
J. Phys. Chem. **82**, 2304–2309 (1978).

[173] B. Grimm, R. J. Porra, W. Rüdiger, and H. Scheer (Eds.).
Chlorophylls and Bacteriochlorophylls, volume 25 of *Advances in Photosynthesis and Respiration.*
Springer (2006).

[174] M. J. Warren, A. G. Smith, A. W. Munro, H. M. Girvan, K. J. McLean, M. R. Cheesman, and D. Leys.
Heme and Hemoproteins.
In *Tetrapyrroles*, pp. 160–183. Springer New York, New York, NY (2009).

[175] P. H. Patel, M. Suzuki, E. Adman, A. Shinkai, and L. A. Loeb.
Prokaryotic DNA polymerase I: evolution, structure, and "base flipping" mechanism for nucleotide selection.
Journal of Molecular Biology **308**, 823–837 (2001).

[176] A. A. Karyakin.
Prussian Blue and Its Analogues: Electrochemistry and Analytical Applications.
Electroanalysis **13**, 813–819 (2001).

[177] J. Bartoll.
The early use of Prussian Blue in paintings.
9. International Conference on NDT of Art (2008).

[178] J. F. Endicott, Y. Chen, and P. Xie.
Electron-transfer spectroscopy: donor–acceptor electronic coupling, reorganizational energies, reaction pathways and dynamics.
Coordination Chemistry Reviews **249**, 343–373 (2005).

[179] H. Prakash and P. Natarajan.
Flash photolysis studies of charge-transfer photochemistry of nickel(II) and cobalt(III) complexes.
Research on Chemical Intermediates **29**, 349–364 (2003).

[180] A. Vogler and H. Kunkely.
Luminescent Metal Complexes: Diversity of Excited States.
In H. Yersin (Ed.), *Transition Metal and Rare Earth Compounds*, volume 213, pp. 143–182. Springer Berlin Heidelberg, Berlin, Heidelberg (2001).

[181] V. J. Antonín.
Mechanistic roles of metal-to-ligand charge-transfer excited states in organometallic photochemistry.
Coordination Chemistry Reviews **177**, 219–256 (1998).

[182] C. Chiorboli, M. T. Indelli, and F. Scandola.
Photoinduced Electron/Energy Transfer Across Molecular Bridges in Binuclear Metal Complexes.
In *Molecular Wires and Electronics*, volume 257, pp. 63–102. Springer Berlin Heidelberg, Berlin, Heidelberg (2005).

[183] D. Philp and J. F. Stoddart.
Self-Assembly in Natural and Unnatural Systems.
Angewandte Chemie International Edition in English **35**, 1154–1196 (1996).

[184] U. Kolb, K. Büscher, C. A. Helm, A. Lindner, A. F. Thünemann, M. Menzel, M. Higuchi, and D. G. Kurth.

The solid-state architecture of a metallosupramolecular polyelectrolyte.
Proceedings of the National Academy of Sciences **103**, 10202 –10206 (2006).

[185] B. J. Holliday and C. A. Mirkin.
Strategies for the Construction of Supramolecular Compounds through Coordination Chemistry.
Angewandte Chemie International Edition **40**, 2022–2043 (2001).

[186] V. A. Friese and D. G. Kurth.
Soluble dynamic coordination polymers as a paradigm for materials science.
Coordination Chemistry Reviews **252**, 199–211 (2008).

[187] G. Schwarz, Y. Bodenthin, T. Geue, J. Koetz, and D. G. Kurth.
Structure and Properties of Dynamic Rigid Rod-Like Metallo-Supramolecular Polyelectrolytes in Solution.
Macromolecules **43**, 494–500 (2010).

[188] R. R. Pal, M. Higuchi, and D. G. Kurth.
Optically Active Metallo-Supramolecular Polymers Derived from Chiral Bis-terpyridines.
Organic Letters **11**, 3562–3565 (2009).

[189] P. R. Andres and U. S. Schubert.
New Functional Polymers and Materials Based on 2,2':6',2'-Terpyridine Metal Complexes.
Advanced Materials **16**, 1043–1068 (2004).

[190] U. Michelsen and C. A. Hunter.
Self-Assembled Porphyrin Polymers.
Angewandte Chemie International Edition **39**, 764–767 (2000).

[191] A. El-ghayoury, H. Hofmeier, B. de Ruiter, and U. S. Schubert.
Combining Covalent and Noncovalent Cross-Linking: A Novel Terpolymer for Two-Step Curing Applications.
Macromolecules **36**, 3955–3959 (2003).

[192] T. K. Sievers, A. Vergin, H. Möhwald, and D. G. Kurth.
Thin Films of Cross-Linked Metallo-Supramolecular Coordination Polyelectrolytes.
Langmuir **23**, 12179–12184 (2007).

[193] H. J. Yoon, J. Kuwabara, J. Kim, and C. A. Mirkin.
Allosteric Supramolecular Triple-Layer Catalysts.
Science **330**, 66 –69 (2010).

[194] M. A. Lawandy, X. Huang, R. Wang, J. Li, J. Y. Lu, T. Yuen, and C. L. Lin.
Two-Dimensional Coordination Polymers with One-Dimensional Magnetic Chains: Hydrothermal Synthesis, Crystal Structure, and Magnetic and Thermal Properties of [MCl2(4,4'-bipyridine)] (M = Fe, Co, Ni, Co/Ni).
Inorg. Chem. **38**, 5410–5414 (1999).

[195] S. Bidault, L. Viau, O. Maury, S. Brasselet, J. Zyss, E. Ishow, K. Nakatani, and H. Le Bozec.
Optically Tunable Nonlinearities in Polymers Based on Photoisomerizable Metal-Based Coordination Complexes.
Advanced Functional Materials **16**, 2252–2262 (2006).

[196] B. Hasenknopf, J. M. Lehn, G. Baum, and D. Fenske.
Self-assembly of a heteroduplex helicate from two different ligand strands and Cu(II) cations.
Proceedings of the National Academy of Sciences **93**, 1397 –1400 (1996).

[197] G. M. Whitesides and M. Boncheva.
Beyond molecules: Self-assembly of mesoscopic and macroscopic components.
Proceedings of the National Academy of Sciences **99**, 4769 –4774 (2002).

[198] M. Shimomura and T. Sawadaishi.
Bottom-up strategy of materials fabrication: a new trend in nanotechnology of soft materials.
Current Opinion in Colloid & Interface Science **6**, 11–16 (2001).

[199] T. Vermonden, J. van der Gucht, P. de Waard, A. T. M. Marcelis, N. A. M. Besseling, E. J. R. Sudhölter, G. J. Fleer, and M. A. Cohen Stuart.
Water-Soluble Reversible Coordination Polymers: Chains and Rings.
Macromolecules **36**, 7035–7044 (2003).

[200] Y. Bodenthin, G. Schwarz, Z. Tomkowicz, M. Lommel, T. Geue, W. Haase, H. Möhwald, U. Pietsch, and D. Kurth.

Spin-crossover phenomena in extended multi-component metallo-supramolecular assemblies.
Coordination Chemistry Reviews **253**, 2414–2422 (2009).

[201] Y. Bodenthin, U. Pietsch, H. Möhwald, and D. G. Kurth.
Inducing Spin Crossover in Metallo-supramolecular Polyelectrolytes through an Amphiphilic Phase Transition.
J. Am. Chem. Soc. **127**, 3110–3114 (2005).

[202] D. G. Kurth, P. Lehmann, and M. Schütte.
A route to hierarchical materials based on complexes of metallo-supramolecular polyelectrolytes and amphiphiles.
Proceedings of the National Academy of Sciences **97**, 5704 –5707 (2000).

[203] D. G. Kurth, N. Severin, and J. P. Rabe.
Perfectly Straight Nanostructures of Metallosupramolecular Coordination-Polyelectrolyte Amphiphile Complexes on Graphite.
Angewandte Chemie International Edition **41**, 3681–3683 (2002).

[204] D. G. Kurth, A. Meister, A. F. Thünemann, and G. Förster.
Structure of a Liquid Crystalline Metallosupramolecular Polyelectrolyte-Amphiphile Complex at the Nanoscopic Level.
Langmuir **19**, 4055–4057 (2003).

[205] N. Severin, I. M. Sokolov, N. Miyashita, D. G. Kurth, and J. P. Rabe.
Self-Sorting of Polyelectrolyte-Amphiphile Complexes on a Graphite Surface.
Macromolecules **40**, 5182–5186 (2007).

[206] F. S. Han, M. Higuchi, and D. G. Kurth.
Metallo-Supramolecular Polymers Based on Functionalized Bisterpyridines as Novel Electrochromic Materials.
Advanced Materials **19**, 3928–3931 (2007).

[207] F. S. Han, M. Higuchi, and D. G. Kurth.
Metallosupramolecular Polyelectrolytes Self-Assembled from Various Pyridine Ring-Substituted Bisterpyridines and Metal Ions: Photophysical, Electrochemical, and Electrochromic Properties.
Journal of the American Chemical Society **130**, 2073–2081 (2008).

[208] K. Sénéchal-David, J. P. Leonard, S. E. Plush, and T. Gunnlaugsson.
Supramolecular Self-Assembly of Mixed f-d Metal Ion Conjugates.
Org. Lett. **8**, 2727–2730 (2006).

[209] M.-a. Haga, T. Takasugi, A. Tomie, M. Ishizuya, T. Yamada, M. D. Hossain, and M. Inoue.
Molecular design of a proton-induced molecular switch based on rod-shaped Ru dinuclear complexes with bis-tridentate 2,6-bis(benzimidazol-2-yl)pyridine derivatives.
Dalton Trans. pp. 2069–2079 (2003).

[210] D. G. Kurth, J. P. López, and W. Dong.
A new Co(II)-metalloviologen-based electrochromic material integrated in thin multilayer films.
Chem. Commun. pp. 2119–2121 (2005).

[211] H. Krass, G. Papastavrou, and D. G. Kurth.
Layer-by-Layer Self-assembly of a Polyelectrolyte Bearing Metal Ion Coordination and Electrostatic Functionality.
Chem. Mater. **15**, 196–203 (2002).

[212] M. Higuchi, Y. Akasaka, T. Ikeda, A. Hayashi, and D. G. Kurth.
Electrochromic Solid-State Devices Using Organic-Metallic Hybrid Polymers.
Journal of Inorganic and Organometallic Polymers and Materials **19**, 74–78 (2008).

[213] Y. Bodenthin, G. Schwarz, and D. G. Kurth.
Spin-Übergänge in supramolekularen Strukturen. Für Speicherbausteine von morgen?
Chemie in unserer Zeit **42**, 256–263 (2008).

[214] M. Schütte, D. G. Kurth, M. R. Linford, H. Cölfen, and H. Möhwald.
Metallosupramolecular Thin Polyelectrolyte Films.
Angewandte Chemie International Edition **37**, 2891–2893 (1998).

[215] D. H. Wilkins and G. Frederick Smith.
2,6-Bis(2-pyridyl)pyridine and alkyl derivatives.Their properties in the formation of ferrous and cobaltous colored complex cations.
Analytica Chimica Acta **9**, 338–348 (1953).

[216] E. C. Constable and H. J. Emeléus.
The Coordination Chemistry of 2,2':6',2'-Terpyridine and Higher Oligopyridines.
In *Advances in Inorganic Chemistry*, volume Volume 30, pp. 69–121. Academic Press (1986).

[217] E. C. Constable and A. M. W. C. Thompson.
Multinucleating 2,2' : 6',2'-terpyridine ligands as building blocks for the assembly of co-ordination polymers and oligomers.
J. Chem. Soc., Dalton Trans. pp. 3467–3475 (1992).

[218] D. G. Kurth, M. Schütte, and J. Wen.
Metallo-supramolecular polyelectrolyte multilayers with cobalt(II): preparation and properties.
Colloids and Surfaces A: Physicochemical and Engineering Aspects **198-200**, 633–643 (2002).

[219] F. Palacio, J. Ramos, and C. Castro.
Magnetic Polymers.
Molecular Crystals and Liquid Crystals Science and Technology. Section A. Molecular Crystals and Liquid Crystals **232**, 173–194 (1993).

[220] D. G. Kurth and M. Higuchi.
Transition metal ions: weak links for strong polymers.
Soft Matter **2**, 915 (2006).

[221] A. Lindner, M. Menzel, F. Renz, D. G. Kurth, and A. F. Thünemann.
Metallosupramolecular coordination polyelectrolytes investigated by Mössbauer spectroscopy.
Hyperfine Interactions **166**, 465–468 (2006).

[222] A. Lapini, P. Foggi, L. Bussotti, R. Righini, and A. Dei.
Relaxation dynamics in three polypyridyl iron(II)-based complexes probed by nanosecond and sub-picosecond transient absorption spectroscopy.
Inorganica Chimica Acta **361**, 3937–3943 (2008).

[223] W. Gawelda, A. Cannizzo, V. Pham, F. van Mourik, C. Bressler, and M. Chergui.
Ultrafast Nonadiabatic Dynamics of [FeII(bpy)3]2+ in Solution.
Journal of the American Chemical Society **129**, 8199–8206 (2007).

[224] J. J. McGarvey and I. Lawthers.
Photochemically induced pertubation of the 1A-reversible-5T equilirium.
Journal of the Chemical Society-Chemical Communications pp. 906–907 (1982).

[225] Y. Bodenthin, G. Schwarz, Z. Tomkowicz, T. Geue, W. Haase, U. Pietsch, and D. G. Kurth.

Liquid Crystalline Phase Transition Induces Spin Crossover in a Polyelectrolyte Amphiphile Complex.
J. Am. Chem. Soc. **131**, 2934–2941 (2009).

[226] M. Förster.
Design and implementation of four-wave-mixing setups in the ultraviolet regime.
Masterarbeit, Würzburg (2011).

[227] P. Nuernberger, G. Krampert, T. Brixner, and G. Vogt.
Rotation-translation device for condensed-phase spectroscopy with small sample volumes.
Review of Scientific Instruments **77**, 083113 (2006).

[228] D. Polli, L. Lüer, and G. Cerullo.
High-time-resolution pump-probe system with broadband detection for the study of time-domain vibrational dynamics.
Review of Scientific Instruments **78**, 103108 (2007).

[229] P. M. Schulze.
Beschreibende Statistik.
Oldenbourg, München [u.a.] (2007).

[230] T. Polack, J. P. Ogilvie, S. Franzen, M. H. Vos, M. Joffre, J. Martin, and A. Alexandrou.
CO vibration as a probe of ligand dissociation and transfer in myoglobin.
Phys. Rev. Lett. **93**, 018102 (2004).

[231] N. Dudovich, D. Oron, and Y. Silberberg.
Single-pulse coherently controlled nonlinear Raman spectroscopy and microscopy.
Nature **418**, 512–514 (2002).

[232] B. von Vacano, W. Wohlleben, and M. Motzkus.
Actively shaped supercontinuum from a photonic crystal fiber for nonlinear coherent microspectroscopy.
Optics Letters **31**, 413–415 (2006).

[233] A. Zumbusch, G. R. Holtom, and X. S. Xie.
Three-Dimensional Vibrational Imaging by Coherent Anti-Stokes Raman Scattering.
Physical Review Letters **82**, 4142–4145 (1999).

[234] M. Cho.
Coherent two-dimensional optical spectroscopy.
Chemical Reviews **108**, 1331–1418 (2008).

[235] U. Selig, F. Langhojer, F. Dimler, T. Löhrig, C. Schwarz, B. Gieseking, and T. Brixner.
Inherently phase-stable coherent two-dimensional spectroscopy using only conventional optics.
Optics Letters **33**, 2851—2853 (2008).

[236] E. M. Grumstrup, S. Shim, M. A. Montgomery, N. H. Damrauer, and M. T. Zanni.
Facile collection of two-dimensional electronic spectra using femtosecond pulse-shaping technology.
Optics Express **15**, 16681–16689 (2007).

[237] N. Forget, V. Crozatier, and T. Oksenhendler.
Pulse-measurement techniques using a single amplitude and phase spectral shaper.
Journal of the Optical Society of America B **27**, 742–756 (2010).

[238] C. Iaconis and I. Walmsley.
Spectral phase interferometry for direct electric-field reconstruction of ultrashort optical pulses.
Optics Letters **23**, 792–794 (1998).

[239] B. von Vacano, T. Buckup, and M. Motzkus.
Shaper-assisted collinear SPIDER: fast and simple broadband pulse compression in nonlinear microscopy.
Journal of the Optical Society of America B **24**, 1091–1100 (2007).

[240] V. V. Yakovlev, C. J. Bardeen, J. Che, J. Cao, and K. R. Wilson.
Chirped pulse enhancement of multiphoton absorption in molecular iodine.
The Journal of Chemical Physics **108**, 2309–2313 (1998).

[241] V. Lozovoy, S. Antipin, F. Gostev, A. Titov, D. Tovbin, O. Sarkisov, A. Vetchinkin, and S. Umanskii.
Experimental demonstration of the coherent control of the molecular iodine vibrational dynamics by chirped femtosecond light pulses.
Chemical Physics Letters **284**, 221–229 (1998).

[242] C. Bardeen, V. Yakovlev, J. Squier, and K. Wilson.

Quantum control of population transfer in green fluorescent protein by using chirped femtosecond pulses.
Journal of the American Chemical Society **120**, 13023–13027 (1998).

[243] Min-Chul Yoon, Dae Hong Jeong, Sung Cho, Dongho Kim, Hanju Rhee, and Taiha Joo.
Ultrafast transient dynamics of Zn(II) porphyrins: Observation of vibrational coherence by controlling chirp of femtosecond pulses.
Journal of Chemical Physics **118**, 164 (2003).

[244] G. Vogt, G. Krampert, P. Niklaus, P. Nuernberger, and G. Gerber.
Optimal Control of Photoisomerization.
Physical Review Letters **94**, 068305 (2005).

[245] G. Vogt, P. Nuernberger, G. Gerber, R. Improta, and F. Santoro.
Femtosecond study on the isomerization dynamics of NK88. II. Excited-state dynamics.
The Journal of Chemical Physics **125**, 044513 (2006).

[246] B. Dietzek, B. Brüggemann, T. Pascher, and A. Yartsev.
Pump-Shaped Dump Optimal Control Reveals the Nuclear Reaction Pathway of Isomerization of a Photoexcited Cyanine Dye.
Journal of the American Chemical Society **129**, 13014–13021 (2007).

[247] A. Lindinger, C. Lupulescu, A. Bartelt, v. Vajda, and L. Wöste.
Coherent control of alkali cluster fragmentation dynamics.
Spectrochimica Acta Part B: Atomic Spectroscopy **58**, 1109–1124 (2003).

[248] V. V. Lozovoy, X. Zhu, T. C. Gunaratne, D. A. Harris, J. C. Shane, and M. Dantus.
Control of Molecular Fragmentation Using Shaped Femtosecond Pulses.
J. Phys. Chem. A **112**, 3789–3812 (2008).

[249] J. Plenge, A. Wirsing, I. Wagner-Drebenstedt, I. Halfpap, B. Kieling, B. Wassermann, and E. Rühl.
Coherent control of the ultrafast dissociative ionization dynamics of bromochloroalkanes.
Phys. Chem. Chem. Phys. **13**, 8705–8714 (2011).

[250] P. Nuernberger, D. Wolpert, H. Weiss, and G. Gerber.
Initiation and control of catalytic surface reactions with shaped femtosecond laser pulses.
Phys. Chem. Chem. Phys. **14**, 1185–1199 (2011).

[251] M. P. A. Branderhorst, P. Londero, P. Wasylczyk, C. Brif, R. L. Kosut, H. Rabitz, and I. A. Walmsley.
Coherent Control of Decoherence.
Science **320**, 638–643 (2008).

[252] D. Wolpert.
Quantum Control of Photoinduced Chemical Reactions.
Dissertation, Universität Würzburg (2008).

[253] R. Spitzenpfeil, S. Eyring, C. Kern, C. Ott, J. Lohbreier, J. Henneberger, N. Franke, S. Jung, D. Walter, M. Weger, C. Winterfeldt, T. Pfeifer, and C. Spielmann.
Enhancing the brilliance of high-harmonic generation.
Applied Physics A **96**, 69–81 (2009).

[254] T. Brixner, G. Krampert, T. Pfeifer, R. Selle, G. Gerber, M. Wollenhaupt, O. Graefe, C. Horn, D. Liese, and T. Baumert.
Quantum Control by Ultrafast Polarization Shaping.
Physical Review Letters **92**, 208301 (2004).

[255] N. Dudovich, D. Oron, and Y. Silberberg.
Quantum Control of the Angular Momentum Distribution in Multiphoton Absorption Processes.
Physical Review Letters **92**, 103003 (2004).

[256] M. Aeschlimann, M. Bauer, D. Bayer, T. Brixner, F. J. García de Abajo, W. Pfeiffer, M. Rohmer, C. Spindler, and F. Steeb.
Adaptive subwavelength control of nano-optical fields.
Nature **446**, 301–304 (2007).

[257] M. Aeschlimann, T. Brixner, S. Cunovic, A. Fischer, P. Melchior, W. Pfeiffer, M. Rohmer, C. Schneider, C. Struber, P. Tuchscherer, and D. V. Voronine.
Nano-optical Control of Hot-Spot Field Superenhancement on a Corrugated Silver Surface.
IEEE Journal of Selected Topics in Quantum Electronics **PP**, 1–8 (2011).

[258] D. Oron, N. Dudovich, and Y. Silberberg.
Femtosecond Phase-and-Polarization Control for Background-Free Coherent Anti-Stokes Raman Spectroscopy.
Physical Review Letters **90**, 213902 (2003).

[259] D. V. Voronine, D. Abramavicius, and S. Mukamel.
Coherent control of cross-peaks in chirality-induced two-dimensional optical signals of excitons.
The Journal of Chemical Physics **125**, 224504 (2006).

[260] T. Löhrig.
Planung und Realisierung eines Aufbaus zur Formung ultrabreitbandiger fs-Laserpulse im sicht- baren Spektralbereich.
Diplomarbeit, Universität Würzburg (2007).

[261] Cambridge Research & Instrumentation, Inc.
SLM Spatial Light Modulator, User's manual (2006).

[262] H. Kogelnik.
Coupled wave theory for thick hologram gratings.
Bell System Technical Journal **48**, 2909–2947 (1969).

[263] J. Arns, W. Colburn, and S. Barden.
Volume phase gratings for spectroscopy, ultrafast laser compressors, and wavelength division multiplexing.
Current Developments in Optical Design and Optical Engineering VIII **3779**, 313–323 (1999).

[264] S. C. Barden, J. A. Arns, W. S. Colburn, and J. B. Williams.
Volume-Phase Holographic Gratings and the Efficiency of Three Simple Volume-Phase Holographic Gratings.
Publications of the Astronomical Society of the Pacific **112**, 809–820 (2000).

[265] P. Blanche, P. Gailly, S. Habraken, P. Lemaire, and C. Jamar.
Volume phase holographic gratings: large size and high diffraction efficiency.
Optical Engineering **43**, 2603–2612 (2004).

[266] I. K. Baldry, J. Bland-Hawthorn, and J. G. Robertson.
Volume Phase Holographic Gratings: Polarization Properties and Diffraction Efficiency.
Publications of the Astronomical Society of the Pacific **116**, 403–414 (2004).

[267] C. B. Schwarz.
Erzeugung, Charakterisierung und Formung ultrabreitbandiger Femtosekunden-Laserpulse im sichtbaren Spektralbereich.
Diplomarbeit, Universität Würzburg (2009).

[268] F. Kanal.
Raytracing-Simulationen zum in der Höhe gefalteten Nulldispersionskompressor.
Praktikumsbericht, Universität Würzburg (2008).

[269] J. M. Diels, J. J. Fontaine, I. C. McMichael, and F. Simoni.
Control and measurement of ultrashort pulse shapes (in amplitude and phase) with femtosecond accuracy.
Applied Optics **24**, 1270–1282 (1985).

[270] D. J. Kane and R. Trebino.
Single-shot measurement of the intensity and phase of an arbitrary ultrashort pulse by using frequency-resolved optical gating.
Optics Letters **18**, 823–825 (1993).

[271] S. Linden, H. Giessen, and J. Kuhl.
XFROG - A new method for amplitude and phase characterization of weak ultrashort pulses.
Physica status solidi B-basic research **206**, 119—124 (1998).

[272] V. V. Lozovoy, I. Pastirk, and M. Dantus.
Multiphoton intrapulse interference. IV. Ultrashort laserpulse spectral phase characterization and compensation.
Optics Letters **29**, 775–777 (2004).

[273] D. Kane and R. Trebino.
Characterization of arbitrary femtosecond pulses using frequency-resolved optical gating.
Quantum Electronics, IEEE Journal of **29**, 571–579 (1993).

[274] X. Gu, L. Xu, M. Kimmel, E. Zeek, P. O'Shea, A. P. Shreenath, R. Trebino, and R. S. Windeler.
Frequency-resolved optical gating and single-shot spectral measurements reveal fine structure in microstructure-fiber continuum.
Optics Letters **27**, 1174–1176 (2002).

[275] A. Baltuska, M. S. Pshenichnikov, and D. A. Wiersma.
Amplitude and phase characterization of 4.5-fs pulses by frequency-resolved optical gating.
Optics Letters **23**, 1474–1476 (1998).

[276] T. S. Clement, A. J. Taylor, and D. J. Kane.
Single-shot measurement of the amplitude and phase of ultrashort laser pulses in the violet.

Optics Letters **20**, 70–72 (1995).

[277] J. Dudley, L. Barry, P. Bollond, J. Harvey, and R. Leonhardt.
Characterizing Pulse Propagation in Optical Fibers around 1550 nm Using Frequency-Resolved Optical Gating.
Optical Fiber Technology **4**, 237–265 (1998).

[278] G. Taft, A. Rundquist, M. M. Murnane, I. P. Christov, H. C. Kapteyn, K. W. DeLong, D. N. Fittinghoff, M. A. Krumbugel, J. N. Sweetser, and R. Trebino.
Measurement of 10-fs laser pulses.
IEEE Journal of Selected Topics in Quantum Electronics **2**, 575–585 (1996).

[279] C. G. Durfee III, S. Backus, H. C. Kapteyn, and M. M. Murnane.
Intense 8-fs pulse generation in the deep ultraviolet.
Optics Letters **24**, 697–699 (1999).

[280] H. Stark.
Image Recovery: Theory and Application.
Academic Press (1987).

[281] J. R. Fienup.
Phase retrieval algorithms: a comparison.
Applied Optics **21**, 2758–2769 (1982).

[282] R. Trebino and D. J. Kane.
Using phase retrieval to measure the intensity and phase of ultrashort pulses: frequency-resolved optical gating.
Journal of the Optical Society of America A **10**, 1101–1111 (1993).

[283] K. W. DeLong, D. N. Fittinghoff, R. Trebino, B. Kohler, and K. Wilson.
Pulse retrieval in frequency-resolved optical gating based on the method of generalized projections.
Optics Letters **19**, 2152–2154 (1994).

[284] K. W. DeLong and R. Trebino.
Improved ultrashort pulse-retrieval algorithm for frequency-resolved optical gating.
Journal of the Optical Society of America A **11**, 2429–2437 (1994).

[285] K. W. DeLong, R. Trebino, and D. J. Kane.
Comparison of ultrashort-pulse frequency-resolved-optical-gating traces for three common beam geometries.

Journal of the Optical Society of America B **11**, 1595–1608 (1994).

[286] J. N. Sweetser, D. N. Fittinghoff, and R. Trebino.
Transient-grating frequency-resolved optical gating.
Optics Letters **22**, 519–521 (1997).

[287] T. Tsang, M. A. Krumbugel, K. W. DeLong, D. N. Fittinghoff, and R. Trebino.
Frequency-resolved optical-gating measurements of ultrashort pulses using surface third-harmonic generation.
Optics Letters **21**, 1381–1383 (1996).

[288] M. Keller.
Erzeugung und Charakterisierung ultrakurzer Lichtpulse im Sichtbaren.
Praktikumsbericht, Würzburg (2007).

[289] S. Shim and M. T. Zanni.
How to turn your pump–probe instrument into a multidimensional spectrometer: 2D IR and Vis spectroscopies via pulse shaping.
Physical Chemistry Chemical Physics **11**, 748–761 (2009).

[290] I. Amat-Roldán, I. Cormack, P. Loza-Alvarez, E. Gualda, and D. Artigas.
Ultrashort pulse characterisation with SHG collinear-FROG.
Optics Express **12**, 1169–1178 (2004).

[291] G. Stibenz and G. Steinmeyer.
Interferometric frequency-resolved optical gating.
Optics Express **13**, 2617–2626 (2005).

[292] A. V. Oppenheim and R. W. Schafer.
Digital Signal Processing.
US ed edition. Prentice Hall (1975).

[293] A. Baltuska, M. Pshenichnikov, and D. Wiersma.
Second-harmonic generation frequency-resolved optical gating in the single-cycle regime.
IEEE Journal of Quantum Electronics **35**, 459–478 (1999).

[294] A. Baltuska and T. Kobayashi.
Adaptive shaping of two-cycle visible pulses using a flexible mirror.
Applied Physics B: Lasers and Optics **75**, 427–443 (2002).

[295] R. Morita, M. Hirasawa, N. Karasawa, S. Kusaka, N. Nakagawa, K. Yamane, L. Li, A. Suguro, and M. Yamashita.
Sub-5 fs optical pulse characterization.
Measurement Science and Technology **13**, 1710–1720 (2002).

[296] B. Wu, D. Tang, N. Ye, and C. Chen.
Linear and nonlinear optical properties of the KBe2BO3F2 (KBBF) crystal.
Optical Materials **5**, 105–109 (1996).

[297] K. Hussain and P. Kumbhakar.
Nonlinear optical properties of some newly developed crystals for measurement of ultrafast laser pulses.
Brazilian Journal of Physics **36**, 1281–1284 (2006).

[298] C. D. McMillen and J. W. Kolis.
Hydrothermal crystal growth of ABe2BO3F2 (A=K, Rb, Cs, Tl) NLO crystals.
Journal of Crystal Growth **310**, 2033–2038 (2008).

[299] D. N. Fittinghoff, J. L. Bowie, J. N. Sweetser, R. T. Jennings, M. A. Krumbügel, K. W. DeLong, R. Trebino, and I. A. Walmsley.
Measurement of the intensity and phase of ultraweak, ultrashort laser pulses.
Optics Letters **21**, 884–886 (1996).

[300] W. J. Walecki, D. N. Fittinghoff, A. L. Smirl, and R. Trebino.
Characterization of the polarization state of weak ultrashort coherent signals by dual-channel spectral interferometry.
Optics Letters **22**, 81–83 (1997).

[301] A. Gerrard and J. M. Burch.
Introduction to Matrix Methods in Optics.
Dover Publications (1994).

[302] T. Brixner.
Adaptive Femtosecond Quantum Control.
Dissertation, Universität Würzburg (2001).

[303] P. Nuernberger, R. Selle, F. Langhojer, F. Dimler, S. Fechner, G. Gerber, and T. Brixner.
Polarization-shaped femtosecond laser pulses in the ultraviolet.
Journal of Optics A: Pure and Applied Optics **11**, 085202 (2009).

[304] C. Dorrer and I. A. Walmsley.
Accuracy criterion for ultrashort pulse characterization techniques: application to spectral phase interferometry for direct electric field reconstruction.
Journal of the Optical Society of America B **19**, 1019–1029 (2002).

[305] P. Nuernberger.
Differences and analogies between linearly chirped and colored double pulses in the femtosecond regime.
Optics Communications **282**, 227–235 (2009).

[306] M. Shapiro and P. Brumer.
Quantum control of chemical reactions.
Journal of the Chemical Society, Faraday Transactions **93**, 1263–1277 (1997).

[307] E. Frishman, M. Shapiro, D. Gerbasi, and P. Brumer.
Enantiomeric purification of nonpolarized racemic mixtures using coherent light.
The Journal of Chemical Physics **119**, 7237–7246 (2003).

[308] E. Frishman, M. Shapiro, and P. Brumer.
Optical purification of racemic mixtures by laser distillation in the presence of a dissipative bath.
Journal of Physics B: Atomic, Molecular and Optical Physics **37**, 2811–2821 (2004).

[309] M. Shapiro, E. Frishman, and P. Brumer.
Coherently Controlled Asymmetric Synthesis with Achiral Light.
Physical Review Letters **84**, 1669 (2000).

[310] K. Hoki, D. Kröner, and J. Manz.
Selective preparation of enantiomers from a racemate by laser pulses: model simulation for oriented atropisomers with coupled rotations and torsions.
Chemical Physics **267**, 59–79 (2001).

[311] S. S. Bychkov, B. A. Grishanin, and V. N. Zadkov.
Laser synthesis of chiral molecules in isotropic racemic media.
Journal of Experimental and Theoretical Physics **93**, 24–32 (2001).

[312] A. Steinbacher.
High-Precision Chirality-Sensitive Spectroscopy in the Liquid Phase.
Masterarbeit, Würzburg (2010).

[313] S. Schott.
Theoretische und experimentelle Konzeption eines Aufbaus zur Erzeugung von Pulsenantiomeren.
Diplomarbeit, Würzburg (2011).

Acknowledgements

It is very important to me to point out that the research presented in this thesis profited strongly from the supportive and cooperative atmosphere in the departement of Physical Chemistry. Many colleagues and cooperation partners contributed in one way or the other to the success of this work. I am grateful to all of them, and I want to mention the most important ones by name.

- Prof. Dr. Tobias Brixner for giving me the opportunity to join his research group, for his support, suggestions and many fruitful discussions. Also for the possibility of working closely with different groups from the Chemistry Department and of broadening my horizon by letting me visit many interesting conferences.

- Prof. Dr. Christoph Lambert for the excellent cooperation regarding the truxenone and the TARA–PCTM projects, especially for providing the chemical background that greatly helped to advance these projects.

- Prof. Dr. Ingo Fischer for fruitful discussions and helpful suggestions regarding the truxenone project.

- Prof. Dr. Dirk Kurth for the cooperation and fruitful discussions regarding the MEPE project.

- Dr. Patrick Nürnberger for his patience and openness, many fruitful discussions and helpful suggestions, no matter which project I bothered him with.

- My Diploma-student Florian Kanal and my Master-student Sabine Keiber for their great work on the spectroscopy projetcs and the fun time in the lab, for never losing their humour even when facing multiple amplifier output pulses, climate-control failures and other kinds of annoyance.

- My colleague Dr. Juliane Köhler for working with me on the truxenone project, for a great and fun cooperation, no matter what time of the day (or night) we spent in the lab to acquire our data.

- My colleague Andreas Steinbacher for his work on the pulse-shaping project, for his humorous personality and lightening up my mood by his "slogan of the week".

- Dr. Dörte Reitzenstein and Iris Hasslauer for preparing and supplying the TARA-PCTM and MEPE samples.

- Everybody who contributed to the spectroscopic measurements, especially Johannes Buback, Stefan Rützel and Martin Kullmann.

- Alexander Schmiedel for his invaluable help in the lab, great parties, barbecues and other social events.

- Our technical staff Sabine Fuchs, Belinda Böhm and Gudrun Mühlrath for their help in the lab and on many other occasions.

- The staff from the mechanics and electronics shop for quickly and reliably manufacturing whatever special components I needed for my setups.

- Our secretary Andrea Gehring for taking care of administrative tasks of all sorts.

- The research training school GRK1221 for helping a physicist understand chemists better (and *vice versa*), for many interesting talks, seminars, conferences, barbecues and social events of all kinds. Being part of this interdisciplinary and supportive research training school was a great experience.

- Florian, Andreas and Patrick for proofreading this thesis, Florian especially for everything hyphenation-related.

- My office mates Christian Rewitz, Philipp Rudolph, Fabian Ebert and Florian Kanal from "Die wilde Dreizehn" for the great atmosphere. With those guys as desktop neighbours, working in the office was always fun.

- Stefan Rützel for the coffee machine. Good coffee definitely increases the productivity.

- Every other member of our group I have not mentioned yet. The atmosphere and the mutual support in the group have always been great, not only regarding scientific matters but also on a more personal level.
- My parents, family and friends for their support and for alyways being there for me.
- My husband Jan for his support, sympathy and belief in me. For being such a wonderful person. And, above all, for his love.

Erklärung

Hiermit erkläre ich an Eides statt, dass ich die Dissertation „Spectroscopic investigation of charge-transfer processes and polarisation pulse shaping in the visible spectral range“ selbstständig angefertigt und keine anderen als die von mir angegebenen Quellen und Hilfsmittel verwendet habe.

Ich erkläre außerdem, dass diese Dissertation weder in gleicher noch in anderer Form bereits in einem Prüfungsverfahren vorgelegen hat.

Ich habe früher außer den mit dem Zulassungsgesuch urkundlich vorgelegten Graden keine weiteren akademischen Grade erworben oder zu erwerben versucht.

Braunschweig, den 24. September 2012

Tatjana Quast